Collège Doctoral du Languedoc-Roussillon

THÈSE

Pour obtenir le grade de

Docteur

Délivré par l'**Université de Montpellier**

Préparée au sein de l'école doctorale **I2S**
Et de l'unité de recherche **IMAG**

Spécialité : **Mathématiques et Modélisation**

Présentée par **Rajnesh Lal**

Data assimilation and uncertainty quantification in cardiovascular biomechanics

Soutenue le 14 June 2017 devant le jury composé de

Pr. Franck Nicoud	IMAG - Univ. de Montpellier	Directeur
Pr. Bijan Mohammadi	IMAG - Univ. de Montpellier	Co-Directeur
Dr. Jean-Frédéric Gerbeau	INRIA Paris - Rocquencourt	Rapporteur
Dr. Pierre-Yves Lagrée	Université Pierre et Marie Curie	Rapporteur
PUPH. Vincent Costalat	CHRU - Gui de Chauliac, Montpellier	Examinateur
Pr. Christophe Prud'homme	IRMA - Université de Strasbourg	Examinateur

UNIVERSITE MONTPELLIER

Abstract

Cardiovascular blood flow simulations can fill several critical gaps in current clinical capabilities. They offer non-invasive ways to quantify hemodynamics in the heart and major blood vessels for patients with cardiovascular diseases, that cannot be directly obtained from medical imaging. Patient-specific simulations (incorporating data unique to the individual) enable individualised risk prediction, provide key insights into disease progression and/or abnormal physiologic detection. They also provide means to systematically design and test new medical devices, and are used as predictive tools to surgical and personalize treatment planning and, thus aid in clinical decision-making. Patient-specific predictive simulations require effective assimilation of medical data for reliable simulated predictions. This is usually achieved by the solution of an inverse hemodynamic problem, where uncertain model parameters are estimated using the techniques for merging data and numerical models known as data assimilation methods.

In this thesis, the inverse problem is solved through a data assimilation method using an ensemble Kalman filter (EnKF) for parameter estimation. By using an ensemble Kalman filter, the solution also comes with a quantification of the uncertainties for the estimated parameters. An ensemble Kalman filter-based parameter estimation algorithm is proposed for patient-specific hemodynamic computations in a schematic arterial network from uncertain clinical measurements. Several in silico scenarii (using synthetic data) are considered to investigate the efficiency of the parameter estimation algorithm using EnKF. The usefulness of the parameter estimation algorithm is also assessed using experimental data from an in vitro test rig and actual real clinical data from a volunteer (patient-specific case). The proposed algorithm is evaluated on arterial networks which include single arteries, cases of bifurcation, a simple human arterial network and a complex arterial network including the circle of Willis.

The ultimate aim is to perform patient-specific hemodynamic analysis in the network of the circle of Willis. Common hemodynamic properties (parameters), like arterial wall properties (Young's modulus, wall thickness, and viscoelastic coefficient) and terminal boundary parameters (reflection coefficient and Windkessel model parameters) are estimated as the solution to an inverse problem using time series pressure values and blood flow rate as measurements. It is also demonstrated that a proper reduced order zero-dimensional compartment model can lead to a simple and reliable estimation of blood flow features in the circle of Willis. The simulations with the estimated parameters capture target pressure or flow rate waveforms at given specific locations.

Keywords: Data assimilation, ensemble Kalman filter, hemodynamic parameter estimation, inverse hemodynamic problems, patient-specific cardiovascular simulations, Young's modulus, 1D blood flow modelling, 0D compartment model, circle of Willis.

Résumé

Les simulations numériques des écoulements sanguins cardiovasculaires peuvent combler d'importantes lacunes dans les capacités actuelles de traitement clinique. En effet, elles offrent des moyens non invasifs pour quantifier l'hémodynamique dans le cœur et les principaux vaisseaux sanguins chez les patients atteints de maladies cardiovasculaires. Ainsi, elles permettent de recouvrer les caractéristiques des écoulements sanguins qui ne peuvent pas être obtenues directement à partir de l'imagerie médicale. Dans ce sens, des simulations personnalisées utilisant des informations propres aux patients aideraient à une prévision individualisée des risques. Nous pourrions en effet, disposer des informations clés sur la progression éventuelle d'une maladie ou détécter de possibles anomalies physiologiques. Les modèles numériques peuvent fournir également des moyens pour concevoir et tester de nouveaux dispositifs médicaux et peuvent être utilisés comme outils prédictifs pour la planification de traitement chirurgical personnalisé. Ils aideront ainsi à la prise de décision clinique. Cependant, une difficulté dans cette approche est que, pour être fiables, les simulations prédictives spécifiques aux patients nécessitent une assimilation efficace de leurs données médicales. Ceci nécessite la solution d'un problème hémodynamique inverse, où les paramètres du modèle sont incertains et sont estimés à l'aide des techniques d'assimilation de données.

Dans cette thèse, le problème inverse pour l'estimation des paramètres est résolu par une méthode d'assimilation de données basée sur un filtre de Kalman d'ensemble (EnKF). Connaissant les incertitudes sur les mesures, un tel filtre permet la quantification des incertitudes liées aux paramètres estimés. Un algorithme d'estimation de paramètres, basé sur un filtre de Kalman d'ensemble, est proposé dans cette thèse pour des calculs hémodynamiques spécifiques à un patient, dans un réseau artériel schématique et à partir de mesures cliniques incertaines. La méthodologie est validée à travers plusieurs scenarii in silico utilisant des données synthétiques. La performance de l'algorithme d'estimation de paramètres est également évaluée sur des données expérimentales pour plusieurs réseaux artériels et dans un cas provenant d'un banc d'essai in vitro et des données cliniques réelles d'un volontaire (cas spécifique du patient).

Le but principal de cette thèse est l'analyse hémodynamique spécifique du patient dans le polygone de Willis, appelé aussi cercle artériel du cerveau. Les propriétés hémodynamiques communes, comme celles de la paroi artérielle (module de Young, épaisseur de la paroi et coefficient viscoélastique), et les paramètres des conditions aux limites (coefficients de réflexion et paramètres du modèle de Windkessel) sont estimés. Il est également démontré qu'un modèle appelé compartiment d'ordre réduit (ou modèle dimension zéro) permet une estimation simple et fiable des caractéristiques du flux sanguin dans le polygone de Willis. De plus, il est ressorti que les simulations avec les paramètres estimés capturent les formes attendues pour les ondes de pression et de débit aux emplacements prescrits par le clinicien.

Mots-clés: Assimilation des données, filtre de Kalman, estimation des paramètres hémodynamiques, problème inverse, simulation cardiovasculaire spécifique au patient, module de Young, modélisation de l'écoulement artériel en 1D, modèle réduit 0D, polygone de Willis.

"Torture the data, and it will confess to anything"

Ronald Coase

To my wife and son.

Acknowledgements

I take this opportunity to extend my sincere gratitude and appreciation to all those who made this Ph.D. thesis possible.

First and foremost, I would like to express my sincere gratitude to my advisors Prof. **Franck NICOUD** and Prof. **Bijan MOHAMMADI** of the Institut Montpelliérain Alexander Grothendieck (IMAG) at the University of Montpellier. I thank them for believing and trusting me as a potential Ph.D. research student when I first contacted them. It has been an honour to be their student. They have taught me, both consciously and unconsciously, how good applied mathematics are done. They have been supportive and cared for my welfare since I applied for my Ph.D. studies at the university. They have helped me come up with the thesis topic and their immense knowledge and guidance helped me in all the time of research and writing of this thesis, also allowing me to work independently the majority of the time. I appreciate all their contributions of time and ideas to make my Ph.D. research experience, productive and stimulating. I very much appreciate their enthusiasm, intensity, continuous support, inspirational discussions, gentle encouragement, and motivation that has contributed immensely to my professional growth in academia. I could not have imagined having better advisors and mentors for my Ph.D. study. I am forever grateful to them.

Merci beaucoup à vous deux.

A special thank goes to Dr. **Simon MENDEZ** for providing support from the beginning. Thank you for your helpful discussions and suggestions during YALES2BIO meetings that contributed to the development of my thesis.

I acknowledge the valuable collaboration of physicians (Prof. **V. COSTALAT** and Dr. **E. LE BARS**) and physicists (Prof. **F. MOLINO** and Dr. **J. DEVERDUN**) at the Department of Neuroradiology at the Centre Hospitalier Regional Universitaire de Montpellier (CHRU), Montpellier, France. I am grateful to them for giving me the opportunity to join their research group as an intern, and for giving access to the laboratory and research facilities. I thank them for their help and support in performing the MRI scans and providing the medical images employed in this thesis, and for training me in the analysis of the acquired images. A further word of thanks for the enthusiastic discussions and feedback on several aspects of the research dealing with the real medical data.

I also appreciate the thesis committee members Dr. **Jean-Frédéric GERBEAU**, Dr. **Pierre-Yves LAGRÉE**, PUPH. **Vincent COSTALAT**, and Dr. **Christophe PRUD'HOMME** for the time, interest, and their critical comments, which enabled me to notice the weaknesses of my thesis and make the necessary improvements according to their comments.

This dissertation would not have been possible without the funding for my Ph.D. studies. I gratefully acknowledge the scholarship received from the **European Union Framework Programme-Erasmus Mundus KITE** by the grant 2013-2617/001-001-EMA2. A special thank goes to former Erasmus Mundus project managers at the University of Montpellier, **Anna BOCHKAREVA** and **Fadhela LAKHDARI** for their support in the administrative work. I am pleased to acknowledge the **French embassy** in Fiji for its administrative work and support. A good support system is important for surviving and staying in a foreign country, and I convey my heartfelt thanks to the **French Government** for supporting and hosting me and my family during my studies in France. I also thank my home university, **Fiji National University**, and the host university, **University of Montpellier**, for offering me an ideal environment in which I felt free and could concentrate on my Ph.D. research.

I thank my fellow lab colleagues and friends for their helpful discussions, sharing of ideas, and for their support and friendship I needed. Thank you, Dr. **Julien SIGUENZA**, for helping me from the beginning, and most importantly, for acting as a volunteer in the acquisition of real medical data for my thesis. I am pleased to acknowledge **Marie Christine BERAUD** for her friendship, company and willingness to assist us at many stages of our stay in France.

I express my profound gratitude to my **parents** and **parents-in-laws** and **families**. Without the many sacrifices made by them, I could have never completed this long journey. I am extremely grateful for their love, prayers, unfailing emotional support and the sacrifices that they have made on my behalf.

I must acknowledge with tremendous and deep thanks to the love, encouragement, eternal support and unwavering belief in me that my wife **Swastika LAL** gave me, without which I would not have been able to complete this long dissertation journey. Her patience and sacrifice will remain my inspiration throughout my life. She has taken care of whatever needed tending to without complaining, just so I could focus on

my research and on completing my dissertation. She has patiently endured many, many long hours alone while I worked on my dissertation. At the same time, she has also given me so many happy and beautiful memories throughout this journey. Thank you with all my heart and soul. Your complete and unconditional love carries me through always. These acknowledgements would not be complete if I did not mention my 4-year-old son **Sashreek LAL**, who has been a twinkle in my eye since he was born. It was wonderful watching him grow in France and his smiles encouraged me to efficiently overcome all difficulties I encountered. I express my deepest love and appreciation to him. Sashreek, I owe you lots and lots of fun hours. Both of you kept things light and me smiling.

To everyone:

Merci beaucoup, Thank you so much, बहुत बहुत धन्यवाद.

R.Lal

Preface

Chapter 4 of this thesis has previously been published as:
Rajnesh Lal, Bijan Mohammadi, and Franck Nicoud, "Data assimilation for identification of cardiovascular network characteristics" in *International Journal for Numerical Methods in Biomedical Engineering*, 2016. doi: 10.1002/cnm.2824.

Part of the chapter 6 has been submitted for publication as:
R. Lal, F. Nicoud, E. Le Bars, J. Deverdun, F. Molino, V. Costalat and B. Mohammadi, "Non invasive blood flow features estimation in cerebral arteries from uncertain medical data" in *Annals of Biomedical Engineering*, 2017.

Contents

List of Figures

List of Tables

Abbreviations

MRI	**M**agnetic **R**esonance **I**maging
KF	**K**alman **F**ilter
EnKF	**E**nsemble **K**alman **F**ilter
MRA	**M**agnetic **R**esonance **A**ngiogram
1D	**O**ne-**D**imensional
0D	**Z**ero-**D**imensional
WK3	**W**indkessel **T**hree element
CR	**C**onstant **R**esistance
CoW	**C**ircle **o**f **W**illis
ICA	**I**nternal **C**arotid **A**rtery
ODE	**O**rdinary **D**ifferential **E**quation(s)
PDE	**P**artial **D**ifferential **E**quations(s)
nobs	**N**umber **o**f **O**bservations
RMSE	**R**oot **M**ean **S**quare **E**rror
R-ICA	**R**ight **I**nternal **C**arotid **A**rtery
L-ICA	**L**eft **I**nternal **C**arotid **A**rtery
MAP	**M**ean **A**rterial **P**ressure
SBP	**S**ystolic **B**lood **P**ressure
DBP	**D**iastolic **B**lood **P**ressure

Chapter 1

Introduction

Contents

1.1 Patient-specific cardiovascular simulations

Considerable progress has been made in recent years towards developing models for blood flow in the cardiovascular system [1–14], that are often based on patient-specific anatomic data.

Patient-specific cardiovascular simulations of healthy and diseased physiologies are very useful to understand the origin and progression of cardiovascular diseases, mechanisms influencing cardiovascular system's function and its physiological and pathological processes, and evaluate the performance of cardiovascular devices through in silico experiments [15]. Mathematical models and simulations are also beneficial and of great interest to biomedical applications such as providing aid in clinical decision-making and treatment through virtual surgeries or virtual implantation of medical devices prior to the actual procedure [16–18].

Computational fluid dynamic (CFD) model [19] based on patient-specific data is used to enhance diagnostic assessment, medical device design and clinical trials [20]. CFD models can compute previously immeasurable hemodynamic parameters such as pressure and flow fields at a temporal and spatial resolution, that is difficult with the current clinical technology [21, 22]. Figure 1.1 describes the specific steps of the CFD simulations and shows the possible computational analysis such as pressure, velocity, and wall shear stress at any point of the 3D model [19].

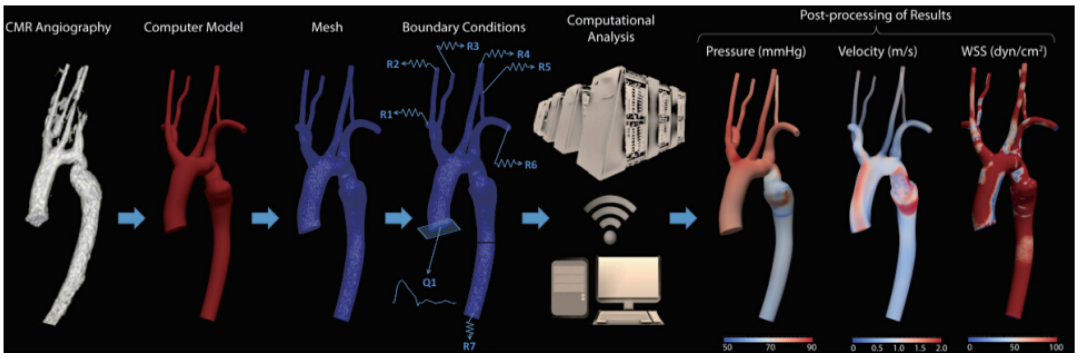

FIGURE 1.1: An example of a patient-specific model and CFD simulation of an aortic coarctation case. The computational analysis is performed and pressure, velocity, and wall shear stress (WSS) in any point of the 3D model are computed. Adapted from Vieira et al. [19].

According to the World Health Organization, cardiovascular diseases are the leading cause of death globally. An estimation of arterial stiffness and pressure in the cerebral arteries are relevant quantities to several cardiovascular diseases. An increase in arterial stiffness is associated with risk factors including hypertension [23], and an estimation of arterial stiffness can be used to assess the cardiovascular condition of a patient [24]. Pressure fluctuations in cerebral arteries are one of the factors related to the formation and risk of rupture of cerebral aneurysms [25–29]. It is possible to solve numerically for the pressure wave system in a network of arteries using one-dimensional (1D) [1, 3, 5, 13, 14] or reduced order zero-dimensional (0D compartment model) [9–12] blood flow models.

A ring-like arterial structure known as the Circle of Willis (CoW) that is located at the base of the brain, linking the main cerebral arterial systems is the pathway for the distribution of oxygenated blood in the cerebral mass [7]. The CoW (see Figure 1.2) is also a common place for intracranial aneurysms (pathological dilatations of the cerebral artery walls) leading to their rupture and causing subarachnoid haemorrhage [30, 31].

The geometric models in this thesis include a network of complex arterial segments from the aorta to the cerebral arteries and including the CoW.

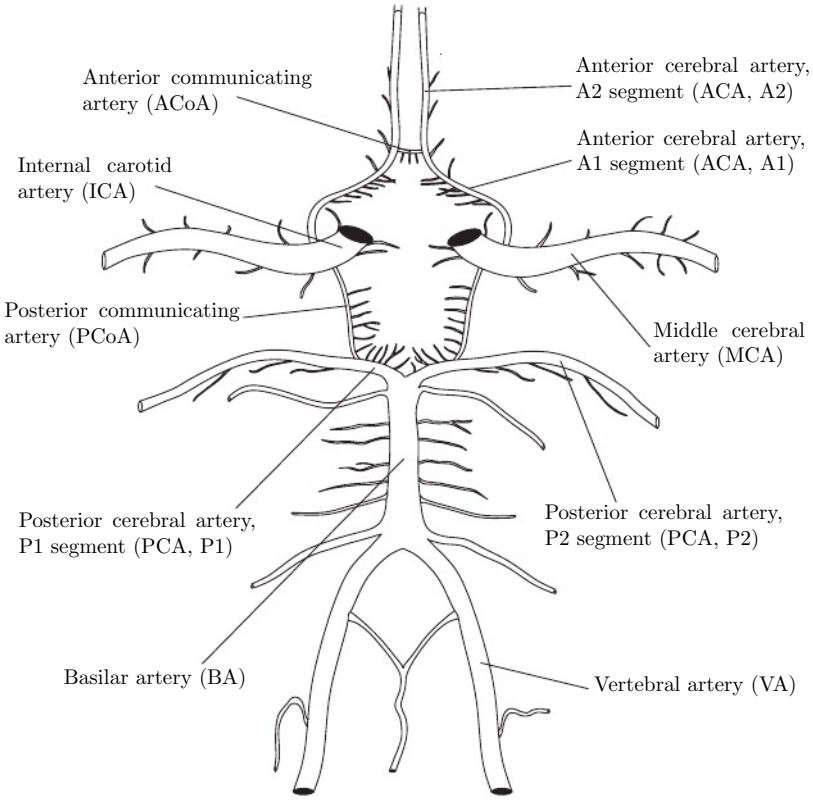

FIGURE 1.2: Schematic representation of the circle of Willis. Adapted from Alastruey et al. [32].

Figure 1.3 shows an example of 1D modelling of blood flow in the CoW. In the figure, the results of the 1D model of Reymond et al. [14] are compared with the in vivo measurement of flow and pressure waves at various cerebral artery locations.

In all cases, mathematical models and numerical simulations require information of the patient's vasculature and physiology together with the geometrical and mechanical properties of arteries. The creation of a patient-specific cardiovascular model simulation typically starts with the acquisition and processing of medical imaging data such as computed tomography (CT), magnetic resonance imaging (MRI), magnetic resonance angiogram (MRA), ultrasound (US), phase contrast magnetic resonance imaging (PCMRI), and positron emission tomography (PET). It is then followed by mesh or grid generation, defining material properties and specifying boundary conditions, and model simulation.

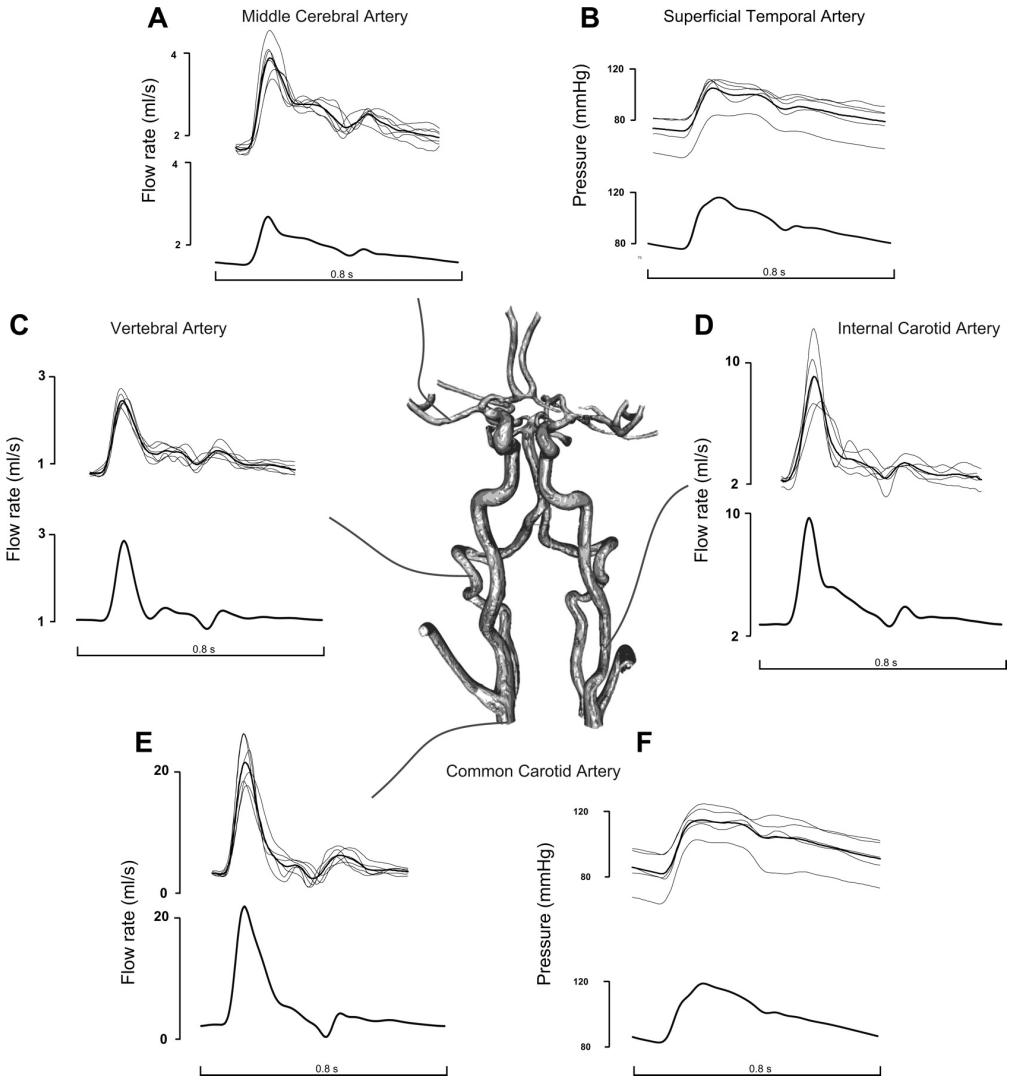

FIGURE 1.3: The 1D model results (bottom) of Reymond et al. [14] compared with in vivo measurements of flow and pressure waves (top panels) at various cerebral artery locations. Average waveforms are represented by thick lines. Figure adapted from [14].

1.2 The role of data assimilation in cardiovascular simulations

The blood flowing in a compliant artery can be observed and the blood flow rate can be measured through imaging techniques such as MRI. Blood pressure on few points can be provided by a catheter, and the geometric properties of arteries (e.g length and diameter) can be acquired from MRI and MRA. However, while these measurements are usually limited to a few locations in space, mechanical properties of arteries, such as Young's modulus and wall thickness, are often unknown. The other unknown model

parameters, including the distal boundary conditions, can be estimated using a parameter estimation algorithm based on a data assimilation technique such as an Unscented Kalman filter (UKF) [33, 34] or its variant - reduced order unscented Kalman filter (ROUKF) [35, 36] or using an ensemble Kalman filter (EnKF) [37]. Techniques of an accurate merging of measures and model simulations for a mathematically sound integration of different sources of information are known as data assimilation (DA) methods [38]. The outcome of DA methods include both the patient-specific measures and the development of numerical models. In the process, model simulation is adapted to the patient-specific data resulting in reliably simulated measurements (predictions). Figure 1.4 shows a patient-specific data assimilation flow chart for an inverse problem in hemodynamics.

1.3 Literature review on inverse problems in hemodynamics

In practice, available clinical data (possibly corrupted by noise) are often indirect observations of the hemodynamic measurements of interest. For reliable estimates of model parameters, an inverse hemodynamics and identification problems are solved using available data. There is rising interest in the area of inverse problems in hemodynamics, focusing on data assimilation and uncertainty quantification in cardiovascular simulations [10, 33–37, 39–44]. Table 1.1 summarises some recent works on inverse problems in hemodynamics, many of which are based on ROUKF for the estimation of the mechanical properties of arteries and to tune boundary condition parameters. In silico techniques are mostly used to test the robustness of a data assimilation method. These techniques are aimed at minimising the time, cost, and risk associated with clinical trials [20].

1.4 Motivations

Many recent studies on the inverse problems in hemodynamics are based on ROUKF. EnKF and in vivo data has been employed in [46] to optimize Windkessel outflow boundary condition parameters of 6 terminal arteries in an arterial network of the circle of Willis consisting of 16 arteries assimilating Doppler ultrasound data.

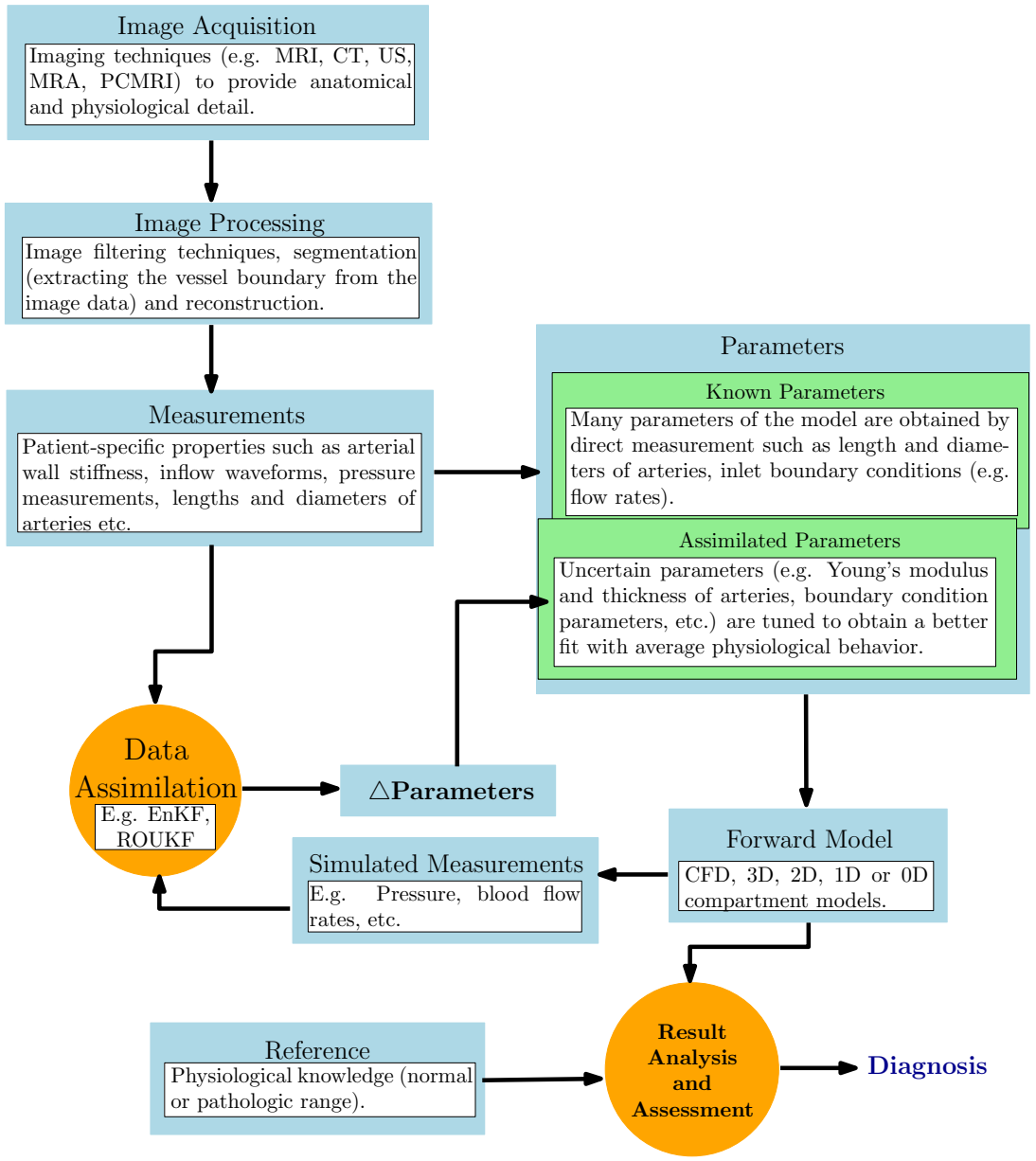

FIGURE 1.4: Patient-specific data assimilation flow chart. Patient-specific modelling is intended to simulate reliable status of a patient, from the clinical measurements. Uncertain parameters are tuned through data assimilation.

Table 1.1: Literature review on inverse problems in hemodynamics.

References	Blood flow model and description of arterial network	DA method and type of data used	Parameters estimated
Lombardi [35]	1D PDE model. Arterial network consisted of the main 55 arteries of the human body.	ROUKF. Synthetic data.	Elastic coefficients and WK3 parameters.
Moireau et al. [36]	FSI. Patient-specific modeling of thoracic aorta.	ROUKF. Synthetic and patient image data (CT scan)	WK3 parameters.
Pant et al. [10]	0D compartment model and 3D CFD simulations. Carotid artery, arterial network of abdominal aorta, and patient-specific modeling of thoracic aorta.	Augmented state space model using UKF. Synthetic and actual patient-specific data	WK3 parameters.
Pant et al. [34]	Lumped parameter model (0D compartment), closed-loop model for single-ventricle physiology.	Augmented state-space model using UKF. Actual patient-specific measurements.	Pulmonary and systemic circulation parameters.
Bertoglio et al. [39, 40]	3D FSI model. Model representation of an abdominal aorta.	ROUKF. Synthetic and MRI data.	Young's modulus and proximal WK3 resistance.
Chabiniok et al. [33]	Biomechanical heart model	UKF Joint state-parameter estimation. Synthetic and actual cardiac Cine-MRI data.	Key biophysical parameters in a beating heart model.
Martin et al. [41]	1D PDE model. Single artery	Adjoint state approach. Synthetic data.	The arterial compliance.
Spilker and Taylor [42]	3D blood flow model. Common carotid artery, an idealized iliac arterial bifurcation, and a patient-specific abdominal aorta.	Quasi-Newton method.	WK3 outlet boundary parameters.
Lassila et al. [43]	Reduced Basis methods. A stenosed artery and a simplified femoral bypass graft model.	Deterministic and Bayesian approaches. Synthetic data.	Young's modulus and amplitude of the residual flow.
Itu et al. [44]	1D PDE model. Patient-specific aortic model, a full body arterial model (29 arteries), and anatomical models representing different arterial segments.	Parameter estimation based on Quasi-Newton and Broyden's method. Synthetic and clinical data.	WK3 parameters.
Caiazzo et al. [45]	1D PDE model. In vitro model of the arterial network consisting of 37 arteries.	ROUKF. Synthetic and experimental data.	Terminal resistances, Young's modulus and arterial wall thickness.
DeVault et al. [46]	1D PDE model. Arterial network of the circle of Willis consisting of 16 arteries.	EnKF. In vivo data using transcranial Doppler ultrasound.	WK3 outflow boundary conditions parameters of 6 terminal arteries.

PDE=partial differential equation; UKF=Unscented Kalman filter; EnKF=ensemble Kalman filter; ROUKF=reduced order unscented Kalman filter; WK3=Windkessel three element model; FSI=Fluid-structure interaction; MRI=magnetic resonance imaging.

However, patient-specific data were not used to obtain the remaining vital model parameters such as the arterial stiffness. In [46], a 1D PDE blood flow model is used. Furthermore, the EnKF uses an ensemble of size 100 to optimise the parameters.

The current contribution differs from previous studies in two essential aspects. First, the present work proposes a parameter estimation algorithm based on the ensemble Kalman filtering techniques to estimate arterial stiffness together with the Windkessel boundary condition parameters. The arterial stiffness can be a relevant indicator in case of cardiovascular pathologies. Second, other works present data assimilation together with 1D or 3D PDE based blood flow models leading to computer intensive inverse problems, especially for complex arterial networks. We would like to break this complexity using either a reduced order 0D model or a 1D PDE model but with very coarse meshes. And we want to still be able to tune the hemodynamic parameters to match given clinical data for patient-specific analysis. Our aim is to bring the cost of each state evaluation to a few seconds instead of hours or days and thus making the approach feasible on standard multi-core computers available in clinics. Being able to proceed with the assimilation inside the clinic and close to the acquisition devices without being obliged to move sensitive medical data out of clinical environment is a major demand for security and confidentiality issues.

To the authors knowledge, this is the first attempt to estimate arterial stiffness and the WK3 boundary parameters in a complex arterial network including the circle of Willis using EnKF coupled with the 0D reduced order blood flow model and real data. The patient-specific arterial network consists of 33 arteries with 11 terminal arteries. Also, the ensemble Kalman filter uses an ensemble size of less than 30 to estimate 21 hemodynamic parameters. This coupling of EnKF with reduced order models has advantages in many aspects: firstly, the data assimilation (and parameter estimation) procedure is fast as the reduced order model only takes a few seconds (depending on the arterial network) to run; secondly, the inverse problem can be run from several initial guesses of hemodynamic parameters without significant increase in computing cost and time; and finally, sensitivity analysis is cheap with reduced order models. Thus, the current work can be used to make patient-specific studies and provide valuable predictions of hemodynamic quantities of interest in a cost-effective manner.

1.5 Aims and outline of the thesis

From the research and outcome of this thesis, it is intended to have some interesting clinical applications. By knowing some patient-specific non-invasive clinical data, we would like to estimate the actual physiological or mechanical constants of this patient. For instance, from blood flow rate measurements in an artery obtained using imaging techniques, we would like to estimate arterial wall properties (arterial stiffness measured through Young's modulus) and boundary condition parameters. From this estimation, the blood pressure (e.g. in cerebral arteries) can be obtained in a totally non-invasive manner.

The thesis presents a detailed assessment of a parameter estimation technique based on the Ensemble Kalman filter (EnKF) in the context of one-dimensional and zero-dimensional blood flow models. The ultimate goal of the thesis is the investigation of the accuracy and of the robustness of the EnKF.

In particular, the main aims of the thesis are:

- to propose an EnKF-based parameter estimation algorithm for inverse problems in hemodynamics,
- to study the feasibility of parameter estimation problems on systemic arterial networks,
- to investigate the effects of using actual clinical and experimental measurements versus synthetic data for the estimation procedure, and
- to identify limitations and potential difficulties of the proposed parameter estimation algorithm for inverse hemodynamic problems.

The thesis is organized as follows:

Chapter 2 provides an introduction to data assimilation methods. In particular, a short derivation of the standard Kalman filter, extended Kalman filter, and unscented Kalman filter is presented. The derivation of Ensemble Kalman filter is discussed in detail and an algorithm for parameter estimation using ensemble Kalman filter is presented. The proposed algorithm is then applied to a simple advection-diffusion model to estimate the model parameters.

Chapter 3 gives the numerical method for the solution of one-dimensional blood flow model. It starts from the derivation of the model, moving to the discretization that is chosen followed by the two common types of boundary conditions that are imposed. Next, we introduce the proposed parameter estimation algorithm to inverse hemodynamic problems using four simple test cases.

Chapter 4 presents the use of parameter estimation algorithm to solve an inverse hemodynamic problem in a series of test cases including a simple human arterial network. For the boundary condition at the outlet of each terminal artery, the 1D blood flow model is coupled with the constant resistance model. The first two tests are purely in silico and the final test case uses experimental data from an in vitro test rig. The sensitivity of the parameter estimation algorithm is also assessed in this chapter.

This chapter is part of: R. Lal, B. Mohammadi, and F. Nicoud," Data assimilation for identification of cardiovascular network characteristics". Published in *International Journal for Numerical Methods in Biomedical Engineering*, 2016 [37].

Chapter 5 presents the use of a reduced order compartment model for the blood flow in arteries and compares it with the classical 1D blood flow model for inverse problems in hemodynamics. A simple as well as a complex arterial network including the circle of Willis is considered for three test cases using in silico and actual real clinical data (blood flow rates acquired from MRI). For the boundary condition, the three element Windkessel model is used. A patient-specific case is presented here as a proof-of-concept.

Part of this chapter has been submitted for publication as: R. Lal, F. Nicoud, E. Le Bars, J. Deverdun, F. Molino, V. Costalat and B. Mohammadi," Non invasive blood flow features estimation in cerebral arteries from uncertain medical data" in *Annals of Biomedical Engineering*, 2017.

Chapter 6 reports on the results and discusses the major findings from the research. The chapter begins with an overview of the work and also addresses research limitations and perspectives.

Chapter 2

Data assimilation

Contents

This chapter provides an introduction to data assimilation methods, mostly developed in fields like meteorology and applied to computational hemodynamics. We start from the standard Kalman filter, moving to the extended Kalman filter, then giving equations for the unscented Kalman filter, and finally showing the derivation for the ensemble Kalman filter. We focus mainly on the latter and provide an algorithm for parameter estimation using an ensemble Kalman filter. A simple advection-diffusion model is used to test the robustness of the proposed algorithm using synthetic data.

2.1 Introduction

Data assimilation (DA) involves the combination of information from observations and numerical models. "Assimilation is the process of finding the model representation which is most consistent with the observations" [47]. Figure 2.1 shows the basic schematic view of the data assimilation cycle for any model that simulates system states. Data assimilation techniques [48–58] have become an important component of modelling for a growing number of applications ranging from the geosciences to engineering.

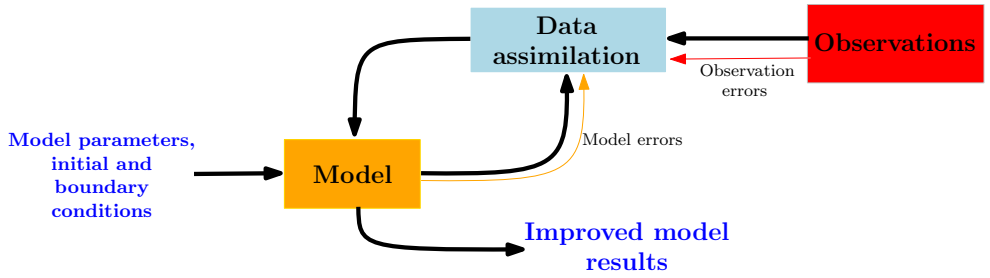

FIGURE 2.1: An illustration of data assimilation. Data assimilation produces improved model results by assimilating model forecasts and available observations.

Assimilation methods can be grouped into two categories: variational and sequential [59]. In variational methods (also referred as batch methods), the model error is generally assumed to be time-invariant. Examples of variational methods include the three-dimensional variational (3DVAR) [49], and the four-dimensional variational (4DVAR) [60] methods. In these methods, as illustrated in Figure 2.2a, the initial conditions of the model are corrected using both the past and present observations to get the best overall fit for the state of observations. The sequential methods (also known as filtering), such as the Kalman filter [48, 50, 52, 57], are part of an estimation theory in which observations are used as they become available to update the present state of the model (see Figure 2.2b). Sequential methods in contrast to the variational methods, have discontinuities in the time series of the corrected state, as illustrated in Figure 2.2b. Common Kalman filter methods include the Extended Kalman filter (EKF) [53, 61], the ensemble Kalman filter (EnKF) [55], and the unscented Kalman filter (UKF) [52, 54].

In variational data assimilation, an adjoint model is used. This requires the model to be differentiable, and the adjoint is obtained by linearising the forward model to

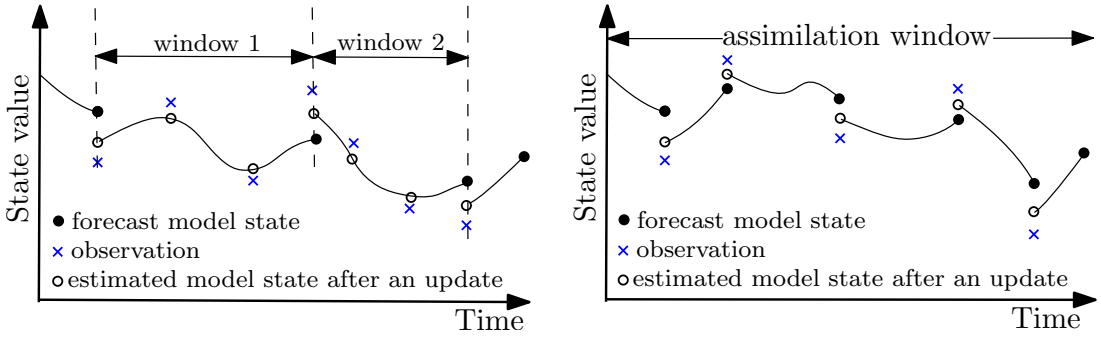

(a) (b)

FIGURE 2.2: Schematic of the data assimilation methods. (2.2a) shows the variational data assimilation approach. The initial conditions of the model are corrected using both the past and present observations. (2.2b) shows the sequential assimilation approach where the state is updated when an observation is available. Figure adapted from [62].

produce the tangent linear model [56]. While the classic Kalman filter [48] provides the optimal state estimate for linear systems, for nonlinear models, the EKF is used. However, the use of EKF requires derivation of a tangent linear model and the forecast model is linearised using a Taylor series expansion. Instead of linearising the nonlinear model as is done in the EKF, the UKF makes use of a set of points which are propagated through the actual nonlinear function. The use of a deterministic sampling approach makes the UKF a derivative-free alternative to EKF [54]. The UKF belongs to a larger class of filters known as Sigma-Point Kalman Filters. The UKF claims a higher accuracy and robustness for nonlinear models than the EKF [63]. The ensemble Kalman filter (EnKF) uses an ensemble of model states that is integrated forward in time using the nonlinear model with replicates of system noise [56]. The EnKF has advantages over EKF and the variational methods as it requires no derivation of a tangent linear operator or adjoint equations. The accurateness of EnKF increases with the increase in the ensemble size [64]. Table 2.1 gives a comparison of the advantages and disadvantages of the ensemble based methods compared to variational methods as provided in Dunne and Entekhabi [56].

Increasingly, DA is now used to estimate or correct uncertain parameters of a model using techniques such as joint state-parameter augmented models [33, 65–68], dual state-parameter estimation models [69], and cases where model parameters are considered as special states [70, 71]. Parameter estimation in hemodynamic problems using an UKF have also been recently proposed [10, 35, 36, 39]. In the following sections, we show the basic derivations and equations involved in the formulation of

TABLE 2.1: Advantages and disadvantages of ensemble-based methods compared to variational methods. Table adapted from Dunne and Entekhabi [56].

	Ensemble based methods	Variational Techniques
Advantages	Any model can be used. Model does not need to be differentiable. Noise can be placed anywhere, for example, on uncertain parameters. Noise can be non-Gaussian and non additive.	Use all data in a batch window to estimate the state.
Disadvantages	Estimates are conditioned on past measurements only.	Model must be differentiable to obtain tangent-linear model. Process noise can only be additive and Gaussian. Changes to model require that adjoint be obtained again.

the linear Kalman filter (KF), EKF, UKF, and the EnKF. An algorithm is then proposed to estimate model parameters using DA with an EnKF.

2.2 Discrete linear Kalman filter

The KF [48] assimilates data into linear systems with Gaussian model and measurement noise, and also serves as the mathematical foundation for an EKF, EnKF, and UKF. The KF minimises the difference between the estimated states and the true states by solving the problem of least squares estimation in a recursive manner and gives an estimate of the state every time a new observation is recorded. Some of the common approaches available in the literature on the derivation of linear KF include using the idea of orthogonal projections [72, 73], using the properties of a multivariate normal distribution [74], and using the weighted least-square approach [75–77].

This section presents the basic equations of the Kalman filter, for discrete-time linear systems using the estimation approach of minimum variance following the derivation of Todling and Cohn [77].

A discrete linear stochastic-dynamic system is considered and represented in matrix-vector notation as

$$\mathbf{x}_{k+1} = \mathbf{A}_k \mathbf{x}_k + \mathbf{w}_k, \tag{2.1a}$$

$$\mathbf{y}_k = \mathbf{H}_k \mathbf{x}_k + \mathbf{v}_k, \tag{2.1b}$$

for the discrete times $k = 1, 2, \ldots$, where $\mathbf{x}_k \in \mathbb{R}^n$ is the model state vector, $\mathbf{A}_k \in \mathbb{R}^{n \times n}$ is the true dynamics (transition) matrix, $\mathbf{y}_k \in \mathbb{R}^m$ is the measurement vector related to the true state $\mathbf{x}$ through the measurement matrix $\mathbf{H}_k \in \mathbb{R}^{m \times n}$, m and n are the dimension of the measurement vector and the state vector respectively. The model error $\mathbf{w}_k \in \mathbb{R}^n$ and the observation error $\mathbf{v}_k \in \mathbb{R}^m$ are independent zero-mean Gaussian processes with covariance matrices $\mathbf{Q}_k$ and $\mathbf{R}_k$ at time t_k, respectively. Letting the symbol $\mathscr{E}$ denote the expectation, we have $\mathscr{E}(\mathbf{w}_k) = 0$ and $\mathscr{E}(\mathbf{v}_k) = 0$.

The DA problem statement is: *given a prior (forecast or background) estimate* $\mathbf{x}_k^f$ *of the system state at time* t_k*, what is the update (or analysis)* $\mathbf{x}_k^a$ *based on the measurements* y_k*?*

The dynamical system in Equation (2.1a) that involves the model error $\mathbf{w}_k$ and an unknown initial state is replaced by a forecast model as

$$\mathbf{x}_{k+1}^f = \mathbf{A}_k \mathbf{x}_k^a \tag{2.2}$$

where the superscripts f and a stand for *forecast* and *analysis*, respectively. The forecast model represents an alternative way of estimating the state of the system at a particular time. An estimate of the state at time t_k is assumed to be a linear combination of the forecast state, given by Equation (2.2), and the observations, given by Equation (2.1b) [77],

$$\mathbf{x}_k^a = \tilde{\mathbf{L}}_k \mathbf{x}_k^f + \tilde{\mathbf{K}}_k \mathbf{y}_k \tag{2.3}$$

where $\tilde{\mathbf{L}}_k$ and $\tilde{\mathbf{K}}_k$ are the two weighting matrices to be determined. The forecast and the analysis errors are defined as

$$\mathbf{e}_k^a = \mathbf{x}_k^a - \mathbf{x}_k; \;\; \mathbf{e}_k^f = \mathbf{x}_k^f - \mathbf{x}_k \tag{2.4}$$

where $\mathbf{x}_k$ is the true state of the system at time t_k. It can be shown that for an unbiased forecast error i.e. $\mathscr{E}\left(\mathbf{e}_k^f\right) = 0$, the analysis error is unbiased if the weighting matrix

$\tilde{\mathbf{L}}_k = \mathbf{I} - \tilde{\mathbf{K}}_k\mathbf{H}_k$ [77]. Equation (2.3) can then be written as

$$\mathbf{x}_k^a = \mathbf{x}_k^f + \tilde{\mathbf{K}}_k \left(\mathbf{y}_k - \mathbf{H}_k\mathbf{x}_k^f\right). \tag{2.5}$$

Subtracting $\mathbf{x}_k$ from both sides of Equation (2.5) and using Equation (2.4), the analysis error is written as

$$\mathbf{e}_k^a = \mathbf{e}_k^f + \tilde{\mathbf{K}}_k \left(\mathbf{y}_k - \mathbf{H}_k\mathbf{x}_k^f\right). \tag{2.6}$$

Substituting Equation (2.1b) into Equation (2.6) the analysis error is rewritten as

$$\mathbf{e}_k^a = (\mathbf{I} - \tilde{\mathbf{K}}_k\mathbf{H}_k)\mathbf{e}_k^f + \tilde{\mathbf{K}}_k\mathbf{v}_k. \tag{2.7}$$

At observation locations, the *gain* matrix $\tilde{\mathbf{K}}_k$ describes the weights given to the observations $\mathbf{y}_k$ and the measurements (forecast variable) $\mathbf{H}_k\mathbf{x}_k^f$ [77]. The gain matrix is measured using the covariances of the forecast and analysis errors which are defined as

$$\mathbf{P}_k^a = \mathscr{E}\left[(\mathbf{e}_k^a)(\mathbf{e}_k^a)^{\mathrm{T}}\right]; \ \mathbf{P}_k^f = \mathscr{E}\left[(\mathbf{e}_k^f)(\mathbf{e}_k^f)^{\mathrm{T}}\right]. \tag{2.8}$$

The two matrices in Equation (2.8) describe the evolution of the analysis and forecast error covariances, respectively, and are written as [77]

$$\mathbf{P}_k^a = (\mathbf{I} - \tilde{\mathbf{K}}_k\mathbf{H}_k)\mathbf{P}_k^f(\mathbf{I} - \tilde{\mathbf{K}}_k\mathbf{H}_k)^{\mathrm{T}} + \tilde{\mathbf{K}}_k\mathbf{R}_k\tilde{\mathbf{K}}_k^{\mathrm{T}} \tag{2.9a}$$

$$\mathbf{P}_{k+1}^f = \mathbf{A}_k\mathbf{P}_k^a\mathbf{A}_k^{\mathrm{T}} + \mathbf{Q}_k. \tag{2.9b}$$

The observation error covariance matrix $\mathbf{R}_k = \mathscr{E}\left(\mathbf{v}_k\mathbf{v}_k^{\mathrm{T}}\right)$, and $\mathbf{Q}_k = 0$ for a perfect model. The gain matrix is obtained from a particular choice of $\tilde{\mathbf{K}}_k$ that is obtained by minimizing the analysis error variance. An estimator $\mathcal{J}_k^a$ is introduced which measures the reliability of the analysis by measuring the distance between the analysis (estimate) and the true value of the state of the system at time t_k [77]:

$$\begin{aligned}
\mathcal{J}_k^a &= \mathscr{E}\left[\|\mathbf{e}_k^a\|^2\mathbf{B}_k\right] \\
&= \mathscr{E}\left[\mathbf{e}_k^a\mathbf{B}_k(\mathbf{e}_k^a)^{\mathrm{T}}\right] \\
&= \mathscr{E}\left[\mathrm{Tr}\left(\mathbf{B}_k\mathbf{e}_k^a\,(\mathbf{e}_k^a)^{\mathrm{T}}\right)\right] \\
&= \mathrm{Tr}\left(\mathbf{B}_k\mathbf{P}_k^a\right)
\end{aligned} \tag{2.10}$$

which follows from the properties of *trace* operator where $\mathbf{B}_k$ is a positive definite, and deterministic $n \times n$ scaling matrix.

Substituting the expression (2.9a) for $\mathbf{P}_k^a$ in Equation (2.10), differentiating with respect to $\tilde{\mathbf{K}}_k$, and equating the result to zero yields

$$\mathbf{B}_k \left\{ \mathbf{H}_k \mathbf{P}_k^f \left(\mathbf{I} - \tilde{\mathbf{K}}_k \mathbf{H}_k \right)^{\mathrm{T}} - \mathbf{R}_k \tilde{\mathbf{K}}_k^{\mathrm{T}} \right\} = 0. \tag{2.11}$$

From Equation (2.11) the minimum value of the estimator $\mathcal{J}_k^a$ is obtained (independently of $\mathbf{B}_k$) when the gain matrix is [48]

$$\tilde{\mathbf{K}}_k = \mathbf{K}_k = \mathbf{P}_k^f \mathbf{H}_k^{\mathrm{T}} \left(\mathbf{H}_k \mathbf{P}_k^f \mathbf{H}_k^{\mathrm{T}} + \mathbf{R}_k \right)^{-1}. \tag{2.12}$$

The matrix $\mathbf{K}_k$ is the optimal weighting matrix referred to as the **Kalman gain**. Substituting this optimal gain into Equation (2.9a) yields a simplified equation for analysis error covariance matrix

$$\mathbf{P}_k^a = \left(\mathbf{I} - \mathbf{K}_k \mathbf{H}_k \right) \mathbf{P}_k^f. \tag{2.13}$$

Finally, the weighting matrix $\tilde{\mathbf{K}}_k$ is replaced by $\mathbf{K}_k$ in Equation (2.5), and the analysis state is obtained as

$$\mathbf{x}_k^a = \mathbf{x}_k^f + \mathbf{K}_k \left(\mathbf{y}_k - \mathbf{H}_k \mathbf{x}_k^f \right). \tag{2.14}$$

2.3 Extended Kalman filter

The EKF algorithm is a recursive procedure to estimate the optimal state vector and the corresponding covariance matrix for nonlinear continuous state vector equation and nonlinear discrete observation vector [78]. Using a predictor-corrector method, EKF approximates an optimal estimate due to the linearisation of the state and measurement system. Mathematical formulation and derivations of EKF can be found in [53, 61, 79].

For general nonlinear dynamical systems, it is assumed that the dynamic system evolves according to a state transition function f and the measurement $\mathbf{y}$ is a function, h, of the current state with and additive Gaussian noise $\mathbf{v_k}$ with covariance $\mathbf{R}_k$:

$$\mathbf{x}_{k+1} = f(\mathbf{x}_k, \mathbf{u}_k) + \mathbf{w_k}, \quad \mathbf{y}_k = h(\mathbf{x}_k) + \mathbf{v_k}. \tag{2.15}$$

$\mathbf{u}_k \in \mathbb{R}^m$ is the control input or parameters while other variables are as defined in Section 2.2.

The EKF linearises the non-linear system around the current state using the Jacobian matrices

$$\mathbf{A}_k = \frac{\partial f(\mathbf{x}, \mathbf{u})}{\partial \mathbf{x}}\Big|_{\mathbf{x}=\mathbf{x}_k^a} \text{and} \quad \mathbf{C}_k = \frac{\partial h(\mathbf{x})}{\partial \mathbf{x}}\Big|_{\mathbf{x}=\mathbf{x}_k^a}. \tag{2.16}$$

The analysis step of EKF is the same as the analysis step in the traditional KF linear Kalman filter given by Equations (2.12)-(2.14). The only difference is that the model and measurement matrices are linearised using Equation (2.16). Therefore, the major steps in EKF are:

$$\left.\begin{aligned} \mathbf{K}_k &= \mathbf{P}_k^f \mathbf{C}_k^{\mathrm{T}} \left(\mathbf{C}_k \mathbf{P}_k^f \mathbf{C}_k^{\mathrm{T}} + \mathbf{R}_k\right)^{-1}, \\ \mathbf{x}_k^a &= \mathbf{x}_k^f + \mathbf{K}_k \left(\mathbf{y}_k - h(\mathbf{x}_k^f)\right), \\ \mathbf{P}_k^a &= \left(\mathbf{I} - \mathbf{K}_k \mathbf{C}_k\right) \mathbf{P}_k^f, \end{aligned}\right\} \quad \text{Analysis step}$$

$$\left.\begin{aligned} \mathbf{x}_{k+1}^f &= f(\mathbf{x}_k^a, \mathbf{u}_k), \\ \mathbf{P}_{k+1}^f &= \mathbf{A}_k, \mathbf{P}_k^a \mathbf{A}_k^{\mathrm{T}} + \mathbf{Q}_k. \end{aligned}\right\} \quad \text{Forecast step}$$

In the EKF the state distribution which is approximated by a Gaussian random variable is no longer normal after undergoing the first-order linearisation. This may affect the performance of the EKF and can lead to filter divergence in extreme cases [54, 80]. To counter this problem, Julier and Uhlmann [52] proposed the improved version of EKF known as *Unscented Kalman Filter*.

2.4 Unscented Kalman filter

To counter the approximation issues of the EKF, the UKF employs a set of sigma-points from the distribution of the state vector $\mathbf{x}$ at the beginning of the time step [63]. These sigma-points are then propagated in time via the nonlinear model. The model forecast and analysis steps in the UKF are preceded by another step for the selection of sigma-points. The mathematical formulations of UKF equations can be found in [51, 52, 54, 81, 82]. We present the basic principles and the algorithm of the UKF following [54, 81, 82].

We again consider a discrete-time nonlinear dynamic system as in Section 2.3:

$$\mathbf{x}_{k+1} = f(\mathbf{x}_k, \mathbf{u}_k) + \mathbf{w_k}, \quad \mathbf{y}_k = h(\mathbf{x}_k) + \mathbf{v_k} \tag{2.15 revisited}$$

where the variables have the same definitions as in Sections 2.2 and 2.3. To linearise non-linear functions f and h, UKF applies the stochastic approximation called Unscented Transform (UT) [51].

UT is used to calculate the statistics of a random variable (rv) undergoing a nonlinear transformation [51, 54]. To illustrate how UT works, a rv, $\mathbf{x} \in \mathbb{R}^n$ with mean $\bar{\mathbf{x}}$ and covariance $\mathbf{P}_\mathbf{x}$ is considered. The objective is to estimate a Gaussian approximation of the distribution by propagating $\mathbf{x}$ through a nonlinear function $\mathbf{z} = g(\mathbf{x})$. The approximation is performed using UT by extracting $2n+1$ sigma points $\mathcal{X}^{[i]}$ according to the following [54]:

$$\begin{aligned}
\mathcal{X}^{[0]} &= \bar{\mathbf{x}} \\
\mathcal{X}^{[i]} &= \bar{\mathbf{x}} + \left(\sqrt{(n+\lambda)\,\mathbf{P}_\mathbf{x}}\right)_i, \quad i = 1, \ldots, n \\
\mathcal{X}^{[i]} &= \bar{\mathbf{x}} - \left(\sqrt{(n+\lambda)\,\mathbf{P}_\mathbf{x}}\right)_i, \quad i = n+1, \ldots, 2n,
\end{aligned} \tag{2.17}$$

where $\lambda = \alpha^2(n+l) - n$ is a scaling parameter. The constant α is a small positive value (e.g. $10^{-4} < \alpha < 1$), that determines the spread of the sigma points around $\bar{\mathbf{x}}$ [54]. To have a semi-positive definite covariance matrix, the scaling parameter l is usually set to $3-n$ [51, 54]. $\left(\sqrt{(n+\lambda)\,\mathbf{P}_\mathbf{x}}\right)_i$ is the i^{th} column of the matrix square root.

The sigma points are passed through the nonlinear function g,

$$\mathcal{Z}^{[i]} = g\left(\mathcal{X}^{[i]}\right), \quad i = 0, \ldots, 2n \tag{2.18}$$

and with the resulted transformed observations, the mean and covariance for $\mathbf{z}$ are computed from the mapped sigma points $\mathcal{Z}^{[i]}$ [54]:

$$\begin{aligned}
\bar{\mathbf{z}} &\approx \sum_{i=0}^{2n} w_m^{[i]} \mathcal{Z}^{[i]} \\
\mathbf{P}_\mathbf{z} &\approx \sum_{i=0}^{2n} w_c^{[i]} \left(\mathcal{Z}^{[i]} - \bar{\mathbf{z}}\right)\left(\mathcal{Z}^{[i]} - \bar{\mathbf{z}}\right)^{\mathrm{T}},
\end{aligned} \tag{2.19}$$

with corresponding weights ($w_m^{[i]}$ for mean and $w_c^{[i]}$ for covariance)

$$\begin{aligned}
w_m^{[0]} &= \lambda/(n+\lambda) \\
w_c^{[0]} &= \lambda/(n+\lambda) + (1 - \lambda^2 + \beta^2) \\
w_m^{[i]} = w_c^{[i]} &= \lambda/\left\{2(n+\lambda)\right\}, \quad i = 1, \ldots, 2n.
\end{aligned} \tag{2.20}$$

For Gaussian distribution β =2 is used as an optimal value [54]. The UKF applies the UT to the transition function f and the observation function h in Equation (2.15). The UKF equations in the forecast and assimilation steps are summarised in Table 2.2.

TABLE 2.2: Summary of Unscented Kalman Filter (UKF) equations. Summarised from [54, 83].

- **Initialisation at** $k = 0$
  The mean, $\bar{\mathbf{x}}_0 = \mathscr{E}[\mathbf{x}_0]$, and the covariance, $\mathbf{P}_\mathbf{x} = \mathscr{E}\left[(\mathbf{x} - \bar{\mathbf{x}}_0)(\mathbf{x} - \bar{\mathbf{x}}_0)^\mathrm{T}\right]$, of the estimate along with the control input, $\mathbf{u}_0$, are assumed to be available.
- **For** $k = 1, 2, \ldots, \infty$
  1. Calculate the sigma points using Equation (2.17):
  $\mathcal{X}_{k-1}^{[i]} = \left[\bar{\mathbf{x}}_{k-1}, \bar{\mathbf{x}}_{k-1} + \left(\sqrt{(n+\lambda)\,\mathbf{P}_\mathbf{x}}\right)_{k-1}, \bar{\mathbf{x}}_{k-1} - \left(\sqrt{(n+\lambda)\,\mathbf{P}_\mathbf{x}}\right)_{k-1}\right]$
  2. **Time-update equations**
  Propagate, each sigma point through the nonlinear process model:
  $\mathcal{X}_k^{\mathrm{f}[i]} = f(\mathcal{X}_{k-1}^{[i]}, \mathbf{u}_{k-1})$ for $i = 0, \ldots, 2n$, where 'f' denotes the forecast (predicted) value.
  Compute the forecast mean and the variance from the resulting sigma points:
  $\bar{\mathbf{x}}_k^\mathrm{f} = \sum_{i=0}^{2n} w_m^{[i]} \mathcal{X}_k^{\mathrm{f}[i]}$; $\mathbf{P}_{\mathbf{x}_k}^\mathrm{f} = \sum_{i=0}^{2n} w_c^{[i]} \left(\mathcal{X}_k^{\mathrm{f}[i]} - \bar{\mathbf{x}}_k^\mathrm{f}\right)\left(\mathcal{X}_k^{\mathrm{f}[i]} - \bar{\mathbf{x}}_k^\mathrm{f}\right)^\mathrm{T}$,
  where the weights w_c^i and w_m^i are as defined in Equation (2.20).
  Propagate the sigma points through the nonlinear measurement model to compute the forecast observations: $\mathcal{Y}_k^{\mathrm{f}[i]} = h\left(\mathcal{X}_k^{\mathrm{f}[i]}\right), \quad i = 0, \ldots, 2n.$
  Compute the mean of the measurement vector: $\bar{\mathbf{y}}_k^\mathrm{f} = \sum_{i=0}^{2n} w_m^{[i]} \mathcal{Y}_k^{\mathrm{f}[i]}$.
  3. **Measurement-update equations**
  Compute the observation covariance matrix:
  $\mathbf{P}_{\mathbf{y}_k\mathbf{y}_k} = \sum_{i=0}^{2n} w_c^{[i]} \left(\mathcal{Y}_k^{\mathrm{f}[i]} - \bar{\mathbf{y}}_k^\mathrm{f}\right)\left(\mathcal{Y}_k^{\mathrm{f}[i]} - \bar{\mathbf{y}}_k^\mathrm{f}\right)^\mathrm{T} + \mathbf{R}_k$, where $\mathbf{R}_k$ is the observation error covariance matrix.
  Compute the cross covariance between the state and observation:
  $\mathbf{P}_{\mathbf{x}_k\mathbf{y}_k} = \sum_{i=0}^{2n} w_c^{[i]} \left(\mathcal{X}_k^{\mathrm{f}[i]} - \bar{\mathbf{x}}_k^\mathrm{f}\right)\left(\mathcal{Y}_k^{\mathrm{f}[i]} - \bar{\mathbf{y}}_k^\mathrm{f}\right)^\mathrm{T}$.
  Calculate the Kalman gain: $\mathbf{K}_k = \mathbf{P}_{\mathbf{x}_k\mathbf{y}_k}\mathbf{P}_{\mathbf{y}_k\mathbf{y}_k}^{-1}$.
  The UKF estimate and its covariance are computed from the standard Kalman update equation:
  $\bar{\mathbf{x}}_k^\mathrm{a} = \bar{\mathbf{x}}_k^\mathrm{f} + \mathbf{K}_k\left(\mathbf{y}_k - \bar{\mathbf{y}}_k^\mathrm{f}\right)$,
  $\mathbf{P}_{\mathbf{x}_k}^\mathrm{a} = \mathbf{P}_{\mathbf{x}_k}^\mathrm{f} - \mathbf{K}_k\mathbf{P}_{\mathbf{y}_k\mathbf{y}_k}\mathbf{K}_k^\mathrm{T}$.

The UKF claims a higher accuracy and robustness for nonlinear models than the EKF [63] and does not require explicit calculations of Jacobian as in EKF. Moireau

and Chapelle [84] recently introduced a reduced-order filtering strategy adapted to Unscented Kalman Filtering. The algorithms for Reduced-Order Unscented Kalman Filter (ROUKF) are derived in discrete time as in the classical UKF formalism. While the algorithm for ROUKF is restricted to the parameter space, it can be used for the estimation of parameters in large dynamical systems [84].

2.5 Ensemble Kalman filter

First introduced by Geir Evenson [55], an Ensemble Kalman Filter (EnKF) solves the Fokker-Plank equation using a Monte Carlo or ensemble integrations [85]. It is a sub-optimal estimator for problems involving high-order non-linear models. The error statistics are predicted using the ensemble of states. Different versions of EnKF are available in the literature: Deterministic Ensemble Kalman filter (DEnKF) [86], Monte Carlo EnKF [55, 87], EnKF [57, 88], Hybrid EnKF [89], Ensemble Transform Kalman filter (ETKF) [90], Ensemble Adjustment Kalman filter (EAKF) [65], Ensemble Square Root filters (EnSRF) [91] and Local Ensemble Kalman filter (LEKF) [92].

2.5.1 Derivation of Ensemble Kalman filter

In EnKF, the forecast error covariance matrix is evaluated using an ensemble of forecasts. In this section, we follow and describe the different steps employed in the formulation of EnKF as presented in [70, 88, 93–95].

We assume that the discrete nonlinear system is described by

$$\mathbf{x}_{k+1} = f(\mathbf{x}_k, \mathbf{u}_k) + \mathbf{w_k}, \quad \mathbf{y}_k = h(\mathbf{x}_k) + \mathbf{v_k}. \tag{2.21}$$

The model state at time t_k is $\mathbf{x}_k \in \mathbb{R}^n$, while the observed state is $\mathbf{y}_k \in \mathbb{R}^{nobs}$. n is the dimension of the model state vector and $nobs$ is the number of observations. $\mathbf{u}_k \in \mathbb{R}^m$ represents a set of model parameters. $\mathbf{w}_k \in \mathbb{R}^n$ and $\mathbf{v}_k \in \mathbb{R}^{nobs}$ are assumed uncorrelated Gaussian model errors with $\mathbf{w}_k \sim \mathcal{N}(0, \mathbf{Q_k})$ and $\mathbf{v}_k \sim \mathcal{N}(0, \mathbf{R_k})$ where $\mathbf{Q_k}$ and $\mathbf{R_k}$ are the covariance matrices. h is the function describing the relationship between the measurement and the states.

The initial forecast ensemble of states (prior ensembles) $\mathbf{X}_k^{\mathrm{f}} = (\mathbf{x}_k^{\mathrm{f}_1}, \ldots, \mathbf{x}_k^{\mathrm{f}_{q_{\mathrm{ens}}}}) \in \mathbb{R}^{n \times q_{\mathrm{ens}}}$ for $i = 1, \ldots, q_{\mathrm{ens}}$ is assumed to be available at $t = k$. f_i denotes the initial i^{th} forecast member of an ensemble size q_{ens}. The mean of the ensemble of forecast state is $\overline{\mathbf{x}}_k^{\mathrm{f}} \in \mathbb{R}^n$ and is given by

$$\overline{\mathbf{x}}_k^{\mathrm{f}} = \frac{1}{q_{\mathrm{ens}}} \sum_{i=1}^{q_{\mathrm{ens}}} \mathbf{x}_k^{\mathrm{f}_i}. \tag{2.22}$$

The forecast covariance matrix, $\mathbf{P}_k^{\mathrm{f}} \in \mathbb{R}^{n \times n}$, is defined by

$$\mathbf{P}_k^{\mathrm{f}} = \frac{1}{q_{\mathrm{ens}} - 1} \sum_{i=1}^{q_{\mathrm{ens}}} \left(\mathbf{x}_k^{\mathrm{f}_i} - \overline{\mathbf{x}}_k^{\mathrm{f}}\right) \left(\mathbf{x}_k^{\mathrm{f}_i} - \overline{\mathbf{x}}_k^{\mathrm{f}}\right)^{\mathrm{T}}. \tag{2.23}$$

After the computation of the Kalman gain $\mathbf{K}_k$, all operations on the ensemble members are independent in the EnKF analysis step and the ensemble members are updated using:

$$\mathbf{x}_k^{\mathrm{a}_i} = \mathbf{x}_k^{\mathrm{f}_i} + \mathbf{K}_k \left[\mathbf{y}_k^i - h\left(\mathbf{x}_k^{\mathrm{f}_i}\right)\right], \quad i = 1, \ldots, q_{\mathrm{ens}}, \tag{2.24}$$

where a_i represents the i^{th} updated or analysed member of the ensemble. To maintain the correct forecast error covariance, a suitable spread of the ensemble members is required. Perturbations are added to the original observation vector to avoid having an updated ensemble with a low variance [96]. An ensemble of the same size q_{ens} consisting of observations is also generated by adding small perturbations to the observation set $\mathbf{y}_k$. Perturbations are generated to have the same distribution as the measurement error and the perturbed observations $\mathbf{y}_k^i$ are defined by

$$\mathbf{y}_k^i = \mathbf{y}_k + \mathbf{e}_k^i, \quad i = 1, \ldots, q_{\mathrm{ens}} \tag{2.25}$$

where $\mathbf{e}_k^i \in \mathbb{R}^{nobs}$ is a Gaussian random vector with zero mean and a specified variance. The measurement error covariance matrix, $\mathbf{R_k}$, is diagonal following the assumption of independent observations [91] and is defined as

$$\mathbf{R_k} = \mathrm{diag}\left[\frac{1}{q_{\mathrm{ens}} - 1} \mathbf{E}\mathbf{E}^{\mathrm{T}}\right], \quad \mathbf{E} = \left[\mathbf{e}_k^1, \ldots, \mathbf{e}_k^{q_{\mathrm{ens}}}\right]. \tag{2.26}$$

For a linear measurement function, h, and if the noise is additive, that is

$$\mathbf{y}_k = \mathbf{H}\mathbf{x}_k + \mathbf{v_k}, \tag{2.27}$$

the Kalman gain is defined by [94]

$$\mathbf{K_k} = \mathbf{P}_k^{\mathrm{f}}\mathbf{H}^{\mathrm{T}}\left(\mathbf{H}\mathbf{P}_k^{\mathrm{f}}\mathbf{H}^{\mathrm{T}} + \mathbf{R}_k\right)^{-1}. \tag{2.28}$$

In Equation (2.28), the observation operator, $\mathbf{H} \in \mathbb{R}^{nobs \times n}$, is linear or linearised. To circumvent the linearisation of a nonlinear measurement function which might be difficult to linearise, Houtekamer and Mitchell [97] re-wrote the two terms $\mathbf{P}_k^{\mathrm{f}}\mathbf{H}^{\mathrm{T}}$ and $\mathbf{H}\mathbf{P}_k^{\mathrm{f}}\mathbf{H}^{\mathrm{T}}$ which appear in the Kalman gain Equation (2.28) as

$$\mathbf{P}_k^{\mathrm{f}}\mathbf{H}^{\mathrm{T}} \equiv \frac{1}{q_{\mathrm{ens}}-1}\sum_{i=1}^{q_{\mathrm{ens}}}\left[\mathbf{x}_k^{\mathrm{f}_i} - \overline{\mathbf{x}}_k^{\mathrm{f}}\right]\left[h\left(\mathbf{x}_k^{\mathrm{f}_i}\right) - \overline{h\left(\mathbf{x}_k^{\mathrm{f}}\right)}\right]^{\mathrm{T}}, \tag{2.29}$$

$$\mathbf{H}\mathbf{P}_k^{\mathrm{f}}\mathbf{H}^{\mathrm{T}} \equiv \frac{1}{q_{\mathrm{ens}}-1}\sum_{i=1}^{q_{\mathrm{ens}}}\left[h\left(\mathbf{x}_k^{\mathrm{f}_i}\right) - \overline{h\left(\mathbf{x}_k^{\mathrm{f}}\right)}\right]\left[h\left(\mathbf{x}_k^{\mathrm{f}_i}\right) - \overline{h\left(\mathbf{x}_k^{\mathrm{f}}\right)}\right]^{\mathrm{T}}, \tag{2.30}$$

where $\overline{h\left(\mathbf{x}_k^{\mathrm{f}}\right)} = \frac{1}{q_{\mathrm{ens}}}\sum_{i=1}^{q_{\mathrm{ens}}} h\left(\mathbf{x}_k^{\mathrm{f}_i}\right)$. It has been argued by Ambadan and Tang [98] that Equations (2.29) and (2.30) approximately hold if the following are true :

$$\overline{h\left(\mathbf{x}_k^{\mathrm{f}}\right)} = h\left(\overline{\mathbf{x}}_k^{\mathrm{f}}\right), \tag{2.31}$$

$$\mathrm{norm}\left(\mathbf{x}_k^{\mathrm{f}_i} - \overline{\mathbf{x}}_k^{\mathrm{f}}\right) \text{ is small for } i = 1, 2, \ldots q_{\mathrm{ens}}. \tag{2.32}$$

Equations (2.29) and (2.30) linearise the nonlinear function h to $\mathbf{H}$ under the conditions of Equations (2.31) and (2.32) [70]. For the nonlinear model with a nonlinear measurement function, a general equation for the Kalman gain can be stated as [70]:

$$\mathbf{K}_k = \mathbf{P}_{\mathbf{xy}_k}^{\mathrm{f}}\left(\mathbf{P}_{\mathbf{yy}_k}^{\mathrm{f}}\right)^{-1}, \tag{2.33}$$

where the error covariance matrices $\mathbf{P}_{\mathbf{xy}_k}^{\mathrm{f}}$ and $\mathbf{P}_{\mathbf{yy}_k}^{\mathrm{f}}$ are defined as follows:

$$\mathbf{P}_{\mathbf{xy}_k}^{\mathrm{f}} = \frac{1}{q_{\mathrm{ens}}-1}\sum_{i=1}^{q_{\mathrm{ens}}}\left[\mathbf{x}_k^{\mathrm{f}_i} - \overline{\mathbf{x}}_k^{\mathrm{f}}\right]\left[h\left(\mathbf{x}_k^{\mathrm{f}_i}\right) - \overline{h\left(\mathbf{x}_k^{\mathrm{f}}\right)}\right]^{\mathrm{T}}, \tag{2.34}$$

$$\mathbf{P}_{\mathbf{yy}_k}^{\mathrm{f}} = \frac{1}{q_{\mathrm{ens}}-1}\sum_{i=1}^{q_{\mathrm{ens}}}\left[h\left(\mathbf{x}_k^{\mathrm{f}_i}\right) - \overline{h\left(\mathbf{x}_k^{\mathrm{f}}\right)}\right]\left[h\left(\mathbf{x}_k^{\mathrm{f}_i}\right) - \overline{h\left(\mathbf{x}_k^{\mathrm{f}}\right)}\right]^{\mathrm{T}} + \mathbf{R}_k. \tag{2.35}$$

We define the **true** state (or parameter) as the **target** of an ideal assimilation. The best forecast state estimate is given by the ensemble mean $\overline{\mathbf{x}}_k^{\mathrm{f}}$. The error between $\overline{\mathbf{x}}_k^{\mathrm{f}}$ and the true state is given by the standard deviation of the ensemble members around $\overline{\mathbf{x}}_k^{\mathrm{f}}$. The final step is the forecast step and involves an ensemble of q_{ens} forecast states for time

$t = k + 1$ as,

$$\mathbf{x}_{k+1}^{\mathrm{f}_i} = f(\mathbf{x}_k^{\mathrm{a}_i}, \mathbf{u}_k) + \mathbf{w}_k^i, \quad i = 1, 2, \ldots q_{\text{ens}}. \tag{2.36}$$

2.5.2 Summary of ensemble Kalman filter algorithm

We now summarize the forecast and the analysis steps of EnKF presented in Section 2.5.1. A schematic description of the EnKF algorithm is shown in Figure 2.3. To start the EnKF, we need to generate an ensemble of q_{ens} forecast estimates of state associated with their random errors. At $t = k - 1$, it is assumed that $\mathbf{x}_{k-1}^{\mathrm{f}_i}$ for $i = 1, \ldots, q_{\text{ens}}$ are available. We let $nobs$ denote the number of observations. At time $t = k$, we generate a set of realizations of the state vector $\mathbf{X}_k = (\mathbf{x}_k^1, \ldots, \mathbf{x}_k^{q_{\text{ens}}})$ and denote the corresponding measurements as $\mathbf{Y}_k = (\mathbf{y}_k^1, \ldots, \mathbf{y}_k^{q_{\text{ens}}}) \in \mathbb{R}^{q_{\text{ens}} \times nobs}$. $\mathbf{Q}$ and $\mathbf{R}$ correspond to the model and observation error covariance matrices, respectively. We write the equations for the EnKF as:

$$\begin{aligned}
\mathbf{x}_k^{\mathrm{f}_i} &= f(\mathbf{x}_{k-1}^{\mathrm{a}_i}, \mathbf{u}_{k-1}) + \mathbf{w}_{k-1}^i, \quad i = 1, \ldots, q_{\text{ens}}, \\
\mathbf{w}_k^i &\sim \mathcal{N}(0, \mathbf{Q}_k), \\
\mathbf{P}_{\mathrm{xy}_k}^{\mathrm{f}} &= \frac{1}{q_{\text{ens}} - 1} \sum_{i=1}^{q_{\text{ens}}} \left[\mathbf{x}_k^{\mathrm{f}_i} - \overline{\mathbf{x}}_k^{\mathrm{f}}\right] \left[h\left(\mathbf{x}_k^{\mathrm{f}_i}\right) - \overline{h\left(\mathbf{x}_k^{\mathrm{f}}\right)}\right]^{\mathrm{T}}, \\
\mathbf{P}_{\mathrm{yy}_k}^{\mathrm{f}} &= \frac{1}{q_{\text{ens}} - 1} \sum_{i=1}^{q_{\text{ens}}} \left[h\left(\mathbf{x}_k^{\mathrm{f}_i}\right) - \overline{h\left(\mathbf{x}_k^{\mathrm{f}}\right)}\right] \left[h\left(\mathbf{x}_k^{\mathrm{f}_i}\right) - \overline{h\left(\mathbf{x}_k^{\mathrm{f}}\right)}\right]^{\mathrm{T}} + \mathbf{R}_k, \\
\mathbf{K}_k &= \mathbf{P}_{\mathrm{xy}_k}^{\mathrm{f}} \left(\mathbf{P}_{\mathrm{yy}_k}^{\mathrm{f}}\right)^{-1}, \\
\mathbf{y}_k^i &= \mathbf{y}_k + \mathbf{e}_k^i, \quad i = 1, \ldots, q_{\text{ens}}, \\
\mathbf{x}_k^{\mathrm{a}_i} &= \mathbf{x}_k^{\mathrm{f}_i} + \mathbf{K}_k \left[\mathbf{y}_k^i - h\left(\mathbf{x}_k^{\mathrm{f}_i}\right)\right], \quad i = 1, \ldots, q_{\text{ens}}.
\end{aligned}$$

In the above steps, the superscripts 'f' and 'a' denote the forecast and the analysis steps respectively. EnKF algorithm yields an ensemble of analyses at time $t = k$, which can be cycled in time.

UKF differs from EnKF by the choice of the sampling. UKF uses a minimal set of deterministically chosen points (sigma points) and propagates this set through the actual non-linear function [10]. In contrast, EnKF uses a Monte-Carlo-based choice of many points (members of the ensemble) for forward propagation. UKF should be preferred if the output of the system deviates from a Gaussian distribution. Except with the computation of the Kalman gain, all the operations on the ensemble members are

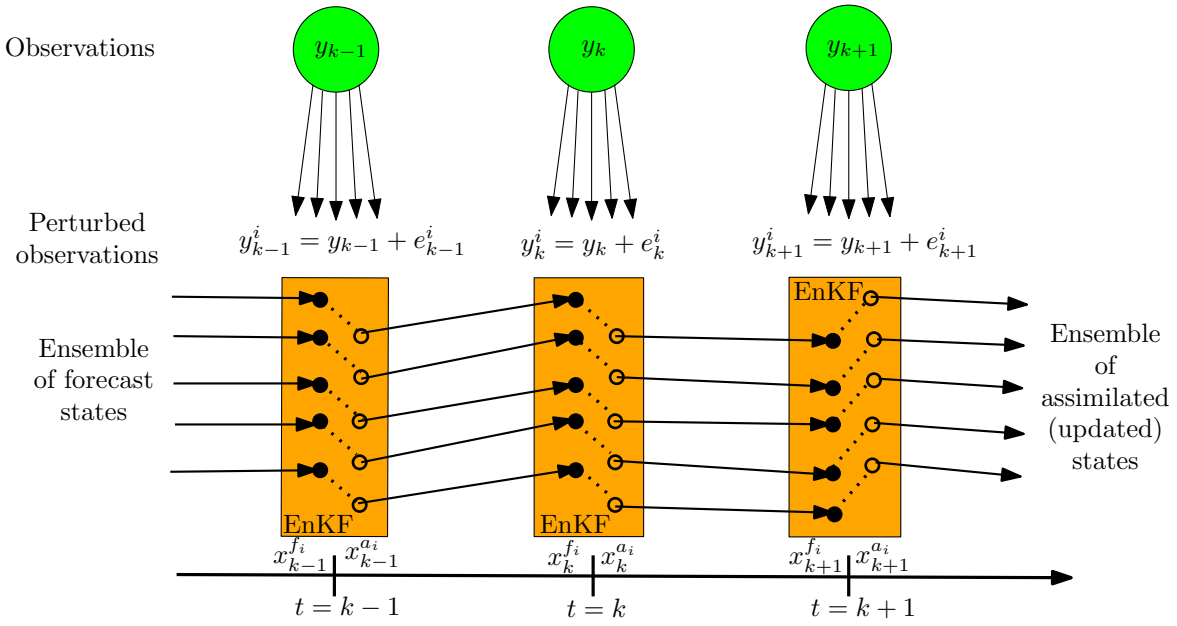

FIGURE 2.3: A schematic description of the Ensemble Kalman Filter. Adapted from [37].

independent. This implies that their parallelization can be trivially carried out. This is one of the reasons for the success and popularity of the EnKF and UKF.

2.6 An algorithm for parameter estimation with data assimilation

The parameter estimation problem tends to improve estimates of a set of poorly known model parameters using DA. Generally, we have observable data for the state, but no direct observable data for the parameters. Parameter estimation can be performed in the same framework as state estimation, by augmenting state vectors by the poorly known parameters that need to be estimated. This framework is referred as joint state-parameter augmented models [65–68]. The augmentation requires a construction of a Kalman filter for the augmented model and parameters is considered as part of the model within the EnKF paradigm, which is updated by the analysis together with the other model's variables. However, in augmented models, an increase in the number of unknown model states and parameters increases the degree of freedom in the system and can make an estimation unstable through parameter collapse and filter divergence [69, 99]. In a dual state-parameter estimation [69] the EnKF requires two separate

state-space representation for the state and parameters through two separate parallel Kalman filters. In dual EnKF, the parameters can be updated first and then the state variables or vice-versa.

In the current work, the EnKF algorithm is used to estimate only the model parameters. The parameters are thus considered as *special state variables* (the state vector contains only the model parameters). The evolution of parameters is characterized by a random walk model [71, 100] and is defined as $\mathbf{x}_{k+1}^{i} = \mathbf{x}_{k}^{i} + \tau_{k}^{i}$. $\tau_k \sim \mathcal{N}(0, \mathbf{T}_k)$ is a small random perturbation with predefined variance $\mathbf{T}$. The parameter estimation algorithm uses a set of $nobs$ observations such as blood pressure, blood flow rates, flow velocity or arterial wall movements to improve a set of given initial estimate of the hemodynamic parameters, $\mathbf{x}$. Numerical simulators can be regarded as nonlinear functions that take parameter vector $\mathbf{x}^i$ as an input and produces a set of output vector, $\mathbf{Y}_k = (\mathbf{y}_k^{f_1}, \ldots, \mathbf{y}_k^{f_{q_{\text{ens}}}}) \in \mathbb{R}^{q_{\text{ens}} \times nobs}$ [101]. Each member, $\mathbf{y}_k^{f_i}$, is defined by $\mathbf{y}_k^{f_i} = \mathcal{H}(\mathbf{x}^{fi})$, where $\mathcal{H}$ is the nonlinear measurement function defined by the numerical simulator. The information from observations are used by the Kalman filter during the analysis step and the Kalman gain Equation (2.24) is applied to update the ensemble members. The use of Equation (2.24) assumes that the parameters follow a Gaussian distribution [101]. The parameter estimation procedure using the EnKF is stated in Algorithm 1 [37]. The algorithm can be stopped when some finite convergence criterion is achieved. At convergence, the mean of the ensemble is taken as the best estimate of the parameters. A flow chart for parameter estimation using EnKF is shown in Figure 2.4

Algorithm 1: Parameter estimation using EnKF. Adapted from Lal et al. [37]

Input: Ensemble size q_{ens}, maximum number of EnKF iteration (j_{max}), variance matrix $\mathbf{T}$, $nobs$, initial estimate of n unknown parameters (mean $\overline{x}_l$ and variance P_l for $l = 1, \ldots, n$).

Initialization: Randomly initialize an ensemble of parameters, $\mathbf{x}^i$, for $i = 1, \ldots, q_{\text{ens}}$ where $\mathbf{x}^i = (x_1, x_2, \ldots, x_n)$ and $x_l \sim \mathcal{N}(\overline{x}_l, P_l)$ for $l = 1, \ldots, n$.

Let $\mathbf{x}^{a_i} = \mathbf{x}^i$

for $j = 1$ ***to*** j_{max} **do**

  -Evolution of ensemble: $\mathbf{x}^{f_i} = \mathbf{x}^{a_i} + \tau^i$, $\tau^i \sim \mathcal{N}(0, \mathbf{T})$ $\forall i = 1, \ldots, q_{\text{ens}}$

  -Ensemble propagation: $\mathbf{y}^{f_i} = \mathcal{H}(\mathbf{x}^{f_i})$ $\forall i = 1, \ldots, q_{\text{ens}}$

  -Perturbation of observations for each ensemble: $\mathbf{y}^i = \mathbf{y} + \mathbf{e}^i$, $\forall i = 1, \ldots, q_{\text{ens}}$

  -Determine R and K using Equations (2.26) and (2.33) respectively.

  -Ensemble update: $\mathbf{x}^{a_i} = \mathbf{x}^{f_i} + \mathbf{K}\left[\mathbf{y}^i - \mathbf{y}^{f_i}\right]$ $\forall i = 1, \ldots, q_{\text{ens}}$.

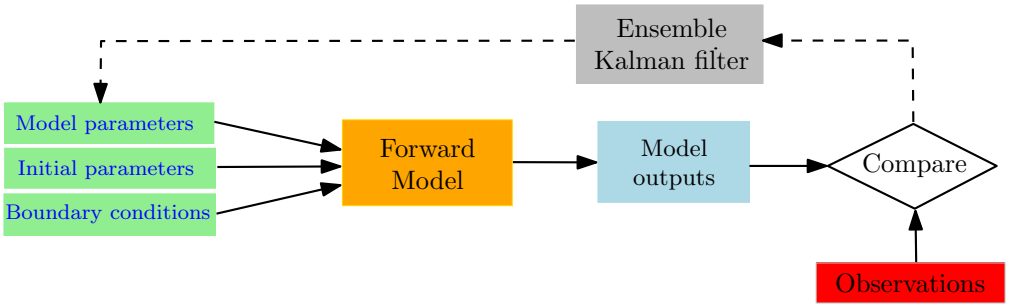

FIGURE 2.4: Parameter estimation flow chart using the ensemble Kalman filter.

2.7 An example of EnKF algorithm application: a test case

2.7.1 Parameter estimation of an advection-diffusion equation

The EnKF parameter estimation algorithm (Algorithm 1) is applied to a simple advection-diffusion problem. We consider the model equation:

$$\frac{\partial s}{\partial t} + v\frac{\partial s}{\partial z} = \mu\frac{\partial^2 s}{\partial z^2}, \tag{2.37}$$

where $s\,(z,t)$ is the model state variable of interest at position z and time t, v is the constant advection velocity, and μ is the viscosity (diffusion coefficient). Using finite difference method, Equation (2.37) is discretized over a spatial grid with N = 100 nodes, resulting in (at time $t = k+1$)

$$\frac{s_{k+1}^j - s_k^j}{\Delta t} = -v\frac{s_k^{j+1} - s_k^{j-1}}{2\Delta z} + \mu\frac{s_k^{j+1} - 2s_k^j + s_k^{j-1}}{(\Delta z)^2} + \mathcal{O}\left(\Delta t, (\Delta z)^2\right) \tag{2.38}$$

for $j = 2, 3, \ldots, N-1$. Model parameters are: the grid size $\triangle z$ = 0.01 m; the domain length L = 1 m; the advection velocity v = 1 ms^{-1} and the viscosity μ = 0.01 m^{2}s^{-1}. The computational domain is set to $[0,1]$. The initial condition is given by $s(z,0) = 1$, and the boundary conditions are defined by

$$s(0,t) = A + B\sin\omega t, \tag{2.39}$$

$$s(1,t) = 2\,s(0.99,t) - s(0.98,t), \tag{2.40}$$

where A = 1.0 m, B = 0.25 m and w = 10 rad·s^{-1}. The model time step, Δt, is chosen such that $\Delta t \leq \min\left\{\frac{\Delta z^2}{2\mu}, \frac{\Delta z}{\mu}\right\}$.

Equation (2.38) can be written as: $\mathbf{s}_{k+1} = \mathbf{f}(\mathbf{s}_k, \mathbf{x}) + \mathbf{w}_k$, where the column vector $\mathbf{s}_k = (s_k^1, s_k^2, \ldots, s_k^{100})^{\mathrm{T}} \in \mathbb{R}^{100}$ is the model state vector. The vector $\mathbf{x} = (v, \mu, A, B, \omega)^{\mathrm{T}} \in \mathbb{R}^5$ is a vector of five model parameters. The operator $\mathbf{f}$ is the linear function describing the evolution of the model state from time $t = k$ to $t = k+1$. The vector of model state error $\mathbf{w}_k$ = 0 assuming the perfect model assumption [102]. Therefore, the uncertainty in the unknown parameters is the only source of the model error.

Twin experiments are performed to illustrate how parameters can be estimated using the EnKF Algorithm 1. In the twin experiments, a reference (target) solution is generated by simulating the model for a relatively long period of time with known parameters, $\mathbf{x} = (v, \mu, A, B, \omega)^{\mathrm{T}}$, together with the initial and boundary conditions as specified above. Four time series values of the state s at positions $z = 0.05, 0.25, 0.45$ and $z = 0.8$ are recorded. We define $nobs$ as the number of positions where a time series of observed state values are available, and thus, for the above four time series synthetic observations, $nobs$ = 4.

For the parameter estimation problem, the aim is to retrieve the original set of parameters, $\mathbf{x}$, using synthetic observations. The problem set-up is shown in Figure 2.5. The uncertain model parameters are treated as special states for estimation and assuming a random walk model, is defined as $\mathbf{x}_{k+1} = \mathbf{x}_k + \tau_{k+1}$, where $\tau_{k+1} \sim \mathcal{N}(0, 1 \times 10^{-7})$. The measurement vector is $\mathbf{y}_k = h(\mathbf{s}_k, \mathbf{x}_k)$, where h is the linear measurement function defined by $h(\mathbf{s}_k, \mathbf{x}_k) = (s_k^5, s_k^{25}, s_k^{45}, s_k^{80})^{\mathrm{T}}$.

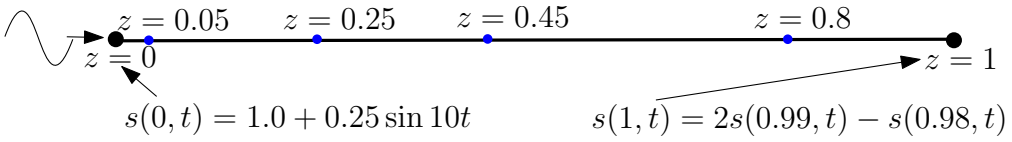

FIGURE 2.5: Illustration of the parameter estimation problem set-up for advection-diffusion model. Observations (time series values of s) are available at positions z=0.05 m, 0.25 m, 0.45 m and 0.8 m.

An ensemble of $q_{\text{ens}} = 25$ members is formed. Each i^{th} forecast member, $\mathbf{x}^{fi}$, runs with different parameter values, in order to estimate the effect of the parameters to be estimated in the model state. The error covariance matrix is defined as $\mathbf{R}_k = 0.002\mathbf{I}_4$. To test the sensitivity to initial parameter values, the performance of the EnKF parameter estimation algorithm is tested using two different sets of initial estimates for the five parameters (v, μ, A, B, ω).

The parameter values are drawn from a Gaussian distribution with initial mean values that are intentionally either lower or higher than the target parameters. The initial mean values for $\{v, \mu, A, B, \omega\}$ are {0.5, 0.05, 0.6, 0.4, 7.5} and {1.5, 0.02, 1.5, 0.05, 15.0}, and the initial ensemble variance are 12.25% of the mean values. The estimation algorithm using the EnKF coupled with the advection-diffusion model is performed using an assimilation window of 100 s with the assimilation taking place every 0.15 s. This means 667 EnKF iterations.

2.7.2 Results and discussion

Figure 2.6 shows the estimated parameter evolution with the two sets of initial estimates of parameters. The parameter ensemble standard deviation (represented by shaded regions around the solid lines in Figure 2.6) evolves with time, showing a decreasing trend. The standard deviations indicate the uncertainties associated with the estimated value of parameters. The final estimates of parameters with their associated uncertainties with the two sets of initial estimates are summarised in Table 2.3. The estimated parameter values converge to the target value with relatively small errors in less than 80 s, after that, the mean values of estimated parameters remain almost constant. It should be noted from Figure 2.6 and Table 2.3 that the algorithm allows retrieving the target value independently on the initial estimate.

TABLE 2.3: Initial and EnKF estimated parameters. The parameter values are based on the ensemble average after 667 EnKF iterations.

Parameter	Target	Initial guess	Final EnKF estimate	Uncertainty (standard deviation)
v (ms^{-1})	1.0	0.5	0.990	0.002
		1.5	1.000	0.002
μ (m^2s^{-1})	0.01	0.05	0.010	0.001
		0.02	0.010	0.001
A (m)	1.0	0.6	1.000	0.002
		1.5	1.000	0.002
B (m)	0.25	0.4	0.250	0.003
		0.05	0.249	0.003
w ($rad{\cdot}s^{-1}$)	10.0	7.5	10.0100	0.0006
		15.0	10.0800	0.0006

The effect of parameter estimation on the error in the model parameters is also analysed. The analysis error for the model parameters are computed using the root

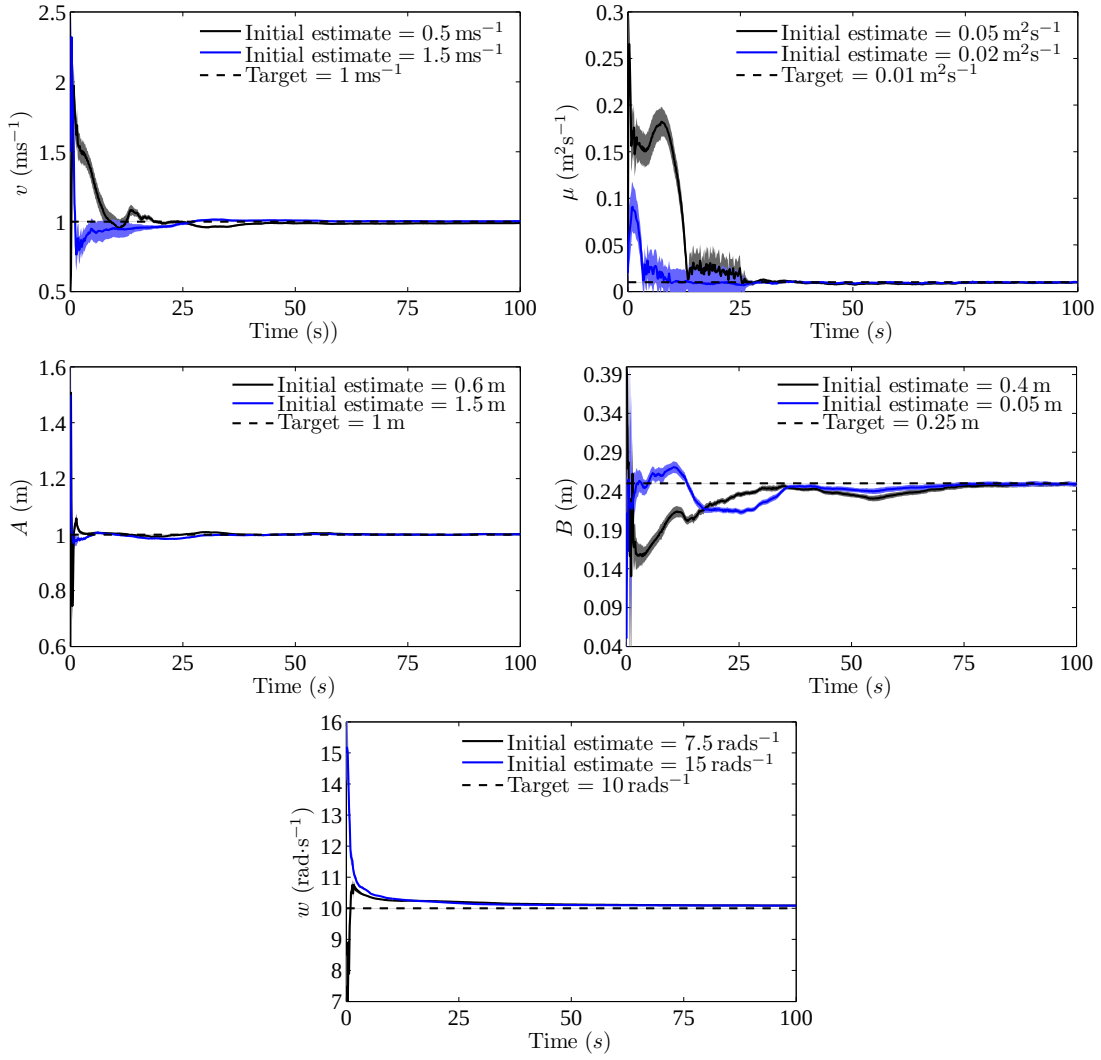

FIGURE 2.6: Time evolution of estimated parameters (ensemble mean values represented by solid lines) using two sets of initial estimates: initial mean estimates of parameters are: $\{v, \mu, A, B, \omega\}$ are {0.5, 0.05, 0.6, 0.4, 7.5} and {1.5, 0.02, 1.5, 0.05, 15.0}. The shaded areas around the estimated parameters indicates the final ensemble spread (standard deviation). The target value of the parameters is shown by the dotted black lines.

mean square error (RMSE),

$$\text{RMSE}\left(\mathbf{x}, \mathbf{x}^{\text{target}}\right) = \sqrt{\frac{1}{n}\left(\mathbf{x} - \mathbf{x}^{\text{target}}\right)\left(\mathbf{x} - \mathbf{x}^{\text{target}}\right)^{\text{T}}} \tag{2.41}$$

where $\mathbf{x}$ and $\mathbf{x}^{\text{target}}$ are EnKF estimated and target parameters respectively, and $n = 5$ is the length of the parameter vector. The time evolution of RMSE in parameter estimates is shown in Figure 2.7a for different ensemble size ranging from $q_{\text{ens}} = 4$ to $q_{\text{ens}} = 50$. From the analysis RMSE, we see that the accuracy of the EnKF increases when the

number of ensemble size increases. Figure 2.7b shows the evolution of the final value of RMSE as a function of the ensemble size. This illustrates the trade-off between EnKF accuracy and the ensemble size. From this figure, the RMSE does not decrease after q_{ens} = 17 and, thus, can be taken as the minimum q_{ens} required by the EnKF parameter estimation algorithm for the current test case.

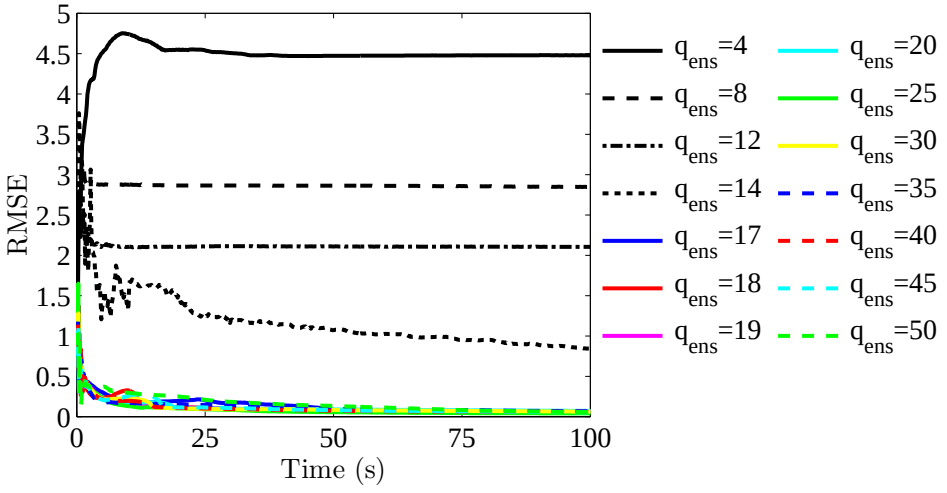

(a)

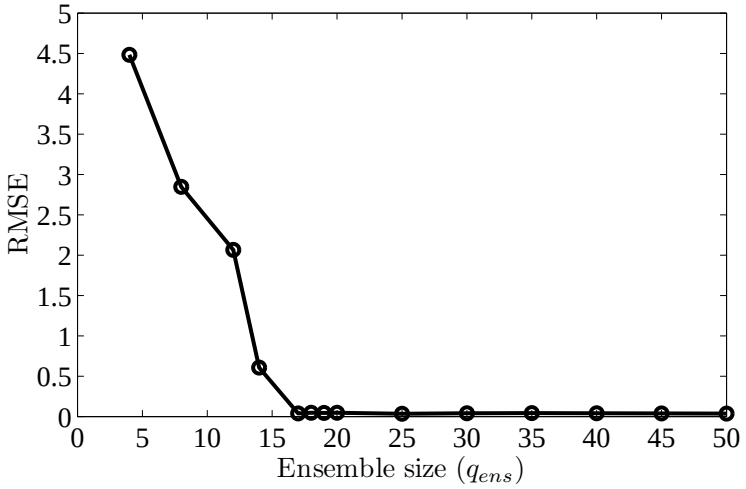

(b)

FIGURE 2.7: Time evolution of RMSE: (2.7a) with different ensemble size ranging from q_{ens} = 4 to q_{ens} = 50 and (2.7b) as a function of ensemble size q_{ens}.

Figures 2.8a and 2.8b show the estimated time evolution solutions of state s obtained with the EnKF estimated parameters at two of the four observation locations (at position $z = 0.05\,\text{m}$ and $z = 0.45\,\text{m}$). The estimated solutions are compared with the initial estimates and the target waveform of the state s at the two positions for two complete

cycles. The forward simulation with the estimated parameters is able to capture the target time evolution solutions of state s at positions where observations were made. Figure 2.8c illustrates the convergence of the estimated solution at t=1.26 s (after 2 cycles) using q_{ens} = 25. The estimated solution when compared with the target state profile (reference solution) shows good agreement over the full computational domain.

Overall, for this simple advection-diffusion problem, the EnKF showed good performance in both estimation of parameters and its accuracy.

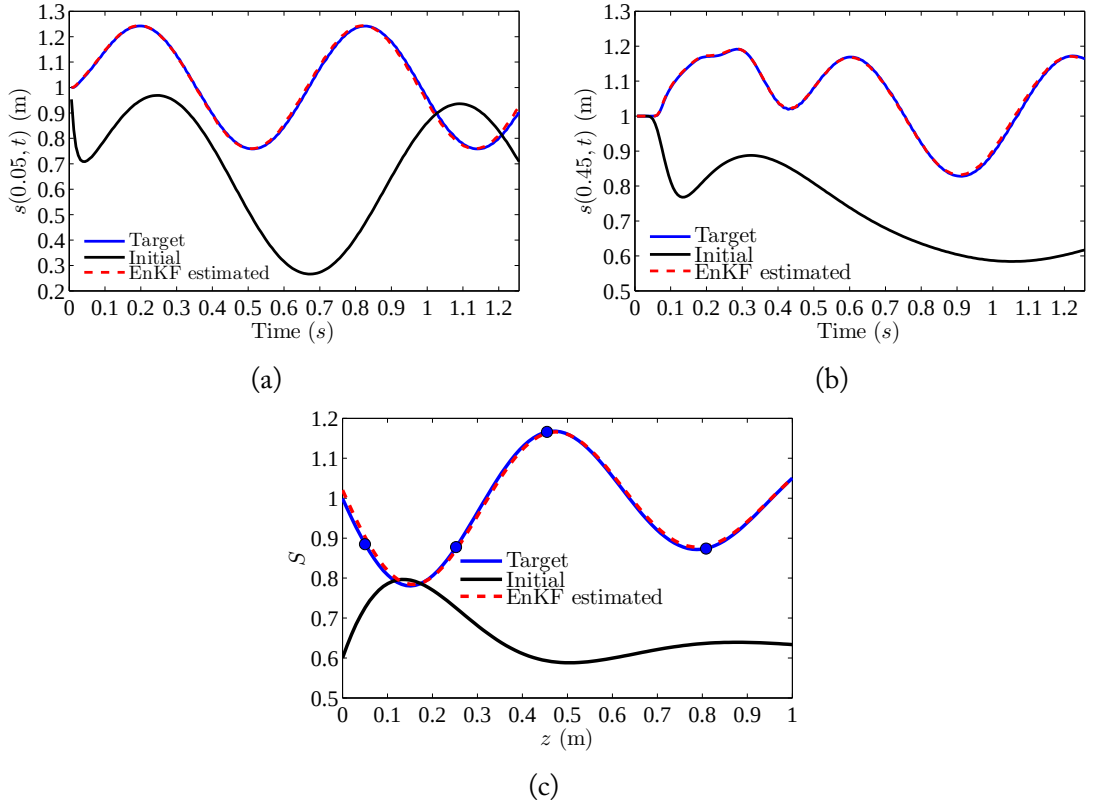

FIGURE 2.8: (2.8a) compares the estimated time evolution solution of the observed state (in dotted red) at z = 0.05 m with the initial (in black) and the target waveform (in blue). (2.8b) shows the corresponding comparison of the observed state at z = 0.45 m. In (2.8c) the plots show the target state profile (in blue), measurements (blue dots), and the EnKF estimate (in dotted red) at time t = 1.26 s.

Chapter 3

One-dimensional blood flow model

Contents

This chapter presents the existing numerical method for the 1D blood flow on systemic networks. It reviews the two types of boundary conditions used in the thesis, the constant resistance model and the three element Windkessel model. The chapter is concluded by applying the ensemble Kalman filter-based parameter estimation to four simple test cases with in silico and real measurements (data).

3.1 Introduction

The one-dimensional (1D) governing equations for the blood flows have been extensively used in hemodynamic applications (especially to study wave propagation phenomena in arteries) due to being computationally cheap compared to three-dimensional (3D) fluid-structure interaction models [3, 5, 103]. The 1D model provides good and accurate results if the 3D effects in the flow can be neglected, and its applicability have been extended to the venous system (e.g. Müller and Toro [104] and Ho et al. [105]). The 1D model can also be used to explore the factors causing changes in flow pulse and pressure waveforms in arteries due to cardiovascular disease [5].

Some of the major contributions to the mathematical formulation of 1D blood flow modelling and its applications to hemodynamics include the works of Hughes and Lubliner [106], Avolio [107], Stettler et al. [108], Stergiopulos et al. [109], Olufsen et al. [110], Formaggia et al. [111], Sherwin et al. [1, 112], Bessems et al. [113], Mynard and Nithiarasu [114], Hellevik et al. [115], Reymond et al. [116], Saito et al. [13], Low et al. [117], Eck et al. [118], Müller and Toro [104, 119], Montecinos et al. [4] and Blanco et al. [3, 120, 121].

1D blood flow models have also been used to capture essential features of blood flow rates and pressure waveforms in large blood vessels. These include using in vitro experiments (e.g. Saito et al. [13], Huberts et al. [122] and Alastruey et al. [123]) and in vivo measurements (e.g. Reymond et al. [116], Steele et al. [124] and Willemet et al. [125]).

3.2 Mathematical model

3.2.1 One-dimensional model for blood flow

The model assumes that blood is a Newtonian fluid in large vessels and can be considered incompressible with constant density ρ and constant dynamic viscosity μ [126]. It is also assumed that the blood vessels have cylindrical geometries with cross section area A, and the cardiovascular system is considered as a network of these interconnected vessels with blood flow in one-dimension (see Figure 3.1).

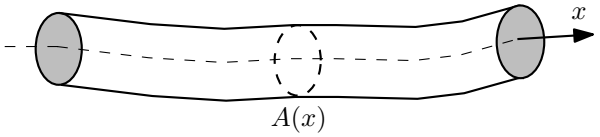

FIGURE 3.1: A simple elastic tube as a model of an artery.

We consider the following governing equations representing mass and momentum conservation [1]:

$$\begin{aligned} \frac{\partial A}{\partial t} + \frac{\partial q}{\partial x} &= 0, \\ \frac{\partial q}{\partial t} + \frac{\partial}{\partial x}\left(\alpha \frac{q^2}{A}\right) + \frac{A}{\rho}\frac{\partial p}{\partial x} &= -k_r \frac{q}{A}, \end{aligned} \tag{3.1}$$

where x and t represent the axial direction and time respectively, $A(x,t)$ is the cross section area, $q(x,t)$ is the flow rate across a section, ρ denotes the density of the blood, p is the average internal pressure over the cross-section, and $u(x,t) = \frac{q(x,t)}{A(x,t)}$ represents the cross section averaged blood velocity. For a flat velocity profile, the momentum-flux correction coefficient, α, equals unity [1]. k_r represents the viscous resistance of the flow per unit length of the vessel. A, q and p are the unknowns in the system (3.1).

A differential constitutive pressure-area relationship is required to close the system and accounts for the fluid-structure interaction of the problem [1, 5]. A nonlinear model for pressure law (or tube law) is adopted according to Kelvin-Voigt model [13]:

$$p = p_e + \frac{\beta}{A_0}\left[\left(\sqrt{A} - \sqrt{A_0}\right) + \epsilon_p \left(\sqrt{A} - \sqrt{A_0}\right)^2\right] + \frac{\gamma}{A_0}\frac{\partial \sqrt{A}}{\partial t}. \tag{3.2}$$

Here, p_e denotes the constant external pressure, $A_0 = A_0(x)$, denotes the vessel sectional area at equilibrium state and ϵ_p is the non linearity coefficient. The term γ is $h\eta\sqrt{\pi}$,

where h is the thickness of the tube and η is the viscoelastic coefficient. The coefficient β, which is related to the arterial stiffness is defined as:

$$\beta = \frac{\sqrt{\pi} h E}{(1-\sigma^2)}, \tag{3.3}$$

where $E = E(x)$ is the Young's modulus and $\sigma = 0.5$ is the Poisson ratio [1].

With a specified inflow boundary condition, the 1D governing equations for the blood flow are solved using the terminal models for the outflow boundary conditions [3].

3.2.2 Characteristics analysis

The 1D model (3.1) can be rewritten in a conservative form,

$$\frac{\partial \mathbf{U}}{\partial t} + \frac{\partial \mathbf{F}(\mathbf{U})}{\partial x} = \mathbf{S}(\mathbf{U}), \tag{3.4}$$

where $\mathbf{U} = [A, q]^T$ denotes the vector of conserved variables, $\mathbf{F}(\mathbf{U})$ are the fluxes and $\mathbf{S}(\mathbf{U})$ are the source terms defined by:

$$\begin{aligned} \mathbf{F}(\mathbf{U}) &= \begin{bmatrix} q \\ \alpha \frac{q^2}{A} + \frac{\beta}{3\rho A_0} A^{\frac{3}{2}} + \frac{\beta \epsilon_p}{\rho A_0} \left(\frac{1}{2} A^2 - \frac{2}{3} \sqrt{A_0} A^{\frac{3}{2}} \right) \end{bmatrix}, \\ \mathbf{S}(\mathbf{U}) &= \begin{bmatrix} 0 \\ -k_r \frac{q}{A} + \frac{\gamma \sqrt{A}}{2\rho A_0} \left(\frac{\partial^2 q}{\partial x^2} - \frac{1}{2A} \frac{\partial A}{\partial x} \frac{\partial q}{\partial x} \right) \end{bmatrix}. \end{aligned} \tag{3.5}$$

The highly coupled system of non-linear equations (3.4) is decoupled to implement the numerical solution with the prescribed boundary conditions [114]. The characteristic system is derived by expressing the system of equations (3.4) in a quasi-linear form which can be expressed as [114]:

$$\frac{\partial \mathbf{U}}{\partial t} + \mathbf{J} \frac{\partial \mathbf{U}}{\partial x} = \mathbf{S}, \tag{3.6}$$

where the Jacobian reads:

$$\mathbf{J}(\mathbf{U}) = \frac{\partial \mathbf{F}}{\partial \mathbf{U}} = \begin{bmatrix} 0 & 1 \\ -\alpha \frac{q^2}{A^2} + \frac{\beta}{2\rho A_0} A^{\frac{1}{2}} + \frac{\beta \epsilon_p}{\rho A_0} \left(A - \sqrt{A_0} \sqrt{A} \right) & 2\alpha \frac{q}{A} \end{bmatrix}. \tag{3.7}$$

Through consideration of the non-linear coefficient (ϵ_p) and viscoelasticity (η) as source terms, the characteristic analysis shows that for all allowable **U** (that is for $A > 0$), the system is hyperbolic and the two real eigenvalues of **J** are [2, 127]:

$$\begin{aligned}\lambda_1 &= \frac{\alpha q}{A} + \sqrt{\frac{\beta}{2\rho A_0} A^{\frac{1}{2}} + \alpha(\alpha-1)\frac{q^2}{A^2}} > 0,\\ \lambda_2 &= \frac{\alpha q}{A} - \sqrt{\frac{\beta}{2\rho A_0} A^{\frac{1}{2}} + \alpha(\alpha-1)\frac{q^2}{A^2}} < 0.\end{aligned} \tag{3.8}$$

When $\alpha = 1$, the associated characteristic variables have the following expressions:

$$\begin{aligned}W_1 &= \frac{q}{A} + 4(c - c_0),\\ W_2 &= \frac{q}{A} - 4(c - c_0),\end{aligned} \tag{3.9}$$

where $c = \sqrt{\frac{\beta}{2\rho A_0}} A^{\frac{1}{4}}$ and $c_0 = \sqrt{\frac{\beta}{2\rho A_0}} A_0^{\frac{1}{4}}$. The characteristic system can be expressed as the decoupled system of equations:

$$\begin{aligned}\frac{\partial w_1}{\partial t} + \lambda_1 \frac{\partial w_1}{\partial x} &= 0,\\ \frac{\partial w_2}{\partial t} + \lambda_2 \frac{\partial w_2}{\partial x} &= 0.\end{aligned} \tag{3.10}$$

The wave velocity which arises from the blood wall coupling may take values as low as 5 m/s in large arteries (e.g. aorta), increasing to values around 20-35 m/s in less distensible peripheral arteries [126]. However, peak flow velocities u are much smaller and usually remain less than around 1 m/s.

3.3 Numerical methods

To solve the 1D equations in the time domain, different formulations and several numerical schemes have been proposed and used. Some of the common methods (or schemes) include the finite element methods such as Galerkin [112–114, 123–125, 128] and Taylor-Galerkin [111, 129] schemes, the method of characteristics [130, 131], finite volume methods [132, 133], finite difference methods such as the Lax-Wendroff [110, 134, 135] and the MacCormack methods [13, 115].

3.3.1 Numerical scheme for one-dimensional blood flow

In this section, we follow Peiró and Veneziani [129] and Formaggia et al. [111], where equations of the 1D model are discretized in their conservative form (3.4) by employing a second order Taylor Galerkin scheme. We denote $\triangle t = t^{n+1} - t^n$ the time step and express the Taylor expansion truncated to the second order at time t^n, giving

$$\mathbf{U}^{n+1} = \mathbf{U}^n + \triangle t \frac{\partial \mathbf{U}}{\partial t}\bigg|^n + \frac{\triangle t^2}{2}\frac{\partial^2 \mathbf{U}}{\partial t^2}\bigg|^n. \tag{3.11}$$

We define the matrix

$$\mathbf{K} = \frac{\partial \mathbf{S}}{\partial \mathbf{U}} = \begin{bmatrix} 0 & 0 \\ k_r \frac{q}{A^2} + \frac{\gamma}{4\rho A_0}\frac{1}{\sqrt{A}}\left(\frac{\partial^2 q}{\partial x^2} + \frac{1}{2A}\frac{\partial A}{\partial x}\frac{\partial q}{\partial x}\right) & -\frac{k_r}{A} \end{bmatrix}, \tag{3.12}$$

and rewrite Equation (3.4) as

$$\frac{\partial \mathbf{U}}{\partial t} = \mathbf{S} - \frac{\partial \mathbf{F}}{\partial x}. \tag{3.13}$$

Using the matrices (3.7) and (3.12), we obtain

$$\begin{aligned} \frac{\partial^2 \mathbf{U}}{\partial t^2} &= \frac{\partial \mathbf{S}}{\partial \mathbf{U}}\frac{\partial \mathbf{U}}{\partial t} - \frac{\partial}{\partial x}\left(\frac{\partial \mathbf{F}}{\partial \mathbf{U}}\frac{\partial \mathbf{U}}{\partial \mathbf{t}}\right) \\ &= \mathbf{K}\frac{\partial \mathbf{U}}{\partial \mathbf{t}} - \frac{\partial}{\partial x}\left(\mathbf{J}\frac{\partial \mathbf{U}}{\partial \mathbf{t}}\right) \\ &= \mathbf{K}\left(\mathbf{S} - \frac{\partial \mathbf{F}}{\partial x}\right) - \frac{\partial(\mathbf{JS})}{\partial x} + \frac{\partial}{\partial x}\left(\mathbf{J}\frac{\partial \mathbf{F}}{\partial \mathbf{x}}\right). \end{aligned} \tag{3.14}$$

At time $t^n = n\triangle t$, the vector of unknowns $\mathbf{U}^n$ satisfies the following time marching scheme:

$$\begin{aligned} \mathbf{U}^{n+1} &= \mathbf{U}^n + \triangle t\left(\mathbf{S}^n - \frac{\partial \mathbf{F}^n}{\partial x}\right) \\ &+ \frac{\triangle t^2}{2}\left(\mathbf{K}^n\left(\mathbf{S}^n - \frac{\partial \mathbf{F}^n}{\partial x}\right) - \frac{\partial(\mathbf{J}^n\mathbf{S}^n)}{\partial x} + \frac{\partial}{\partial x}\left(\mathbf{J}^n\frac{\partial \mathbf{F}^n}{\partial x}\right)\right). \end{aligned} \tag{3.15}$$

The spatial discretization uses linear finite elements. The domain Ω is subdivided into N_{el} finite elements Ω_e of size h_e. We let V_h be the set of continuous vector functions in Ω, linear on each element and V_h^0 the subspace of V_h whose functions are zero at the endpoints [129]. The solution of (3.15) requires, for $n \geq 0$, to determine $\mathbf{U}^{n+1}$ in V_h

such that $\forall \phi_h \in V_h^0$,

$$\begin{aligned}\left(\mathbf{U}^{n+1}, \phi_h\right) &= \left(\mathbf{U}^n, \phi_h\right) + \triangle t \left(\mathbf{S}^n, \phi_h\right) + \triangle t \left(\mathbf{F}^n, \frac{\partial \phi_h}{\partial x}\right) \\ &+ \frac{\triangle t^2}{2}\left(\mathbf{K}^n\left(\mathbf{S}^n - \frac{\partial \mathbf{F}^n}{\partial x}\right), \phi_h\right) \\ &+ \frac{\triangle t^2}{2}\left(\mathbf{J}^n\left(\mathbf{S}^n - \frac{\partial \mathbf{F}^n}{\partial x}\right), \frac{\partial \phi_h}{\partial x}\right),\end{aligned} \tag{3.16}$$

where $(\mathbf{U}, \phi) = \int_0^L \mathbf{U}.\phi dx$.

For the stability of the numerical method, we follow Formaggia et al. [111] and impose the following limitation for the time step:

$$\triangle t \leq \text{CFL} \times \min_{0 \leq i \leq N_{el}} \left[\frac{h_i}{\max(\lambda_{1,i}\lambda_{1,i+1})}\right] \tag{3.17}$$

where $\lambda_{1,i}$ is the value of λ_1 at mesh node x_i and the maximum CFL number is $\frac{\sqrt{3}}{3}$ [111].

3.3.2 Initial and boundary conditions

The initial conditions for (3.15) are given by:

$$A(x,0) = A_0(x),\ q(x,0) = 0,\ p(x,0) = p_0(x), \tag{3.18}$$

where $A_0(x)$ and $p_0(x)$ are the prescribed functions. The hyperbolic nature of the system permits to impose the flow rate q or area A at the inlet [1]. At the inlet usually, the flow rate is specified [136],

$$q(0,t) = q_{\text{in}}(t). \tag{3.19}$$

Information from the outside and inside of the domain are carried by the incoming characteristics (W_1) and the outgoing characteristics (W_2) respectively [137]. At each end of the tube, a single boundary condition is implemented. This is due to the characteristic analysis and using the fact that the flow is subcritical (the eigenvalues [$\lambda_1$and λ_2] in Equation (3.8) have opposite signs) under physiological conditions [1, 138]. At the inlet at $x = 0$, $\mathbf{U}^n$ is assumed to be known and λ_2 in (3.10) is linearised by taking its value at time t^n. It can be shown that at the time t^{n+1}, the

solution corresponding to this linearised problem yields [1, 114]

$$W_2^{n+1}(0) = W_2^n(-\lambda_2^n(0) \triangle t). \tag{3.20}$$

Equation (3.20) is a first order extrapolation of W_2 from the previous time step. Similar treatment at the outlet $x = L$, leads to:

$$W_1^{n+1}(L) = W_1^n(L - \lambda_1^n(L) \triangle t). \tag{3.21}$$

3.3.3 Terminal boundary conditions

To reduce the complexity of the blood flow simulation, peripheral vessels (small arteries, arterioles and capillaries), which are downstream of the truncation points are not explicitly accounted for but their effect is represented by proper outflow boundary conditions [139]. The two most common types of terminal boundary conditions used are the *constant or single resistance model* [1, 13, 114, 137, 139, 140] and the *three-element Windkessel model* [5, 14, 32, 139, 141–143], that can be obtained using an analogy based on electric circuit components.

3.3.3.1 The constant resistance model

The constant resistance (CR) model (see Figure 3.2) is represented by a peripheral resistor R [139], where it is assumed that the blood pressure, $p(t) - p_0$, is proportional to the blood flow rate $q(t)$. p_0 is the peripheral pressure. The relation between the blood pressure and the flow is given by $p(t) - p_0 = R \cdot q(t)$. Wave reflections at the end of the terminal vessel occurs due to change in the characteristic impedance that are caused by changes in the vessel properties or branching [114, 131]. The reflection coefficient (R_t) is commonly used to express the ratio of the change in pressure across the reflected wave dP_0 and the incident wave $\triangle P_0$. The relation between the reflection coefficient and the peripheral resistance at the end of a terminal artery, is given by $R_t = \frac{\mathrm{d}P_0}{\triangle P_0} = \frac{R - Z_0}{R + Z_0}$, where $Z_0 = \frac{\rho\, c_0}{A_0}$ is the characteristic impedance of the 1-D vessel [144]. For a dead end terminal (R tends to infinity), there is a full reflection ($R_t = 1$), for an open end ($R = 0$), total negative reflection occurs ($R_t = -1$). For a well matched branch ($R = Z_0$) no reflection occurs ($R_t = 0$).

The terminal reflection coefficient for a wavefront travelling in the $+x$ direction can also be defined in terms of the incoming and outgoing characteristics as [114, 137]

$$R_t = -\frac{\triangle W_2}{\triangle W_1} = -\frac{W_2^{n+1} - W_2^0}{W_1^{n+1} - W_1^0}. \tag{3.22}$$

The values for W_1^{n+1} are determined using Equation (3.21), whereas W_1^0 and W_2^0 are the initial values [114]. The unknown W_2^{n+1} is determined by rearranging Equation (3.22), giving

$$W_2^{n+1} = W_2^0 - R_t(W_1^{n+1} - W_1^0). \tag{3.23}$$

The characteristic value W_2 is then related to the primitive variables (q, A and p) for the nodes using Equations (3.2) and (3.9).

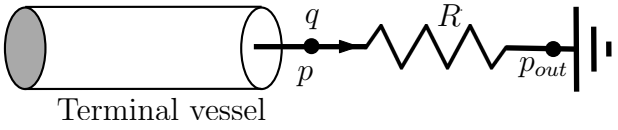

FIGURE 3.2: Electric analogue of a constant resistance (CR) model.

3.3.3.2 Windkessel model

Windkessel models are lumped-parameter models (0D) describing the hemodynamics of the arterial system and is required in models with large compliant arteries as the peripheral vessels [5]. In the three-element Windkessel model (WK3), there are three physical quantities, namely, the proximal (characteristic) resistance (R_P), the distal resistance (R_D) and the capacitance (C) [5, 109, 139, 141, 145]. $R_T = R_P + R_D$ represents the total resistance of a peripheral bed. Figure 3.3 shows the analogy of WK3 model to an electric model, where the instantaneous pressure at the inlet of the WK3 model, $p(t)$, corresponds to the voltage, and the instantaneous flow rate, $q(t)$, corresponds to the electric current. The capacitance, C, describes the compliance of the downstream arterial walls. p_{out} is the pressure (assumed to be zero) at which flow through the microcirculation is zero [142, 145, 146]. The WK3 model relates the instantaneous blood pressure and the flow rate as follows:

$$\frac{dp(t)}{dt} + \frac{p - p_{out}}{R_D C} = R_P \frac{dq(t)}{dt} + \frac{q(R_P + R_D)}{R_D C}. \tag{3.24}$$

By approximating the derivatives using forward finite difference of first order and letting $p_{out} = 0$, Equation (3.24) is coupled to the 1-D terminal branch using the following

relation:

$$a_1 p^{n+1} - p^n - a_2 q^{n+1} + a_3 q^n = 0, \tag{3.25}$$

where the coefficients are $a_1 = \left(1 + \frac{\triangle t}{R_D C}\right)$, $a_2 = \left(R_P + \frac{R_P + R_D}{R_D C} \triangle t\right)$ and $a_3 = R_P$. This relation, together with the equation for the forward characteristic, is a nonlinear system for q^{n+1}, p^{n+1} that is solved using Newton method with the initial guess q^n, p^n.

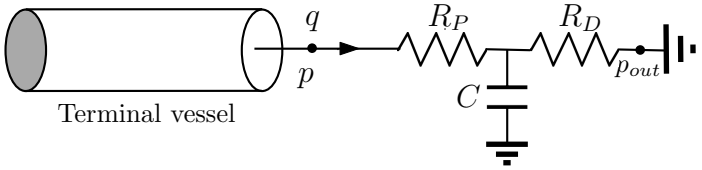

FIGURE 3.3: Electric analogue of a Windkessel (WK3) model.

3.3.4 Junctions

The coupling of several 1D vessels at branching points or bifurcations (Figure 3.4a) and merging points (Figure 3.4b) is treated following the methodology proposed in Sherwin et al. [112] and Wang et al. [137].

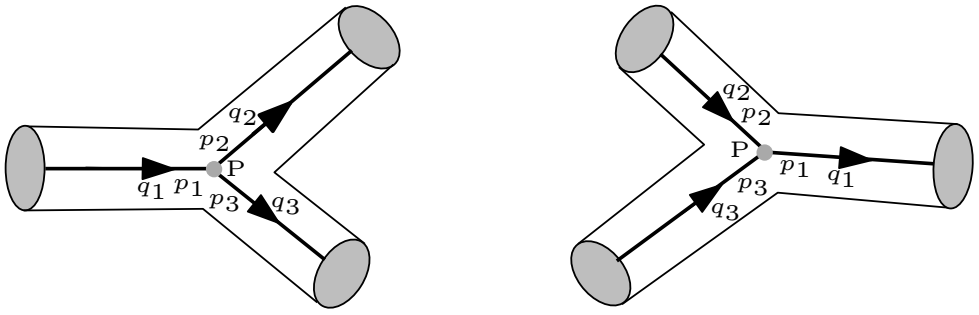

(a) (b)

FIGURE 3.4: Model geometry for coupling of blood vessels: branching points or bifurcations (3.4a) and merging flows (3.4b). The pressure losses at point P of a blood vessel are assumed to be negligible.

The pressure losses at point P (from artery index 1 to arteries 2 and 3 for bifurcations, and from artery index 2 and 3 to artery 1 for merging points) of a blood vessel are assumed to be negligible. The following coupling equations representing the conservation of flow rate and the total pressure continuity are enforced at the junction

(point P in Figure 3.4):

$$\begin{aligned} \sum_{i=1}^{3} q_i &= 0, \\ \frac{1}{2}\rho\left(\frac{q_1}{A_1}\right)^2 + p_1 &= \frac{1}{2}\rho\left(\frac{q_i}{A_i}\right)^2 + p_i, \quad i = 2, 3. \end{aligned} \tag{3.26}$$

At each bifurcation, a system involving six equations with six unknowns (cross section area and the flux for the corresponding three arteries), i.e. A_1^{n+1} and q_1^{n+1} for the outlet of the parent artery and A_2^{n+1}, q_2^{n+1}, A_3^{n+1} and q_3^{n+1} for the inlets of the two daughter arteries on Figure 3.4a, is solved. The system is made of:

1. Equation (3.26): the conservation of flow rate and the total pressure continuity equations,

2. three compatibility conditions for the characteristic variables of the hyperbolic system: $(W_1)_1, (W_2)_2$ and $(W_2)_3$.
   In the parent artery, $(W_1)_1^{n+1}$ is given by the data on the n-th time step with the interpolation formula (3.21), which must be equal to $W_1(\mathbf{U}_1^{n+1})$ given by Equation (3.9). The same rule holds for W_2 on the two daughter arteries. Hence the equations are:
   $(W_1)_1^{n+1} - W_1(\mathbf{U}_1^{n+1}) = 0,$
   $(W_2)_i^{n+1} - W_2(\mathbf{U}_i^{n+1}) = 0, \quad i = 2, 3.$

The above system consisting of 6 equations and 6 unknowns is solved by Newton's iterative method with $\mathbf{U}^n$ as the initial guess.

3.4 Coupling of EnKF estimation algorithm and the blood flow model

In this section, a series of test cases is presented in which the ensemble Kalman filter (Algorithm 1 in chapter 2) is used to solve parameter estimation problems. The hemodynamic parameters being estimated are limited to Young's modulus and boundary condition parameters (reflection coefficient and WK3 parameters). The first three cases are purely in *silico* (use synthetic data) and the final case involves real measurements in the carotid artery. The test cases are performed on a single artery and

a network of three arteries representing a bifurcation case. In the test cases, $nobs$ refers to the number of locations where a time series of pressure is available.

3.4.1 Test case 1: Parameter estimation on a single artery

3.4.1.1 Estimation of Young's modulus and reflection coefficient

The first test case deals with an estimation of Young's modulus and the boundary condition parameter (reflection coefficient) for a blood vessel representing a common carotid artery as shown in Figure 3.5. We first describe the procedure for generating the synthetic data. A Young's modulus of 0.5 MPa (assumed uniformly distributed) is assigned to the carotid artery. The length (L) of the vessel is 18 cm, the radius (r) is 6 mm and the vessel wall thickness (h) is chosen to have a uniform value of 0.063 cm.

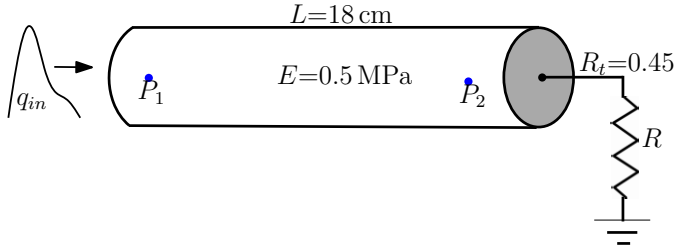

FIGURE 3.5: Test case 1: Parameter estimation on a single artery. At the inlet, q_{in} (Figure 3.6) is imposed. The outlet is coupled to a constant resistance model. The measurements (pressure values) are taken at locations $0.1L$ (pressure P_1) and $0.9L$ (pressure P_2).

A periodic flow rate [146] boundary condition $q_{\text{in}}(t)$, with a period of 0.9 s (Figure 3.6) is imposed at the inlet of the simple model. A CR model is applied at the outlet of the computational domain with a reflection coefficient of $R_t = 0.45$ as the boundary condition parameter. The density (ρ) of the fluid is taken as 1050 kg/m^3, the viscosity (μ) of 4×10^{-3} Pa·s and the Poisson coefficient (σ) of 0.5. The viscoelastic coefficient (η) and the nonlinearity coefficient (ϵ_p) of the vessel are set to 0.5 kPa·s and 0.5 m^{-1} respectively for the forward simulation. The 1D blood flow model is then executed with the above parameters using a time step of 0.1 ms. Using $nobs$ = 2, the simulated time series pressure values at locations $0.1L$ and $0.9L$ are recorded at every 0.01 s (90 per cardiac cycle) over 6 cardiac cycles.

For the estimation problem, Young's modulus (E) and the reflection coefficient (R_t) are sought. An ensemble of $q_{\text{ens}} = 20$ members is taken, and for each member of the

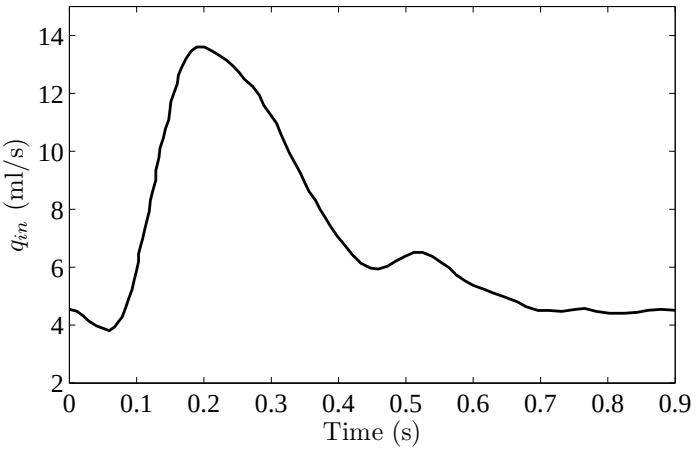

FIGURE 3.6: Periodic flow rate [146] imposed as inlet boundary condition $q_{\text{in}}(t)$.

ensemble, the observations (recorded pressure values) are perturbed by a random vector drawn from the observation error pdf $\sim \mathcal{N}(0, \sigma_p^2)$. σ_p represents the standard deviation and the error covariance matrix is assumed to be constant in time and set as $\mathbf{R} = \sigma_p^2 \mathbf{I}_2$. In test case 1, σ_p is set to 0.2. Initial estimates for Young's modulus and the reflection coefficient assume an error of 30% and 33% respectively, i.e. the initial mean value for Young's modulus is 0.7 MPa and for the reflection coefficient is 0.6. The initial ensemble standard deviation for E and R_t is 0.05 MPa and 0.05 respectively.

The parameters are then estimated using EnKF Algorithm 1 which is executed for 5 s (approximately 6 cardiac cycles). The evolution of estimated Young's modulus and the reflection coefficient are shown in Figure 3.7. The initial and final estimates of the parameters are shown in Table 3.1. The algorithm is able to converge to the target E and R_t in 6 cardiac cycles with relatively small percentage deviation from the target values. Figure 3.8 shows the comparison between the pressure solutions (pressure P_1 at $0.1L$ in Figure 3.5) obtained with the initial estimate of parameters, the final estimated pressure solution, and the target pressure solution. We see that there is a good agreement between the estimated and the target pressure waveforms.

TABLE 3.1: Test case 1: Initial and estimated parameters.

Parameter	Target	Initial guess	Final EnKF estimate	% deviation from target
E (MPa)	0.5	0.7	0.506	1.2
R_t	0.45	0.6	0.447	-0.9

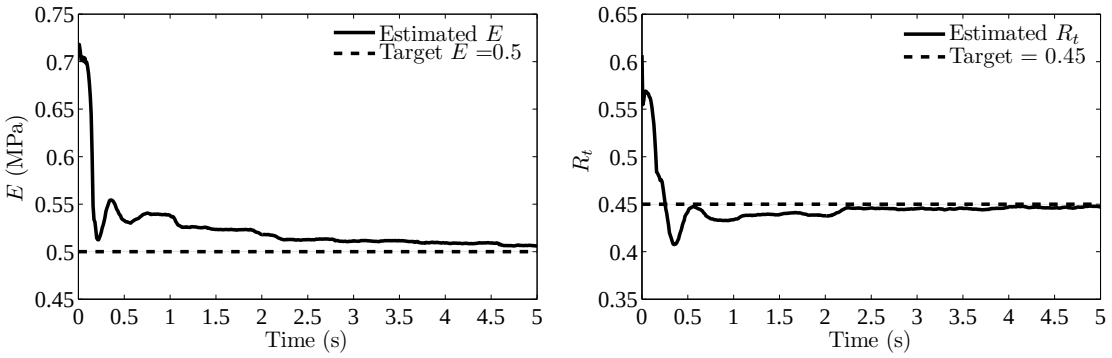

(a) (b)

FIGURE 3.7: Test case 1: Evolution of estimated parameters. (3.7a) shows the evolution of the Young's modulus, E and (3.7b) shows the evolution of the reflection coefficient, R_t. The dotted lines represents the target value of E = 0.5 MPa and R_t = 0.45.

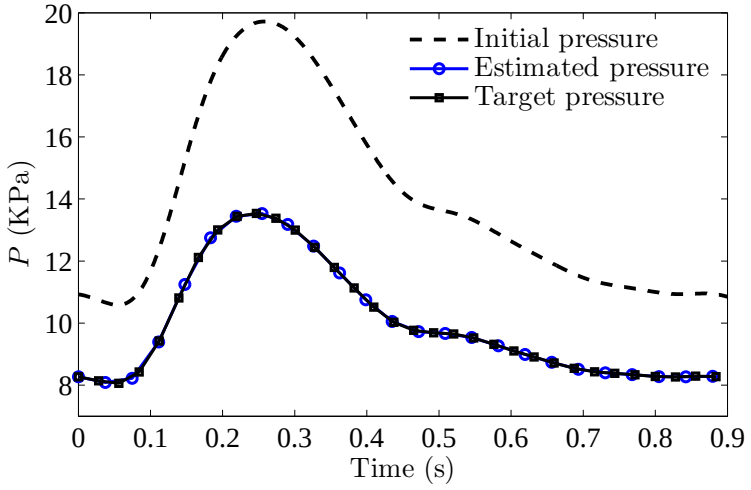

FIGURE 3.8: Test case 1: Estimated pressure solution. The figure shows the comparison between the pressure solutions (pressure P_1 at $0.1L$ in Figure 3.5) obtained with the initial estimate of parameters, the final estimated pressure solution, and the target pressure curve.

3.4.1.2 Sensitivity analysis

In this section, we look at the sensitivity of the parameter estimation algorithm for test case 1 with respect to the level of observation perturbation defined by σ_p. The observations (pressure) are perturbed by Gaussian noises which are created by adding noise ($\sim (\mathcal{N}(0, \sigma_p^2)$), to the observation values. The parameter estimation procedure is performed with two more levels of observation perturbations with σ_p set to 0.1 and 0.4. All other parameters and settings are same as in test case 1. Figures 3.9a and 3.9b show

the evolutions of the estimated Young's modulus and reflection coefficient using different values of σ_p. With different values of σ_p, the estimated E's and R_t's converge to the target values, but with a slightly different rate. The approach seems therefore quite robust with respect to the level of uncertainty on the observations.

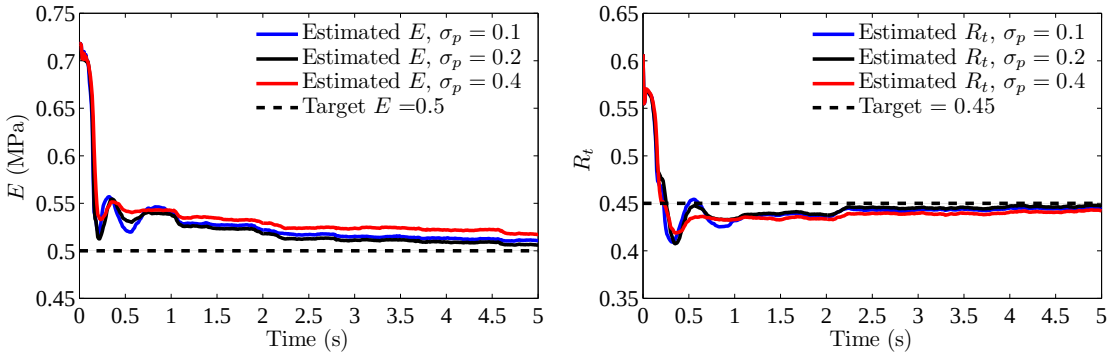

(a) (b)

FIGURE 3.9: Sensitivity analysis for test case 1: Evolution of estimated parameters. (3.9a) shows the evolution of the Young's modulus and (3.9b) shows the evolution of the reflection coefficient with different level of observation perturbation defined by σ_p. The dotted lines represents the target value of E = 0.5 MPa and R_t = 0.45.

3.4.2 Test case 2: Linearly distributed parameter on a single artery

Test case 2 involves an artery of length $L = 21$ cm that is divided longitudinally into three segments of equal lengths. Each segment is then assigned a different value of Young's modulus as shown in the Figure 3.10. A CR model with a reflection coefficient of R_t = 0.4 is applied as the boundary condition parameter. At the inlet, the flow rate q_{in} (Figure 3.6) is imposed as in test case 1.

The other parameters ($h, r, \rho, \mu, \sigma, \epsilon_p$ and η) are as in test case 1. Using a time step of 0.1 ms and $nobs$ = 3, a forward simulation is performed and time series pressure values P_1, P_2 and P_3, at locations $\frac{1}{3}L$, $\frac{2}{3}L$ and L respectively are recorded at every 0.01 s (90 per cardiac cycle).

The aim is to recover the reflection coefficient and Young's modulus for the three segments using observations P_1, P_2 and P_3. An ensemble of size q_{ens} = 20 is employed in this case and the standard deviation σ_p is set to 0.15. The initial estimate (mean of ensemble) for the Young's modulus (E_1, E_2 and E_3) and reflection coefficient (R_t) is

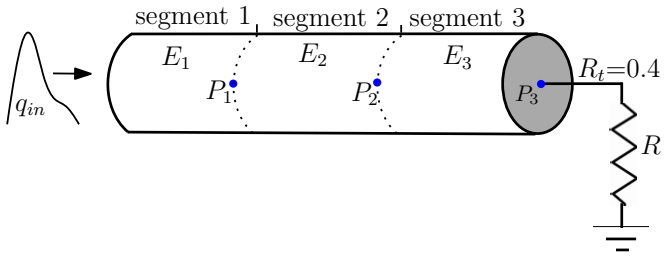

FIGURE 3.10: Test case 2: Illustration of the parameter estimation problem set-up. The artery is divided into three segments, each with different value Young's modulus ($E_1 = 0.85$ MPa, $E_2 = 0.65$ MPa, and $E_3 = 0.5$ MPa). A CR model with a reflection coefficient is used as the boundary condition parameter. Pressure values, P_1, P_2 and P_3, are observed at locations $\frac{1}{3}L$, $\frac{2}{3}L$ and L respectively.

0.7 MPa and 0.6 respectively. The initial ensemble standard deviation for E and R_t is 0.05 MPa and 0.05 respectively.

Figure 3.11 shows the evolution of the estimated parameters using EnKF with the assimilation taking place at every 0.01 s (90 per cardiac cycle). Initial and final estimates of the four parameters after 2 s (approximately 2 cardiac cycles) are shown in Table 3.2. We note that all four parameters converge to the target values used to generate the synthetic data (time series pressure values) with an error of less than 2%.

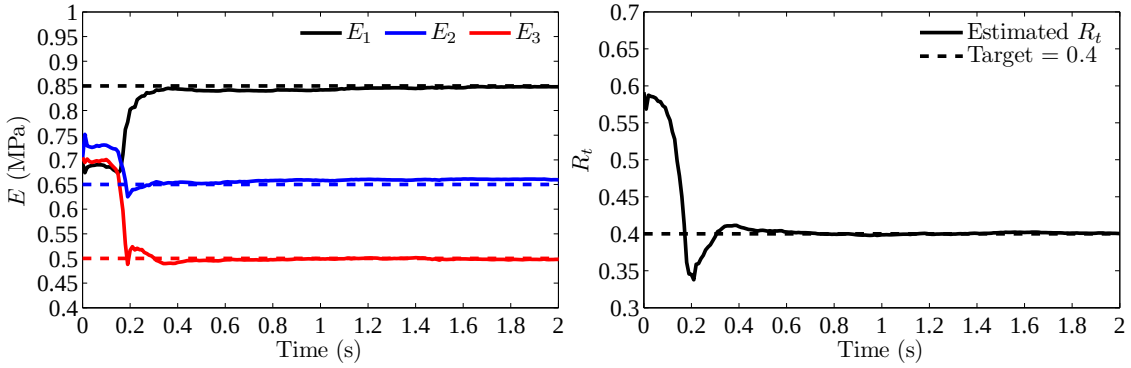

(a) (b)

FIGURE 3.11: Test case 2: Evolution of estimated parameters. (3.11a) shows the evolution of the Young's modulus, E. The dotted lines represent the target values of 0.85 MPa, 0.65 MPa, and 0.5 MPa for E_1, E_2 and E_3 respectively. (3.11b) shows the evolution of the reflection coefficient, R_t where the dotted lines represent the target value of 0.4.

TABLE 3.2: Test case 2: Initial and estimated parameters.

Parameter	Target	Initial guess	Final EnKF estimate	% deviation from target
E_1 (MPa)	0.85	0.7	0.848	-0.24
E_2 (MPa)	0.65	0.7	0.66	1.54
E_3 (MPa)	0.5	0.7	0.498	-0.4
R_t	0.4	0.6	0.4	0

In Figure 3.12, the estimated pressure solution (pressure P_2) is compared with the synthetic target pressure waveform. The forward simulation with the estimated parameters is able to recover the target pressure waveform.

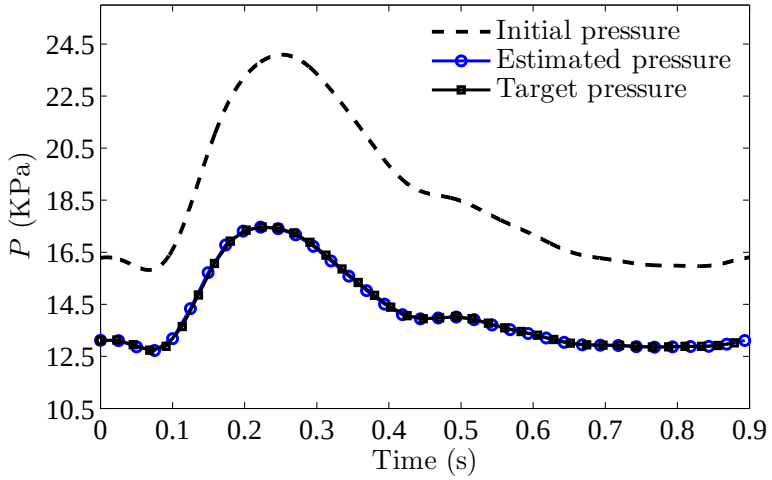

FIGURE 3.12: Test case 2: Estimated pressure solution. The figure shows the comparison between the pressure solution at location P_2 (in Figure 3.10) obtained with the initial estimate of parameters, the final estimated pressure solution, and the target pressure curve.

3.4.3 Test case 3: Parameter estimation on a bifurcation

The EnKF parameter estimation algorithm is tested on a bifurcation network as shown in Figure 3.13. The parent vessel and two daughter vessels have different geometries and are assigned with different values of Young's modulus. The terminal ends of the daughter vessels are coupled with the CR model using different values of reflection coefficients. A periodic flow rate, q_{in} (Figure 3.6), is imposed at the inlet of the parent vessel. Table 3.3 shows the geometry, Young's modulus and terminal parameters of the bifurcation network.

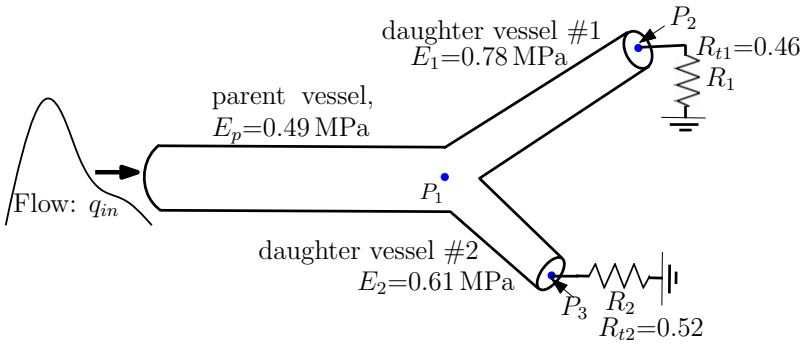

FIGURE 3.13: Test case 3: Problem set-up. Parameter estimation on a bifurcation. Time series pressure values (P_1, P_2 and P_3) are recorded for observations in data assimilation at extreme ends of the parent and two daughter vessels.

TABLE 3.3: Geometric properties, Young's modulus and terminal parameters corresponding to the bifurcation network in Figure 3.13.

Name	L (cm)	r (cm)	h (mm)	E (MPa)	R_t
Parent vessel	12.13	0.39	0.63	0.49	-
Daughter vessel 1	13.21	0.28	0.45	0.78	0.52
Daughter vessel 2	6.09	0.23	0.42	0.61	0.46

The parameters $\rho, \mu, \sigma, \epsilon_p$ and η are as in test case 1. With a time step of 0.1 ms, the blood flow model is simulated using the above parameters and time series pressure values at the extreme ends of the vessels are recorded at every 0.01 s (90 per cardiac cycle). Thus, $nobs$ = 3 corresponds to pressure values P_1, P_2 and P_3 on Figure 3.13 respectively.

For the inverse problem, three Young's modulus (E_p, E_1 and E_2) and two reflection coefficients (R_{t1} and R_{t2}) are sought using the observations P_1, P_2 and P_3. The parameter estimation algorithm uses an ensemble of size q_{ens} = 20 and σ_p = 0.25. An initial estimate (ensemble mean) of 0.7 MPa and 0.7 are assigned to all Young's modulus and the two reflection coefficients respectively. The corresponding initial ensemble standard deviations for E and R_t are 0.05 MPa and 0.05 respectively. The pressure losses at the bifurcation are neglected.

The estimation algorithm is executed for 13 cardiac cycles with EnKF assimilation taking place at every 0.01 s (90 per cardiac cycle). The evolutions of estimated parameters are shown in Figure 3.14 and the final estimated values in Table 3.4. All five parameters converge to the target values with an error (% deviation from target) of less than 0.5%. Furthermore, with the estimated parameters, the blood flow model is able to recover the

target pressure solution P_1. This comparison between the estimated and target pressure waveform is shown in Figure 3.15.

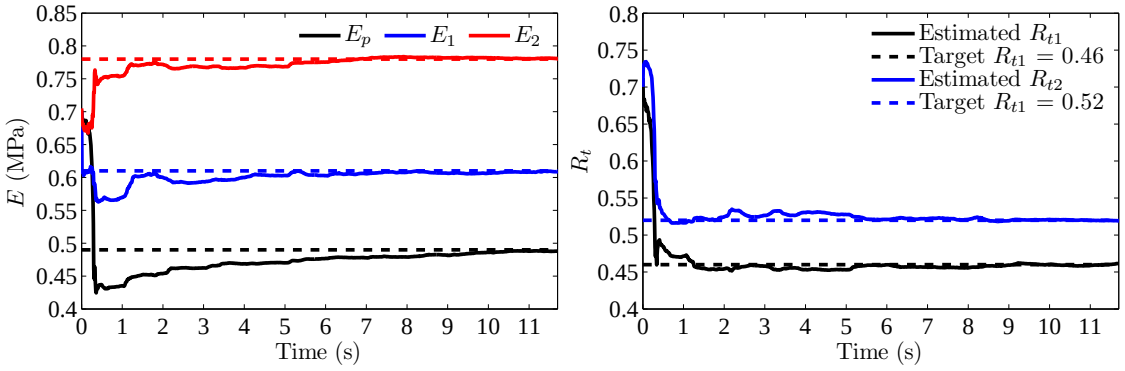

(a) (b)

FIGURE 3.14: Test case 3: Evolution of estimated parameters on a bifurcation network. (3.14a) shows the evolution of the Young's modulus for the parent vessel (E_p) and the two daughter vessels (E_1 and E_2). The dotted lines represent the target values of E_p = 0.49 MPa, E_1 = 0.61 MPa, and E_2 = 0.78 MPa for the parent and two daughter vessels respectively. Similarly, (3.14b) shows the evolution of the reflection coefficients (R_{t1} and R_{t2}).

TABLE 3.4: Test case 3: Initial and estimated parameters.

Parameter	Target	Initial guess	Final EnKF estimate	% deviation from target
E_p (MPa)	0.49	0.7	0.488	-0.4
E_1 (MPa)	0.78	0.7	0.781	0.13
E_2 (MPa)	0.61	0.7	0.609	-0.16
R_{t1}	0.46	0.7	0.461	0.22
R_{t2}	0.52	0.7	0.519	-0.19

3.4.4 Test case 4: Real measurements in the carotid artery

In this test case, an estimation of Windkessel (WK3) boundary condition parameters using a clinically measured aperiodic flow rate is presented. The aperiodic flow rate is due to the heart rate variability. The case is taken from Vignon-Clementel et al. [147] where using a pulsed-Doppler ultrasound, the cross-sectional area, wall thickness and length of the left common carotid artery of a 27-year-old healthy female subject were measured. At the inlet of the common carotid artery, the mean velocity was recorded over time (see Figure 3.16), and the flow rate $q(t)$ was obtained as the product of the

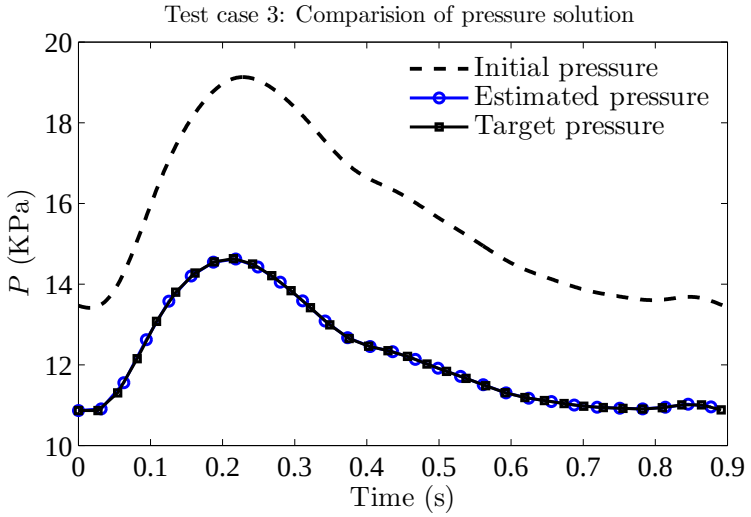

FIGURE 3.15: Test case 3: Estimated pressure solution. The figure shows the comparison between the pressure solutions (P_1 in Figure 3.5) obtained with the initial estimate of parameters, the final estimated pressure solution, and the target pressure curve.

instantaneous mean velocity and the average cross sectional area [147]. The flow rate was mapped into a parabolic velocity profile and was used as the inlet boundary condition for a 3D FSI numerical simulation in the analysis of Vignon-Clementel et al. [147].

The geometry of the carotid artery, Young's modulus and the Windkessel (WK3) outlet boundary parameters used for the numerical simulation in Vignon-Clementel et al. [147] are shown in Table 3.5. The values of corresponding pressure, p_{out}, and the flow rate, q_{out}, at the outlet of the carotid artery obtained from the 3D FSI numerical simulation are shown in the Figure 3.17 [147] for seven complete cardiac cycles.

TABLE 3.5: Geometrical parameters and Young's modulus of the left common carotid artery of a 27-year-old healthy female patient, coupled to a three-element Windkessel model [147].

Parameter	value
cross-sectional area, A	0.24 cm^2
wall thickness, h	0.09 cm
length, l	3.5 cm
Young's modulus, E	0.418 Mpa
Windkessel resistance, R_P	0.838 mmHg·s/ml
Windkessel resistance, R_D	9.108 mmHg·s/ml
Windkessel compliance, C	0.0423 ml/mmHg

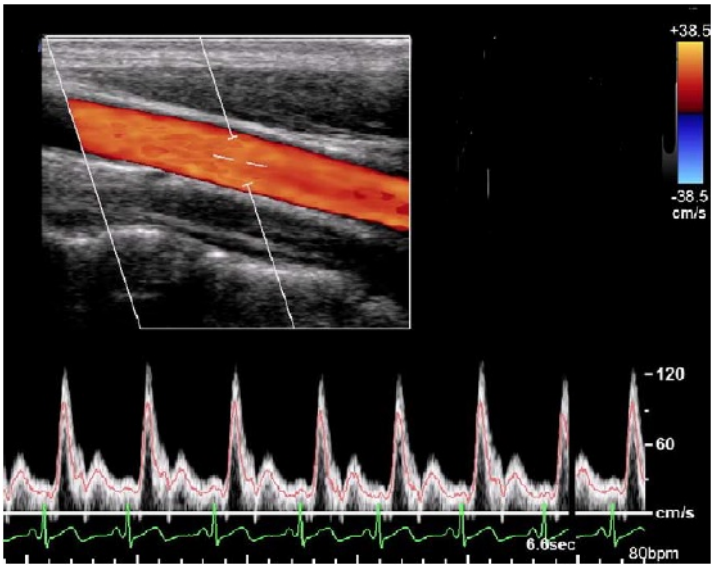

FIGURE 3.16: Real ultrasound velocity measurement in the carotid artery. The mean aperiodic velocity is indicated by the red curve and the corresponding ECG tracing by the green curve. The Doppler signal in a longitudinal cut of the carotid is shown in the upper part of the figure. It indicates the forward flow along and across the artery and the colour bar on the right indicates the velocity value and its direction. Figure adapted from Vignon-Clementel et al. [147].

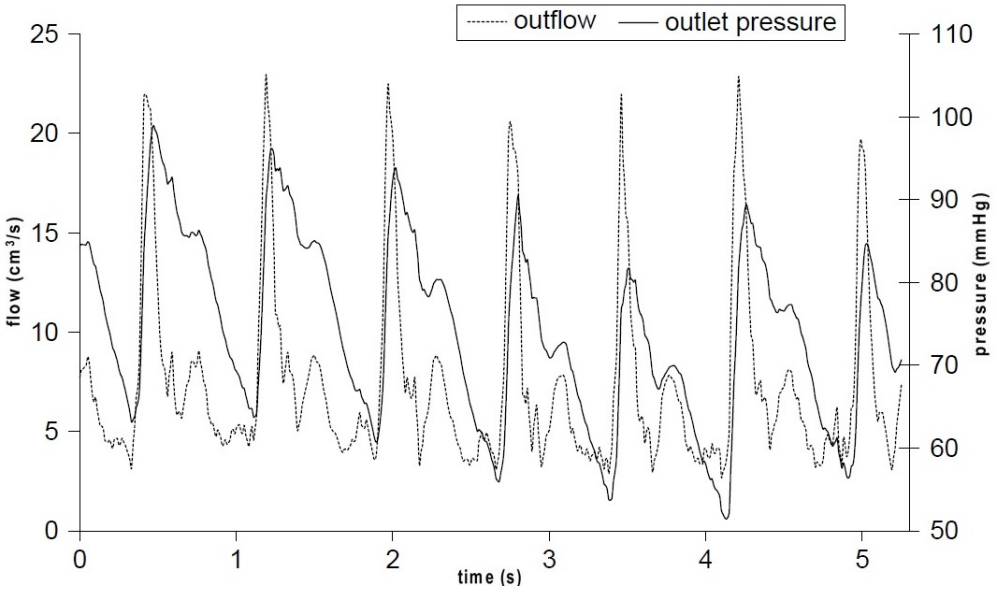

FIGURE 3.17: Aperiodic flow rate (q_{out}) and the pressure (P_{out}) waveforms at the outlet of the carotid model resulting from the 3D FSI numerical simulation in the analysis of Vignon-Clementel et al. [147]. The numerical solutions obtained using the parameters from Table 3.5 are shown for seven cardiac cycles [147]. Figure adapted from Vignon-Clementel et al. [147].

The EnKF estimation problem considers P_{out} and q_{out} to estimate the Windkessel (WK3) parameters used in 3D fluid structure interaction simulations (in the analysis of [147]). The flow rate values q_{out} are used as the inlet boundary condition q_{in} to drive the forward blood flow model and P_{out} is provided as the observation ($nobs$ = 1) in the data assimilation. This set-up is shown in Figure 3.18.

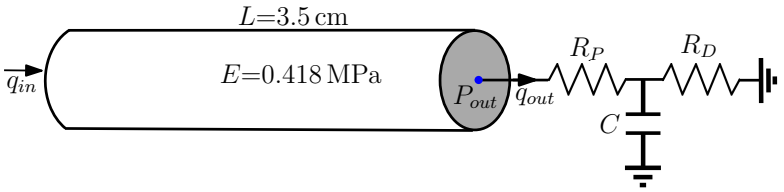

FIGURE 3.18: Test case 4: Set-up for real measurements in the carotid artery. P_{out} is used as the observation in the EnKF parameter estimation algorithm. The forward blood flow model is driven by q_{in} that takes the values of q_{out}. P_{out} and q_{out} (see Figure 3.17) are from the results of Vignon-Clementel et al. [147].

Blood rheological parameters (ρ and μ), σ, ϵ_p and η are as in Test case 1. To restrict the assimilated parameters to positive values, the three Windkessel parameters are redefined as $x = x_{\text{ini}} 2^{\theta}$. x_{ini} is the initial estimate of the parameter to be estimated and θ is the actual value used in the EnKF algorithm. The EnKF algorithm uses an ensemble size of $q_{\text{ens}} = 20$ and θ for the ensemble members initialization follows $\mathcal{N}(0, 0.5)$. x_{ini} (the ensemble mean values for the initial guess of WK3 parameters) is taken to $R_P = 2.0$ mmHg·s/ml, $R_D = 14.0$ mmHg·s/ml and $C = 0.02$ ml/mmHg [5]. The measurement error covariance matrix (**R**) is defined by Equation (2.26), where observations (the values of P_{out}) are perturbed by a random vector that is drawn from a Gaussian distribution with zero mean and a standard deviation at 10% of the observation values. The parameter estimation algorithm is executed for 5 s with EnKF assimilation taking place at every 5 ms (200 per second). The evolutions of estimated Windkessel parameters (the proximal resistance R_P, the distal resistance R_D, and the compliance C) with their associated uncertainties (standard deviation) are shown in Figure 3.19.

With $nobs$ = 1, the algorithm is able to recover the WK3 parameters with good accuracy. The maximum error of 10.2% is found to be associated with the estimated value of the compliance C. Table 3.6 shows the comparison between estimated values of the WK3 parameters and the ones used to obtain the pressure P_{out} from the 3D FSI numerical simulation in the analysis of Vignon-Clementel et al. [147].

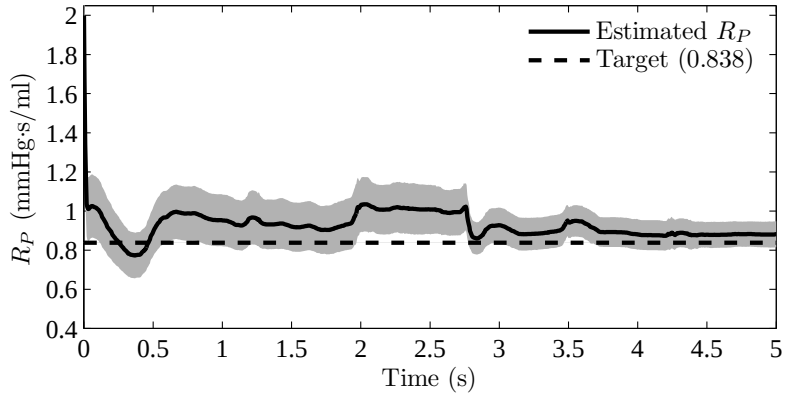

(a)

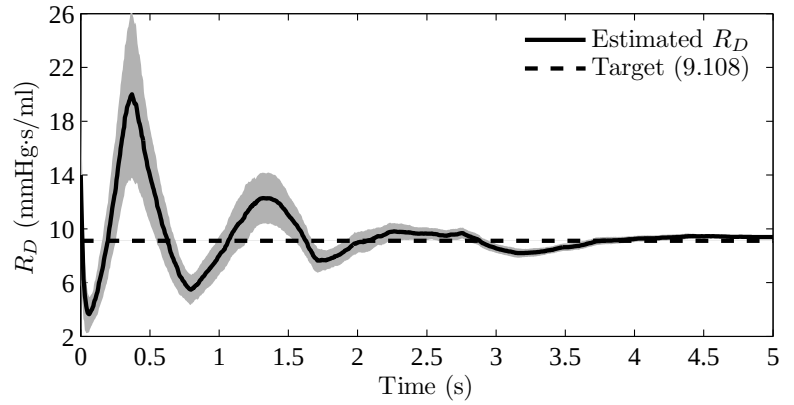

(b)

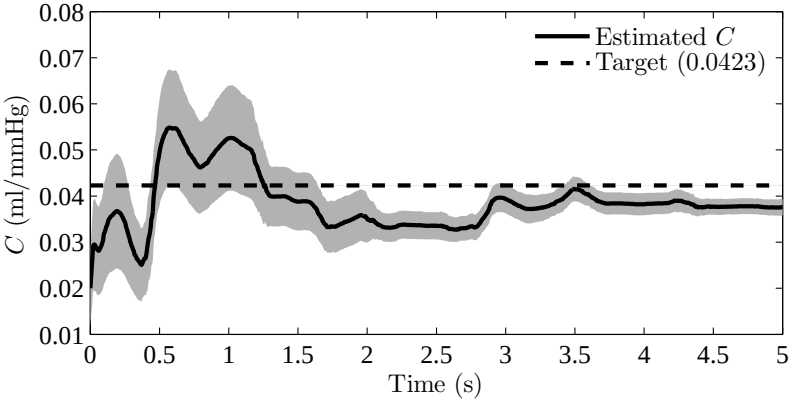

(c)

FIGURE 3.19: The evolution of the estimated Windkessel parameters using EnKF with real measurements in the carotid artery. (3.19a): the initial estimate of R_1 is 2.0 mmHg·s/ml and the best estimate of R_1 using EnKF is 0.895 mmHg·s/ml, (3.19b): the initial estimate of R_2 is 14.0 mmHg·s/ml and the best estimate of R_2 is 9.401 mmHg·s/ml and (3.19c): the initial estimate of C is 0.02 ml/mmHg and the final estimate of C using EnKF is 0.0379 ml/mmHg. The shaded areas represent the standard deviation around the ensemble mean values (solid lines).

TABLE 3.6: Test case 4: Initial and estimated parameters.

Parameter	Target	Initial guess	Final EnKF estimate	% deviation from target
R_P (mmHg·s/ml)	0.838	2.0	0.895	6.8
R_D (mmHg·s/ml)	9.108	14.0	9.401	3.2
C (ml/mmHg)	0.0423	0.02	0.038	-10.2

Moreover, there is a good agreement between the estimated pressure solution (blood flow model simulated with the estimated WK3 parameters) and the target pressure solution P_{out}. The initial, target and estimated pressure solutions are shown in Figure 3.20. The result shows a good fit between the estimated and target pressure waveforms.

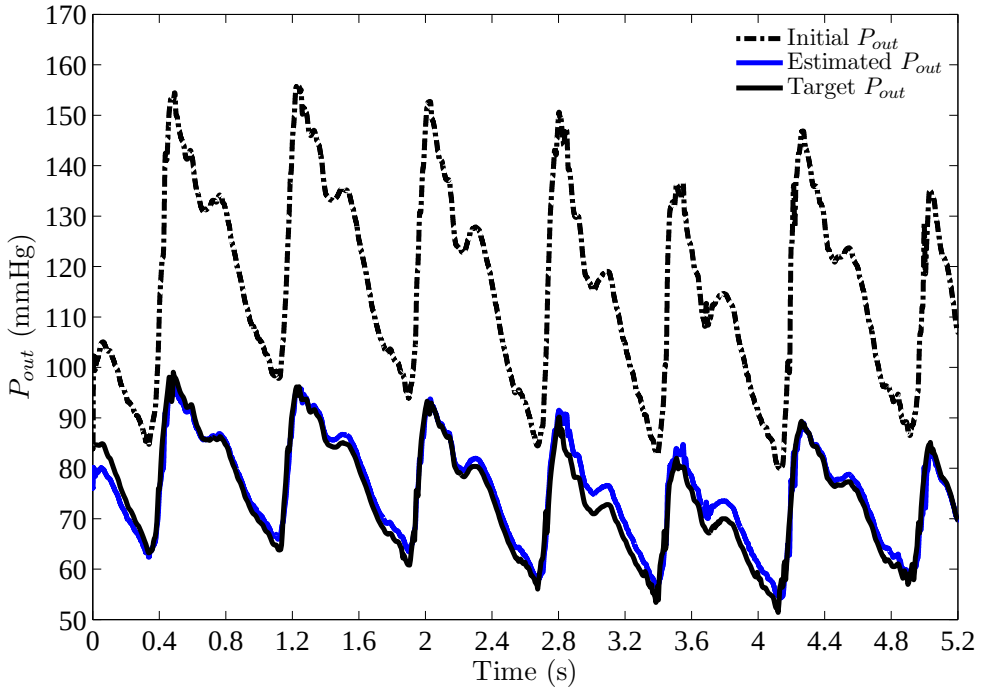

FIGURE 3.20: Pressure profiles for the case of Windkessel parameter estimation using real measurements in the carotid artery. The profiles show the comparison between the pressure signal obtained with initially guessed parameters (in dash black), the target pressure solution, p_{out} [147] (in solid black), and the one obtained by using the blood flow model with the estimated WK3 parameter values (in blue).

This case demonstrates the usefulness of the estimation algorithm in situations when measurements (q_{in} in the current case) are not available at locations of interest and can be substituted by measurements (e.g. q_{out}) in a nearby location (in close vicinity).

3.5 Discussion

The feasibility of estimating hemodynamic parameters using EnKF has been demonstrated. Tests have been carried out on a simple network of arteries and the parameters are limited to the stiffness of arteries (Young's modulus), and the boundary condition parameters (reflection coefficients and Windkessel WK3 parameters). For all cases, pressure data are considered as observations (measurements) in the data assimilation. However, we note the fact that acquisition of pressure data may not be feasible at all locations of interest (such as arteries in the circle of Willis) when dealing with real clinical data. In such situations, alternative observation data, such as blood flow rates measured using Magnetic Resonance Imaging (MRI) can be used. In the next two chapters, we demonstrate the usefulness and efficiency of EnKF in parameter estimation on the complex arterial network and using a different type of observation data, such as the blood flow rate. The use of experimental data from an in vitro test rig and real clinical data are considered along with synthetic data for test cases in the following two chapters.

Chapter 4

Data assimilation for identification of cardiovascular network characteristics

Contents

The chapter has been published as:

Rajnesh Lal, Bijan Mohammadi, and Franck Nicoud, "Data assimilation for identification of cardiovascular network characteristics" in *International Journal for Numerical Methods in Biomedical Engineering*, 2016. doi: 10.1002/cnm.2824.

The numbering of sections, figures and tables in the original publication have been altered for this chapter, to be consistent with the thesis chapter numbering. The references have been incorporated into the global references at the end of the thesis.

Part of chapter 4 has been presented in the previous chapters as follows:

- section 4.2 is taken from section 2.5 of chapter 2,
- part of section 4.3 has been presented in section 2.6 of chapter 2,
- section 4.4 is taken from sections 3.2 and 3.3 of chapter 3.

The rest of the sections (sections 4.5 and onwards) of this chapter presents new materials focusing on the application of EnKF to 1D blood flow model.

Abstract

A method to estimate the hemodynamic parameters of a network of vessels using an Ensemble Kalman filter is presented. The elastic moduli (Young's modulus) of blood vessels and the terminal boundary parameters are estimated as the solution of an inverse problem. Two synthetic test cases and a configuration where experimental data is available are presented. The sensitivity analysis confirms that the proposed method is quite robust even with a few numbers of observations. The simulations with the estimated parameters recovers target pressure or flow rate waveforms at given specific locations, improving the state of the art predictions available in the literature. This shows the effectiveness and the efficiency of both the parameters estimation algorithm and the blood flow model.

Keywords: Ensemble Kalman filter, 1D blood flow, parameter estimation, inverse problem

4.1 Introduction

An increase in arterial stiffness has been shown to be linked with age including other health problems or risk factors such as diabetes and hypertension [23]. The stiffness of arteries can be measured using different techniques such as by measuring the pulse wave velocity (PWV) or with the analysis of local variations in local pressure and volume [148]. PWV is directly related to the arterial wall elasticity and to the Young's modulus of the arteries [148].

"Assimilation is the process of finding the model representation which is most consistent with the observations" [47]. The use of inaccurate parameters in the model equations can give rise to model errors [149]. The parameter estimation problem tends to improve initial estimates of the model parameters so that the difference between the measurements and the model solution are minimised. In parameter estimation problem, it is assumed that the uncertainties in the model parameters are the sources of errors for the model errors [66]. According to Annan et al. [150], it is important to tune the parameters to gain a better confidence in the predictions of the state values. Generally, we have observable data for the state, but no direct observable data for the parameters.

In recent years, parameter estimation has been carried out using a similar framework as for the state estimation. The state vectors can be augmented by the poorly known parameters for estimating by having a Kalman filter for the state-parameter augmented model [65–68]. In state-parameter augmentation, parameters are considered as part of the model, which are updated in the analysis step of the data assimilation algorithm together with the model variables [150]. An evolution model for model parameters is required for the state-parameter augmented model [151]. The common evolution model includes the random walk model [71, 100] and the persistence model [68, 152]. Combining the model variables and model parameters during the analysis step can also introduce problems such as parameter collapse and filter divergence [99]. In [99, 153], parameter estimation using an Ensemble Kalman Filter (EnKF) is presented using augmentation method, but without updating the model states during the assimilation step.

Some recent works on inverse problems in hemodynamics include the work of Lombardi [35], Moireau et al. [36], Pant et al. [10], Bertoglio et al. [39], Chabiniok et al., [33], Martin et al. [41], Spilker et al. [42] and Lassila et al. [43]. In Lombardi [35], a sequential approach based on the reduced order unscented Kalman filter (ROUKF) is presented for the identification of arterial stiffness parameters in 1D haemodynamics. In Moireau et al. [36], ROUKF is used to identifiy the boundary condition parameters in a fluid structure vascular model utilising patient image data. In Pant et al. [10], a sequential estimation technique using the unscented Kalman filter (UKF) is presented to estimate lumped model parameters from clinical measurements. In Bertoglio et al. [39], parameter estimation using ROUKF for fluid-structure interaction problems is presented. In Chabiniok et al. [33], the use of sequential joint state-parameter data assimilation to a biomechanical heart model with actual cardiac Cine-MRI data are presented. In Martin et al. [41], a variational method (adjoint state approach) is presented to identify the parameters of one-dimensional models for blood flow in arteries. In Spilker and Taylor [42], a quasi-Newton method is used to adjust the parameters of the outlet boundary conditions of blood flow models to achieve target profiles of flow and pressure waveforms. In Lassila et al. [43], the solution of inverse problems in hemodynamics is proposed using deterministic and Bayesian approaches.

Recent works on inverse problems in hemodynamics are either based on joint state augmented model (Chabiniok et al. [33]) or ROUKF (Pant et al. [10], Lombardi [35],

Moireau et al. [36], Bertoglio et al. [39]). We use Ensemble Kalman filters (EnKF) to identify the Young's modulus and the terminal boundary parameters as the solution of inverse problems. Our aim is to show that this can be achieved with only a few number of observations and without using the joint state formulation hence reducing a modification of the state equations. We think this is important in order to minimize the coupling between the assimilation tool and the state equations solver. Also, one originality is to ensure positivity for the solutions of the inversion introducing an adequate reformulation of the problem through logarithmic variable changes. Finally, one important result of the paper is to show that joint use of data assimilation and flow solution by a CFD code greatly improves available results in the literature for a realistic human arterial model with available experimental references [13].

In this paper, first, we present a review of the data assimilation method using an Ensemble Kalman filter (EnKF) and propose a method for hemodynamic parameter estimation as the solution to an inverse problem. In the second section, a blood flow model of the cardiovascular network is presented. In section three, test cases are presented where we show the applicability of an Ensemble Kalman filter to 1D blood flow model in parameter estimation. The first two test cases use synthetic data and the final test case involves the use of an experiments data [13]. The test cases are limited to the estimation of Young's modulus and the boundary condition parameter, i.e. reflection coefficient and the viscoelastic coefficient.

4.2 Ensemble Kalman filter

First introduced by Geir Evenson [55], an Ensemble Kalman Filter (EnKF) solves the Fokker-Plank equation using a Monte Carlo or ensemble integrations [85]. It is a sub-optimal estimator for problems involving high-order non-linear models. The error statistics are predicted using the ensemble of states. Different versions of EnKF are available in the literature: Deterministic Ensemble Kalman filter (DEnKF) [86], Monte Carlo EnKF [55, 87], EnKF [57, 88], Hybrid EnKF [89], Ensemble Transform Kalman filter (ETKF) [90], Ensemble Adjustment Kalman filter (EAKF) [65], Ensemble Square Root filters (EnSRF) [91] and Local Ensemble Kalman filter (LEKF) [92].

4.2.1 Derivation of ensemble Kalman filter

In EnKF, the forecast error covariance matrix is evaluated using an ensemble of forecasts. In this section, we follow and describe the different steps employed in the formulation of EnKF as presented in [70, 88, 93–95].

We will assume that the discrete nonlinear system is described by

$$\mathbf{x}_{k+1} = f(\mathbf{x}_k) + \mathbf{w_k}, \quad \mathbf{y}_k = h(\mathbf{x}_k) + \mathbf{v_k}. \tag{4.1}$$

The model state at time t_k is $\mathbf{x}_k \in \mathbb{R}^n$, while the observed state is $\mathbf{y}_k \in \mathbb{R}^{nobs}$. n is the dimension of the model state vector and $nobs$ is the number of observations. $\mathbf{w}_k \in \mathbb{R}^n$ and $\mathbf{v}_k \in \mathbb{R}^{nobs}$ are assumed uncorrelated Gaussian model errors with $\mathbf{w}_k \sim \mathcal{N}(0, \mathbf{Q_k})$ and $\mathbf{v}_k \sim \mathcal{N}(0, \mathbf{R_k})$ where $\mathbf{Q_k}$ and $\mathbf{R_k}$ are the covariance matrices. h is the function describing the relationship between the measurement and the states.

At time t_k, it is assumed that an ensemble of q_{ens} forecast state estimates (prior ensembles); $\mathbf{X}_k^{\text{f}} = (\mathbf{x}_k^{\text{f}_1}, \ldots, \mathbf{x}_k^{\text{f}_{q_{\text{ens}}}}) \in \mathbb{R}^{n \times q_{\text{ens}}}$ is available. f_i represents the i-th forecast member of the ensemble. The mean of the ensemble of forecast state is $\overline{\mathbf{x}}_k^{\text{f}} \in \mathbb{R}^n$ and is given by

$$\overline{\mathbf{x}}_k^{\text{f}} = \frac{1}{q_{\text{ens}}} \sum_{i=1}^{q_{\text{ens}}} \mathbf{x}_k^{\text{f}_i}. \tag{4.2}$$

The forecast covariance matrix, $\mathbf{P}_k^{\text{f}} \in \mathbb{R}^{n \times n}$, is defined by

$$\mathbf{P}_k^{\text{f}} = \frac{1}{q_{\text{ens}} - 1} \sum_{i=1}^{q_{\text{ens}}} \left(\mathbf{x}_k^{\text{f}_i} - \overline{\mathbf{x}}_k^{\text{f}}\right) \left(\mathbf{x}_k^{\text{f}_i} - \overline{\mathbf{x}}_k^{\text{f}}\right)^{\text{T}}. \tag{4.3}$$

After the computation of the Kalman gain $\mathbf{K}_k$, all operations on the ensemble members are independent in the EnKF analysis step and the ensemble members are updated using:

$$\mathbf{x}_k^{\text{a}_i} = \mathbf{x}_k^{\text{f}_i} + \mathbf{K}_k \left[\mathbf{y}_k^i - h\left(\mathbf{x}_k^{\text{f}_i}\right)\right], \quad i = 1, \ldots, q, \tag{4.4}$$

where a_i represents the i-th updated or analysed member of the ensemble. Without adding perturbations to the original observation vector, an updated ensemble with a low variance can be obtained [96]. Hence, to maintain the correct forecast error covariance, a suitable spread of the ensemble members is required. This is achieved by using an ensemble of perturbed observations [96]. An ensemble of the same size q_{ens} consisting of observations is also generated by adding small perturbations to the observation set $\mathbf{y}_k$.

Perturbations are generated to have the same distribution as the measurement error and the perturbed observations $\mathbf{y}_k^i$ are defined by

$$\mathbf{y}_k^i = \mathbf{y}_k + \mathbf{e}_k^i, \quad i = 1, \ldots, q_{\text{ens}} \tag{4.5}$$

where $\mathbf{e}_k^i \in \mathbb{R}^{nobs}$ is a Gaussian random vector with zero mean and a specified variance. The measurement error covariance matrix, $\mathbf{R_k}$, is diagonal following the assumption of independent observations [91] and is defined as

$$\mathbf{R_k} = \text{diag}\left[\frac{1}{q_{\text{ens}} - 1}\mathbf{E}\mathbf{E}^{\text{T}}\right], \quad \mathbf{E} = \left[\mathbf{e}_k^1, \ldots, \mathbf{e}_k^{q_{\text{ens}}}\right]. \tag{4.6}$$

For a linear measurement function, h, and if the noise is additive, that is

$$\mathbf{y}_k = \mathbf{H}\mathbf{x}_k + \mathbf{v_k}, \tag{4.7}$$

the Kalman gain is defined by [94]

$$\mathbf{K_k} = \mathbf{P}_k^{\text{f}}\mathbf{H}^{\text{T}}\left(\mathbf{H}\mathbf{P}_k^{\text{f}}\mathbf{H}^{\text{T}} + \mathbf{R}_k\right)^{-1}. \tag{4.8}$$

In Equation (4.8), the observation operator, $\mathbf{H} \in \mathbb{R}^{nobs \times n}$, is linear or linearized. To circumvent the linearization of a nonlinear measurement function which might be difficult to linearize, Houtekamer and Mitchell [97] re-wrote the two terms $\mathbf{P}_k^{\text{f}}\mathbf{H}^{\text{T}}$ and $\mathbf{H}\mathbf{P}_k^{\text{f}}\mathbf{H}^{\text{T}}$ which appear in the Kalman gain Equation (4.8) as

$$\mathbf{P}_k^{\text{f}}\mathbf{H}^{\text{T}} \equiv \frac{1}{q_{\text{ens}} - 1}\sum_{i=1}^{q_{\text{ens}}}\left[\mathbf{x}_k^{\text{f}_i} - \overline{\mathbf{x}}_k^{\text{f}}\right]\left[h\left(\mathbf{x}_k^{\text{f}_i}\right) - \overline{h\left(\mathbf{x}_k^{\text{f}}\right)}\right]^{\text{T}}, \tag{4.9}$$

$$\mathbf{H}\mathbf{P}_k^{\text{f}}\mathbf{H}^{\text{T}} \equiv \frac{1}{q_{\text{ens}} - 1}\sum_{i=1}^{q_{\text{ens}}}\left[h\left(\mathbf{x}_k^{\text{f}_i}\right) - \overline{h\left(\mathbf{x}_k^{\text{f}}\right)}\right]\left[h\left(\mathbf{x}_k^{\text{f}_i}\right) - \overline{h\left(\mathbf{x}_k^{\text{f}}\right)}\right]^{\text{T}}, \tag{4.10}$$

where $\overline{h\left(\mathbf{x}_k^{\text{f}}\right)} = \frac{1}{q_{\text{ens}}}\sum_{i=1}^{q_{\text{ens}}} h\left(\mathbf{x}_k^{\text{f}_i}\right)$. It has been argued by Tang and Ambadan [98] that Equations (4.9) and (4.10) approximately hold if the following are true :

$$\overline{h\left(\mathbf{x}_k^{\text{f}}\right)} = h\left(\overline{\mathbf{x}}_k^{\text{f}}\right), \tag{4.11}$$

$$\text{norm}\left(\mathbf{x}_k^{\text{f}_i} - \overline{\mathbf{x}}_k^{\text{f}}\right) \text{ is small for } i = 1, 2, \ldots q_{\text{ens}}. \tag{4.12}$$

Equations (4.9) and (4.10) linearize the nonlinear function h to $\mathbf{H}$ under the conditions of Equations (4.11) and (4.12) [70]. For the nonlinear model with a

nonlinear measurement function, a general equation for the Kalman gain can be stated as [70]:

$$\mathbf{K}_k = \mathbf{P}^{\mathrm{f}}_{\mathrm{xy}_k} \left(\mathbf{P}^{\mathrm{f}}_{\mathrm{yy}_k} \right)^{-1}, \tag{4.13}$$

where the error covariance matrices $\mathbf{P}^{\mathrm{f}}_{\mathrm{xy}_k}$ and $\mathbf{P}^{\mathrm{f}}_{\mathrm{yy}_k}$ are defined as follows:

$$\mathbf{P}^{\mathrm{f}}_{\mathrm{xy}_k} = \frac{1}{q_{\mathrm{ens}} - 1} \sum_{i=1}^{q_{\mathrm{ens}}} \left[\mathbf{x}^{\mathrm{f}_i}_k - \bar{\mathbf{x}}^{\mathrm{f}}_k \right] \left[h\left(\mathbf{x}^{\mathrm{f}_i}_k \right) - \overline{h\left(\mathbf{x}^{\mathrm{f}}_k \right)} \right]^{\mathrm{T}}, \tag{4.14}$$

$$\mathbf{P}^{\mathrm{f}}_{\mathrm{yy}_k} = \frac{1}{q_{\mathrm{ens}} - 1} \sum_{i=1}^{q_{\mathrm{ens}}} \left[h\left(\mathbf{x}^{\mathrm{f}_i}_k \right) - \overline{h\left(\mathbf{x}^{\mathrm{f}}_k \right)} \right] \left[h\left(\mathbf{x}^{\mathrm{f}_i}_k \right) - \overline{h\left(\mathbf{x}^{\mathrm{f}}_k \right)} \right]^{\mathrm{T}} + \mathbf{R}_k. \tag{4.15}$$

We define the **true** state (or parameter) as the **target** of an ideal assimilation. The best forecast state estimate is given by the ensemble mean $\bar{\mathbf{x}}^{\mathrm{f}}_k$. The error between $\bar{\mathbf{x}}^{\mathrm{f}}_k$ and the true state is given by the standard deviation of the ensemble members around $\bar{\mathbf{x}}^{\mathrm{f}}_k$. The final step is the forecast step and involves an ensemble of q_{ens} forecast states for time $t = k + 1$ as,

$$\mathbf{x}^{\mathrm{f}_i}_{k+1} = f(\mathbf{x}^{\mathrm{a}_i}_k) + \mathbf{w}^i_k, \quad i = 1, 2, \ldots q_{\mathrm{ens}}. \tag{4.16}$$

4.2.2 Summary of ensemble Kalman filter algorithm

We now summarize the forecast and the analysis steps of EnKF presented in section 4.2.1. A schematic description of the EnKF algorithm is shown in Figure 4.1. To start the EnKF, we need to generate an ensemble of q_{ens} forecast estimates of state associated with their random errors. At $t = k - 1$, it is assumed that $\mathbf{x}^{\mathrm{f}_i}_{k-1}$ for $i = 1, \ldots, q_{\mathrm{ens}}$ are available. We let $nobs$ denote the number of observations. At time $t = k$, we generate a set of realizations of the state vector $\mathbf{X}_k = (\mathbf{x}^1_k, \ldots, \mathbf{x}^{q_{\mathrm{ens}}}_k)$ and denote the corresponding measurements as $\mathbf{Y}_k = (\mathbf{y}^1_k, \ldots, \mathbf{y}^{q_{\mathrm{ens}}}_k) \in \mathbb{R}^{q_{\mathrm{ens}} \times nobs}$. $\mathbf{Q}$ and $\mathbf{R}$ correspond to the model and observation error covariance matrices, respectively.

We write the equations for the EnKF as:

$$
\begin{aligned}
\mathbf{x}_k^{\mathrm{f}_i} &= f(\mathbf{x}_{k-1}^{\mathrm{a}_i}) + \mathbf{w}_{k-1}^i, \quad i = 1, \ldots, q_{\mathrm{ens}}, \\
\mathbf{w}_k^i &\sim \mathcal{N}(0, \mathbf{Q}_k), \\
\mathbf{P}_{\mathbf{xy}_k}^{\mathrm{f}} &= \frac{1}{q_{\mathrm{ens}} - 1} \sum_{i=1}^{q_{\mathrm{ens}}} \left[\mathbf{x}_k^{\mathrm{f}_i} - \overline{\mathbf{x}_k^{\mathrm{f}}}\right] \left[h\left(\mathbf{x}_k^{\mathrm{f}_i}\right) - \overline{h\left(\mathbf{x}_k^{\mathrm{f}}\right)}\right]^{\mathrm{T}}, \\
\mathbf{P}_{\mathbf{yy}_k}^{\mathrm{f}} &= \frac{1}{q_{\mathrm{ens}} - 1} \sum_{i=1}^{q_{\mathrm{ens}}} \left[h\left(\mathbf{x}_k^{\mathrm{f}_i}\right) - \overline{h\left(\mathbf{x}_k^{\mathrm{f}}\right)}\right] \left[h\left(\mathbf{x}_k^{\mathrm{f}_i}\right) - \overline{h\left(\mathbf{x}_k^{\mathrm{f}}\right)}\right]^{\mathrm{T}} + \mathbf{R}_k, \\
\mathbf{K}_k &= \mathbf{P}_{\mathbf{xy}_k}^{\mathrm{f}} \left(\mathbf{P}_{\mathbf{yy}_k}^{\mathrm{f}}\right)^{-1}, \\
\mathbf{y}_k^i &= \mathbf{y}_k + \mathbf{e}_k^i, \quad i = 1, \ldots, q_{\mathrm{ens}}, \\
\mathbf{x}_k^{\mathrm{a}_i} &= \mathbf{x}_k^{\mathrm{f}_i} + \mathbf{K}_k \left[\mathbf{y}_k^i - h\left(\mathbf{x}_k^{\mathrm{f}_i}\right)\right], \quad i = 1, \ldots, q_{\mathrm{ens}}.
\end{aligned}
$$

In the above steps, the superscripts 'f' and 'a' denote the forecast and the analysis steps respectively. EnKF algorithm yields an ensemble of analyses at time $t = k$, which can be cycled in time.

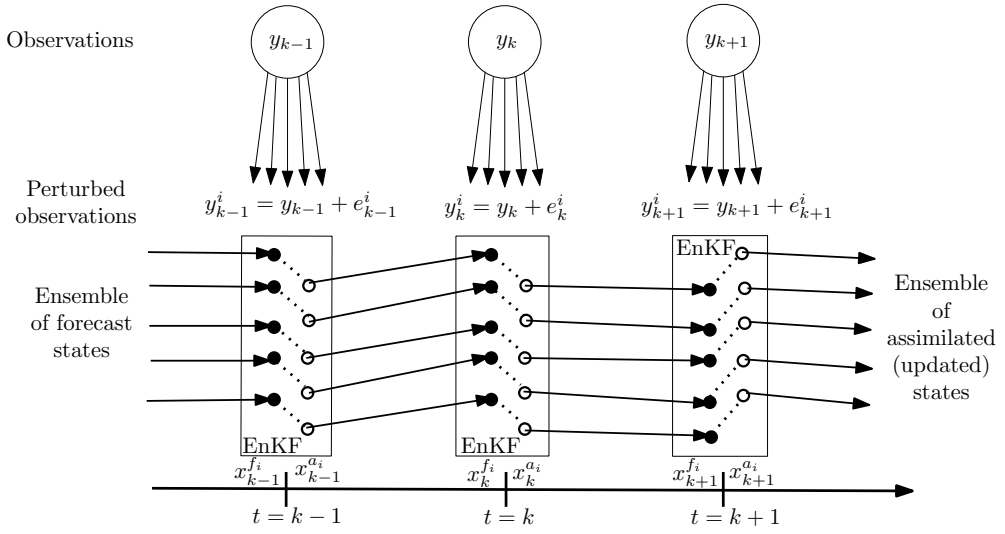

FIGURE 4.1: A schematic description of the Ensemble Kalman Filter.

UKF differs from EnKF by the choice of the sampling. UKF uses a minimal set of deterministically chosen points (sigma points) and propagates this set through the actual non-linear function [10]. In contrast, EnKF uses a Monte-Carlo-based choice of many points (members of the ensemble) for forward propagation. UKF should be preferred if the output of the system deviates from a Gaussian distribution. Except with the computation of the Kalman gain, all the operations on the ensemble members are

independent. This implies that their parallelization can be trivially carried out. This is one of the reasons for the success and popularity of the EnKF and UKF.

4.3 Parameter estimation using ensemble Kalman filter

In the current work, the EnKF algorithm is used to estimate only the model parameters. The parameters are thus considered as *special state variables* (the state vector contains only the model parameters). The evolution of parameters is characterized by a random walk model [71, 100] and is defined as $\mathbf{x}_{k+1}^{i} = \mathbf{x}_{k}^{i} + \tau_{k}^{i}$. $\tau_k \sim \mathcal{N}(0, \mathbf{T}_k)$ is a small random perturbation with predefined variance $\mathbf{T}$. Numerical simulators can be regarded as nonlinear functions that take parameter vector $\mathbf{x}^i$ as an input and produces an output vector $\mathbf{y}^i = \mathcal{H}(\mathbf{x}^i)$ [101]. $\mathcal{H}$ is the nonlinear measurement function defined by the numerical simulator. The information from observations are used by the Kalman filter during the analysis step and the Kalman gain Equation (4.4) is applied to update the ensemble members. The use of Equation (4.4) assumes that the parameters follow a Gaussian distribution [101]. The parameter estimation procedure using the EnKF is stated in Algorithm 1 [101]. The algorithm can be stopped when some finite convergence criterion is achieved. A flowchart for parameter estimation using EnKF is shown in Figure 4.2.

Algorithm 1: Parameter estimation using EnKF

Input: Ensemble size (q_{ens}), maximum number of EnKF iteration (j_{max}), variance matrix $\mathbf{T}$, number of observations ($nobs$), initial guess of the parameters (mean $\tilde{\mathbf{x}}_0$ and covariance $\mathbf{P}_0$).

Initialization:
Initialize randomly q_{ens} states into special state matrix $\mathbf{X}$
for $j = 1$ ***to*** j_{max} **do**
  -Perturb the ensemble using random walk model
  $\mathbf{x}^{\text{f}_i} = \mathbf{x}^{\text{a}_i} + \tau^i$, $\tau^i \sim \mathcal{N}(0, \mathbf{T})$ $\forall i = 1, \ldots, q_{\text{ens}}$
  -Propagate the ensemble
  $\mathbf{y}^{\text{f}_i} = \mathcal{H}(\mathbf{x}^{\text{f}_i})$ $\forall i = 1, \ldots, q_{\text{ens}}$
  -Perturb the observations for each ensemble
  $\mathbf{y}^i = \mathbf{y} + \mathbf{e}^i$, $\forall i = 1, \ldots, q_{\text{ens}}$
  -Update the ensemble
  Estimate $\mathbf{R}$ using Eq. (4.6) and Kalman gain, $\mathbf{K}$, using Eq. (4.13, 4.14 and 4.15)
  $\mathbf{x}^{\text{a}_i} = \mathbf{x}^{\text{f}_i} + \mathbf{K}\left[\mathbf{y}^i - \mathbf{y}^{\text{f}_i}\right]$ $\forall i = 1, \ldots, q_{\text{ens}}$.

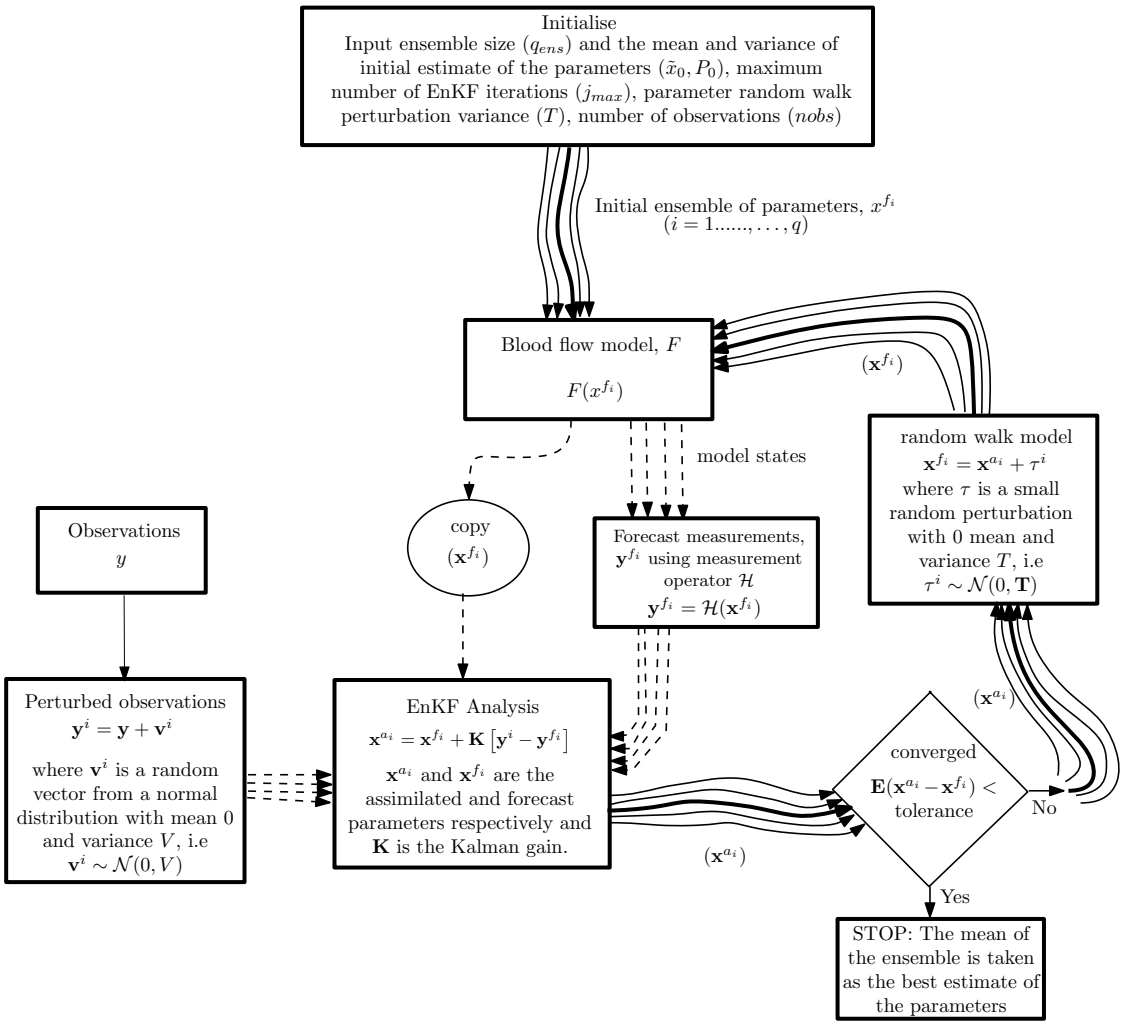

FIGURE 4.2: Parameter estimation flow chart using the ensemble Kalman filter.

Positivity issues are physically important but often difficult to enforce in assimilation processes. In this study the parameters (e.g. the Young's modulus) need to remain positive. To avoid negative values of the Young's modulus during the assimilation procedure, we introduce a change of variable. More precisely, in the sequel all the parameters are redefined as $x = x_{ref}2^{\theta}$. x is the real parameter (e.g the Young's modulus), θ is the parameter used for estimation in EnKF and x_{ref} is a reference value (initial mean value for the Young's modulus). With this change of variable, the values of estimated parameters remain positive [10]. The EnKF implementation uses an ensemble of θ such that $\theta \sim \mathcal{N}(0, 1)$.

4.4 The blood flow model

We first recall the one-dimensional (1D) governing equations for the blood flows in variables u (cross section averaged blood velocity), A (cross section area) and p (cross section averaged static pressure), which have been widely used in hemodynamic applications [1–3, 13, 14, 114, 126, 127, 129, 137, 138]. 1D modelling of arterial networks being computationally cheap is a common method adopted to perform numerical simulations of the hemodynamics in arterial vessels [3, 5]. The model assumes that blood is a Newtonian fluid in large vessels and can be considered incompressible with constant density ρ and constant dynamic viscosity μ [126].

4.4.1 Governing equations

For an incompressible and Newtonian fluid in an elastic tube, the system of equations that represents continuity of mass and momentum can be stated as [1]:

$$\begin{aligned} \frac{\partial A}{\partial t} + \frac{\partial q}{\partial x} &= 0, \\ \frac{\partial q}{\partial t} + \frac{\partial}{\partial x}\left(\alpha \frac{q^2}{A}\right) + \frac{A}{\rho}\frac{\partial p}{\partial x} &= -k_r \frac{q}{A}, \end{aligned} \tag{4.17}$$

where x is the axial direction, $A = A(x,t)$ is the cross section area at time t, $q = q(x,t)$ is the flow rate across a section, ρ is the constant density of the blood, p is the cross section average static internal pressure and $u(x,t) = \frac{q(x,t)}{A(x,t)}$ denotes the cross section averaged blood velocity. The term α is the momentum-flux correction coefficient. For a flat velocity profile it is assumed that $\alpha = 1$ [1]. k_r denotes the viscous resistance of the flow per unit length of the tube. A, q and p are the unknowns in the system (4.17). The system is closed by explicitly providing a differential constitutive pressure-area relationship [1]. A nonlinear model for pressure law is adopted according to Kelvin-Voigt model [13]:

$$p = p_{ext} + \frac{\beta}{A_0}\left[\left(\sqrt{A} - \sqrt{A_0}\right) + \epsilon_p\left(\sqrt{A} - \sqrt{A_0}\right)^2\right] + \frac{\gamma}{A_0}\frac{\partial \sqrt{A}}{\partial t}, \tag{4.18}$$

where p_{ext} denotes the constant external pressure, $A_0 = A_0(x)$, denotes the vessel sectional area at equilibrium state and ϵ_p is the non linearity coefficient. The term γ is $h\eta\sqrt{\pi}$, where h is the thickness of the tube and η is the viscoelastic coefficient. The

coefficient β, which is related to the arterial stiffness is defined as:

$$\beta = \frac{\sqrt{\pi} h E}{(1-\sigma^2)}, \tag{4.19}$$

where $E = E(x)$ is the Young's modulus and $\sigma = 0.5$ is the Poisson ratio [1].

With a specified inflow boundary condition, the 1D governing equations for the blood flow are solved using the terminal models for the outflow boundary conditions [3].

4.4.2 Characteristic variables

The 1D model (4.17) can be rewritten in a conservative form,

$$\frac{\partial \mathbf{U}}{\partial t} + \frac{\partial \mathbf{F}(\mathbf{U})}{\partial x} = \mathbf{S}(\mathbf{U}), \tag{4.20}$$

where $\mathbf{U} = [A, q]^T$ denotes the vector of conserved variables, $\mathbf{F}(\mathbf{U})$ are the fluxes and $\mathbf{S}(\mathbf{U})$ are the source terms defined by:

$$\begin{aligned} \mathbf{F}(\mathbf{U}) &= \begin{bmatrix} q \\ \alpha \frac{q^2}{A} + \frac{\beta}{3\rho A_0} A^{\frac{3}{2}} + \frac{\beta \epsilon_p}{\rho A_0} \left(\frac{1}{2} A^2 - \frac{2}{3} \sqrt{A_0} A^{\frac{3}{2}} \right) \end{bmatrix}, \\ \mathbf{S}(\mathbf{U}) &= \begin{bmatrix} 0 \\ -k_r \frac{q}{A} + \frac{\gamma \sqrt{A}}{2\rho A_0} \left(\frac{\partial^2 q}{\partial x^2} - \frac{1}{2A} \frac{\partial A}{\partial x} \frac{\partial q}{\partial x} \right) \end{bmatrix}. \end{aligned} \tag{4.21}$$

The highly coupled system of nonlinear equations (4.20) is decoupled to implement the numerical solution with the prescribed boundary conditions [114]. The characteristic system is derived by expressing the system of equations (4.20) in a quasi-linear form which can be expressed as [114]:

$$\frac{\partial \mathbf{U}}{\partial t} + \mathbf{J} \frac{\partial \mathbf{U}}{\partial x} = \mathbf{S}, \tag{4.22}$$

where the Jacobian reads:

$$\mathbf{J}(\mathbf{U}) = \frac{\partial \mathbf{F}}{\partial \mathbf{U}} = \begin{bmatrix} 0 & 1 \\ -\alpha \frac{q^2}{A^2} + \frac{\beta}{2\rho A_0} A^{\frac{1}{2}} + \frac{\beta \epsilon_p}{\rho A_0} \left(A - \sqrt{A_0} \sqrt{A} \right) & 2\alpha \frac{q}{A} \end{bmatrix}. \tag{4.23}$$

Through consideration of the non-linear coefficient (ϵ_p) and viscoelasticity (η) as source terms, the characteristic analysis shows that for all allowable $\mathbf{U}$ (that is for $A > 0$), the system is hyperbolic and the two real eigenvalues of $\mathbf{J}$ are [2, 127]:

$$\begin{aligned}\lambda_1 &= \frac{\alpha q}{A} + \sqrt{\frac{\beta}{2\rho A_0} A^{\frac{1}{2}} + \alpha(\alpha-1)\frac{q^2}{A^2}} > 0,\\ \lambda_2 &= \frac{\alpha q}{A} - \sqrt{\frac{\beta}{2\rho A_0} A^{\frac{1}{2}} + \alpha(\alpha-1)\frac{q^2}{A^2}} < 0.\end{aligned} \tag{4.24}$$

When $\alpha = 1$, the associated characteristic variables have the following expressions:

$$\begin{aligned}W_1 &= \frac{q}{A} + 4(c - c_0),\\ W_2 &= \frac{q}{A} - 4(c - c_0),\end{aligned} \tag{4.25}$$

where $c = \sqrt{\frac{\beta}{2\rho A_0}} A^{\frac{1}{4}}$ and $c_0 = \sqrt{\frac{\beta}{2\rho A_0}} A_0^{\frac{1}{4}}$. The characteristic system can be expressed as the decoupled system of equations:

$$\begin{aligned}\frac{\partial w_1}{\partial t} + \lambda_1 \frac{\partial w_1}{\partial x} &= 0,\\ \frac{\partial w_2}{\partial t} + \lambda_2 \frac{\partial w_2}{\partial x} &= 0.\end{aligned} \tag{4.26}$$

The wave velocity which arises from the blood wall coupling may take values as low as 5 m/s in large arteries (e.g. aorta), increasing to values around 20-35 m/s in less distensible peripheral arteries [126]. However, peak flow velocities u are much smaller and usually remain less than around 1 m/s.

4.4.3 Numerical approximation

Several methods have been used [1, 14, 111, 129, 137], for the numerical approximation of the 1D system of conservation laws (4.17). In this section, we follow Peiró and Veneziani [129] and Formaggia et al. [111], where equations of the 1D model are discretized in their conservative form (4.20) by employing a second order Taylor Galerkin scheme. We denote $\triangle t = t^{n+1} - t^n$ the time step and express the Taylor expansion truncated to the second order at time t^n, giving

$$\mathbf{U}^{n+1} = \mathbf{U}^n + \triangle t \frac{\partial \mathbf{U}}{\partial t}\bigg|^n + \frac{\triangle t^2}{2}\frac{\partial^2 \mathbf{U}}{\partial t^2}\bigg|^n. \tag{4.27}$$

We define the matrix

$$\mathbf{K} = \frac{\partial \mathbf{S}}{\partial \mathbf{U}} = \begin{bmatrix} 0 & 0 \\ k_r \frac{q}{A^2} + \frac{\gamma}{4\rho A_0} \frac{1}{\sqrt{A}} \left(\frac{\partial^2 q}{\partial x^2} + \frac{1}{2A} \frac{\partial A}{\partial x} \frac{\partial q}{\partial x} \right) & -\frac{k_r}{A} \end{bmatrix}, \tag{4.28}$$

and rewrite (4.20) as

$$\frac{\partial \mathbf{U}}{\partial t} = \mathbf{S} - \frac{\partial \mathbf{F}}{\partial x}. \tag{4.29}$$

Using the matrices (4.23) and (4.28), we obtain

$$\begin{aligned} \frac{\partial^2 \mathbf{U}}{\partial t^2} &= \frac{\partial \mathbf{S}}{\partial \mathbf{U}} \frac{\partial \mathbf{U}}{\partial t} - \frac{\partial}{\partial x} \left(\frac{\partial \mathbf{F}}{\partial \mathbf{U}} \frac{\partial \mathbf{U}}{\partial \mathbf{t}} \right) \\ &= \mathbf{K} \frac{\partial \mathbf{U}}{\partial \mathbf{t}} - \frac{\partial}{\partial x} \left(\mathbf{J} \frac{\partial \mathbf{U}}{\partial \mathbf{t}} \right) \\ &= \mathbf{K} \left(\mathbf{S} - \frac{\partial \mathbf{F}}{\partial x} \right) - \frac{\partial (\mathbf{JS})}{\partial x} + \frac{\partial}{\partial x} \left(\mathbf{J} \frac{\partial \mathbf{F}}{\partial \mathbf{x}} \right). \end{aligned} \tag{4.30}$$

At time $t^n = n\triangle t$, the vector of unknowns $\mathbf{U}^n$ satisfies the following time marching scheme:

$$\begin{aligned} \mathbf{U}^{n+1} &= \mathbf{U}^n + \triangle t \left(\mathbf{S}^n - \frac{\partial \mathbf{F}^n}{\partial x} \right) \\ &+ \frac{\triangle t^2}{2} \left(\mathbf{K}^n \left(\mathbf{S}^n - \frac{\partial \mathbf{F}^n}{\partial x} \right) - \frac{\partial (\mathbf{J}^n \mathbf{S}^n)}{\partial x} + \frac{\partial}{\partial x} \left(\mathbf{J}^n \frac{\partial \mathbf{F}^n}{\partial x} \right) \right). \end{aligned} \tag{4.31}$$

The spatial discretization uses linear finite elements. The domain Ω is subdivided into N_{el} finite elements Ω_e of size h_e. We let V_h be the set of continuous vector functions in Ω, linear on each element and V_h^0 the subspace of V_h whose functions are zero at the endpoints [129]. The solution of (4.31) requires, for $n \geq 0$, to determine $\mathbf{U}^{n+1}$ in V_h such that $\forall \phi_h \in V_h^0$,

$$\begin{aligned} \left(\mathbf{U}^{n+1}, \phi_h \right) &= \left(\mathbf{U}^n, \phi_h \right) + \triangle t \left(\mathbf{S}^n, \phi_h \right) + \triangle t \left(\mathbf{F}^n, \frac{\partial \phi_h}{\partial x} \right) \\ &+ \frac{\triangle t^2}{2} \left(\mathbf{K}^n \left(\mathbf{S}^n - \frac{\partial \mathbf{F}^n}{\partial x} \right), \phi_h \right) \\ &+ \frac{\triangle t^2}{2} \left(\mathbf{J}^n \left(\mathbf{S}^n - \frac{\partial \mathbf{F}^n}{\partial x} \right), \frac{\partial \phi_h}{\partial x} \right), \end{aligned} \tag{4.32}$$

where $(\mathbf{U}, \phi) = \int_0^L \mathbf{U}.\phi dx$.

For the stability of the numerical method, we follow Formaggia et al. [111] and impose the following limitation for the time step:

$$\triangle t \leq \text{CFL} \times \min_{0 \leq i \leq N_{el}} \left[\frac{h_i}{\max(\lambda_{1,i} \lambda_{1,i+1})} \right] \tag{4.33}$$

where $\lambda_{1,i}$ is the value of λ_1 at mesh node x_i and the maximum CFL number is $\frac{\sqrt{3}}{3}$ [111].

4.4.4 Initial and boundary conditions

The initial conditions for (4.31) are given by:

$$A(x,0) = A_0(x), \;\; q(x,0) = 0, \;\; p(x,0) = p_0(x), \tag{4.34}$$

where $A_0(x)$ and $p_0(x)$ are the prescribed functions. The hyperbolic nature of the system permits to impose the flow rate q or area A at the inlet [1]. At the inlet usually, the flow rate is specified [136],

$$q(0,t) = q_{\text{in}}(t). \tag{4.35}$$

Information from the outside and inside of the domain are carried by the incoming characteristics (W_1) and the outgoing characteristics (W_2) respectively [137].

At each end of the tube, a single boundary condition is implemented. This is due to the characteristic analysis and using the fact that the flow is subcritical (the eigenvalues [$\lambda_1$and λ_2] in (4.24) have opposite signs) under physiological conditions [1, 138]. At the inlet at $x = 0$, $\mathbf{U}^n$ is assumed to be known and λ_2 in (4.26) is linearised by taking its value at time t^n. It can be shown that at the time t^{n+1}, the solution corresponding to this linearised problem yields [1, 114]

$$W_2^{n+1}(0) = W_2^n(-\lambda_2^n(0) \triangle t). \tag{4.36}$$

Equation (4.36) is a first order extrapolation of W_2 from the previous time step. Similar treatment at the outlet $x = L$, leads to:

$$W_1^{n+1}(L) = W_1^n(L - \lambda_1^n(L) \triangle t). \tag{4.37}$$

4.4.5 Terminal vessels

To reduce the complexity of the blood flow simulation, smaller arteries, which are downstream of the truncation points are not explicitly accounted for but their effect is represented by proper outflow boundary conditions [139]. The two most common models used are the *constant resistance model* [13, 114, 137, 139, 141] and the *Windkessel model* [14, 139, 141], that can be obtained using an analogy based on electric circuit components.

The constant resistance (CR) model (see Figure 4.3) is represented by a resistor R_t [139] where it is assumed that the blood pressure, $p(t) - p_0$, is proportional to the blood flow rate $q(t)$. The relation between the blood pressure and the flow is given by $p(t) - p_0 = R_t q(t)$, where R_t represents the terminal reflection coefficient. The terminal reflection coefficient for a wavefront travelling in the $+x$ direction can be defined in terms of the incoming and outgoing characteristics as [114, 137]

$$R_t = -\frac{\triangle W_2}{\triangle W_1} = -\frac{W_2^{n+1} - W_2^0}{W_1^{n+1} - W_1^0}. \tag{4.38}$$

The values for W_1^{n+1} are determined using Eq. (4.37), whereas W_1^0 and W_2^0 are the initial values [114]. The unknown W_2^{n+1} is determined by rearranging Eq. (4.38), giving

$$W_2^{n+1} = W_2^0 - R_t(W_1^{n+1} - W_1^0). \tag{4.39}$$

A reflection coefficient of $R_t = 0$ represents a non-reflecting boundary condition.

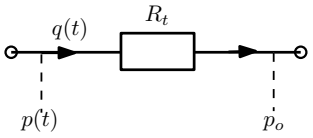

FIGURE 4.3: A constant resistance (CR) model representing an outflow boundary condition.

4.4.6 Treatment of bifurcations

At bifurcation of a blood vessel, we assume that pressure losses are negligible. We follow Wang et al. [137] and enforce the following conditions:

$$\begin{aligned} \sum_{i=1}^{3} q_i &= 0, \\ \frac{1}{2}\rho\left(\frac{q_1}{A_1}\right)^2 + p_1 - \frac{1}{2}\rho\left(\frac{q_i}{A_i}\right)^2 - p_i &= 0, \quad i = 2,3 \end{aligned} \tag{4.40}$$

representing the conservation of flow rate and total pressure continuity equations respectively.

4.5 Application of EnKF to 1D blood flow model

In this section, we present the use of the EnKF algorithm to solve the parameter estimation problem in a series of test cases. The first two tests are purely *in silico*, i.e. we use only synthetic data (observations) which are obtained from a forward simulation where the model parameters are set to some known or target values. From these observations, the parameter estimation problem then starts with an initial estimate for the parameters that differs significantly from the target values. With synthetic data, an inverse problem is always admissible when the objective is to recover the target parameters. By admissible we mean that because the target is generated with the model, the solution of the inversion targeting this results obviously exists, but still there is no guarantee of uniqueness. Indeed, regardless of existence of solution which is guaranteed in this case, several distributions of the parameters could achieve the target. The final test case uses data from the experiment performed by Saito et al. [13]. In this latter case, unlike with the synthetic data, there is no guarantee that the solution to the inverse problem actually exists.

In Saito et al. [13], a simple human arterial network was designed using polymer tubes to validate the applicability of the 1D blood flow model. The network was made with four bifurcations and consisted of the main artery, a left carotid artery, femoral arteries (left and right), and subclavian-radial arteries (left and right). The schematic of this simple human arterial model is shown in Figure 4.4 and the geometry of the arteries (length, diameter and the thickness) in Table 4.1 [13]. An appropriate length of blood

vessels was defined according to the vessel data of an average adult man. The diameter and thickness were defined to achieve a negligible reflection coefficient at bifurcation point [13]. For all test cases, we use the simple arterial model as in Figure 4.4. We limit our parameters of interest to Young's modulus and terminal model parameters (reflection coefficient), which are within a physiological range.

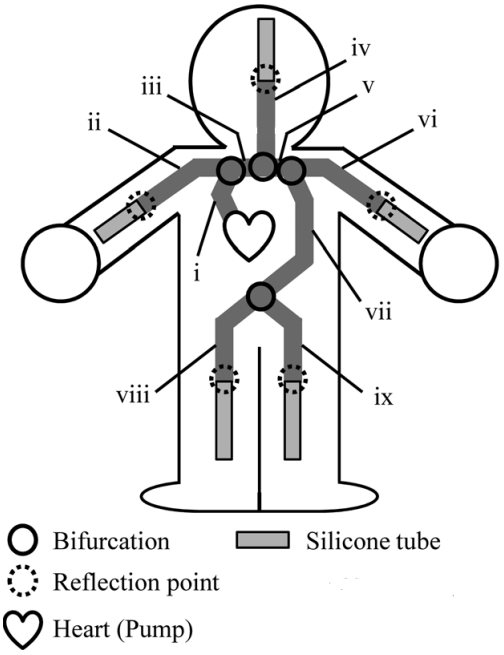

FIGURE 4.4: Schematic of a simple human arterial model with nine vessels and four bifurcations. Artery numbers corresponds to those in Table 4.1. Figure adapted from [13].

TABLE 4.1: Geometrical data (L = length, D = diameter and h = thickness) of a simple human arterial model (Figure 4.4) [13].

	Name	L **(mm)**	D **(mm)**	h **(mm)**
i	Aorta arch A	35	12	2
ii	R.subclavian radial artery	800	6	1.5
iii	Aorta arch B	20	11	2
iv	L.carotid artery	675	6	1.5
v	Aorta arch C	40	10	2
vi	L.Subclavian radial artery	710	6	1.5
vii	Aorta	470	8	1.5
viii	R.femoral artery	365	6	1.5
ix	L.femoral artery	365	6	1.5

4.5.1 Two test cases with synthetic data

One of the important parameters for EnKF is q_{ens}, the ensemble size. It is expected that the EnKF parameter estimation procedure would improve as the ensemble size increases. The increase in an ensemble size will also increase the computational cost associated with it. In our test cases, we assume that the blood flow model errors and uncertainties arise from the errors in the parameters and thus an ensemble is generated with perturbed parameters. As detailed in what follows, we therefore performed a parametric study to select a proper ensemble size.

We first simulate the blood flow model using an arbitrary set of parameters $\{E, R_t\}$. The resulting simulated model states are stored as $p^{\text{sim}} \in \mathbb{R}^n$. An ensemble of size q_{ens} is generated where the ensemble members are $\left\{E^{'}, R_t^{'}\right\}_i$ for $i = 1 \ldots, q_{\text{ens}}$. For each i, $E^{'}$ is a random normal variable with mean E and standard deviation of $0.1E$. Similarly, $R_t^{'}$ is a random normal variable with mean R_t and standard deviation of $0.1R_t$. The blood flow model is then simulated with each member of the ensemble and the observed pressure values at the end of the simulation are stored as $p^{obs_i} \in \mathbb{R}^n$. To select an ensemble size for the EnKF analysis, we calculated the root mean square error defined for each member of the ensemble as: $\text{RMSE}_i = \sqrt{\frac{1}{n}\sum_{j=1}^{n}(p_j^{sim} - p_j^{obs_i})^2}$. Finally, we find the mean RMSE for the ensemble of size q_{ens} as: $\text{RMSE} = \frac{1}{q_{\text{ens}}}\sum_{i=1}^{q_{\text{ens}}} \text{RMSE}_i$. The procedure was repeated with different ensemble sizes between $q_{\text{ens}} = 2$ and $q_{\text{ens}} = 60$. From Figure 4.5 which shows the output of the procedure with different random seeds, the mean RMSE decreases sharply initially with q_{ens} increasing. From this figure, the error does not decrease after $q_{\text{ens}} \approx 20$ and this latter value was thus retained in the present study.

4.5.1.1 Test case 1:

The first test case deals with the estimation of the Young's modulus for a single artery. We first describe the procedure for generating the synthetic data. All arteries except Aorta (number vii in Figure 4.4) is assigned a Young's modulus of 0.2 MPa and to Aorta (number vii), we assigned 0.25 MPa assuming some pathology there locally increasing its stiffness. A CR model is applied to the terminal vessels. A reflection coefficient of $R_t = 0.6$ is assigned to the terminal vessels ii, iv and vi and for terminal vessels vii and ix, $R_t = 0.65$. Figure 4.6 shows the periodic inlet flow rate boundary condition $q_{\text{in}}(t)$ (with a period of 0.8 s and an average inlet flow of 5.625 ml/s) imposed at the aorta arch

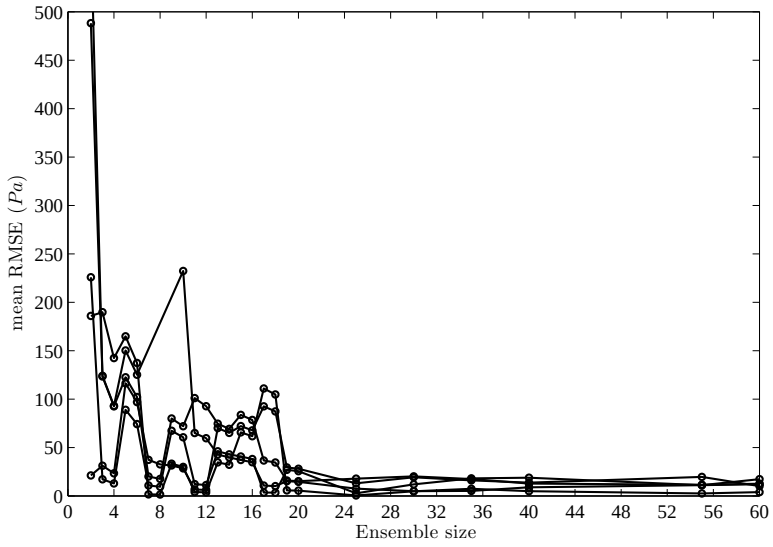

FIGURE 4.5: Mean RMSE as a function of ensemble size. Five sets of RMSE are calculated with different random seeds.

A of the simple arterial model. The density of the fluid is taken as 1000.0 kg/m^3, the viscosity of 1×10^{-3} Pa.s and the Poisson coefficient is taken as 0.5. The viscoelastic coefficient η and the non-linearity coefficient ϵ_p of the vessel are set to 0 for the forward simulation. The time step for the forward simulation is 0.1 ms, corresponding to $CFL = 0.05$. Synthetic pressure observations are taken at every 0.01 s.

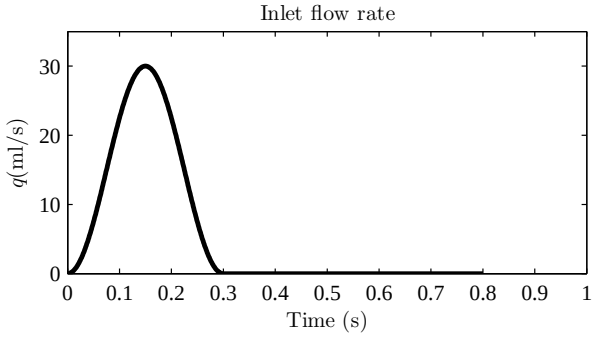

FIGURE 4.6: Periodic inlet flow rate $q_{\text{in}}(t)$ imposed at the aorta arch A.

The first objective is to determine the minimum number of observations ($nobs$), needed for a proper parameter estimation. $nobs$ refers to the number of locations where a time series of pressure is available. Other time series can be considered and we will present also simulations with flow rate time series in section 4.5.1.2. Algorithm 1 is executed initially with $nobs = 6$; $nobs$ is then decreased in steps of one to a minimum of 1. These observations are assumed to be available from the left and right

subclavian radial arteries (artery # ii and vi) and the left carotid artery (artery # iv). The locations of these observations are shown in Table 4.2.

TABLE 4.2: Location of observations on the right subclavian radial artery (ii), left carotid artery (iv) and left subclavian artery (vi) for synthetic test cases. L is the length of the artery.

Artery #	$nobs = 1$	$nobs = 2$	$nobs = 3$	$nobs = 4$	$nobs = 5$	$nobs = 6$
ii		$0.25L$	$0.25L$	$0.25L$	$0.25L$, $0.75L$	$0.25L$, $0.75L$
iv	$0.2L$	$0.2L$	$0.2L$	$0.2L$, $0.8L$	$0.2L$	$0.2L$, $0.8L$
vi			$0.33L$	$0.33L$	$0.33L$, $0.67L$	$0.33L$, $0.67L$

For the estimation problem, the Young's modulus is sought for the stiffest aorta, denoted by vii in Figure 4.4. An ensemble of $q_{\text{ens}} = 20$ members is considered in all the cases. For each member of the ensemble, the observations are perturbed by a random vector drawn from the zero mean Gaussian distribution with a standard deviation at 5% of the observation value. We compute the measurement error covariance matrix $\mathbf{R}$ using Eq. (4.6). The initial guess for the Young's modulus assumes an error of 100%, i.e. initial mean value for $E = 0.5$ MPa.

The parameter estimation using Algorithm 1 is then performed with different numbers of observations, $nobs$. The EnKF assimilation is executed for 10 s and the evolution of the estimated Young's modulus are shown in Figure 4.7a. It appears that convergence only takes place after some time. This kind of trend is often observed in optimization, especially with methods involving a learning feature. Indeed, there is no guarantee that the first search iterations are performed in a direction (in parameter space) pointing towards a minimum of the error. This behaviour also comes from the fact that the method is by nature explicit, as in gradient based methods. Table 4.3 shows the value of estimated Young's modulus with errors (percentage deviation from target value) using different number of observations. The percentage deviations from target E were all less than 5%. For this test case, a minimum of 1 observation was enough to recover the Young's modulus requested in the given interval of time. In Figure 4.7b, the pressure solutions obtained by using the estimated Young's modulus at the first observation point on left carotid are compared with the target and the initial guessed pressure profiles. The comparison is shown for Young's modulus estimated using $nobs = 2$. Even though the solution in the vessel whose Young's modulus is sought for is not directly observed, the simulated pressure waveforms are similar in

shape to the target pressure waveform with an error of less than 0.2% in the maximum pressure.

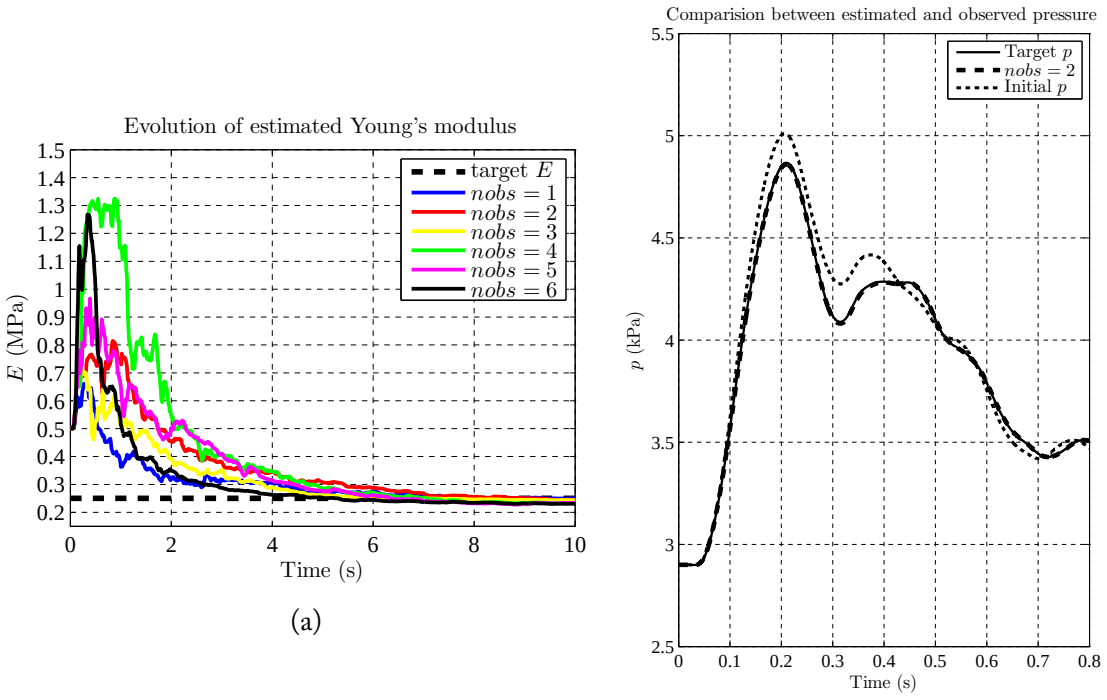

FIGURE 4.7: (4.7a) shows the evolution of the estimated Young's modulus using EnKF for test case 1 using a different number of observations. The initial value is 0.5 MPa and the target is 0.25 MPa. (4.7b) shows the comparison between the target pressure solution, the initial pressure profile and the one obtained by using the estimated Young's modulus with $nobs = 2$ at 0.2L of the left carotid artery.

TABLE 4.3: Test case1: Estimated Young's modulus and corresponding errors (percentage deviation from target value) using different number of observations.

	$nobs = 1$	$nobs = 2$	$nobs = 3$	$nobs = 4$	$nobs = 5$	$nobs = 6$
Estimated E (MPa)	0.239	0.245	0.243	0.245	0.241	0.246
% deviation from target E	-4.49	-1.95	-2.64	-1.82	-3.52	-1.79

4.5.1.2 Sensitivity analysis:

In this section, we look at the sensitivity of the parameter estimation algorithm for test case 1 with respect to the following items: (i) initial estimate of the parameter, (ii) level

of observation perturbation, (iii) the effect of introducing bias in the known parameter values and (iv) the observation type.

(i) Initial guess: we study the performance of EnKF by considering different initial values of the Young's modulus for the parameter estimation problem. Two more initial values of $E = 0.15$ MPa (-40% error) and 0.35 MPa (+40% error) were taken as the mean values of the initial ensembles. All other parameters and settings were same as in section 4.5.1.1. Through the use of $nobs = 2$, the EnKF assimilation is executed for 10 s and the evolution of estimated Young's modulus with their uncertainty (standard deviations) is shown in Figure 4.8a for three different initial values, including for $E = 0.5$ MPa (+100% error). The algorithm allows retrieving the target value independently on the initial guess. Table 4.4 compares the initial and final estimates of the Young's modulus with their associated uncertainties.

TABLE 4.4: Sensitivity with different initial values: final estimates of Young's modulus with their associated uncertainties. All values are in MPa.

Initial guess of E	Final estimate of E	Uncertainty ($\pm$ standard deviation)
0.15	0.2367	0.0228
0.35	0.2370	0.0250
0.50	0.2450	0.0245

(ii) The level of observation perturbation: As in section 4.2.1, the observations are perturbed by Gaussian noises. The noises represents possible errors in the measurement. For unbiased observations, perturbed observations are created by adding noise ($\sim (\mathcal{N}(0, \sigma^2)$), to the observation values; σ represents the standard deviation. In test case 1, σ equals 5% of observation values and for the analysis, we chose two more levels of observation perturbations with σ being 1% and 10% of observations values respectively. Using $nobs = 2$, we perform the estimation procedure for 10 s. The estimated Young's modulus with their uncertainty (standard deviations) are shown in Figure 4.8b for the three different levels of observation perturbations. With different values of σ, the estimated E's converge to the target value, but with a slightly different rate. With a lower σ (at 1% of observation values), the convergence rate is a little slower compared to the other two σ's, which was not anticipated. Table 4.5 compares the initial and final estimates of the Young's modulus with their uncertainties for the different level of perturbations used.

TABLE 4.5: Sensitivity with different level of observation perturbation: The initial guess of $E = 0.5$ MPa and the final estimates of Young's modulus with their associated uncertainties are shown below. Perturbed observations are created by adding noise ($\sim (\mathcal{N}(0, \sigma^2)$), to the observation values. All values of E and standard deviation are in MPa.

σ	Final estimate of E	Uncertainty ($\pm$ standard deviation)
1% of observation values	0.2556	0.0122
5% of observation values	0.2450	0.0245
10% of observation values	0.2441	0.0398

(iii) Bias in the known parameter values: In test case 1, we estimated the Young's modulus for artery #vii assuming that we know the values of E for all other arteries. We also assumed that all reflection coefficients were known. The performance of the estimation algorithm was tested by introducing biases in the known values of E and R_t. Three different tests were carried out as follows: (i) we randomly perturbed the values of reflection coefficients, R_t, with Gaussian noises having mean zero and a standard deviation at 5% of the values of R_t, (ii) the known values of Young's modulus, E are randomly perturbed with Gaussian noises having mean zero and a standard deviation at 10% of the values of E and (iii) known values of both reflection coefficients and Young's modulus are randomly perturbed with Gaussian noises having mean zero and a standard deviation at 5% of the values of R_t and 10% of the values of E. Pressure values in space were used as observations with the level of observation perturbation set at 5% of observation values and the estimation procedure is executed for 10 s. For all tests, the initial value of E assumes an error of 100%. The evolution of the estimated Young's modulus with their uncertainties for three different tests is shown in Figure 4.8c together with the evolution of estimated E when known Young's modulus and reflection coefficients are unbiased. For all the cases, the estimated values converge, but they slightly deviate from the target value as reported in Table 4.6 which also gives indications of the level of uncertainties in these inversions.

(iii) Observation type: In inverse hemodynamic problems, observations such as blood pressure, cross section blood flow rates, artery wall movements or cross-section flow velocity can be made available. In test case 1, the observations are pressure values histories at some specific locations in space. The behaviour of the estimation algorithm with different kinds of observations. To this end, we consider the flow rate in space as observations instead of the pressure. We perform the estimation procedure for 10 s

TABLE 4.6: Sensitivity test: bias in the known parameter values. The initial guess of $E = 0.5$ MPa and the final estimates of Young's modulus with their associated uncertainties are shown. All values of E and standard deviation are in MPa.

Random perturbation of known values of parameters by adding noise ($\sim (\mathcal{N}(0, \sigma^2))$.	Final estimate of E	Uncertainty ($\pm$ standard deviation)
unperturbed known parameters values	0.2450	0.0245
σ is 5% of R_t values	0.2580	0.0132
σ is 10% of E values	0.2752	0.0129
σ is 5% of R_t values and 10% of E values	0.2480	0.0161

using $nobs = 2$ with the level of observation perturbation set at 5% of the observed values. We compare these results to those obtained with the pressure as observation. The evolution of estimated Young's modulus with the associated uncertainties is shown in Figure 4.8d. With both types of observations, the estimated Young's modulus converges to the target value with relatively small errors (-1.95% and +2.24% with pressure and flow rate as observations respectively). However, when the observations are based on the flow rates, the convergence is slightly faster, at least in this particular case. The final estimate of E is 0.2450 ± 0.0245 MPa when pressure is considered as the observed quantity. On the other hand, with the flow rate as observation, the final estimate of E is 0.2556 ± 0.0059 MPa.

4.5.1.3 Test case 2:

The second test case deals with the estimation of the Young's modulus of all the arteries (i-ix) and the reflection coefficient at all the outlet boundaries (ii,iv,vi,vii,ix). All arteries are assumed to have the identical stiffness and thus, a Young's modulus of $E = 0.2$ MPa is assigned to all. A reflection coefficient of $R_t = 0.6$, is assigned at all terminal vessels. The viscoelastic coefficient η and the non-linearity coefficient ϵ_p of the vessels are set to 0.115 kPa.s and 0 respectively for the forward simulation. The rest of the parameters are as in section 4.5.1.1. For the estimation problem, the Young's modulus of the arteries and the reflection coefficient at terminal arteries are sought using various numbers of observations. The ensemble size q_{ens} and the error covariance matrix $\mathbf{R}$ are as in section 4.5.1.1. The mean values for the initial guess of the Young's modulus and the reflection coefficient are set to $E = 0.4$ MPa and $R_t = 0.8$. The EnKF assimilation is executed for 12 s, and the evolution of estimated E and R_t is shown in Figures 4.9a and 4.9b respectively, for the different numbers of observations.

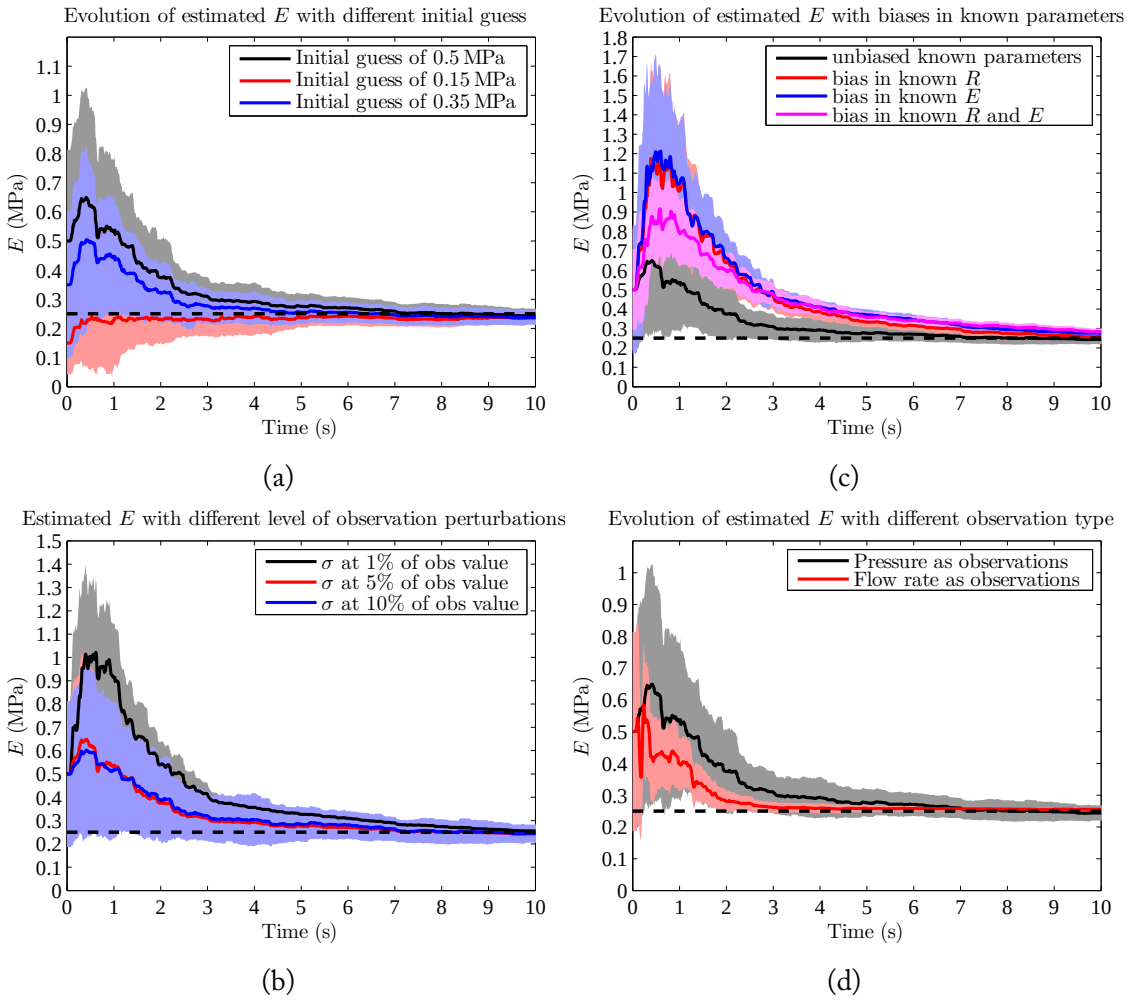

FIGURE 4.8: Sensitivity analysis for test case 1. In all the figures, the dashed line represents the target Young's modulus of 0.25 MPa and the shaded areas represents the standard deviation around the mean values (solid lines). (4.8a) shows the evolutions of the estimated Young's modulus from three different initial values. (4.8b) shows the evolution of estimated Young's modulus for three different levels of observation perturbations. (4.8c) shows the evolution of the estimated Young's modulus for different bias in the known parameters: R_t perturbed with Gaussian noises having mean zero and a standard deviation at 5% of the values of R_t (in red), E randomly perturbed with Gaussian noises having mean zero and a standard deviation at 10% of the values of E (in blue), both E and R_t randomly perturbed with Gaussian noises having mean zero and a standard deviation at 5% of the values of R_t and 10% of the values of E (in magenta). The evolution of estimated E with unbiased known parameters is shown in black. (4.8d) shows the evolution of the estimated Young's modulus with pressure and flow rates as observation types.

The estimation procedure was able to identify the parameters with different $nobs$, though the convergence rate was much slower with $nobs = 1$. From these evolutions, we see that even if $nobs = 1$ is enough to recover the values of E and R_t, one should attempt to at least have two observations for faster convergence. The Young's modulus also appears to be simpler to identify than the reflection coefficient. This is possibly because the time required to propagate the information contained in any boundary condition throughout the whole domain is of order L/c where L is the size of the network and c the wave speed. Instead, the Young's modulus directly impacts the wave speed so that it requires only Ls/c to feel any change in E, where $Ls < L$ is the distance between two consecutive observation location. Table 4.7 shows the value of estimated Young's modulus and the reflection coefficients with errors (percentage deviation from target value) using different number of observations. In Figure 4.9c, the pressure solution obtained with the estimated parameters using $nobs = 2$, at the first observation point on left carotid is compared with the target and initial pressure profiles. The simulated and the target pressure waveforms have very similar shape with an error of less than 0.2% in the maximum pressure.

The next configuration involves a more realistic situation with available experimental data.

TABLE 4.7: Test case 2: Estimated Young's modulus and reflection coefficients with errors (percentage deviation from target values) using different numbers of observations.

	Estimated E (MPa)	Estimated R_t	% deviation from target E	% deviation from target R_t
$nobs = 1$	0.2064	0.5995	3.20	-0.08
$nobs = 2$	0.1993	0.6013	-0.35	0.22
$nobs = 3$	0.1988	0.6030	-0.60	0.50
$nobs = 4$	0.2006	0.5973	0.30	-0.45
$nobs = 5$	0.1992	0.5994	-0.40	-0.10
$nobs = 6$	0.2003	0.5994	0.15	-0.10

4.5.2 A test case with experimental data

The efficiency of parameter estimation using the EnKF is presented where experimental data is used as the observations. We refer to the experiment in Saito et al. [13], where a simple human arterial network (see Figure 4.4) with four bifurcations was designed using

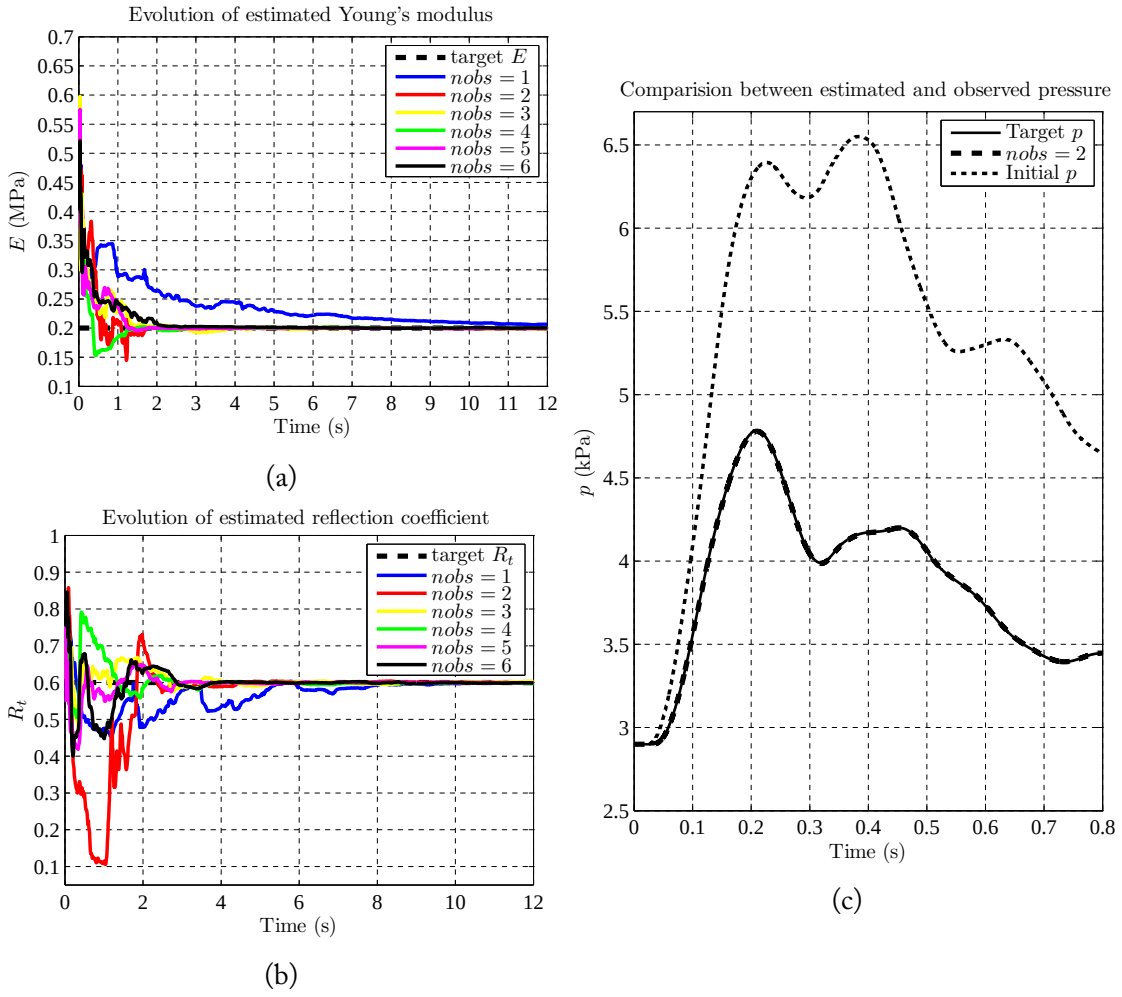

FIGURE 4.9: (4.9a) shows the evolution of the Young's modulus using a different number of observations for case 2. The initial value is 0.4 MPa and the target is 0.2 MPa. (4.9b) shows the evolution of the reflection coefficient using a different number of observations. The initial value is 0.8 and the target is 0.6. (4.9c) shows the comparison between the pressure signal obtained with initially guessed parameters, the target pressure solution and the one obtained by using the estimated parameters with $nobs = 2$, at 0.2L of the left carotid artery.

polymer tubes ($E = 0.185$ MPa) to validate the applicability of the blood flow model as presented in [13]. The tubes are filled with water, and to realize the reflection coefficients of approximately 0.5, silicone tubes are connected at the end of the tubes to act as virtual peripheral sites. A pulse flow with the profile of half a cycle of a sinusoidal wave is used as input from the pump. The period of the pulse is 0.3 s with the total flow volume of 4.5 ml. The pressure waves propagating in the viscoelastic tubes were experimentally measured using a pressure sensor at 150 mm from the second bifurcation, which in an actual human body roughly corresponds to the carotid artery of the neck [13].

For this test case, we do not know if the solution of the inverse problem exists as the target has not been generated with the blood flow code. The aim is then to determine the best estimate of the Young's modulus (E), reflection coefficient (R_t) and viscoelastic coefficient (η) from the values of the experimentally measured pressure, which are taken as observations for the inverse problem. It is assumed that E and η are identical for all tubes and R_t is same at each terminal tube. The ensemble size $q_{\text{ens}} = 20$ and the error covariance matrix $\mathbf{R}$ are defined as in section 4.5.1.1. The pressure measurements are only available at one point on the carotid artery. The frequency of data assimilation is 0.01 s.

To test the sensitivity to initial parameter values, we investigate the performance of the EnKF parameter estimation algorithm using three different sets of initial guess for the three parameters (E, R_t and η). The mean values for the initial guess of the parameters were: $(E(MPa), R_t, \eta(KPa \cdot s)) \in \{(0.2, 0.6, 0.3), (0.6, 0.3, 0.4), (0.4, 0.8, 0.5)\}$. The estimated parameter values do not change significantly after 16 s of EnKF assimilation as shown in Figure 4.10. From Figure 4.10, we see that the different guesses for initial mean values of the parameters seem not to have a significant impact on the converged assimilated result. The initial guess of the parameters and their best estimates obtained with their associated uncertainty (standard deviation) with three different initial guesses using the EnKF are shown in Table 4.8.

TABLE 4.8: Sensitivity to initial parameter values for the test with experimental data. The initial guess of the parameters and their best EnKF estimates with their associated uncertainty (standard deviation).

Parameter	Initial guess	EnKF estimate	Error ($\pm$ standard deviation)
E (MPa)	0.2	0.1111	0.0024
	0.6	0.1226	0.0025
	0.4	0.1150	0.0028
R_t	0.6	0.5199	0.0033
	0.3	0.5146	0.0075
	0.8	0.5290	0.0048
η (KPa·s)	0.3	0.3710	0.0124
	0.4	0.3760	0.0104
	0.5	0.3810	0.0157

The blood flow model is then used with the estimated parameters to obtain the pressure profile at the observation point. Figure 4.11 shows the comparison between

the pressure profile obtained with the three sets of estimated parameters, the numerical pressure profiles from the 1D blood flow model as reported in Saito et al. [13], the measured pressure waves obtained from the experiment and the pressure profile obtained from the three different sets of initial parameters. The simulated waveforms are similar to the target pressure waveform. We compare the systolic (maximum) pressure between the target (experimental pressure waveform) and the simulated pressures obtained from different sets of estimated parameters. The difference is shown in Table 4.9. In all the cases, the error is less than 2%. The results demonstrate that even with $nobs = 1$, the Young's modulus, reflection coefficient, and the viscoelastic coefficient can be estimated with good accuracy using the proposed method.

TABLE 4.9: Test case 3: Comparison of the systolic (maximum) pressure between the target (experimental pressure waveform) and the simulated pressures obtained from different sets of estimated parameters. The target systolic pressure is 4.02 MPa.

Estimated parameter set $\{E\,(MPa), R_t, \eta\,(kPa.s)\}$	Maximum pressure (MPa)	% error
set 1 $(0.1111, 0.5199, 0.371)$	4.01	-0.24
set 2 $(0.1226, 0.5146, 0.376)$	4.08	1.50
set 3 $(0.1150, 0.529, 0.381)$	4.04	0.51

4.6 Discussions

In this paper, we have demonstrated the applicability of EnKF to estimate the Young's modulus, reflection coefficient, and viscoelastic coefficient. A similar approach can also be used to estimate other hemodynamic parameters such as resistance and compliance in a Windkessel model. The EnKF and thus the estimation algorithm provides the estimates of poorly known parameter values with their uncertainties. Sensitivity analysis with respect to the initial guess of parameters, the level of observation perturbation, the effect of bias in known parameter values and the type of observations is carried out. Further analysis can be done on the efficiency of the estimation algorithm with respect to the locations of available observations. We need to make sure the size of the ensemble is correctly chosen. One also sees that very few spatial observation are necessary as the approach performs even with solely one spatial observation point. We also discussed the robustness of the inversion for different types of target observations (pressure or flow rate). We have shown a method of choosing an ensemble size using RMSE, but the

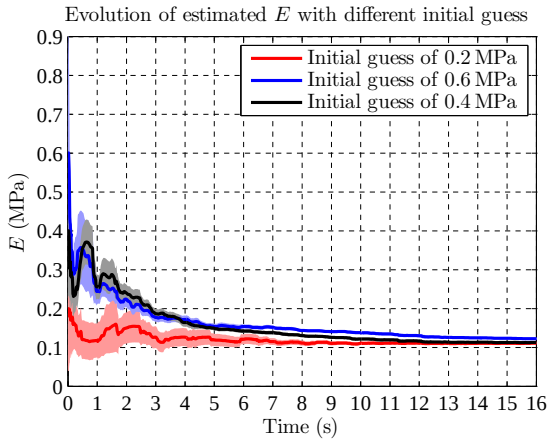

(a)

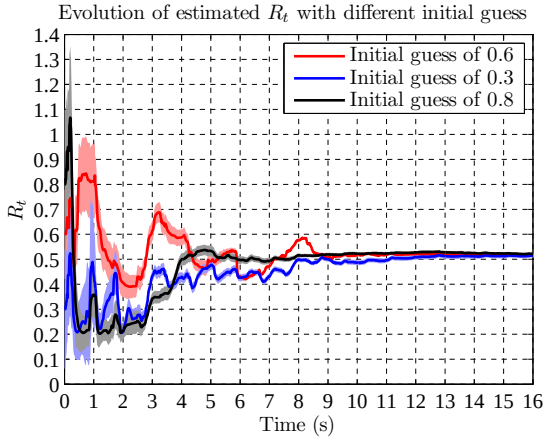

(b)

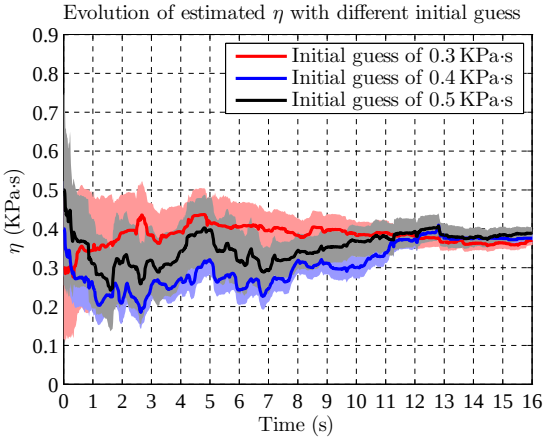

(c)

FIGURE 4.10: Sensitivity of EnKF parameter estimation to different sets of initial parameter values. 4.10a-4.10c show the evolution of Young's modulus, reflection coefficient, and viscoelastic coefficient respectively for the test case using the experimental data with different sets of initial values. The set of initial guess of the parameters, $\{E\,(MPa), R_t, \eta\,(kPa.s)\}$ are: in RED $\{0.2, 0.6, 0.3\}$, in BLUE $\{0.6, 0.3, 0.4\}$, in BLACK $\{0.4, 0.8, 0.5\}$. The shaded areas represent one standard deviation around the mean values (solid lines).

efficiency of the EnKF parameter estimation algorithm may depend on other factors such as level of observation perturbation, the location of the observations, their types and also on the type of parameters to be estimated. The approach needs to be seen as a help to diagnosis tool and not a definite opinion. We mentioned that one issue is that uniqueness is not guaranteed. This might, therefore, impact clinical applications. Indeed, an incorrect Young's modulus might be obtained still providing a nice model fit and obviously, this might mislead the clinician. The approach, therefore, needs to be adopted in a Bayesian procedure with a priori information on the admissibility of the

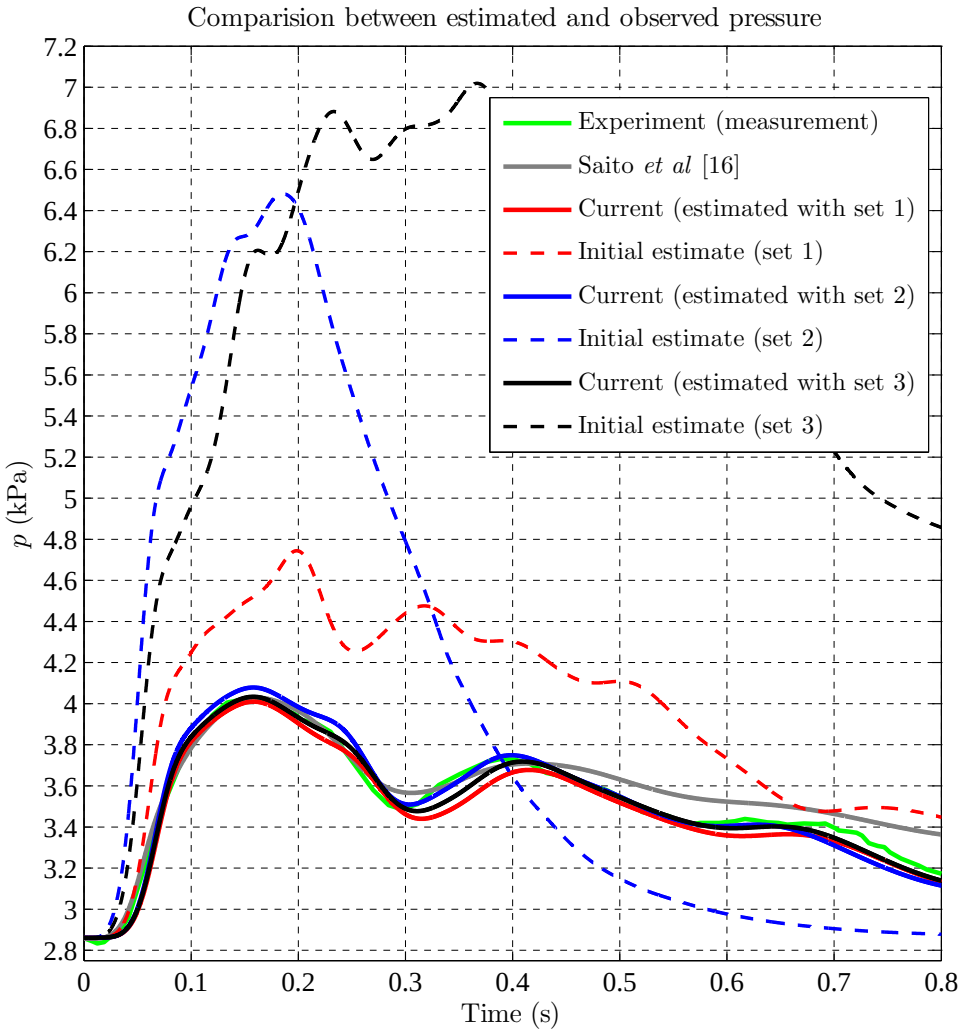

FIGURE 4.11: Comparison between the pressure profile obtained with the three sets of estimated parameters, the numerical pressure profiles from the 1D blood flow model as reported in [13], the measured pressure waves obtained from the experiment and the pressure profile obtained from the three different sets of initial parameters. The dashed lines are the initial pressure waveforms and the solid lines are the ones obtained from the estimated parameters. The set of initial guess of the parameters, $\{E\,(MPa), R_t, \eta\,(kPa.s)\}$ are: set 1 $\{0.2, 0.6, 0.3\}$, set 2 $\{0.6, 0.3, 0.4\}$ and set 3 $\{0.4, 0.8, 0.5\}$.

outcome by the clinicians and the outcome should definitely not been considered as a final opinion.

We aim at having an approach with moderate complexity to describe the physics of the problem and which is usable in practice. This is why any forward model based on a multi-dimensional flow model is out of the table. Other works, for instance, present data assimilation together with three-dimensional flow models based on fully 3D Navier-Stokes [10], which require heavy computational effort in addition to an increase in the complexity of the inverse problem. These approaches also require good know-how by the user and substantial learning efforts. We use a reduction in dimension to bring the cost of one state evaluation to the order of a minute on standard computers available in clinics. Then natural parallelism in EnKF makes a time to solution of the order of the number of EnKF iterations in minutes, which in the present case leads to approximately two hours. Still this can be considered too costly and our current effort is to reduce complexity even further.

4.7 Study limitations

The first limitation of our current study is concerned with the size of the arterial network being adopted. We used a network consisting of 9 vessels, and the efficiency of the proposed estimation algorithm has to be tested for a larger arterial network, including complex network such as the circle of Willis in the cerebral vasculature. Secondly, an ensemble size of 20 is taken as an optimal size for the parameter estimation in the current study. An effect of taking a larger sample size on the estimation procedure can also be studied. The efficiency and convergence rate also depends on the level of observation perturbation, and another limitation is to identify the optimal level. It is also important to investigate the maximum number of parameters that can be estimated for a given arterial network with a given number of measurements available. In the current study, we adopted 1D blood flow model with a constant resistance boundary condition. As discussed before, there is no real limitation regarding the boundary description and thus, the estimation algorithm can be applied to a blood flow model coupled to a Windkessel model.

4.8 Conclusion

A parameter estimation technique to compute the uncertain elastic and the terminal properties of networks of 1D blood vessels using the Ensemble Kalman filter has been studied. The tests have been limited to the estimation of elastic moduli (Young's modulus) of the network, the reflection coefficient at the terminal vessels and the viscoelastic coefficient. The results confirm that the method is quite robust and permits to recover the arteries stiffness in a reasonable amount of time consistent with patient observation time at the hospital. Except with the computation of the Kalman gain, all the operations on the ensemble members are independent. This implies that their parallelization can be trivially carried out, thus decreasing the computational time needed to solve the inverse hemodynamic problem. The time to solution for this simulation is about 30 minutes on a parallel computer with 20 cores, which is basically one node of current standard distributions. The model simulations performed with the estimated parameter values produced accurate pressure profiles, which followed closely with the target profiles showing the effectiveness and the efficiency of both the estimation algorithm and the blood flow model. Also, it has been shown that the approach is effective with only a few observations, well suited to real clinical applications.

Acknowledgment

Research done under the European Union Framework Programme Erasmus Mundus KITE (2013-2617 / 001-001 - EMA2)

Chapter 5

Non invasive blood flow features estimation in cerebral arteries from uncertain medical data

Contents

Part of this chapter has been submitted for publication as:

R. Lal, F. Nicoud, E. Le Bars, J. Deverdun, F. Molino, V. Costalat and B. Mohammadi, "Non invasive blood flow features estimation in cerebral arteries from uncertain medical data" in *Annals of Biomedical Engineering*, 2017.

The numbering of sections, figures and tables in the original manuscript have been altered for this chapter, to be consistent with the thesis chapter numbering. The references have been incorporated into the global references at the end of the thesis.

Part of chapter 5 has been presented in the previous chapters as follows:

- section 5.2.1 presents a summary of sections 3.2 and 3.3 of chapter 3,
- section 5.2.4 presents a summary of sections 2.5 and 2.6 of chapter 2.

The rest of the sections of this chapter present new materials focusing on the application of EnKF to 0D model for the cardiovascular system. The aim of this chapter is to show that 0D model can lead to simple and reliable predictions of blood flow circulation in the circle of Willis and compare the simulations with the results by our previous 1D PDE model. A 0D model is used to fasten the parameter estimation procedure and also to keep low the cost of data assimilation in case of larger arterial networks. An interesting a posteriori consequence of this analysis is that the 0D model also permitted to understand that much coarser space meshes can be considered for the 1D PDE model in the presence of waves with large wavelengths.

Abstract

A methodology for non invasive estimation of the pressure in internal carotid arteries is proposed. It uses data assimilation and Ensemble Kalman filters in order to identify unknown parameters in a mathematical description of the cerebral network. The approach uses patient specific blood flow rates extracted from Magnetic Resonance Angiography and Magnetic Resonance Imaging. This construction is necessary as the simulation of blood flows in complex arterial networks, such as the circle of Willis, is not straightforward because hemodynamic parameters are unknown as well as the boundary conditions necessary to close this complex system with many outlets. For instance, in clinical cases, the values of Windkessel model parameters including Young's modulus of arteries are not available on per-patient cases. To make the approach computational efficient, a reduced order zero-dimensional compartment model is used for blood flow dynamics. The approach is illustrated on both synthetic and real data cases. In particular, it is shown that the technique well performs with target flow rate time series from either the right or left internal carotid arteries. The inversion appears quite robust and similar Young's modulus are recovered with either the right or the left flow rate times series used during the inversion.

Keywords: MRA, MRI, EnKF, reduced order compartment blood model, parameter estimation, circle of Willis, hemodynamic inverse problems

5.1 Introduction

One of the key factors identified to be associated with the formation and the risk of rupture of cerebral aneurysms is the blood pressure fluctuations in cerebral arteries [25–29, 154].

This work proposes to estimate these pressure variations for an arterial network representative of the cerebral circulation using an integrated observation/simulation/assimilation procedure to exploit available Magnetic Resonance Angiography and Magnetic Resonance Imaging (MRA&MRI) observation data by ensemble Kalman filter parameter estimation techniques using reduced order blood flow models.

The analysis of the cardiovascular system can be carried out using one-dimensional (1D) [1–5] or multi-dimensional modelling (2D or 3D) [6–8] or in a simplified manner using a lumped model (0D compartment model) [9, 12, 155, 156]. It is possible to numerically solve the pressure wave system, taking place in a network of interconnected arteries representing all or part of the cardiovascular system. Using imaging data such as MRI, the geometric properties of each blood vessels such as diameter and length can be acquired. However, the structural properties of the vessels such as wall thickness and the Young's modulus are difficult to identify. Still in patient-specific simulations, such unknown properties need to be estimated as well as the distal boundary conditions. These unknown parameters can be estimated using an algorithm based on a data assimilation technique such as using an Unscented Kalman filter (UKF) [10] or an Ensemble Kalman filter (EnKF) [37]. The idea of the underlying algorithm is to estimate the input parameter values used in the numerical model to reproduce the best available observations such as brachial blood pressure, carotid flow rate, temporal pressure or aortic flow rate. Once the assimilation process is completed and the parameters are estimated, the interconnected network of arteries becomes a good approximation of the patient specific cardiovascular system on which the morphological data are collected and hemodynamic observations are made. It is then possible to use the blood flow model to estimate the hemodynamic variables whose measurement is only possible invasively (e.g. to access aneurysm pressure).

The blood flow simulation and interactions involving the full human arterial tree, including the capillary bed involve a high demand for supercomputing resources [157]. In the current work, the arterial networks are represented by both a 1D blood flow model and a simple 0D model. For the boundary condition at the outlet of each terminal artery, we coupled the blood flow models with the 0D Windkessel model (WK3).

1D modelling of arterial networks offers good accuracy and is commonly used due to being computationally cheap compared to 3D models [3, 5, 103]. The inverse hemodynamic problem involving clinical data when using 1D modelling can be quite challenging and thus regarded as one of the disadvantages of using 1D modelling when finding the unknown model input parameters [103]. In the 1D formulation, the network of arteries is fragmented into segments that connect to each other at nodes. The number of unknown model parameters that need to be estimated increases as the number of arterial segments increases [103].

A ring-like arterial structure known as the Circle of Willis (CoW) that is located at the base of the brain, linking the main cerebral arterial systems (the internal carotid arteries and the vertebrobasilar) is the pathway for the distribution of oxygenated blood in the cerebral mass [7, 158]. The role of CoW is also to compensate for the reduction of cerebral perfusion pressure during internal carotid artery (ICA) occlusion [159]. Approximately 50% of the population have a complete CoW [160, 161]. The two common variations include an underdeveloped CoW (hypoplasia) and cases where some blood vessels are completely absent in a CoW [161]. The possible variations may influence the reduced ability for the collateral flow of the blood through CoW, causing a major health risk such as an ischaemic stroke [7, 158]. The CoW is also a common place for aneurysms [30]. There have been many types of research done on hemodynamics and the blood flow in the CoW [7, 14, 32, 155, 158, 162–165] focusing on the understanding of factors increasing the risk of stroke and the blood flow distribution in the brain.

Recent works on the application of data assimilation to inverse problems in hemodynamics include the work of Moireau et al. [36], Pant et al. [10, 34], Lombardi [35], Spilker and Taylor [42], Bertoglio et al. [39], Chabiniok et al. [33], Martin et al. [41], Lassila et al. [43] and Lal et al. [37]. In all of the above work, except Lal et al. [37], the data assimilation techniques are either based on a joint state augmented model or reduced order unscented Kalman filter (ROUKF). In [37], we have demonstrated the use of EnKF for inverse hemodynamic problems using either synthetic or experimental data from an in vitro test rig [13] where a simple reflection coefficient are used as the outlet boundary conditions. In this paper, we demonstrate the usefulness of EnKF in the case where WK3 is used to represent the outlet boundary conditions for both synthetic and actual clinical data. We then estimate the blood pressure (diastolic and systolic) in internal carotid arteries from the assimilated blood flow model.

The outline of the paper is as follows: We first present a review of the 1D blood flow model and 0D lumped compartment model which will be used to represent the cardiovascular network. Next, the Ensemble Kalman data assimilation technique is briefly reviewed and our algorithm for parameter estimation given. We then show the application of our procedure to test cases with synthetic and actual clinical data. The later corresponds to the cerebral network, including the complete circle of Willis (CoW), of a healthy subject.

5.2 Materials and methods

5.2.1 1D blood flow model

1D blood flow models of arterial networks are commonly used due to being computationally cheap compared to 3D models [3, 5, 103]. They provide good and accurate results if the 3D effects in the flow can be neglected. The mathematical formulation and the derivations of 1D modelling can be found in [1–3].

We assume that the blood vessels have cylindrical geometries, and the cardiovascular system is considered as a network of these interconnected vessels with blood flow in one-dimension. We consider the following governing equations representing mass and momentum conservation [1]:

$$\begin{aligned} \frac{\partial A}{\partial t} + \frac{\partial q}{\partial x} &= 0, \\ \frac{\partial q}{\partial t} + \frac{\partial}{\partial x}\left(\alpha \frac{q^2}{A}\right) + \frac{A}{\rho}\frac{\partial p}{\partial x} &= -k_r \frac{q}{A}, \end{aligned} \tag{5.1}$$

where x and t represent the axial direction and time respectively, $A(x,t)$ is the cross section area, $q(x,t)$ is the flow rate across a section, ρ denotes the density of the blood, p is the average internal pressure over the cross-section. For a flat velocity profile, the momentum-flux correction coefficient, α, equals unity [1]. k_r represents the viscous resistance of the flow per unit length of the vessel. The system (5.1) is completed by the following differential constitutive pressure-area relation [1]:

$$p = p_e + \frac{\sqrt{\pi} h E}{(1-\sigma^2) A_0}\left[\left(\sqrt{A} - \sqrt{A_0}\right) + \epsilon_p \left(\sqrt{A} - \sqrt{A_0}\right)^2\right] + \frac{h\eta\sqrt{\pi}}{A_0}\frac{\partial \sqrt{A}}{\partial t}, \tag{5.2}$$

where p_e is the constant external pressure, A_0 represents the vessel sectional area at a reference pressure and ϵ_p is the nonlinearity coefficient. h is the thickness of the vessel, η is the viscoelastic coefficient, E is the Young's modulus and the Poisson ratio, $\sigma = 0.5$ [1].

The pressure losses at a bifurcation (from artery index 1 to arteries 2 and 3) of a blood vessel are assumed to be negligible. Following Wang et al. [137], the following coupling equations representing the conservation of flow rate and the pressure continuity

are enforced at the bifurcation:

$$\begin{aligned} \sum_{i=1}^{3} q_i = 0, \\ \frac{1}{2}\rho\left(\frac{q_1}{A_1}\right)^2 + p_1 - \frac{1}{2}\rho\left(\frac{q_i}{A_i}\right)^2 - p_i = 0, \quad i = 2, 3. \end{aligned} \tag{5.3}$$

At the outlet of each terminal artery, the 1D blood flow model is coupled to the three-element Windkessel model (WK3-lumped parameter model) [5] to include the effect of the downstream vasculature. In the WK3 model (see Figure 5.1), the instantaneous blood pressure and the flow rate are related as follows:

$$\frac{dp(t)}{dt} + \frac{p - p_{out}}{R_D C} = R_P \frac{dq(t)}{dt} + \frac{q(R_P + R_D)}{R_D C}, \tag{5.4}$$

where p is the instantaneous pressure at the inlet of the WK3 model, q is the instantaneous flow rate, R_P, and R_D are the proximal (characteristic) and distal resistance respectively of the vascular beds, and C is the compliance. $R_T = R_P + R_D$ represents the total resistance of a peripheral bed. p_{out} is the pressure (assumed to be zero) at which flow through the microcirculation is zero [146]. In this study, a second order finite element Taylor-Galerkin scheme is used to solve the set of Equations (5.1)-(5.3).

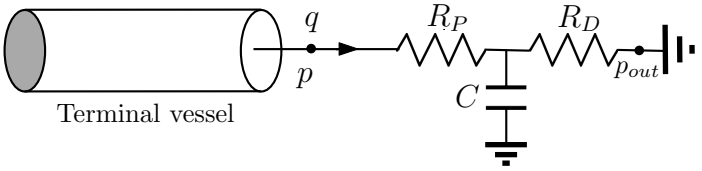

FIGURE 5.1: Electric analogue of Windkessel (WK3) model.

5.2.2 0D model for cardiovascular system

The human cardiovascular system can be modelled using an electrical analogy to represent different mechanical properties of arteries [9, 12, 155, 156]. In this model, the arterial network is divided into different compartments comprising a resistor (resistance of blood due to blood viscosity, R), an inductor (blood inertance L) and a capacitor (compliance of the artery, C) as shown in Figure 5.2.

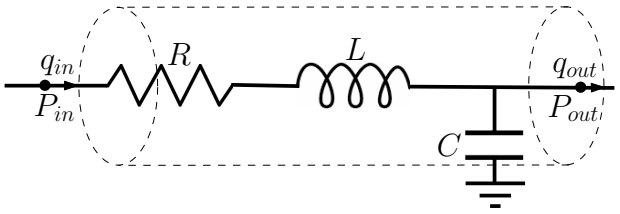

FIGURE 5.2: Single compartment circuit representation.

The spatial variation of parameters (R, L, and C) in lumped parameter models is neglected in each spatial compartment and thus the parameters are assumed to be uniform [147]. The dynamics in each compartment are characterised by a set of ordinary differential equations. For a single compartment assuming an incompressible Newtonian fluid, the governing equations for the 0D model relating the variables R, L and C and representing mass and momentum conservation read [9, 12, 155, 156]

$$\begin{aligned} C\frac{dP_{out}}{dt} &= q_{in} - q_{out} \\ L\frac{dq_{in}}{dt} + Rq_{in} &= P_{in} - P_{out} \end{aligned} \tag{5.5}$$

where P_{in}, q_{in} and P_{out}, q_{out} are the blood pressure and flow rate at the inlet and outlet of the compartment (artery) respectively. The inertance L expresses the relative significance of inertia within the vessel and if its effect is ignored, the flow rate is then given by $q_{in} = (P_{in} - P_{out})/R$.

The parameters R, L and C for each of the compartment representing different arterial segments are calculated using the following equations [10, 107]: Hagen-Poiseuille law for resistance, $R = 8\mu l/\pi r^4$, $L = \rho l/\pi r^2$ and $C = 3\pi r^3 l/2Eh$, where E, h, ρ, μ, l and r are the Young's modulus, arterial wall thickness, the blood density, the blood viscosity, the length of the arterial segment and, the radius of the artery respectively.

Conservation of mass and momentum are enforced for diverging flows at the bifurcation (Figure 5.3a) and for merging flows at the junction (Figure 5.3b). The flow at node 1 in Figure 5.3a is $q_1 = q_2 + q_3$ (conservation of mass) and due to the continuity of pressure $p_1 = p_2 = p_3$. Similarly for merging flows in Figure 5.3b, $q_1 + q_2 = q_3$ and $p_1 = p_2 = p_3$.

Solution of Equation (5.5) needs care as this system is very stiff ($L/C \in [10^{18}, 10^{20}]$). This first order differential equations system is solved using the

implicit numerical integration solver DVODE [166, 167]. The Fortran version of DVODE is available on http://www.radford.edu/~thompson/vodef90web/.

(a) (b)

FIGURE 5.3: Model geometry for diverging (5.3a) and merging flows (5.3b).

5.2.3 Comparison of modelling techniques

Our aim in introducing the 0D modelling is mainly to reduce the CPU cost. We still need to make sure that the corresponding results are close to those from the 1D PDE description of chapter 3. In this section, we show how a 'best practice' guidance can be established for the definition of the number of compartments in a segment in order for the ODE model to recover the PDE results.

5.2.3.1 Comparison between 1D PDE and ODE models in a test case

A blood vessel in an arterial network can be partitioned into m segments (compartments). In multi-compartment models, each segment (or compartment), is described by its own resistance $R = 8\mu l/\pi r^4$, compliance $C = 3\pi r^3 l/2Eh$ and inductance $L = \rho l/\pi r^2$. Let us compare the two modelling techniques (1D PDE and 0D compartment model) using a simple test case.

A blood vessel of length (l) of 40 cm, thickness (h) of 0.63 mm, radius (r) of 0.25 cm, and with Young's modulus of 0.4 MPa is considered for the test case. A periodic flow rate boundary condition $q_{\text{in}}(t)$ is imposed at the inlet of the simple model. A WK3 model is applied at the outlet of the computational domain with $R_P = 1.87$ mmHg·s/ml, $R_D = 12.02$ mmHg·s/ml and $C = 0.02$ ml/mmHg. The set-up is shown in Figure 5.4.

The density (ρ) of the fluid is taken as 1050 kg/m^3, the viscosity (μ) of 4×10^{-3} Pa·s and the Poisson coefficient (σ) of 0.5. The viscoelastic coefficient (η) and the nonlinearity

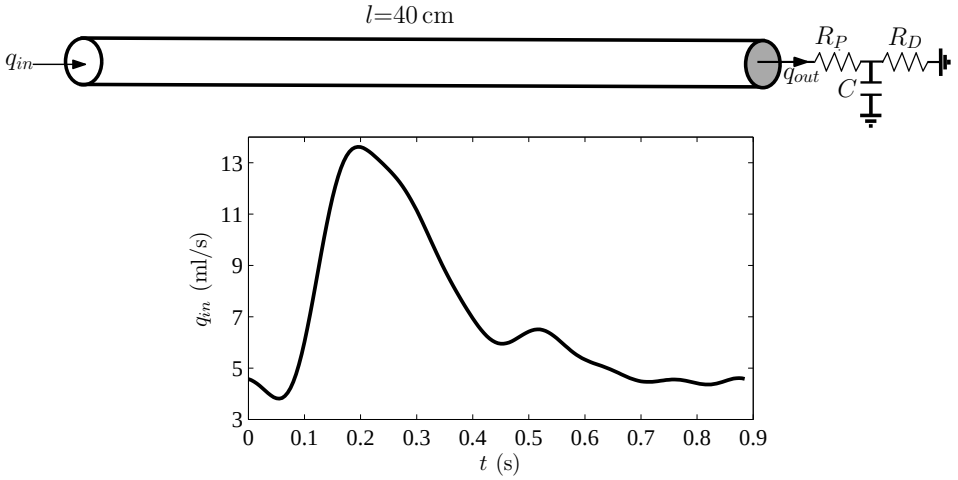

FIGURE 5.4: Comparison of modelling techniques. Set-up (top) and the inlet flow rate q_{in} (bottom).

coefficient (ϵ_p) of the vessel are both set to zero. The 1D blood flow model is then executed with the above parameters using CFL=0.6 and with a mesh of 40 elements of 1 cm. This discretization is the coarser one still producing mesh independent results. The periodic solution at the end of the vessel, q_{out}, is recorded. For comparison purpose, the compartment model is then applied to the set-up with different numbers for m starting from 1. A periodic solution (q_{out}) is recorded for each m.

Also, to see the sensitivity of the results with respect to Young's modulus, the above procedure is repeated for the blood vessel with Young's modulus of 1.6 MPa.

Figures 5.5a and 5.5b compare the 1D PDE and 0D compartment model flow rate waveforms at the vessel outlet. In both cases, the compartment model waveforms for $m \geq 3$ are similar to the 1D PDE waveform. The agreement between the two models for the two cases are good for $m \geq 2$ with the root mean square error between the models of less than 2% for $m = 3$. However, the variability increases with the decrease in Young's modulus.

In all cases, considering the range of Young's modulus we face in these applications, these simulations suggest that for the ODE model to reproduce the PDE results, one should avoid 0D compartments with length l larger than 20 cm $\left(\frac{40\,cm}{m} \text{ with } m = 2\right)$ for both E = 0.4 MPa and E = 1.6 MPa.

In other words, this analysis indicates that one needs nearly 35 compartments by wavelength which in our case is around 7 m for the case of E = 0.4 MPa and 70 compartments when E = 1.6 MPa where the wavelength is 14 m. These considerations

suggest that when applied to an ensemble of cerebral arteries which are very short and with large Young's modulus, m = 1 is quite a safe choice.

It is important to notice that with $m = 2$ the computational cost of the ODE model versus PDE is reduced by a factor of more than 300 which means that 10 iterations of EnKF with an ensemble of size 30 is performed at the cost of one PDE direct simulation on a mesh with 40 elements.

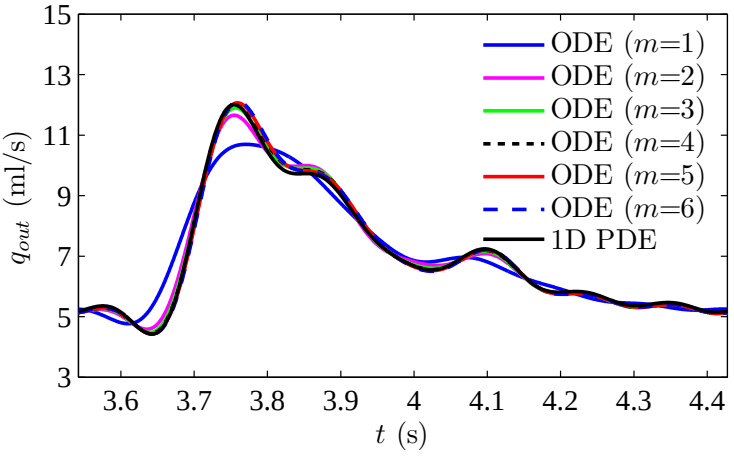

(a)

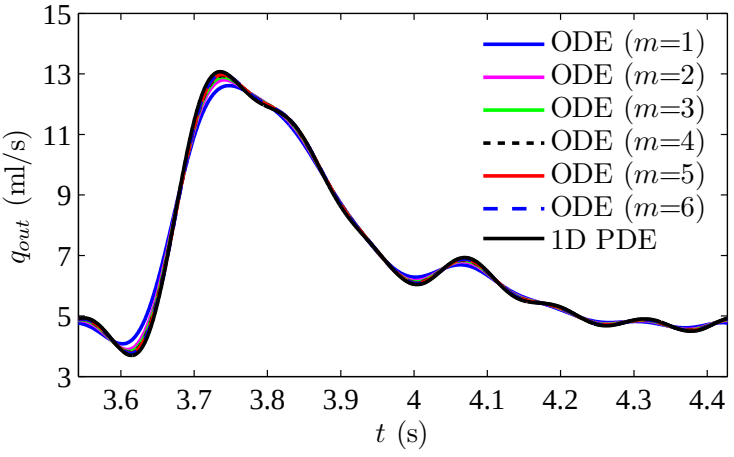

(b)

FIGURE 5.5: Comparison of the 1D PDE (40 elements) and 0D compartment model solutions (flow rate): (5.5a) blood vessel with E = 0.4 MPa and (5.5b) with higher Young's modulus of E = 1.6 MPa . m is the number of segments (compartments) in the compartment model.

5.2.3.2 Trade off between space accuracy and computational efficiency for the PDE model

We saw the interest of using the 0D model in term of computational efficiency. However, this implies that we need to maintain two simulation codes for the 0D and 1D models. As the ODE model seems to produce satisfactory results with very few compartments, a natural idea is to see if the same can be done with the PDE model on very coarse meshes. Hence, to avoid maintaining two codes, it would be nice to see if there is possibility to keep using the 1D PDE model but on coarser meshes than above. Figure 5.6 shows the comparison of flow rates histories at the outlet for two coarse meshes for the 1D PDE model versus the PDE model on the fine mesh and the ODE results for the blood vessel with E = 0.4 MPa. We see that the same flow rate histories are obtained with the 1D PDE model on the 3 and 40 elements meshes. This means that the PDE model is competitive in term of computational cost if coarse meshes can be used on each of the network segments and suggests that one should be able to maintain only one direct simulation code in the assimilation platform.

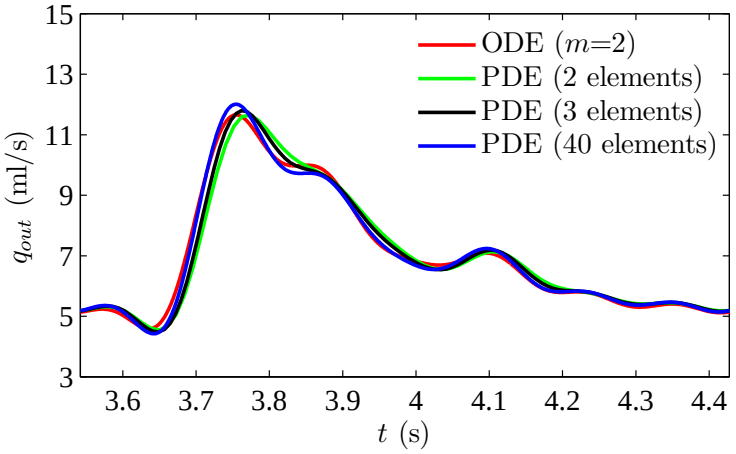

FIGURE 5.6: Comparison of flow rates histories at the outlet for coarse meshes (2 and 3 elements) for the 1D PDE model versus the PDE model on the fine mesh (40 elements) and the ODE results (m = 2) for the blood vessel with Young's modulus E = 0.4 MPa.

The same analysis applied to the circle of Willis shows that the 0D and 1D models give the same results for extremely coarse discretizations. Indeed, mesh independent results are achieved with only one compartment or one element in the PDE mesh. We recall that, as mentioned in the previous section, m = 1 is a safe choice when applied to an ensemble of short cerebral arteries with large Young's modulus.

5.2.4 Estimation of hemodynamic parameters using an Ensemble Kalman Filter

In Lal et al. [37], we have shown the use of a data assimilation technique using the Ensemble Kalman filter for the estimation of hemodynamic parameters using both synthetic and in vitro data. We refer the reader to Lal et al. [37] for a detailed mathematical analysis of EnKF and we summarise the algorithm used to estimate the hemodynamic model parameters in the following.

The EnKF is a suboptimal estimator for problems that involves nonlinear models of higher order, where an ensemble of states is used to predict the error statistics [37]. The unknown hemodynamic parameters, $\mathbf{x} \in \mathbb{R}^n$, are treated as special state variables whose evolutions at time $t = k + 1$ are defined using a random walk model [100]

$$\mathbf{x}_{k+1} = \mathbf{x}_k + \tau_k. \tag{5.6}$$

$\tau_k \sim \mathcal{N}(0, \mathbf{T}_k)$ is a small Gaussian random perturbation with a variance $\mathbf{T}$. The initial forecast ensemble of parameters $\mathbf{x}_k^{\mathrm{f}_i}$ for $i = 1, \ldots, q_{\text{ens}}$ are assumed to be available at $t = k$. f_i denotes the initial i^{th} forecast member of an ensemble of size q_{ens} which is used to determine the forecast error covariance matrix in EnKF. The parameter estimation algorithm uses a set of $nobs$ observations such as blood pressure, blood flow rates, flow velocity or arterial wall movements to improve a set of given initial estimate of the hemodynamic parameters, $\mathbf{x}$. $\mathbf{Y}_k = (\mathbf{y}_k^{f_1}, \ldots, \mathbf{y}_k^{f_{q_{\text{ens}}}}) \in \mathbb{R}^{q_{\text{ens}} \times nobs}$ is a set of output vector that is generated at time $t = k$. Each member, $\mathbf{y}_k^{f_i}$, is defined by $\mathbf{y}_k^{f_i} = \mathcal{H}(\mathbf{x}^{fi})$, where $\mathcal{H}$ is the nonlinear measurement function defined by the blood flow model describing the relation between measurements and parameters. An ensemble of perturbed observations, $\mathbf{y}_k^i$ (for $i = 1, \ldots, q_{\text{ens}}$) is generated by adding perturbations to the original observation vector $\mathbf{y}_k \in \mathbb{R}^{nobs}$:

$$\mathbf{y}_k^i = \mathbf{y}_k + \mathbf{e}_k^i, \quad i = 1, \ldots, q_{\text{ens}}, \tag{5.7}$$

where $\mathbf{e}_k^i \in \mathbb{R}^{nobs}$ is a random vector drawn from the zero mean Gaussian distribution with a specified variance. The discrepancies between perturbed observations and measurements are then used to update (assimilate) parameters using:

$$\mathbf{x}_k^{\mathrm{a}_i} = \mathbf{x}_k^{\mathrm{f}_i} + \mathbf{K}_k \left[\mathbf{y}_k^i - \mathbf{y}_k^{\mathrm{f}_i} \right], \quad i = 1, \ldots, q_{\text{ens}}, \tag{5.8}$$

where a_i represents the updated (assimilated) parameters and $\mathbf{K}_k$ is the Kalman gain matrix. The matrix $\mathbf{K}_k$ is defined by three error covariance matrices:

$$\mathbf{K}_k = \mathbf{P}^{\mathrm{f}}_{\mathbf{xy}_k} \left(\mathbf{P}^{\mathrm{f}}_{\mathbf{yy}_k} + \mathbf{R}_k \right)^{-1}. \tag{5.9}$$

$\mathbf{R}_k$ is the diagonal measurement error covariance matrix defined by

$$\mathbf{R_k} = \mathrm{diag}\left[\frac{1}{q_{\mathrm{ens}} - 1} \mathbf{E}\mathbf{E}^{\mathrm{T}} \right], \quad \mathbf{E} = \left[\mathbf{e}^1_k, \ldots, \mathbf{e}^{q_{\mathrm{ens}}}_k \right]. \tag{5.10}$$

The other two error covariance matrices are given by [37]

$$\mathbf{P}^{\mathrm{f}}_{\mathbf{xy}_k} = \frac{1}{q_{\mathrm{ens}} - 1} \sum_{i=1}^{q_{\mathrm{ens}}} \left[\mathbf{x}^{\mathrm{f}_i}_k - \overline{\mathbf{x}}^{\mathrm{f}}_k \right] \left[\mathbf{y}^{f_i}_k - \overline{\mathbf{y}}^{f}_k \right]^{\mathrm{T}}, \tag{5.11}$$

$$\mathbf{P}^{\mathrm{f}}_{\mathbf{yy}_k} = \frac{1}{q_{\mathrm{ens}} - 1} \sum_{i=1}^{q_{\mathrm{ens}}} \left[\mathbf{y}^{f_i}_k - \overline{\mathbf{y}}^{f}_k \right] \left[\mathbf{y}^{f_i}_k - \overline{\mathbf{y}}^{f}_k \right]^{\mathrm{T}} \tag{5.12}$$

where $\overline{\mathbf{x}}^{\mathrm{f}}_k = \frac{1}{q_{\mathrm{ens}}} \sum_{i=1}^{q_{\mathrm{ens}}} \mathbf{x}^{\mathrm{f}_i}_k$ and $\overline{\mathbf{y}}^{f}_k = \frac{1}{q_{\mathrm{ens}}} \sum_{i=1}^{q_{\mathrm{ens}}} \mathcal{H}\left(\mathbf{x}^{\mathrm{f}_i}_k \right)$. The ensemble updated parameters (5.8) at time $t = k$ is then cycled in time and the parameter estimation using the EnKF can be stopped upon reaching some finite convergence criterion. At convergence, the mean of the ensemble is taken as the best estimate of the parameters. The parameter estimation algorithm is summarised in Algorithm 1 [37]. Henceforth, *nobs* will refer to the number of locations on an arterial network where a time series of observations such as pressure values or blood flow rate is available.

Algorithm 1: Parameter estimation using EnKF [37]

Input: q_{ens}, maximum number of EnKF iteration (j_{max}), variance matrix $\mathbf{T}$, $nobs$, initial estimate of n unknown parameters (mean $\overline{x}_l$ and variance P_l for $l = 1, \ldots, n$).

Initialization: Randomly initialize an ensemble of parameters, $\mathbf{x}^i$, for $i = 1 \ldots, q_{\mathrm{ens}}$ where $\mathbf{x}^i = (x_1, x_2, \ldots, x_n)$ and $x_l \sim \mathcal{N}(\overline{x}_l, P_l)$ for $l = 1, \ldots, n$.

Let $\mathbf{x}^{\mathrm{a}_i} = \mathbf{x}^i$

for $j = 1$ ***to*** j_{max} **do**

- **-Evolution of ensemble:** $\mathbf{x}^{\mathrm{f}_i} = \mathbf{x}^{\mathrm{a}_i} + \tau^i$, $\tau^i \sim \mathcal{N}(0, \mathbf{T})$ $\forall i = 1, \ldots, q_{\mathrm{ens}}$
- **-Ensemble propagation:** $\mathbf{y}^{\mathrm{f}_i} = \mathcal{H}(\mathbf{x}^{\mathrm{f}_i})$ $\forall i = 1, \ldots, q_{\mathrm{ens}}$
- **-Perturbation of observations for each ensemble:** $\mathbf{y}^i = \mathbf{y} + \mathbf{e}^i$, $\forall i = 1, \ldots, q_{\mathrm{ens}}$
- **-Determine R and K using Eqs. (5.10) and (5.9) respectively.**
- **-Ensemble update:** $\mathbf{x}^{\mathrm{a}_i} = \mathbf{x}^{\mathrm{f}_i} + \mathbf{K}\left[\mathbf{y}^i - \mathbf{y}^{\mathrm{f}_i} \right]$ $\forall i = 1, \ldots, q_{\mathrm{ens}}$.

5.2.5 Test Cases with synthetic and patient specific data

We test the efficiency of the parameter estimation technique using the EnKF with test cases involving both synthetic and patient specific data. The synthetic cases are to illustrate the procedure on situations where the solution is known. They also permit to see the impact on the assimilation of a degradation of the flow modelling from 1D to 0D in forward simulations. A simple arterial network consisting of 9 arteries and a more complex network with 33 arteries are used in the blood flow models. The complex network of arteries consists of the circle of Willis. The objective is to identify (estimate) a set of model parameters within the physiological range, given measured values of arterial blood flow rate or blood pressure. The model parameters are limited to material properties (Young's modulus) and the terminal parameters (Windkessel parameters). The other parameters, such as geometrical, are either measured (in patient specific) or assumed known or, in the case of missing data (patient specific case), taken from the literature.

5.2.5.1 Case 1: Simple arterial network with synthetic data

In the first case, we consider the in vitro model of a simple human arterial network described in Saito et al. [13]. Figure 5.7 shows a network of vessels consisting of 9 arteries. At the inlet (vessel #1) we impose a periodic flow rate, $q_{in}(t)$, with period of 0.8 s as shown in the Figure 5.7. The terminal vessels are coupled with 0D Windkessel WK3 model. For sake of simplicity, outlet boundaries i, ii and iii are modeled with the same WK3 parameters: R_{P1} = 0.53$\times 10^9$ Pa·s·m^{-3}, R_{D1} = 4.75$\times 10^9$ Pa·s·m^{-3} and C_1 = 0.53$\times 10^{-10}$ m^3·Pa^{-1}; while outlets iv and v are coupled with: R_{P2} = 0.48$\times 10^9$ Pa·s·m^{-3}, R_{D2} = 4.3$\times 10^9$ Pa·s·m^{-3} and C_2 = 0.58$\times 10^{-10}$ m^3·Pa^{-1}. The geometrical data of the arterial network is shown in Table 5.1. The Young's modulus of all vessels is assigned a value of 0.4 MPa. Blood rheological parameters for the test case are taken as: ρ = 1050 kg/m^3 and μ = 0.004 Pa·s. The nonlinearity coefficient (ϵ_p) and the viscoelastic coefficient (η) are both set to zero. With these parameters, a forward simulation is executed using the 1D blood flow model. The pressure values from two different locations: in the centre of the left carotid artery (vessel #4) and in the centre of the right femoral artery (vessel #8) are recorded.

The inverse hemodynamic problem is set-up as follows: Starting from an initial guess, the Windkessel boundary parameters are estimated using the pressure values as

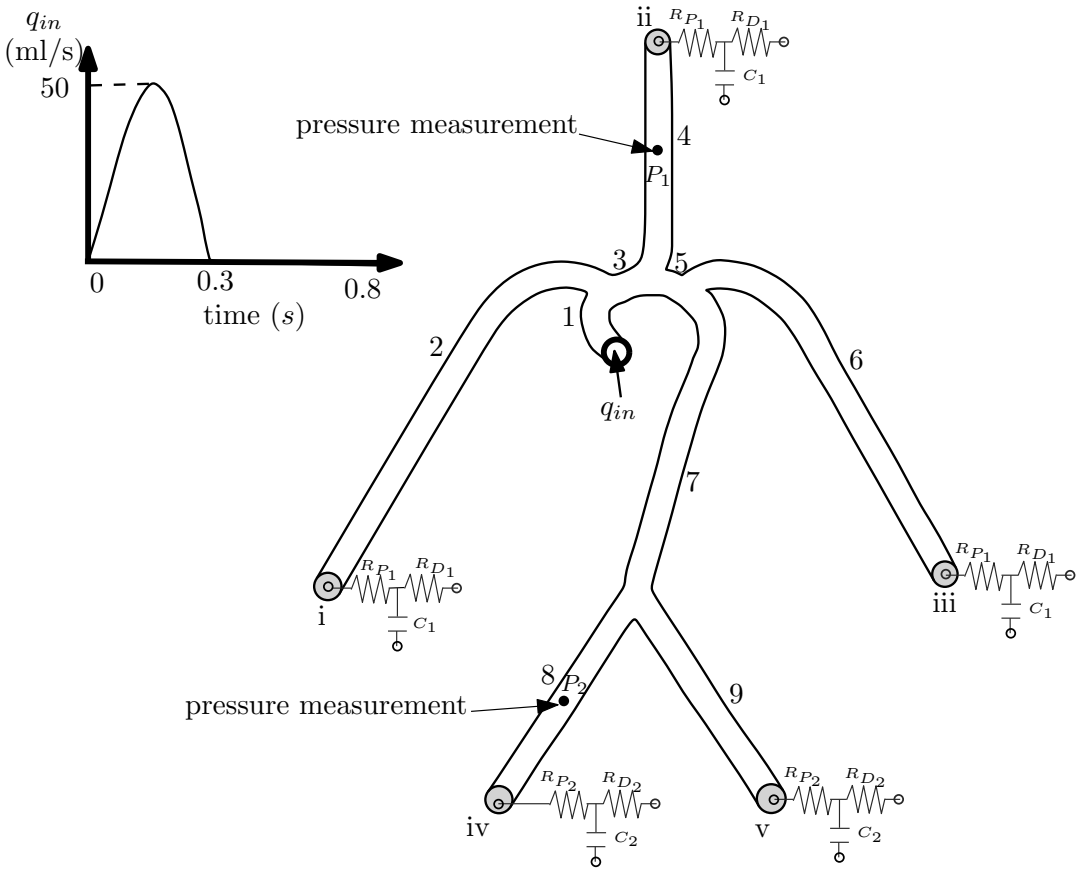

FIGURE 5.7: A simple human arterial network consisting of 9 arteries [13]. Artery numbers correspond to those in Table 5.1. The terminal arteries are coupled with a WK3 model. The pressure values in the centre of vessel #4 (P_1) and in the centre of vessel #8 (P_2) are used as observations.

TABLE 5.1: Geometric, Young's modulus and Windkessel terminal parameters corresponding to arterial segments in Figure 5.7. Length (l), radius (r), and the thickness (h) come from the model in Saito et al. [13].

id	Name	l (cm)	r (cm)	h (mm)	E (MPa)	R_P ($\times 10^9$ Pa·s·m^{-3})	R_D ($\times 10^9$ Pa·s·m^{-3})	C ($\times 10^{-10}$ m^{3}Pa^{-1})
1	Aorta arch A	3.50	0.6	2	0.4	-	-	-
2	R.subclavian radial artery	80.0	0.3	1.5	0.4	0.53	4.75	0.53
3	Aorta arch B	2.0	0.55	2	0.4	-	-	-
4	L.carotid artery	67.5	0.3	1.5	0.4	0.53	4.75	0.53
5	Aorta arch C	4.0	0.5	2	0.4	-	-	-
6	L.Subclavian radial artery	71.0	0.3	1.5	0.4	0.53	4.75	0.53
7	Aorta	47.0	0.4	1.5	0.4	-	-	-
8	R.femoral artery	36.5	0.3	1.5	0.4	0.48	4.30	0.58
9	L.femoral artery	36.5	0.3	1.5	0.4	0.48	4.30	0.58

observations in the data assimilation technique using EnKF. Since the pressure values are recorded in two locations, we denote the number of observations *nobs*=2. Henceforth, *nobs* will refer to the number of locations on an arterial network where a time series of observations such as pressure values or blood flow rate is available. All other geometrical and material properties are assumed to be known for this synthetic case. For the parameter estimation set-up, we seek an estimation of 6 parameters with an ensemble of size q_{ens} = 20. The initial guess of resistances (R_P and R_D) and compliances (C) assumes errors of 50% and 150% respectively (compared to the exact values used for the forward simulation mentioned above). To restrict the assimilated parameters to positive values, all parameters are redefined as $x = x_{\text{ref}}2^{\theta}$. x_{ref} is the reference or initial guess of the parameter to be estimated and θ is the actual value used in the EnKF during the assimilation step. In our ensemble simulations, θ for the ensemble members initialization follows $\mathcal{N}(0, 1)$. The measurement error covariance matrix is defined by Equation (5.10), where the observations (pressure values) are perturbed by a random vector that is drawn from a Gaussian distribution with zero mean and a standard deviation at 5% of the pressure values. The estimation algorithm using the EnKF coupled with the 1D blood flow model is executed for 20 s (corresponding to 25 cycles) with the assimilation taking place every 0.005 s. This means 4000 EnKF iterations, or 160 per cardiac cycle.

5.2.5.2 Case 2: Circle of Willis with synthetic data

The parameter estimation algorithm is tested using an arterial network (Figure 5.8) consisting of the aorta, brachial, carotid and vertebral arteries as well as a complete CoW which is adapted from Alastruey et al. [32]. A similar network of arteries has been studied in Mulder et al. [162]. The geometrical parameters (length, radius and thickness) and WK3 boundary parameters of 33 arteries in Figure 5.8 are also adapted from Alastruey et al. [32] and are shown in Table 5.2.

In Reymond et al. [14], an empirical formula relating arterial radius (in mm) and pulse wave velocity (PWV in ms^{-1}) has been derived as PWV=$\alpha/(2r)^{\beta}$, where α and β are 13.3 and 0.3 respectively. Using Moens-Korteweg formula for PWV, an expression for the product of E and h as a function of r can be derived and written as

$$Eh = \frac{0.001\rho\alpha^2}{(2r)^{(2\beta-1)}}. \tag{5.13}$$

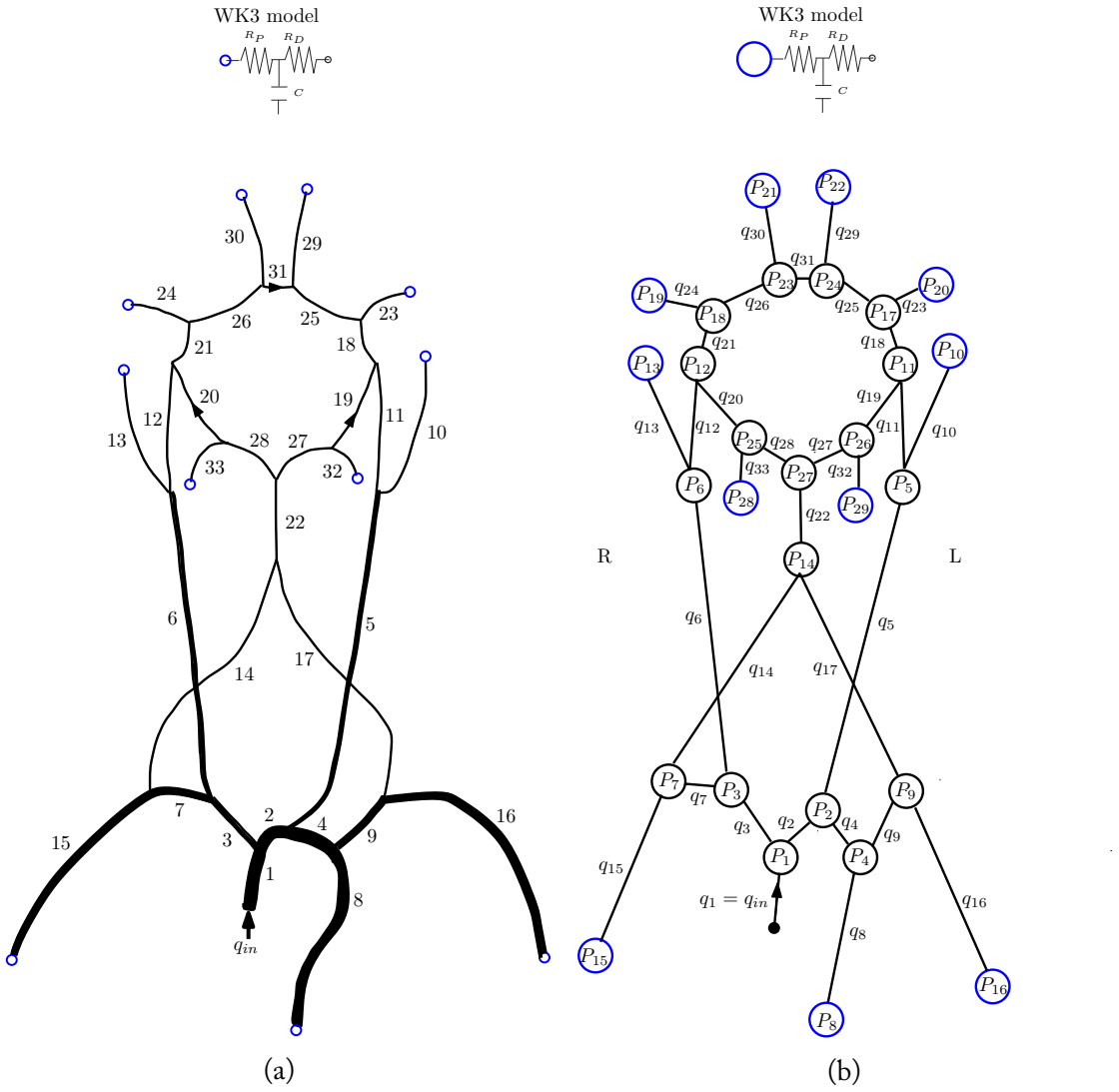

FIGURE 5.8: (5.8a) The network [32] of a one-dimensional blood flow model of the upper body arteries and of the circle of Willis. Artery numbers corresponds to those in Table 5.2. Arrows indicate the direction of flow. (5.8b) The equivalent 0D compartment model. Flow rates are assigned the compartment numbers corresponding to those in Table 5.2. The inlet flow rate, q_{in}, in the figures above is given by Equation (5.15). The terminal arteries and compartments are coupled with the WK3 model.

TABLE 5.2: Geometric and Windkessel terminal parameters corresponding to arterial segments (and compartments) in Figure 5.8 from Alastruey et al. [32]. The product Eh is calculated using $Eh = k_1 r + k_2$.

id	Name	l (cm)	r (cm)	Eh (Pa·m)	R_P ($\times 10^9$ Pa·s·m^{-3})	R_D ($\times 10^9$ Pa·s·m^{-3})	C ($\times 10^{-10}$ m^{3}Pa^{-1})
1	Ascending aorta	4.0	1.200	702.8	-	-	-
2	Aortic arch I	2.0	1.120	671.28	-	-	-
3	Brachiocephalic	3.4	0.620	474.28	-	-	-
4	Aortic arch II	3.9	1.070	651.58	-	-	-
5	Left common carotid	20.8	0.250	328.5	-	-	-
6	Right common carotid	17.7	0.250	328.5	-	-	-
7	Right subclavian	3.4	0.423	396.66	-	-	-
8	Thoracic aorta	15.6	0.999	623.61	0.02	0.16	38.70
9	Left subclavian	3.4	0.423	396.66	-	-	-
10	Left external carotid	17.7	0.150	289.1	1.67	3.76	1.27
11	Left internal carotid I	17.7	0.200	308.8	-	-	-
12	Right internal carotid I	17.7	0.200	308.8	-	-	-
13	Right external carotid	17.7	0.150	289.1	1.67	3.76	1.27
14	Right vertebral	14.8	0.136	283.58	-	-	-
15	Right brachial	42.2	0.403	388.78	0.13	2.53	2.58
16	Left brachial	42.2	0.403	388.78	0.13	2.53	2.58
17	Left vertebral	14.8	0.136	283.58	-	-	-
18	Left internal carotid II	0.5	0.200	308.8	-	-	-
19	Left post. comm. artery (PCoA)	1.5	0.073	258.76	-	-	-
20	Right post. comm. artery (PCoA)	1.5	0.073	258.76	-	-	-
21	Right internal carotid II	0.5	0.200	308.80	-	-	-
22	Basilar	2.9	0.162	293.83	-	-	-
23	Left middle cerebral artery (MCA)	11.9	0.143	286.34	2.605	3.365	1.16
24	Right middle cerebral artery (MCA)	11.9	0.143	286.34	2.605	3.365	1.16
25	Left anterior cerebral artery A1 (ACA, A1)	1.2	0.117	276.10	-	-	-
26	Right anterior cerebral artery A1 (ACA, A1)	1.2	0.117	276.10	-	-	-
27	Left post. cerebral artery P1 (PCA, P1)	0.5	0.107	272.16	-	-	-
28	Right post. cerebral artery P1 (PCA, P1)	0.5	0.107	272.16	-	-	-
29	Left anterior cerebral artery A2 (ACA, A2)	10.3	0.120	277.28	3.70	4.48	0.815
30	Right anterior cerebral artery A2 (ACA, A2)	10.3	0.120	277.28	3.70	4.48	0.815
31	Anterior comm. artery (ACoA)	0.3	0.074	259.16	-	-	-
32	Left post. cerebral artery P2 (PCA, P2)	8.6	0.105	271.37	4.83	6.25	0.62
33	Right post. cerebral artery P2 (PCA, P2)	8.6	0.105	271.37	4.83	6.25	0.62

Equation (5.13) is linearised to get an approximate relation

$$Eh = k_1 r + k_2 \tag{5.14}$$

using values of r from Alastruey et al. [32]. A least square fitting of the mentioned data by this linear model (see Figure 5.9) gives the constants k_1= 39.4 Pa and k_2= 2.3$\times 10^2$ Pa·m.

For this synthetic case, the Young's modulus, radius and thickness of the arteries are assumed to be related by the Equation (5.14) with the given constants k_1 and k_2. An inlet flow rate, q_{in} with period of 1 s, is imposed at the proximal end of ascending aorta.

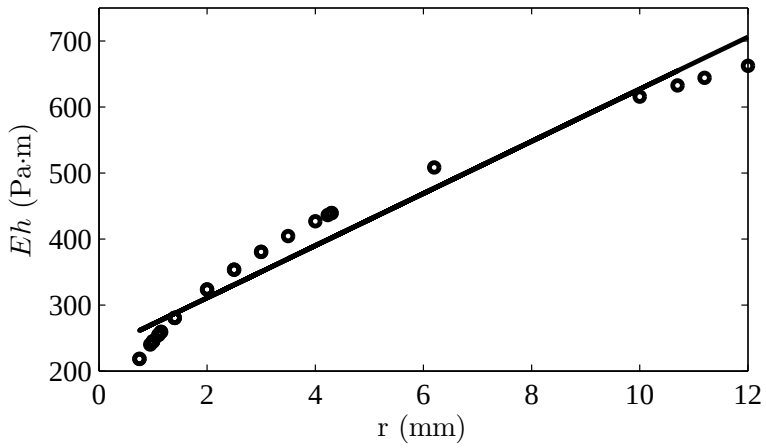

FIGURE 5.9: Eh versus r: least square fitting to get k_1 and k_2 in Equation 5.14.

For each cardiac cycle, q_{in} in ml/s is defined as [32]:

$$q_{in}(t) = \begin{cases} 485 \sin(\pi t/\tau) & \text{if } t < \tau, \\ 0 & \text{otherwise} \end{cases} \tag{5.15}$$

where τ = 0.3 s.

Two different scenarii are considered, namely, Case2PDE and Case2ODE.
For the first scenario (Case2PDE), a reference simulation using 1D blood flow code with known geometrical parameters, material properties (Young's modulus) together with the inlet flow rate (q_{in}) and WK3 boundary conditions is executed. Blood rheological parameters are as in case 1. The blood flow rates in the middle of common carotid arteries (artery #5 and #6 in the Figure 5.8a) and in the middle of external carotid arteries (artery #10 and #11 in the Figure 5.8a) are stored as synthetic observations. Using $nobs$ = 4, and using the 1D blood flow model for forward simulation during data assimilation, we estimate k_1 and k_2 assuming all other parameters are known. The initial guess for the parameters to be estimated are set as k_1= 19.7 Pa and k_2= 3.45$\times 10^2$ Pa·m. The EnKF parameters are set as follows: q_{ens} = 20, $\theta \sim \mathcal{N}(0, 0.25)$, the measurement error covariance matrix, **R**, is defined by Equation (5.10), where the observations (blood flow rates) are perturbed by a random vector that is drawn from a Gaussian distribution with zero mean and a standard deviation at 5% of the flow rate values, and the assimilation is taken at every 0.01 s (100 EnKF per cycle). A small variance is taken for the random walk model: $\tau_k \sim \mathcal{N}(0, 0.003)$. The parameter estimation algorithm is executed for 10 cardiac cycles.

In the second scenario (Case2ODE), the 0D compartment model (Section 5.2.2) for forward simulations during the EnKF data assimilation process is used. The idea is to test if parameters can be estimated using the 0D compartment model, using the observations that are synthetically generated by the 1D blood flow model. In this synthetic case, the effects of inertia are ignored in the compartment model. Each artery in Figure 5.8a is represented by 1 compartment. Figure 5.8b shows the equivalent network of 33 compartments where the terminal compartments are coupled with the 0D Windkessel WK3 model. Using the flow rate measurements q_5, q_6, q_{10} and q_{13} from the forward simulation of 0D compartment model during data assimilation, we estimate k_1 and k_2 using the same initial guesses as in scenario 1. The matrix $\mathbf{R}$ is defined as in scenario 1 with the uncertainty for the flow rate assumed to follow $\mathcal{N}(0, 0.01)$ which is typical of a 10% standard deviation in measurement devices for the flow rate. The EnKF parameters q, θ, τ_k and the assimilation frequency are as in scenario 1. The parameter estimation algorithm is executed for 10 cardiac cycles.

5.2.5.3 Case 3: Patient specific PC-MRA&MRI-based blood flow rates

The patient-specific data used in the current study has been acquired at the Department of Neuroradiology at the *Centre Hospitalier Regional Universitaire de Montpellier (CHRU), Montpellier, France.*

2D phase-contrast imaging is performed on a Siemens 3T Skyra MR Scanner. We consider the ascending aorta and the internal carotid arteries (right and left ICA's) for the analysis of blood flow rates. More precisely, 2D Fast cine PC-MRI pulse sequence (one 5mm slice perpendicular to the arteries) with retrospective peripheral gating, and 32 frames covering the entire cardiac cycle are acquired. The imaging parameters for ICA's are a velocity encoding sensitivity (Venc) of 80 $\mathrm{cm{\cdot}s^{-1}}$, a repetition time (TR) of 28.86 ms, an echo time (TE) of 8.79 ms, a flip angle of 15^o, and a voxel size of 0.53 mm$\times$0.53 mm$\times$5.0 mm.

Figure 5.10 shows one pair of the acquired images (magnitude and phase contrast image) for ICA's. For the flow rate analysis, the `Bio Flow Image` software (http://www.tidam.fr/) was employed. For each of the arteries, a region of interest (ROI) is segmented with its lumen size defined by thresholding.

For the ascending aorta, the imaging parameters are: Venc = 200 $\mathrm{cm{\cdot}s^{-1}}$, TR = 28.72 ms, TE = 8.79 ms, flip angle 15^o and a voxel size 0.57 mm$\times$0.57 mm$\times$5.0 mm.

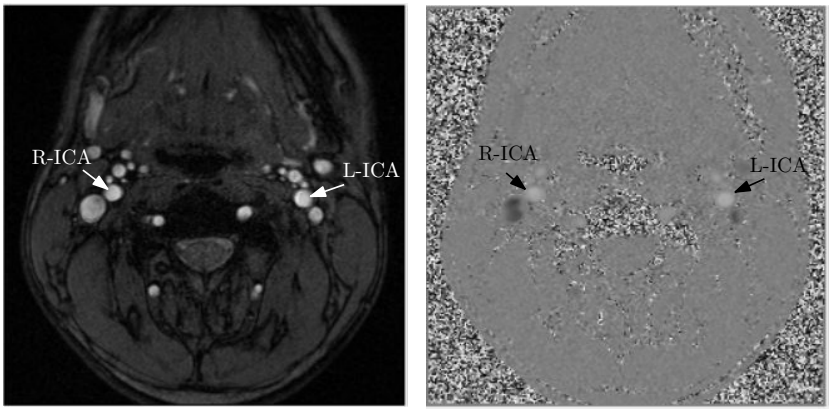

(a)

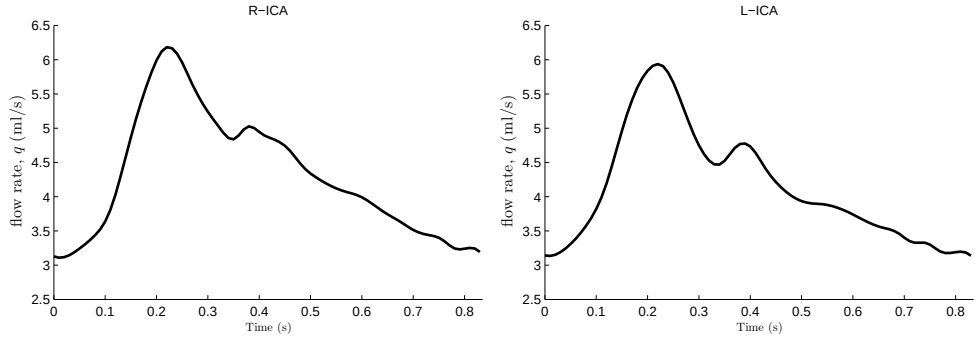

(b)

FIGURE 5.10: (5.10a) PC-MRI of the patient-specific internal carotid arteries (right and left) showing the blood flow through one of the selected slices. On the left is the magnitude image and in the centre is the phase contrast image with Venc setting of 80 $cm{\cdot}s^{-1}$. (5.10b) The instantaneous blood flow rate values, $q(t)$, are acquired at each time frame and is plotted against time for one cardiac cycle.

Figure 5.11 shows one pair of the magnitude and phase contrast image acquired for the ascending aorta. The corresponding blood flow rate is also shown in the same figure.

A 3D Time of Flight magnetic resonance angiography (3D-TOF-MRA) of the circle of Willis is obtained with the parameters: acquired voxel $0.31 \times 0.31 \times 0.55$ mm, 28 slices, TR=21.0 ms, TE=3.49 ms and flip angle of 28^o.

The 3D model (and morphology) of the circle of Willis (see Figure 5.12) is determined through segmentation of the TOF MRA using `RadiAnt DICOM Viewer` software (`http://www.radiantviewer.com/`). The geometric measurements of lengths and radius of CoW's blood vessel are measured from MRA using `RadiAnt DICOM Viewer` and are shown in Table 5.3. The carotid vascular tree could not be obtained because this acquisition requires the injection of contrast agent which is impossible to achieve

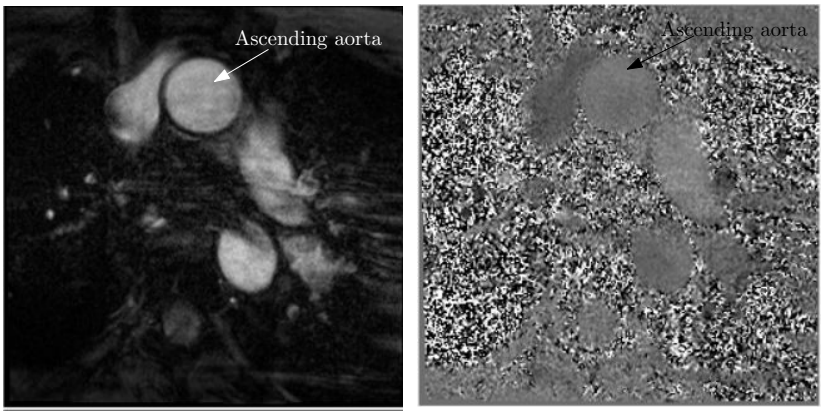

(a)

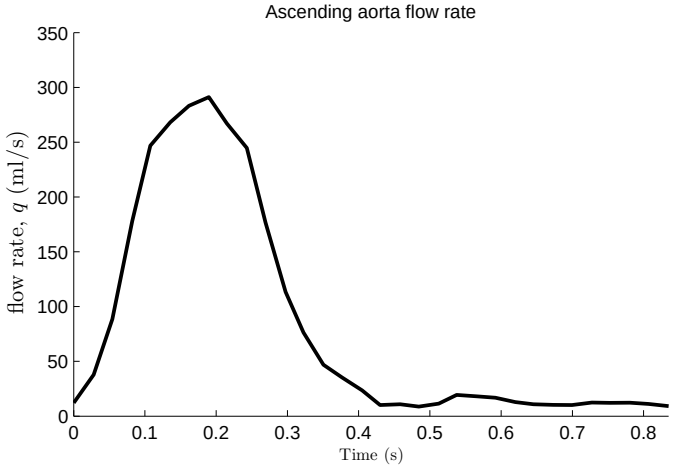

(b)

FIGURE 5.11: (5.11a) PC-MRI of the patient-specific ascending aorta showing the blood flow through one of the selected slices. On the left is the magnitude image and in the centre is the phase contrast image with Venc setting of 200 cm·s^{-1}. (5.11b) The instantaneous blood flow rate values, $q(t)$, are acquired at each time frame and is plotted against time for one cardiac cycle.

on healthy volunteers. The missing geometry of other arteries of the full network (Figure 5.8b) is obtained from average data reported in the literature [14, 32].

The inverse hemodynamic problem is set-up as follows: using data assimilation, we seek for arterial stiffness (Young's modulus) and WK3 model boundary parameters for the network as shown in Figure 5.8b. The acquired flow rate waveform for the right internal carotid (R-ICA) is used as observations during EnKF assimilation steps in the parameter estimation problem. The flow rate waveforms for the left internal carotid (L-ICA) is used in a posteriori validation process. For the forward simulation during the data assimilation the 0D compartment model is employed. At the inlet (ascending aorta, compartment #1), specific values of flow rates, q_{in}, is imposed as measured by PC-MRI

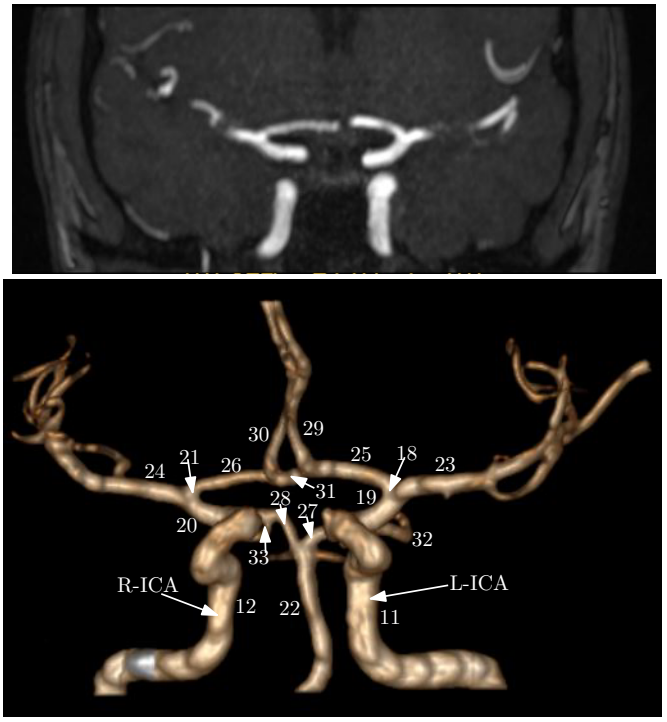

FIGURE 5.12: A TOF MRI scan (top) and the resulting segmented 3D model of the complete circle of Willis (bottom) for patient-specific case. The numbers on segmented model correspond to the ID's of the arterial segments in Table 5.3.

(see Figure 5.11). Blood rheological parameters are taken as: ρ = 1050 kg·m^{-3} and μ = 0.004 Pa·s. We perform two scenarii, namely ODE15 and ODE21, for parameter estimation as described below.

Scenario 1 (ODE15): For ODE15 the Young's modulus is assumed to be a function of radius given by an expression $E = k_1\, e^{k_2 r} + k_3$ [139], with unknown constants k_1, k_2 and k_3. We seek for an estimation of the above constants with initial guesses $k_1 = 2.0 \times 10^7$ g·cm^{-1}s^{-2}, $k_2 = -6.0$ cm^{-1} and $k_3 = 4.0 \times 10^6$ g·cm^{-1}s^{-2}. The thickness of larger arteries is adopted from Alastruey et al. [32] (see Table 5.2) and for all cerebral arteries, the thickness is assumed to be 25% of the mean radius [32]. The WK3 parameters (R_D and C) for the 11 terminal compartments in Figure 5.8b are estimated. The proximal resistance (R_P) is assumed to match the characteristic impedance (Z_c) of the terminal compartment [14, 32]:

$$R_P = Z_c = \frac{\rho c_0}{A_0} \quad \text{where} \quad c_0^2 = \frac{\sqrt{\pi} E h}{(1-\sigma^2)(2\rho A_0^{\frac{1}{2}})}. \tag{5.16}$$

Furthermore, we assume a same WK3 boundary parameters for left and right pairs of

TABLE 5.3: Geometric parameters corresponding to arterial segments (and compartments) in Figure 5.12 measured from MRI. The thickness h is taken as 25% of the measured radius. The missing geometry (marked with an astrix) of larger arteries is adopted from the average data in the literature [14, 32].

id	l (cm)	r (cm)	h (cm)	id	l (cm)	r (cm)	h (cm)
1	4.00*	1.200*	0.163*	18	0.50	0.200	0.050
2	2.00*	1.120*	0.126*	19	1.20	0.075	0.019
3	3.40*	0.620*	0.080*	20	1.20	0.075	0.019
4	3.90*	1.070*	0.115*	21	0.50	0.200	0.05
5	20.8*	0.250*	0.063*	22	2.70	0.150	0.038
6	17.7*	0.250*	0.063*	23	11.9	0.143	0.028
7	3.40*	0.423*	0.067*	24	11.9	0.143	0.028
8	15.6*	0.999*	0.110*	25	1.20	0.117	0.029
9	3.40*	0.423*	0.067*	26	1.20	0.117	0.029
10	17.7*	0.150*	0.038*	27	0.56	0.110	0.028
11	17.7*	0.200	0.050*	28	0.56	0.110	0.028
12	17.7*	0.200	0.050*	29	10.3	0.120	0.030
13	17.7*	0.150*	0.038*	30	10.3	0.120	0.030
14	14.8*	0.136*	0.034*	31	0.30	0.074	0.019
15	42.2*	0.403*	0.067*	32	8.50	0.100	0.025
16	42.2*	0.403*	0.067*	33	8.50	0.100	0.025
17	14.8*	0.136*	0.034*				

terminal compartments. For instance, the terminal compartments #10 and #13 are assigned with the same WK3 boundary parameters. Thus, 15 parameters consisting of 6 distal resistances, 6 compliances and 3 constants defining Young's modulus are estimated. The initial estimates for compliances are taken from Alastruey et al. [32]. The initial guesses for R_D are chosen such that the ratio $R_P/(R_P + R_D) = 0.2$ [109], i.e $R_D = 4R_P$.

Using $nobs$ = 1 and the 0D compartment for forward simulation during data assimilation, 15 unknown parameters are estimated. In ODE15, the inertial effect is neglected and the flow rate is defined by $q_{in} = (P_{in} - P_{out})/R$ in the compartment model. The EnKF parameters are set as follows: q_{ens} = 30, $\theta \sim \mathcal{N}(0, 0.25)$, the measurement error covariance matrix, **R**, is defined by Equation (5.10), where the observations (blood flow rates) are perturbed by a random vector that is drawn from a Gaussian distribution with zero mean and a standard deviation at 10% of the flow rate values of the R-ICA, and the assimilation time interval is 0.0835 s. A small variance is taken for the random walk model: $\tau_k \sim \mathcal{N}(0, 0.001)$. The parameter estimation algorithm is executed for 60 s (approximately 72 cardiac cycles).

Scenario 2 (ODE21): For ODE21 the product of Young's modulus and thickness of arteries is assumed to be given by an empirical formula $Eh = r(k_1\, e^{k_2 r} + k_3)$ [168]. Unlike as in ODE15 where we estimated E, here we find an estimation of the product Eh by seeking an estimation of the unknown constants with their initial guesses as $k_1 = 2.0 \times 10^7\,\mathrm{g{\cdot}cm^{-1}s^{-2}}$, $k_2 = -22.0\,\mathrm{cm^{-1}}$ and $k_3 = 8.0 \times 10^5\ \mathrm{g{\cdot}cm^{-1}s^{-2}}$. The same assumption on WK3 boundary parameters for left and right pairs of terminal compartments as in ODE15 is taken here. In ODE21, we also estimate the proximal resistance R_P. Thus, a total of 21 parameters consisting of 6 proximal resistances, 6 distal resistances, 6 compliances and 3 constants defining the product Eh are estimated. The initial estimates for proximal resistances and compliances are taken from Alastruey et al. [32]. As in ODE15, the initial guesses for R_D are chosen such $R_D = 4R_P$. For arteries with $r < 0.2\,\mathrm{cm}$, the inertial effect is ignored [169] in the compartment model during the forward simulation. The assimilation time interval is 0.04175 s (20 EnKF iterations per cardiac cycle) and the rest of the EnKF parameters are as in the ODE15 case.

Table 5.4 provides a summary of the cases with different scenarii considered in this section.

TABLE 5.4: The summary of parameter estimation for the three test cases.

Case	Scenario	Number of segments	Number of uncertain parameter	*nobs* and type of observations	Type of data used in data assimilation	Type of model
1	-	9	6	*nobs* = 2, Pressure	Synthetic	1D blood flow
2	Case2PDE	33	2	*nobs* = 4, Flow rate	Synthetic	1D blood flow
2	Case2ODE	33	2	*nobs* = 4, Flow rate	Synthetic	0D compartment
3	ODE15	33	15	*nobs* = 1, Flow rate	Actual clinical data	0D compartment
3	ODE21	33	21	*nobs* = 1, Flow rate	Actual clinical data	0D compartment

5.3 Results

In this section, we investigate the efficiency and the accuracy of the parameter estimation algorithm using EnKF. The numerical analysis is performed for the three cases described in Section 5.2.5 and summarized in Table 5.4.

5.3.1 Case 1

Figure (5.13a - 5.13c) shows the evolution of the six estimated WK3 parameters with their associated uncertainties defined by the standard deviation. The target parameter values have been used to generate synthetic observations for data assimilation. The initial and final estimates (with associated uncertainties) of the parameters are shown in Table 5.5. The estimated values converge to the target with small errors (3% deviation from the target values). In Figure 5.13d, we compare the pressure in the carotid artery. The estimated pressure profile (obtained using estimated parameters) is similar with an error of less that 0.15% in the systolic pressure compared to the target one.

TABLE 5.5: Case 1: Estimated parameters with their corresponding uncertainties and percentage deviations from target values. The resistances are in ($\times 10^9$ Pa·s·m^{-3}) and the compliances are in ($\times 10^{-10}$ m^3·Pa^{-1})

Parameter	Target	Initial guess	Final EnKF estimate ($\pm$ standard deviation)	% deviation from target
R_{P1}	0.53	0.265	0.545$\pm$0.008	2.83
R_{P2}	0.48	0.240	0.496$\pm$0.016	3.33
R_{D1}	4.75	2.375	4.630$\pm$0.125	-2.53
R_{D2}	4.30	2.150	4.420$\pm$0.150	2.79
C_1	0.53	0.795	0.535$\pm$ 0.007	0.94
C_2	0.58	0.870	0.595$\pm$ 0.010	2.59

5.3.2 Case 2

The evolutions of estimated parameters using both the 1D and 0D compartment (Equation (5.5)) models are shown in Figure 5.14. The results are summarised in Table 5.6. The estimated values deviated between -2.5% to 4% from the target values. Even though the target flow rate is synthetically generated by the 1D blood flow model, the compartment model is able to retrieve them within approximately 5% errors.

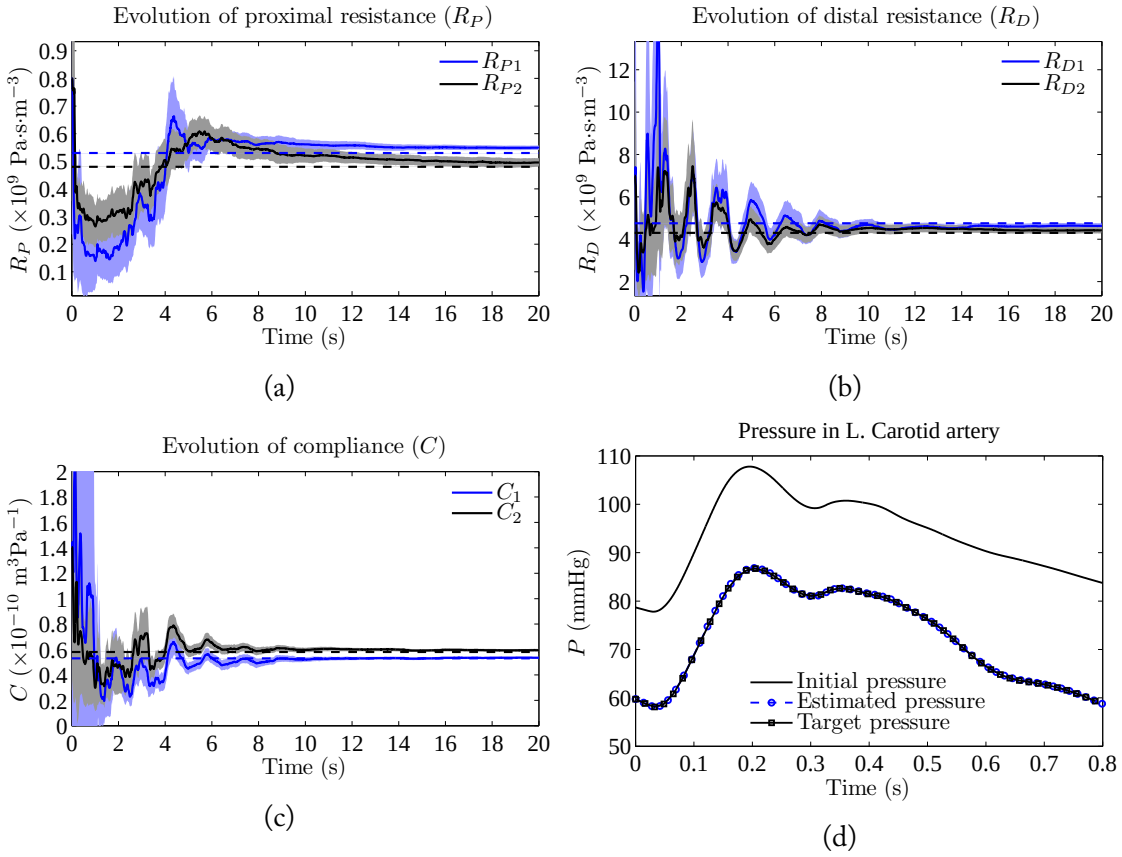

FIGURE 5.13: Estimated parameters and pressure solution for case 1. (5.13a - 5.13c) shows the evolution of WK3 parameters (proximal and distal resistances and the compliance). The dotted lines represent the target value of the parameters being estimated. The shaded areas represent the standard deviation around the mean values (solid lines). (5.13d) shows the comparison between the pressure solutions (in the left carotid artery) obtained with the initial estimate of parameters, the final estimated pressure solution, and the target pressure curve.

Both parameter estimations converge after approximately 10 s of observation (about 10 cycles). Using the compartment model, however, the computational time is approximately 60 times shorter.

TABLE 5.6: (Case2PDE and Case2ODE): Estimated parameters (k_1 and k_2) using two blood flow models with their corresponding uncertainties and percentage deviations from target values.

Parameter	Target	Initial guess	Final EnKF estimate		% deviation from target	
			Case2PDE	Case2ODE	Case2PDE	Case2ODE
k_1 (Pa·m)	39.4	19.70	40.2±0.4	37.3±0.5	1.93	-5.25
k_2 ($\times 10^2$ Pa)	2.30	3.45	2.39±0.03	2.37±0.04	3.91	3.04

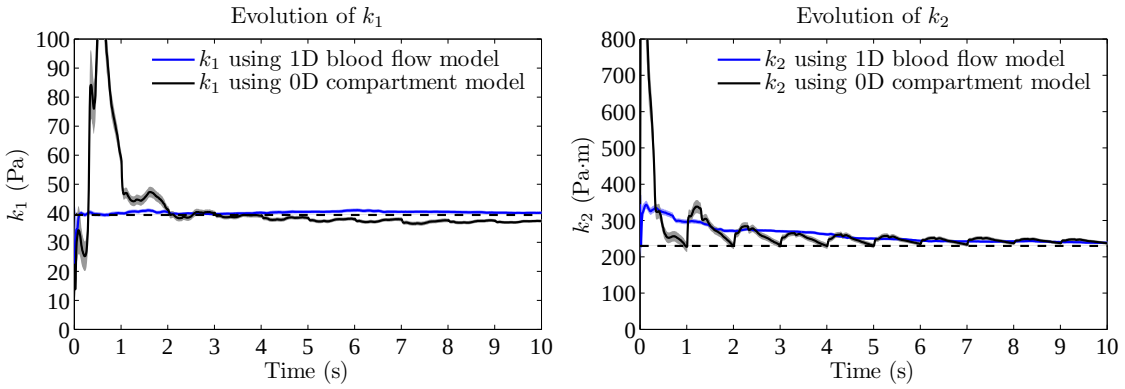

(a) (b)

FIGURE 5.14: Evolution of estimated parameters for case 2 using the 1D (Case2PDE) and compartment (Case2ODE) blood flow models. (5.14a) shows the evolution of k_1 and (5.14b) shows the evolution of k_2. The dotted lines represent the target values of k_1 = 39.4 Pa and k_2 = 2.3×10^2 Pa·m. The shaded areas represent the standard deviation around the mean values (solid lines).

Figure 5.15a shows the comparison of solutions (blood flow rate in the left common carotid artery) with estimated parameters using the 1D and the compartment blood flow models. For comparison, the 1D blood flow model is also simulated with the parameters that are estimated using the compartment model during EnKF iterations. Except with the compartment model alone, the curves show similar waveforms. The waveform produced by the simulated 1D blood flow model with parameters that are estimated using the compartment model shows a good match with the target waveform. However, with the compartment model, the peak flow rate is approximately 5.8% higher than the target peak flow rate. This can be explained by the fact that two blood flow models are completely different and there is 5.25% difference in the estimated value of k_1. Also, we notice that with the compartment model, the second peak (dicrotic notch) is not present in the flow rate waveform. This is probably due to the absence of inertial effects in the compartment model.

In Figure 5.15b the pressure waveform simulated using the two models are shown for the left common carotid artery. The waveforms are compared with the pressure curve produced using the 1D blood flow model simulated with the target parameters. Again, we notice that the waveforms are similar except for the one simulated using the compartment model. With the compartment model, the systolic pressure is approximately 1% higher compared with synthetically generated pressure curve. Similarly, the diastolic pressure is 7.8% lower and the dicrotic notch is not visible in

the pressure waveform. Still, it is remarkable that the overall pressure variation over the cardiac cycle is well retrieved (within a few percents) when using the 0D model.

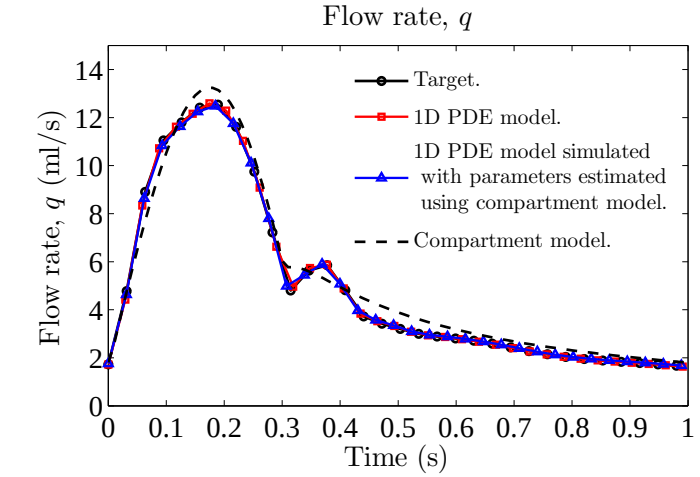

(a)

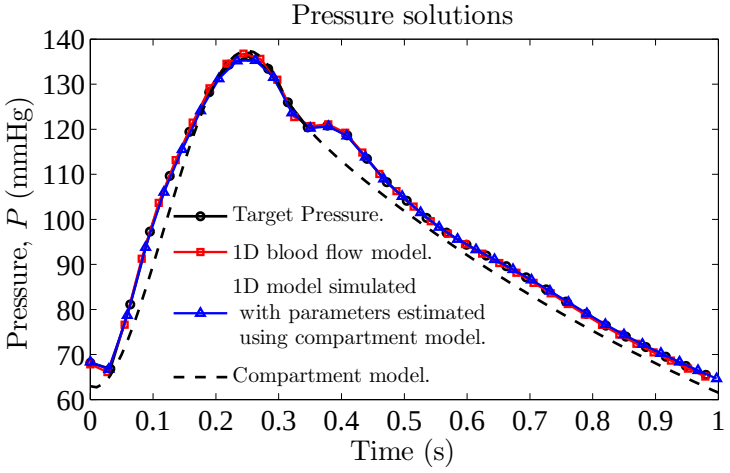

(b)

FIGURE 5.15: Flow rate and pressure waveform comparison in the left common carotid artery for Case 2 (scenarii Case2PDE and Case2ODE). (5.15a) shows the flow rate comparisons with the target flow rate (solid black line). The other three waveforms are obtained from the 1D blood flow model (in red), the 1D blood model with the parameters estimated using the compartment model (in blue) and the compartment model (dotted black line). (5.15b) shows the corresponding pressure waveforms from the two blood flow models.

5.3.3 Case 3

The evolutions of the parameters with two scenarii (ODE15 and ODE21) are shown in Figure 5.16. In both scenarii, the EnKF algorithm is able to reach convergence in 60 s

(EnKF iteration time), corresponding to approximately 72 cardiac cycles. The initial and final estimated values of the parameters with their associated uncertainties using the two scenarii are shown in Table 5.7.

TABLE 5.7: Case 3: Estimated parameters (with associated errors) for the patient specific fitting using ODE15 and ODE21. The values of constants k_1, k_2, and k_3 are in $\times 10^7$ g·cm^{-1}s^{-2}, cm^{-1}, and $\times 10^6$ g·cm^{-1}s^{-2} respectively. The proximal (R_P) and distal (R_D) resistances are in $\times 10^9$ Pa·s·m^{-3} and the compliance (C) are in $\times 10^{-10}$ m^{3}Pa^{-1}. In the forward simulation with ODE15, the values of R_P are calculated using Equation (5.16).

Parameter	Initial guess (ODE15, ODE21)	Final EnKF estimate ± error ODE15	ODE21
k_1	2.00, 2.00	1.93 ± 0.33	4.99 ± 0.36
k_2	-6.00, -22.0	-3.86 ± 0.44	-8.47 ± 0.32
k_3	4.00, 0.85	2.98 ± 0.29	0.66 ± 0.02
R_{P8}	-, 0.02	-	0.031 ± 0.002
R_{P13}	-, 1.67	-	0.62 ± 0.05
R_{P15}	-, 0.13	-	0.15 ± 0.01
R_{P24}	-, 2.61	-	3.71 ± 0.26
R_{P30}	-, 3.70	-	1.23 ± 0.07
R_{P33}	-, 4.83	-	2.04 ± 0.22
R_{D8}	0.23, 0.08	2.16 ± 0.25	0.46 ± 0.04
R_{D13}	21.23, 6.68	22.37 ± 5.57	10.44 ± 1.40
R_{D15}	2.03, 0.52	1.65 ± 0.20	0.71 ±0.09
R_{D24}	25.82, 10.44	3.45 ± 0.77	20.42 ± 2.13
R_{D30}	39.57, 14.80	11.50 ± 1.89	2.33 ± 0.33
R_{D33}	6.52, 19.32	4.42 ± 0.76	1.70 ± 0.15
C_8	38.78, 38.78	18.74 ± 3.09	31.90 ± 2.47
C_{13}	1.27, 1.27	0.43 ± 0.27	1.73 ± 0.36
C_{15}	2.58, 2.58	4.73 ± 1.30	2.00 ± 0.18
C_{24}	1.16, 1.16	0.65 ± 0.09	0.04 ± 0.004
C_{30}	0.82, 0.82	0.26 ± 0.05	0.49 ± 0.03
C_{33}	0.62, 0.62	1.38 ± 0.27	0.37 ± 0.04

The comparison between the observation (blood flow rate measurement in the right ICA from MRI data) and blood flow model simulations (based on assimilated parameters) using the estimated parameters are displayed in Figure 5.17a. Four flow rate waveforms are compared with the target waveform obtained from the PC-MRI analysis. (ODE15) using ODE15 as the forward simulator with the estimated parameters from scenario 1, (ODE21) using ODE21 as the forward simulator with the estimated parameters from scenario 2, (PDE15) using 1D blood flow model as the

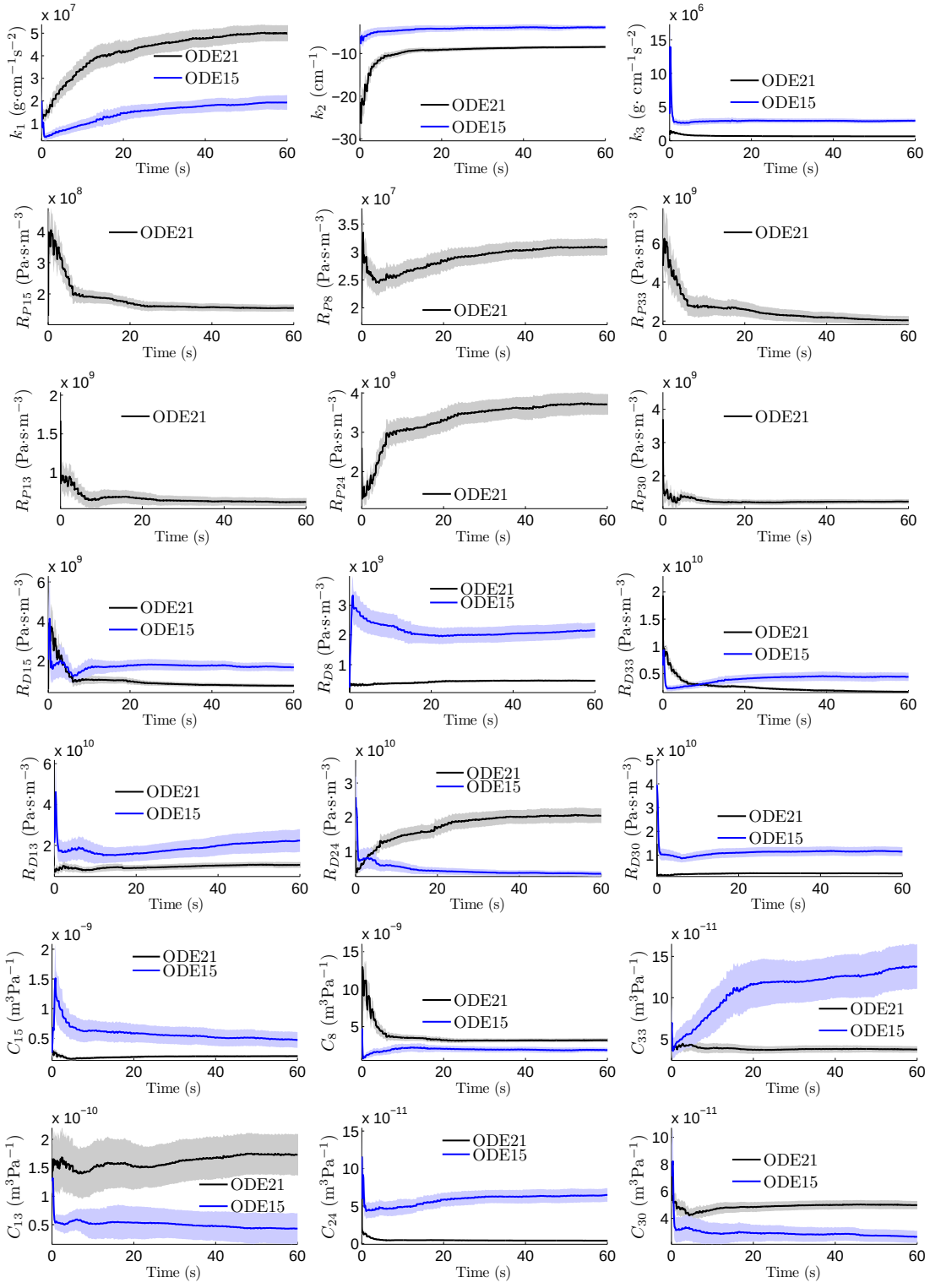

FIGURE 5.16: Case 3: The patient-specific fitting. Time evolution of estimated parameters using ODE15 and ODE21. The shaded areas represent the standard deviation around the ensemble mean values (solid lines).

forward simulator with the estimated parameters from scenario 1 and (PDE21) using 1D blood flow model as the forward simulator with the estimated parameters from scenario 2. For ODE15 and ODE21, the waveforms are plotted with their associated errors (shaded areas in the figure denoting standard deviation computed from the ensemble statistics). The secondary peak is not visible in the flow rate waveform for the ODE15 assimilation. With (ii-iv), slight secondary peaks are observed. The best results is with the ODE21 assimilation. We recall that ODE21 includes inertial effects for arteries with $r \geq 0.2\,\text{cm}$. Additionally, ODE21 reveals a good agreement between the simulated and the target blood flow rate waveform. The diastolic values has smaller errors (less than 5%) compared to systolic values. The difference between measured and the simulated systolic flow rate reaches 12%. This maximum difference is observed with PDE15. With ODE21, there is an error of -1.5% in the simulated systolic flow rate.

Figure 5.17b shows the analysis of the blood flow in the left ICA. Since this flow rate signal was not used as observation during data assimilation, we use it for a posteriori validation purposes. Similar waveforms than for the right ICA are obtained. ODE21 provides the best fit for L-ICA. As before, the diastolic values has smaller errors (less than 5%), with a maximum relative difference between the measured and simulated systolic value of 13.5% for PDE15. With ODE21, there is an error of -3.4% in simulated systolic flow rate.

In Figure 5.18, the simulated pressure waveforms in the two ICA's are shown using ODE15, ODE21, PDE15 and PDE21. For left and right ICA's, similar waveforms are observed. The estimated pressure (including diastolic and systolic) with ODE21 and PDE21 are lower compared to the pressure estimated using ODE15 and PDE15. It is also noted that pressure estimated using a 1D blood flow model (PDE) is within the range of pressure uncertainties estimated using ODE. These uncertainties are shown by the shaded areas (denoting standard deviation) around the mean pressure values in Figures 5.18a and 5.18b.

5.4 Sensitivity analysis

A parameter estimation sensitivity analysis is performed using two more scenarii for the patient-specific case (case 3). We are interested by the relative sensitivity of the estimated

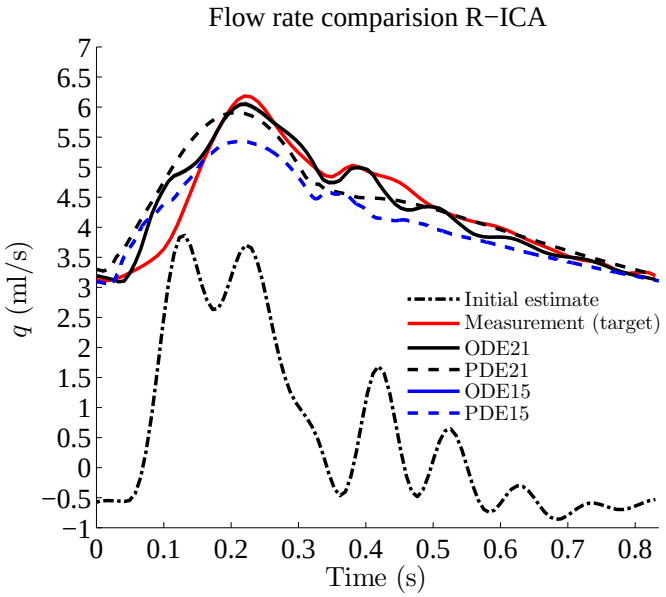

(a)

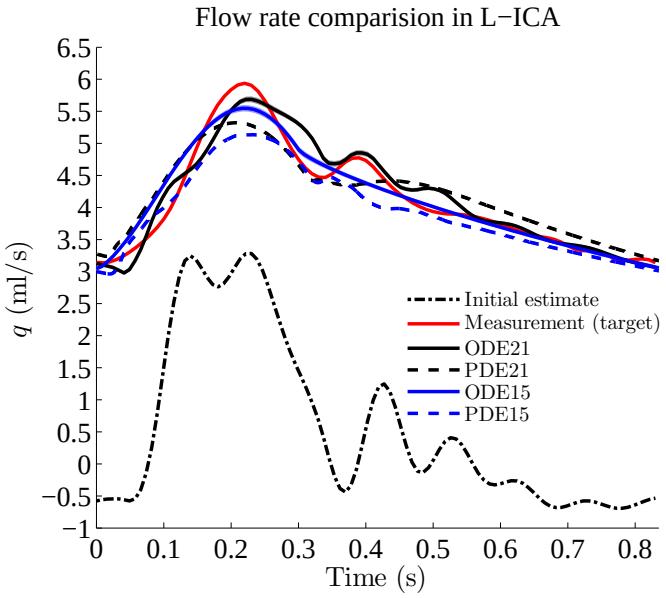

(b)

FIGURE 5.17: (5.17a) Comparison between the blood flow rate measurement in the right ICA from MRI data (red) and blood flow model simulations (patient specific-fitting). ODE15 indicates the forward simulator with the estimated parameters from scenario 1 and ODE21 with the parameters from scenario 2. PDE15 indicates the results with the 1D blood flow model as forward simulator with the estimated parameters from scenario 1 and PDE21 with the parameters from scenario 2. The flow rate signal obtained with initially guessed parameters are also shown in dash-dot lines. The shaded areas represent the standard deviation around the ensemble mean values for ODE15 and ODE21. (5.17b) shows the corresponding a posteriori analysis of the blood flow in the left ICA.

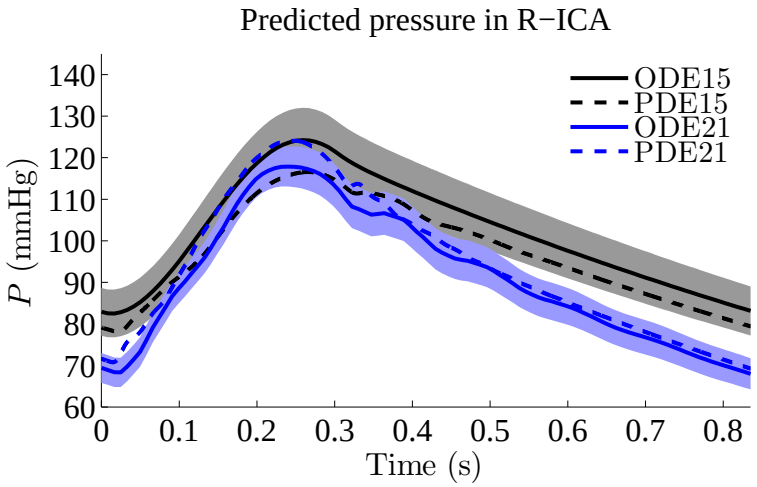

(a)

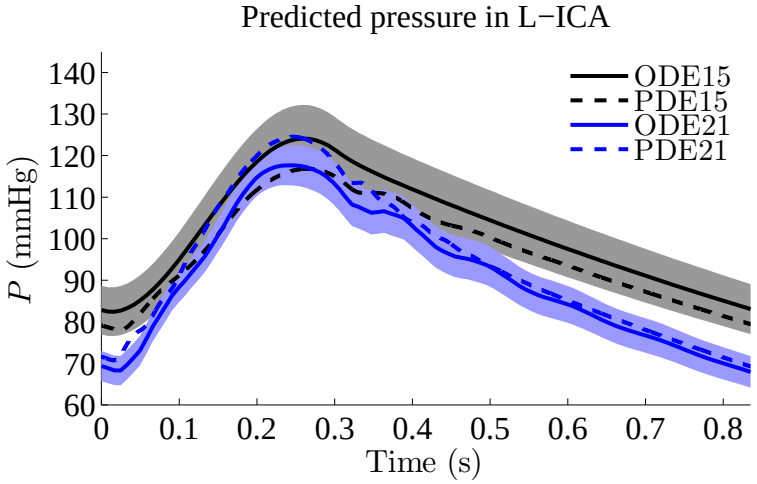

(b)

FIGURE 5.18: The model simulated pressure waveforms in the right (5.18a) and left ICA's (5.18b) using ODE15, ODE21, PDE15, and PDE21. The uncertainties are shown by shaded areas (denoting standard deviation) around the mean pressure values with ODE15 and ODE21.

parameters with respect to the observation location and their numbers $nobs$.

We recall that the previous scenario (in section 5.2.5.3), ODE21, uses $nobs = 1$ and estimates 21 parameters using the flow rate waveform for the R-ICA as observations. To see the impact of a change in the target observations, we consider the acquired flow rate waveform for the left internal carotid (L-ICA) as target during EnKF assimilation steps while the a posteriori validation process considers the flow rate waveforms in the right internal carotid (R-ICA). We call this scenario ODE21L.

Also, to see the impact of a change in the number of observations, we consider both available observations as target which means $nobs = 2$. This is called scenario ODE21RL. This is the best one can expect as all the available information is now mobilized.

All other parameters and settings are same as for the scenario ODE21. The initial estimates of the 21 unknown parameters are also same as in ODE21, and the ENKF parameter estimation is executed for 60 s (about 72 cardiac cycles).

Figure 5.19 shows the time evolution of estimated parameters with changes in the observation location and $nobs$ (scenarii ODE21L and ODE21RL, respectively). The results are also compared with ODE21 in the same figure. With all scenarii, the filter converged in about 72 cardiac cycles and the estimated parameters converged to different values for the three scenarii. The final estimates of the 21 parameters with their associated uncertainties using the three scenarii (ODE21, ODE21L, and ODE21RL) are summarised in Table 5.8.

Figure 5.20 shows the comparison between the observed (clinically measured blood flow rates using MRI) and blood flow model simulations (predictions) based on 21 estimated parameters using the three scenarii, i.e. ODE21, ODE21L, and ODE21RL. From the results, the comparison between the assimilated 0D model and in vivo data (MRI) is fair. It is observed that secondary peaks in the flow rate waveforms are reproduced in the model. Also, the 0D compartment blood flow model and the EnKF parameter estimation algorithm are seen to be compatible with $nobs$ of more than 1.

Table 5.9 summarizes the cardiac cycle-averaged (mean) and maximum (peak) volumetric flow rates measured in the ICA's using MRI and simulated values using the model with estimated parameters. All mean, peak (systolic), and diastolic flow rates measurements and model outputs (for all scenarii) differ by less than 6%. Additionally, the mean and peak values are compared with and found to be within the reported range in Ford et al. [170]. Furthermore, it is observed that errors (see Table 5.9) in peak and mean values of the blood flow rate in the ICA's are least with the scenario ODE21RL when compared with the MRI data.

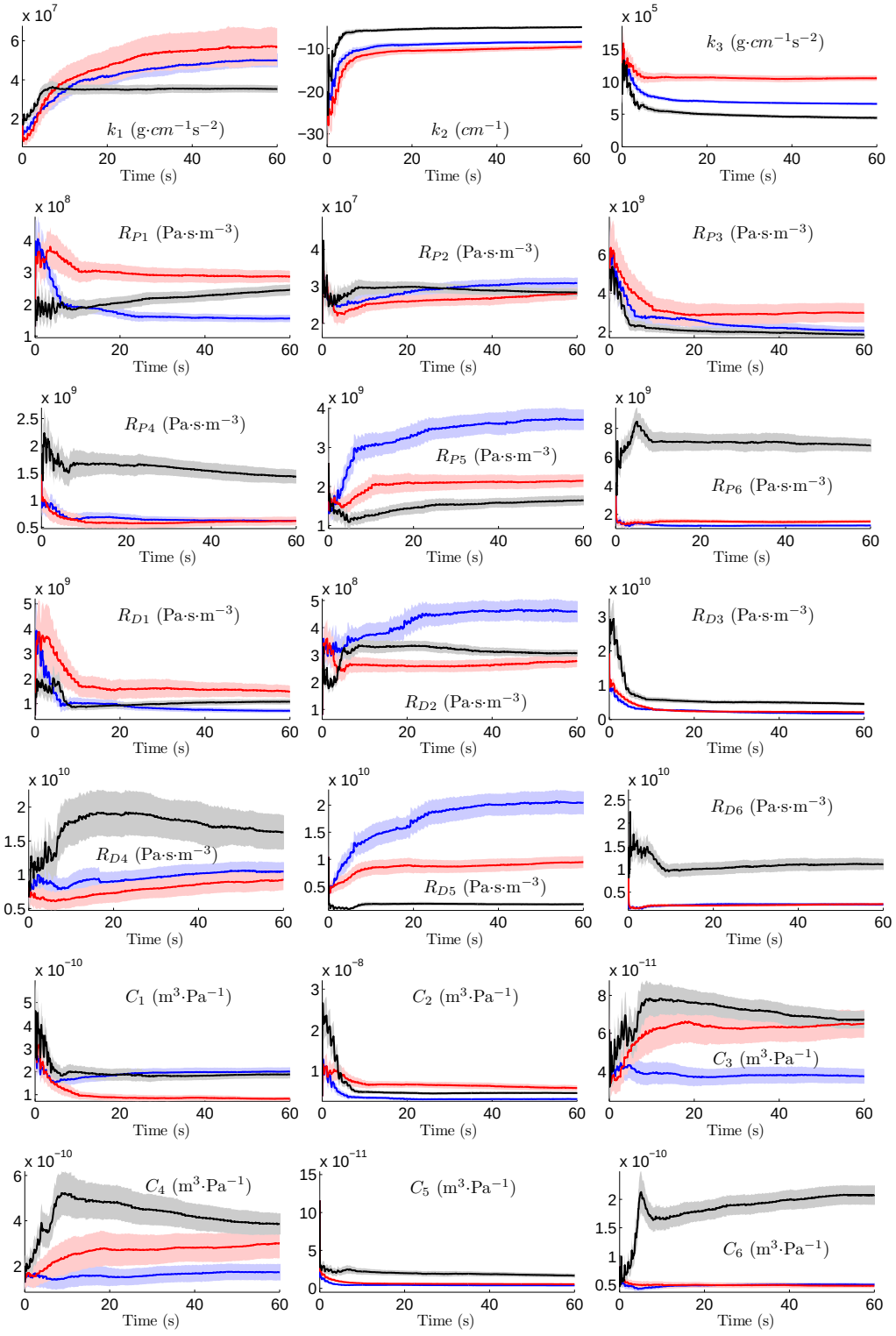

FIGURE 5.19: Sensitivity analysis: The patient-specific fitting. Time evolution of estimated parameters with the three scenarii: ODE21 (in blue), ODE21L (in red), and ODE21RL (in black). The shaded areas represent the standard deviation around the ensemble mean values (solid lines).

TABLE 5.8: Sensitivity analysis: Estimated parameters (with associated errors) for the patient specific fitting with the three scenarii: ODE21, ODE21L, and ODE21RL. The values of constants k_1, k_2, and k_3 are in $\times 10^7$ g·cm^{-1}s^{-2}, cm^{-1}, and $\times 10^5$ g·cm^{-1}s^{-2} respectively. The proximal (R_P) and distal (R_D) resistances are in $\times 10^9$ Pa·s·m^{-3} and the compliance (C) are in $\times 10^{-10}$ m^{3}Pa^{-1}.

Parameter	Initial guess	Final EnKF estimate ± error		
		ODE21	ODE21L	ODE21RL
k_1	2.00	4.99 ± 0.36	5.70 ± 0.96	3.53 ± 0.19
k_2	-22.0	-8.47 ± 0.32	-9.62 ± 0.60	-5.00 ± 0.27
k_3	8.5	6.60 ± 0.20	10.52 ± 0.41	4.44 ± 0.25
R_{P8}	0.02	0.031 ± 0.002	0.03 ± 0.002	0.028 ± 0.001
R_{P13}	1.67	0.62 ± 0.05	0.62 ± 0.08	1.43 ± 0.13
R_{P15}	0.13	0.15 ± 0.01	0.29 ± 0.02	0.24 ± 0.02
R_{P24}	2.61	3.71 ± 0.26	2.15 ± 0.16	1.64 ± 0.13
R_{P30}	3.70	1.23 ± 0.07	1.51 ± 0.12	6.81 ± 0.44
R_{P33}	4.8	2.04 ± 0.22	2.98 ± 0.49	1.84 ± 0.15
R_{D8}	0.08	0.46 ± 0.04	0.28 ± 0.001	0.31 ± 0.001
R_{D13}	6.68	10.44 ± 1.40	9.23 ± 0.20	16.19 ± 0.22
R_{D15}	0.52	0.71 ±0.09	1.48 ± 0.016	1.00 ± 0.01
R_{D24}	10.44	20.42 ± 2.13	9.48 ± 0.08	1.69 ± 0.02
R_{D30}	14.80	2.33 ± 0.33	2.40 ± 0.03	11.03 ± 0.08
R_{D33}	19.32	1.70 ± 0.15	2.13 ± 0.04	4.53 ± 0.04
C_8	38.78	31.90 ± 2.47	58.78 ± 6.86	46.44 ± 2.54
C_{13}	1.27	1.73 ± 0.36	3.00 ± 0.65	3.86 ± 0.47
C_{15}	2.58	2.00 ± 0.18	0.82 ± 0.10	1.88 ± 0.18
C_{24}	1.16	0.04 ± 0.004	0.06 ± 0.006	0.17 ± 0.03
C_{30}	0.82	0.49 ± 0.03	0.48 ± 0.04	2.12 ± 0.17
C_{33}	0.62	0.37 ± 0.04	0.65 ± 0.07	0.66 ± 0.05

TABLE 5.9: Sensitivity analysis: comparison of the cardiac cycle-averaged (mean) and maximum (peak) volumetric flow rates of model simulated values with scenarii ODE21, ODE21L, and ODE21RL to measured values using MRI in the ICA's. The percentage difference between the model results and the MRI data are stated in red in parenthesis. The model results are also compared with the reported values in Ford et al. [170].

ICA	Maximum (peak) flow rate (ml/s)					Mean flow rate (ml/s)				
	MRI	Model			Ford et al. [170]	MRI	Model			Ford et al. [170]
		ODE21	ODE21L	ODE21RL			ODE21	ODE21L	ODE21RL	
Right	6.18 (±0.90)	6.05 (±0.89) (2.12%)	6.03 (±0.91) (2.5%)	6.07 (±0.90) (1.8%)	7.76 (±1.55)	4.31 (±0.90)	4.33 (±0.89) (0.46%)	4.25 (±0.91) (1.4%)	4.32 (±0.90) (0.23%)	4.62 (±0.93)
Left	5.94 (±0.82)	5.70 (±0.82) (4.12%)	5.61 (±0.80) (5.71%)	5.73 (±0.83) (3.6%)	7.35 (±1.72)	4.13 (±0.82)	4.18 (±0.82) (1.2%)	4.18 (±0.79) (1.2%)	4.18 (±0.83) (1.2%)	4.53 (±1.00)

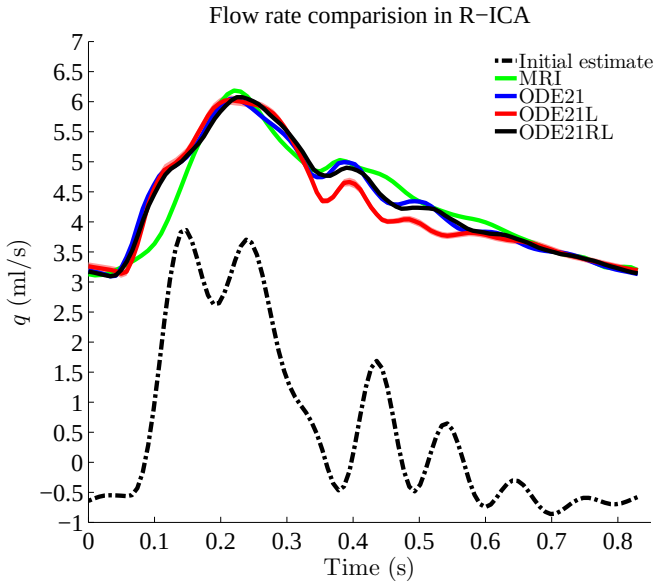

(a)

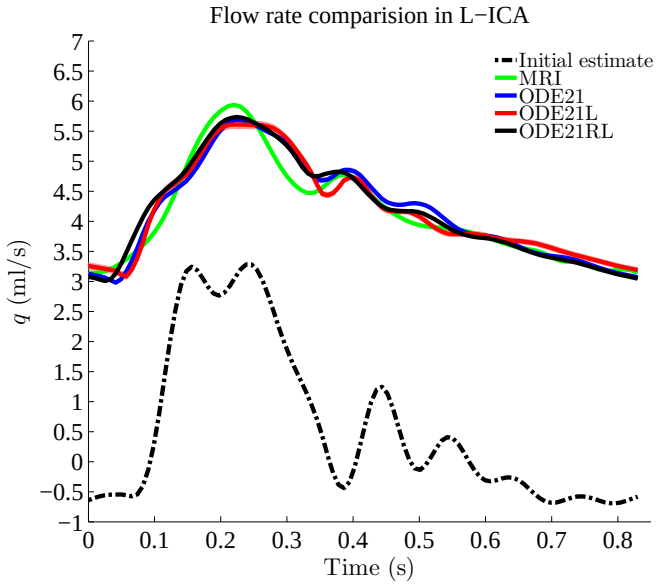

(b)

FIGURE 5.20: (5.20a) Comparison of the simulated blood flow rate waveform with the three scenarii: ODE21 (in blue), ODE21L (in red - as a posteriori validation), and ODE21RL (in black) to the target (MRI data in green) in the R-ICA. The dotted black line is the model simulation based on the initial estimate of parameters. The shaded areas represent the standard deviation around the ensemble mean values. (5.20b) shows the corresponding comparison of the blood flow in the L-ICA using the scenario ODE21 (in blue as a posteriori validation), ODE21L (in red), and ODE21RL (in black).

In order to better compare the precision of the three different scenarii, we also computed the percentage norm of the analysis error in the converged model solution relative to the norm of the target MRI measurement:

$$\frac{\| q_a - q_{\text{mri}} \|}{\| q_{\text{mri}} \|} \times 100\% \tag{5.17}$$

where q_a denotes the converged solution (blood flow rate) when the model is simulated with the parameters estimated using the three different scenarii, q_{mri} is the blood flow rate acquired using MRI (target), and $\| \cdot \|$ is the L_2 norm. The analysis errors provide us with information on the closeness of different scenarii and also they give the difference between the predicted and the observed data. The percentage norm of the analysis error with the three scenarii is shown in Table 5.10. Scenario ODE21RL produces the smallest analysis errors showing a slight improvement in the errors with $nobs = 2$.

TABLE 5.10: Sensitivity analysis: the percentage norm of the analysis error in the converged model solution relative to the norm of the target MRI measurement on the right and left internal carotid arteries using the scenarii ODE21, ODE21L and ODE21RL.

Artery	Scenario		
	ODE21	ODE21L	ODE21RL
R-ICA	6.12%	7.94%	5.60%
L-ICA	5.26%	5.22%	4.75%

From a clinical point of view, an estimation of vessel stiffness can be a relevant indicator in case of cardiovascular pathologies [23, 171]. The arterial stiffness are mainly determined by the Young's modulus (E) and the wall thickness (h) and is assumed to vary with radius (r) [168], i.e.

$$\frac{Eh}{r} = k_1 \, e^{k_2 r} + k_3 \tag{5.18}$$

where the three constants (k's) are estimated using the three scenarii. Figure 5.21 shows the arterial stiffness ($\frac{Eh}{r}$) as a function of r for the three scenarii ODE21, ODE21L, and ODE21RL. This Figure shows that there is a small variation in the estimated arterial stiffness when $nobs$ increases from 1 to 2, though, a similar trend is observed for all the three scenarii. With $nobs = 1$, a good agreement (relative RMSE errors of less than 4%) between the arterial stiffness estimated using scenarii ODE21

and ODE21L is shown. This shows that the arterial stiffness can be estimated with EnKF using observations from independent locations. This can be particularly useful in the clinical practice when the measurements are difficult to acquire at the locations of interest. Scenario ODE21RL, which is the best one can expect, compared to ODE21 and ODE21L, has a relative RMSE error of approximately 14%. As expected, ODE21RL has the smallest percentage norm of the analysis error (giving a better fit to the observed MRI data) and relevant improvement is obtained in the peak and mean blood flow rates, for which relative errors are the smallest. Also, it is noted that with the three scenarios the constants k_1, k_2 and k_3 converged to different values (see Figure 5.19), yet the estimated arterial stiffness does not differ much.

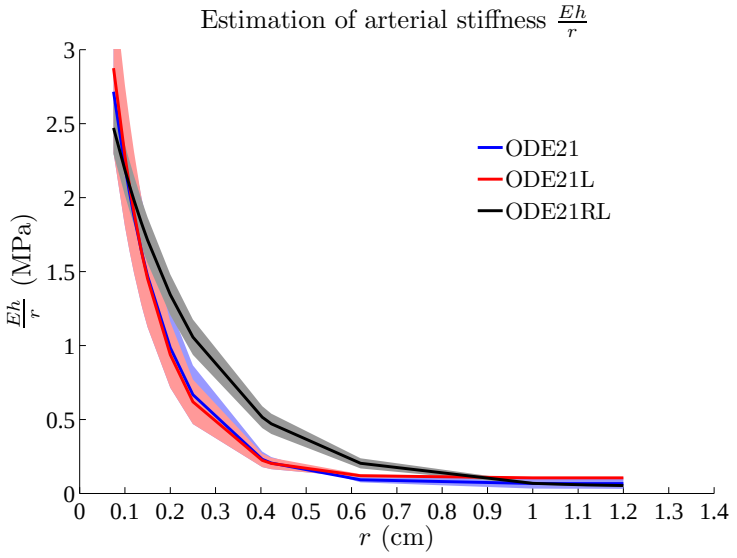

FIGURE 5.21: Estimated arterial stiffness ($\frac{Eh}{r}$) as a function of r for the three scenarii: ODE21, ODE21L, and ODE21RL. The shaded region denotes the standard deviation around the mean (solid lines).

In Figure 5.22, the simulated pressure waveforms in the two ICA's are shown. For right and left ICA's, similar waveforms are observed by the three scenarii. The uncertainties in pressure values are shown by the shaded areas around the mean predicted pressure values in Figures 5.22a and 5.22b. There is a slight discrepancy (relative error of less than 2%) between the peak pressure estimated using scenarii ODE21 and ODE21L. With scenario ODE21RL the relative error in the predicted peak pressure in the ICA's is less than 4% compared to ODE21 and ODE21L. As no clinical measurements of pressure are available for validation, the confidence in pressure predictions of the model are based on the convergence of estimated

parameters and from the fit between observed and predicted blood flow rate from the model using estimated parameters.

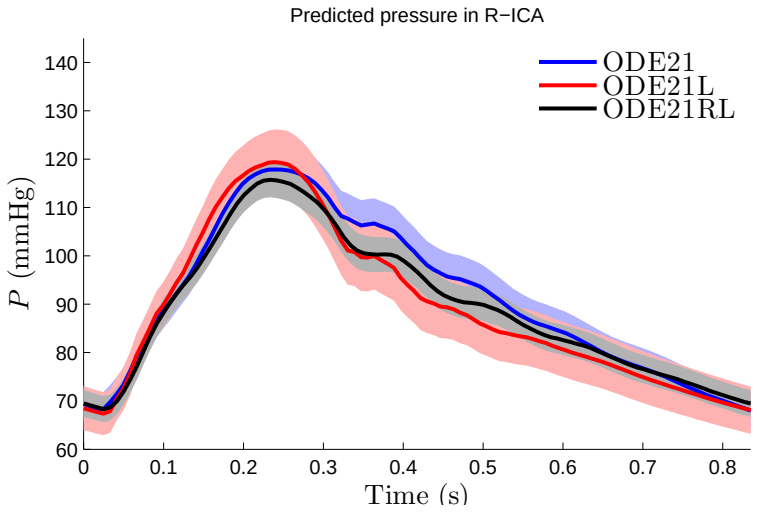

(a)

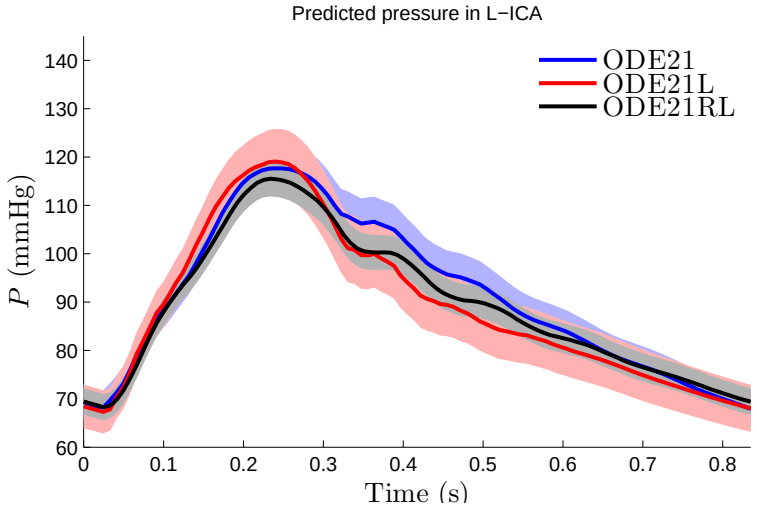

(b)

FIGURE 5.22: The model simulated pressure waveforms in the right (5.22a) and left ICA's (5.22b) with the three scenarii: ODE21, ODE21L, and ODE21RL. The uncertainties are shown by the shaded areas (denoting standard deviation) around the mean pressure values.

The systolic blood pressure (SBP) and diastolic blood pressure (DBP) in major arteries constituting the circle of Willis, vertebral arteries, and some larger arteries are predicted using the scenarii ODE21, ODE21L, and ODE21RL. The predicted pressure's (SBP and DBP) are shown in Figure 5.23. In the Seventh Report of the Joint National Committee on Prevention, Detection, Evaluation, and Treatment

[172], blood pressure for adults is classified as normotensive (SBP $<$ 120 and DBP $<$ 80 mmHg), prehypertension (SBP 120-139 mmHg or DBP 80-90 mmHg), and hypertensive (SBP $\geq$ 140 and/or DBP $\geq$ 90 mmHg). With all the scenarii the predicted pressures in the arteries constituting the CoW are within the physiological values of a healthy patient. With ODE21L, slightly higher SBP is predicted in all the arteries. In the ascending aorta and common carotid arteries, the predicted pressures fall in the prehypertension category following Chobanian et al. [172].

Despite these little differences, one can however conclude that the three inversions give nearly the same pressure level predictions in the different arteries.

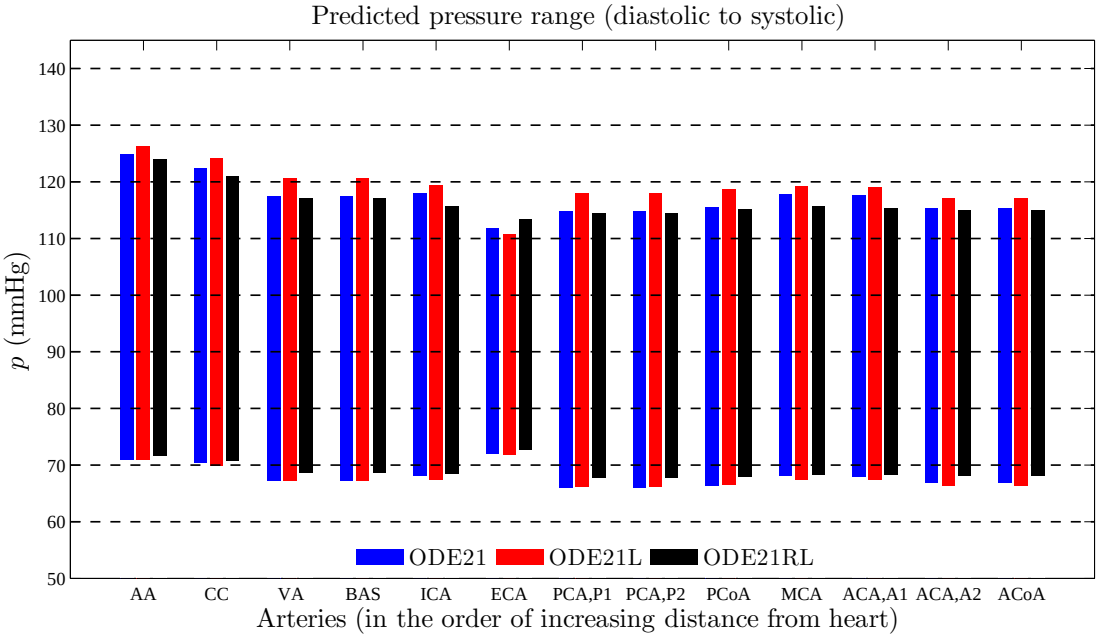

FIGURE 5.23: The pressure (SBP and DBP) in major arteries constituting the circle of Willis, vertebral arteries, and larger arteries as predicted using the three scenarii: ODE21, ODE21L, and ODE21RL. The names of the arteries are written using acronyms which correspond to those in Table 5.11.

Finally, mean pressure values per cardiac cycle are computed in each of the arteries in Figure 5.23. The mean arterial pressure (MAP) that is usually calculated from a patient's SBP and DBP is often used as an index of overall blood pressure [173]. In clinical practice, the brachial artery MAP is usually estimated at the upper arm as: MAP $=$ $\frac{1}{3}$SBP + $\frac{2}{3}$DBP [173–176]. Table 5.11 compares the computed mean pressure values in the arteries to the MAP calculated using the clinical formula above. Overall, the error between the computed mean pressure values and calculated MAP is less than 9%.

Moreover, all the mean values are within the normal range of hemodynamic parameter for a healthy patient, i.e. MAP of 70-105 mmHg [174, 176, 177].

TABLE 5.11: Comparison of computed mean pressure values in the arteries with model (using the three scenarii: ODE21, ODE21L, and ODE21RL) to the MAP (in parenthesis) calculated as $\frac{1}{3}$SBP + $\frac{2}{3}$DBP. MAP of 70-105 mmHg is considered as a normal hemodynamic parameter for a healthy patient [174, 176, 177]. All values are in mmHg.

Artery	ODE21	ODE21L	ODE21RL
Ascending aorta (AA)	96.79 (88.88)	94.43 (89.26)	94.77 (89.02)
Common carotid (CC)	94.91 (87.70)	92.56 (87.88)	93.04 (87.42)
Vertebral artery (VA)	90.78 (83.91)	89.36 (84.99)	90.14 (84.64)
Basilar (BAS)	90.78 (83.91)	89.36 (84.99)	90.14 (84.64)
Internal carotid artery (ICA)	91.26 (84.62)	89.05 (84.70)	89.43 (84.10)
External carotid artery (ECA)	92.19 (85.14)	89.42 (84.66)	91.23 (86.18)
Post. cerebral artery P1 (PCA, P1)	88.82 (82.16)	87.69 (83.36)	88.62 (83.17)
Post. cerebral artery P2 (PCA, P2)	88.83 (82.16)	87.70 (83.36)	88.63 (83.18)
Post. comm. artery (PCoA)	89.34 (82.62)	88.13 (83.78)	89.02 (83.56)
Middle cerebral artery (MCA)	91.18 (84.55)	88.96 (84.62)	89.33 (84.02)
Anterior cerebral artery A1 (ACA, A1)	91.07 (84.45)	88.85 (84.49)	89.24 (83.92)
Anterior cerebral artery A2 (ACA, A2)	89.52 (82.98)	87.46 (83.17)	88.95 (83.67)
Anterior comm. artery (ACoA)	89.52 (82.98)	87.46 (83.17)	88.95 (83.67)

5.5 Discussion

The objectives of cases 1 to 3 are to identify a set of model parameters (Young's modulus and outlet boundary condition parameters) from measured values (observations) of flow rate. Towards this end, a 0D compartment model is used and shown to be much faster than a classical 1D PDE-based blood flow model yet providing very similar results in terms of blood pressure and flow rate signals. In determining the Kalman gain, the EnKF uses estimates that are based on the ensemble size and its members. An ensemble size of less than 30 is shown to be enough for all the cases considered, using either synthetical or medical observation, with up to 21 uncertainties. The analysis shows good agreement between the measured flow rate from MRI and the outcome of the assimilated compartment model. The pressure estimated in the internal carotid arteries and the arteries in the circle of Willis are within the physiological values of a healthy patient for all the assimilation problems. This shows a valuable robustness of the identification procedure. The secondary peaks present in the MRI flow rate signals are only obtained by scenarii ODE21, ODE21L,

and ODE21RL showing the importance of inertial effects in the physical model. All inversions provide with similar levels for the predicted pressure in the arteries. These numerical tests show that it is also possible to estimate arterial stiffness of a complex network such as the circle of Willis with only few observations. We can also see that the results improve with increasing observation data implying that all available clinical data should be mobilized.

5.6 Study limitations

One of the limitations could be the choice of the formula relating Young's modulus, thickness, and radius for the cerebral arteries. We assumed the same relation for both large and cerebral arteries. The other factor might be the adaptation of missing data from the literature, such as the geometrical parameters of the arteries. For the patient specific case, the parameter estimation algorithm is only tested with a compartment model (reduced order ODE) and not with a 1D blood flow model. This is because the observed computational cost of the PDE-based model for this configuration made it non feasible on standard computers. The PDE-based model is therefore only used for a posteriori validation.

The lack of measured pressure data prevents from testing the model pressure results. This, unfortunately, cannot be avoided as measuring the pressure in these arteries is impossible. However, we have some confidence on the results because the flow rate and pressure are physically linked through the model and that the computed flow rate matches well the observations. Also, the pressure signal has been well retrieved in the synthetic cases. Concerning the limitations and possible improvements, one could mention that the approach assumes zero pressure loss at bifurcations. Also, this study should be seen as a proof of concept as solely one clinical case has been considered. More extensive tests (including the cases of hypertension) are definitely necessary before definite and final conclusions can be drawn.

5.7 Conclusion

The ensemble Kalman filter has been used to estimate the product of Young's modulus and thickness (Eh) and the Windkessel outflow boundary parameters of the

Windkessel model from MRA&MRI data. The patient specific case involves a complex arterial network consisting of the circle of Willis and several larger arteries. To ease up the computational complexity and cost, a reduced order compartment model is coupled with the data assimilation algorithm, leading to an affordable CPU time of less than 3 hours for the most complex case on a standard computer. A relatively good-patient specific fitting is achieved even in the presence of partial geometrical parameters with values filled from the literature. The best performing method for a patient-specific case is with the flow physics described by a compartment model including inertia. In particular, the fit with the extracted flow rate from MRA&MRI observations is found best with the capture of secondary peaks (dicrotic notch) in the waveforms. This appears also necessary to avoid possible false prediction of prehypertension for healthy patients. From the results, the comparison between the assimilated 0D model and in vivo data is fair. Parameter estimation using Ensemble Kalman filter is thus useful in estimating hemodynamic parameters using possible clinical measurements such as blood flow rates or time series pressure values in the arteries.

Conflict of Interest

The authors do not have any conflicts of interest to declare.

Acknowledgment

The authors greatly thank Dr. J. Siguenza for acting as a volunteer in the acquisition procedure.
Research done under the European Union Framework Programme Erasmus Mundus KITE (2013-2617 / 001-001 - EMA2)

Chapter 6

Concluding remarks

Contents

This chapter provides conclusions of the results and discussions of the study research presented in this thesis. The chapter begins with an overview of the work and also addresses research limitations and future research directions.

6.1 Overview of the research and discussions

A general framework and algorithm for hemodynamic parameter estimation using EnKF for patient-specific cardiovascular simulations and prediction are presented. The robustness of the filter is investigated through successful applications in several idealised cases (synthetic data), an in vitro case (experimental data from an in vitro test rig) and a patient-specific case (real clinical data from a volunteer). Common hemodynamic parameters such as arterial wall properties (Young's modulus, wall thickness, and viscoelastic coefficient) and terminal boundary parameters (reflection coefficient and Windkessel model parameters) are estimated (with uncertainties) using time series pressure values and blood flow rate as measurements. Overall, there is a good agreement between the measured and computed quantities for all test cases, validating the approach. Furthermore, sensitivity analysis is carried out to assess the efficiency of EnKF. Sensitivity analysis included the effect of using different types of

observations (or measurements) for data assimilation and the impact on the final assimilated parameter with different initial guesses.

The assimilated parameters were found to be independent on the three different initial guesses and they lead to a good agreement with the measured pressure over the cardiac cycle for the in vitro case. However, we hypothesise that making the initial guesses of parameters to be estimated (for in vitro or clinical case) further from the true (or target) values, at some point we will start to see non-convergence to the true parameters, or convergence to different parameters.

The analysis confirms that the proposed method is quite robust even with a few numbers of measurements, well suited to real clinical applications (cases) where measurements are usually available at only a few locations. We also showed that a reduced order model enables to get a reliable and robust solution of the inverse hemodynamic problem. The compartment model is found to be computationally cheap, and is able to capture the key features of the hemodynamics, like the pressure and blood flow rate waveforms, systolic (peak) and diastolic blood flow rates, and the mean volumetric blood flow rate per cardiac cycle. For the patient-specific case, the goals were to determine the model parameters (Young's modulus, thickness, and WK3 boundary condition parameters) and to match the MRI measured blood flow rate in the internal carotid arteries. The comparison between the assimilated reduced order (0D) model and in vivo data is fair. Sensitivity analysis for the patient specific case revealed that more than one observation signal is necessary to obtain a good estimate and thus a better fit of predicted data with the observed clinical data. Reduced order compartment model seems to be a good approximation to assess the blood pressure in cerebral arteries in a non-invasive manner.

The approach permitted to estimate hemodynamic parameters (arterial wall properties and WK3 boundary parameters) in a complex arterial network including the circle of Willis in a time efficient manner. This approach paves the way for complete patient-specific vascular modelling, in which available uncertain clinical measurements (such as blood flow rates or time series pressure values in the arteries) could be used to estimate (or tune) various uncertain parameters needed for the patient-specific simulations. The methodology has potential clinical applications such as providing reliable predictions of hemodynamic quantities of interest or in-patient treatment planning to assess the cardiovascular condition of a patient.

6.2 Study limitations and future directions

The parameter estimation algorithm has only been tested with reduced order models. The EnKF-based parameter estimation with more sophisticated blood flow models such as 3D FSI will be investigated in the future. Furthermore, the blood flow models do not take into account the pressure loss at bifurcations and suggest for future studies in this area. The model and the parameter estimation algorithm were tested with only one patient-specific dataset as a proof of concept and should be primarily seen as a feasibility study. More extensive patient-specific test and validation are necessary for the perspective of clinical applications before final conclusions are made. Blood flow model accuracy for patient-specific simulations are dependent on the quality of input data from imaging techniques. In order to fully exploit the potential of the EnKF-based parameter estimation algorithm, an improvement in both blood flow modelling and data acquisition procedures is required. Patient-specific models will become increasingly important and with continuing improvements in image acquisition and image processing, it will add accuracy to patient-specific data assimilation. The lack of patient-specific measurements of pressure in the cerebral arteries prevents from testing the model simulated pressure results. This calls for additional work to validate the estimated parameters and blood flow model against measurements of pressure in cerebral arteries. Future work will also involve investigating the choice of modelling assumptions, for example, the formula relating Young's modulus, thickness, and radius for the cerebral arteries.

Bibliography

[1] SJ Sherwin, L Formaggia, J Peiro, and V Franke. Computational modelling of 1D blood flow with variable mechanical properties and its application to the simulation of wave propagation in the human arterial system. *International Journal for Numerical Methods in Fluids*, 43(6-7):673–700, 2003.

[2] Luca Formaggia, Daniele Lamponi, Massimiliano Tuveri, and Alessandro Veneziani. Numerical modeling of 1D arterial networks coupled with a lumped parameters description of the heart. *Computer methods in Biomechanics and Biomedical Engineering*, 9(5):273–288, 2006.

[3] PJ Blanco, SM Watanabe, and RA Feijóo. Identification of vascular territory resistances in one-dimensional hemodynamics simulations. *Journal of Biomechanics*, 45(12):2066–2073, 2012.

[4] Gino I Montecinos, Lucas O Müller, and Eleuterio F Toro. Hyperbolic reformulation of a 1D viscoelastic blood flow model and ADER finite volume schemes. *Journal of Computational Physics*, 266:101–123, 2014.

[5] Etienne Boileau, Perumal Nithiarasu, Pablo J Blanco, Lucas O Müller, Fredrik Eikeland Fossan, Leif Rune Hellevik, Wouter P Donders, Wouter Huberts, Marie Willemet, and Jordi Alastruey. A benchmark study of numerical schemes for one-dimensional arterial blood flow modelling. *International Journal for Numerical Methods in Biomedical Engineering*, 31(10):1–33, 2015.

[6] Olivia Miraucourt, Stéphanie Salmon, Marcela Szopos, and Marc Thiriet. Blood flow in the cerebral venous system: modeling and simulation. *Computer Methods in Biomechanics and Biomedical Engineering*, pages 1–12, 2016.

[7] S Moore, T David, JG Chase, J Arnold, and J Fink. 3D models of blood flow in the cerebral vasculature. *Journal of Biomechanics*, 39(8):1454–1463, 2006.

[8] SA Urquiza, PJ Blanco, MJ Vénere, and RA Feijóo. Multidimensional modelling for the carotid artery blood flow. *Computer Methods in Applied Mechanics and Engineering*, 195(33):4002–4017, 2006.

[9] Vuk Milišić and Alfio Quarteroni. Analysis of lumped parameter models for blood flow simulations and their relation with 1D models. *ESAIM: Mathematical Modelling and Numerical Analysis*, 38(4):613–632, 2004.

[10] Sanjay Pant, Benoit Fabrèges, J-F Gerbeau, and IE Vignon-Clementel. A methodological paradigm for patient-specific multi-scale CFD simulations: from clinical measurements to parameter estimates for individual analysis. *International Journal for Numerical Methods in Biomedical Engineering*, 30(12):1614–1648, 2014.

[11] Patricia Garcia-Canadilla, Paula A Rudenick, Fatima Crispi, Monica Cruz-Lemini, Georgina Palau, Oscar Camara, Eduard Gratacos, and Bart H Bijens. A computational model of the fetal circulation to quantify blood redistribution in intrauterine growth restriction. *PLoS Comput Biol*, 10(6):e1003667, 2014.

[12] Mauro Ursino and Massimo Giannessi. A model of cerebrovascular reactivity including the circle of Willis and cortical anastomoses. *Annals of Biomedical Engineering*, 38(3):955–974, 2010.

[13] Masashi Saito, Yuki Ikenaga, Mami Matsukawa, Yoshiaki Watanabe, Takaaki Asada, and Pierre-Yves Lagrée. One-dimensional model for propagation of a pressure wave in a model of the human arterial network: comparison of theoretical and experimental results. *Journal of Biomechanical Engineering*, 133(12):121005, 2011.

[14] Philippe Reymond, Fabrice Merenda, Fabienne Perren, Daniel Rüfenacht, and Nikos Stergiopulos. Validation of a one-dimensional model of the systemic arterial tree. *American Journal of Physiology-Heart and Circulatory Physiology*, 297 (1):H208–H222, 2009.

[15] Rostislav Khlebnikov and C Alberto Figueroa. Crimson: Towards a software environment for patient-specific blood flow simulation for diagnosis and treatment. In *Workshop on Clinical Image-Based Procedures*, pages 10–18. Springer, 2015.

[16] Viorel Mihalef, Razvan Ioan Ionasec, Puneet Sharma, Bogdan Georgescu, Ingmar Voigt, Michael Suehling, and Dorin Comaniciu. Patient-specific modelling of whole heart anatomy, dynamics and haemodynamics from four-dimensional cardiac CT images. *Interface Focus*, 1(3):286–296, 2011.

[17] Giovanni Biglino, Claudio Capelli, Jan Bruse, Giorgia M Bosi, Andrew M Taylor, and Silvia Schievano. Computational modelling for congenital heart disease: how far are we from clinical translation? *Heart*, pages 1–6, 2016.

[18] Claudio Capelli, Andrew M Taylor, Francesco Migliavacca, Philipp Bonhoeffer, and Silvia Schievano. Patient-specific reconstructed anatomies and computer simulations are fundamental for selecting medical device treatment: application to a new percutaneous pulmonary valve. *Philosophical Transactions of the Royal Society of London A: Mathematical, Physical and Engineering Sciences*, 368(1921): 3027–3038, 2010.

[19] Miguel Silva Vieira, Tarique Hussain, and Carlos Alberto Figueroa. Patient-specific image-based computational modeling in congenital heart disease: A clinician perspective. *Journal of Cardiology and Therapy*, 2(6):436–448, 2015.

[20] Paul D Morris, Andrew Narracott, Hendrik von Tengg-Kobligk, Daniel Alejandro Silva Soto, Sarah Hsiao, Angela Lungu, Paul Evans, Neil W Bressloff, Patricia V Lawford, D Rodney Hose, et al. Computational fluid dynamics modelling in cardiovascular medicine. *Heart*, 102(1):18–28, 2016.

[21] Shu Chien. Mechanotransduction and endothelial cell homeostasis: the wisdom of the cell. *American Journal of Physiology-Heart and Circulatory Physiology*, 292 (3):H1209–H1224, 2007.

[22] John F LaDisa, Lars E Olson, Robert C Molthen, Douglas A Hettrick, Phillip F Pratt, Michael D Hardel, Judy R Kersten, David C Warltier, and Paul S Pagel. Alterations in wall shear stress predict sites of neointimal hyperplasia after stent implantation in rabbit iliac arteries. *American Journal of Physiology-Heart and Circulatory Physiology*, 288(5):H2465–H2475, 2005.

[23] Athanase Benetos, Bernard Waeber, Joseph Izzo, Gary Mitchell, Lawrence Resnick, Roland Asmar, and Michel Safar. Influence of age, risk factors, and cardiovascular and renal disease on arterial stiffness: clinical applications. *American Journal of Hypertension*, 15(12):1101–1108, 2002.

[24] Stephane Laurent, John Cockcroft, Luc Van Bortel, Pierre Boutouyrie, Cristina Giannattasio, Daniel Hayoz, Bruno Pannier, Charalambos Vlachopoulos, Ian Wilkinson, and Harry Struijker-Boudier. Expert consensus document on arterial stiffness: methodological issues and clinical applications. *European Heart Journal*, 27(21):2588–2605, 2006.

[25] Vincent Costalat, Mathieu Sanchez, Dominique Ambard, L Thines, Nicolas Lonjon, Franck Nicoud, H Brunel, JP Lejeune, Henri Dufour, P Bouillot, et al. Biomechanical wall properties of human intracranial aneurysms resected following surgical clipping (IRRAs project). *Journal of Biomechanics*, 44(15): 2685–2691, 2011.

[26] Mathieu Sanchez, Dominique Ambard, Vincent Costalat, Simon Mendez, Franck Jourdan, and Franck Nicoud. Biomechanical assessment of the individual risk of rupture of cerebral aneurysms: a proof of concept. *Annals of Biomedical Engineering*, 41(1):28–40, 2013.

[27] Christopher L Taylor, Zhong Yuan, Warren R Selman, Robert A Ratcheson, and Alfred A Rimm. Cerebral arterial aneurysm formation and rupture in 20,767 elderly patients: hypertension and other risk factors. *Journal of Neurosurgery*, 83 (5):812–819, 1995.

[28] Alexander Keedy. An overview of intracranial aneurysms. *McGill Journal of Medicine: MJM*, 9(2):141, 2006.

[29] Yoshiteru Tada, Kosuke Wada, Kenji Shimada, Hiroshi Makino, Elena I Liang, Shoko Murakami, Mari Kudo, Keiko T Kitazato, Shinji Nagahiro, and Tomoki Hashimoto. Roles of hypertension in the rupture of intracranial aneurysms. *Stroke*, 45(2):579–586, 2014.

[30] AWJ Hoksbergen, B Fülesdi, DA Legemate, and L Csiba. Collateral configuration of the circle of Willis transcranial color-coded duplex ultrasonography and comparison with postmortem anatomy. *Stroke*, 31(6): 1346–1351, 2000.

[31] AG Radaelli, Luca Augsburger, JR Cebral, M Ohta, DA Rüfenacht, R Balossino, G Benndorf, DR Hose, A Marzo, R Metcalfe, et al. Reproducibility of haemodynamical simulations in a subject-specific stented aneurysm model—a

report on the virtual intracranial stenting challenge 2007. *Journal of Biomechanics*, 41(10):2069–2081, 2008.

[32] J Alastruey, KH Parker, J Peiró, SM Byrd, and SJ Sherwin. Modelling the circle of Willis to assess the effects of anatomical variations and occlusions on cerebral flows. *Journal of Biomechanics*, 40(8):1794–1805, 2007.

[33] Radomir Chabiniok, Philippe Moireau, P-F Lesault, Alain Rahmouni, J-F Deux, and Dominique Chapelle. Estimation of tissue contractility from cardiac cine-MRI using a biomechanical heart model. *Biomechanics and Modeling in Mechanobiology*, 11(5):609–630, 2012.

[34] Sanjay Pant, Chiara Corsini, Catriona Baker, Tain-Yen Hsia, Giancarlo Pennati, Irene E Vignon-Clementel, Modeling of Congenital Hearts Alliance (MOCHA) Investigators, et al. Data assimilation and modelling of patient-specific single-ventricle physiology with and without valve regurgitation. *Journal of Biomechanics*, 2015.

[35] Damiano Lombardi. Inverse problems in 1D hemodynamics on systemic networks: A sequential approach. *International Journal for Numerical Methods in Biomedical Engineering*, 30(2):160–179, 2014.

[36] Philippe Moireau, Cristobal Bertoglio, Nan Xiao, C Alberto Figueroa, CA Taylor, Dominique Chapelle, and J-F Gerbeau. Sequential identification of boundary support parameters in a fluid-structure vascular model using patient image data. *Biomechanics and Modeling in Mechanobiology*, 12(3):475–496, 2013.

[37] Rajnesh Lal, Bijan Mohammadi, and Franck Nicoud. Data assimilation for identification of cardiovascular network characteristics. *International Journal for Numerical Methods in Biomedical Engineering*, 2016. doi: 10.1002/cnm.2824.

[38] Luca Bertagna, Marta D'Elia, Mauro Perego, and Alessandro Veneziani. Data assimilation in cardiovascular fluid–structure interaction problems: An introduction. In *Fluid-Structure Interaction and Biomedical Applications*, pages 395–481. Springer, 2014.

[39] Cristóbal Bertoglio, Philippe Moireau, and Jean-Frederic Gerbeau. Sequential parameter estimation for fluid–structure problems: Application to hemodynamics. *International Journal for Numerical Methods in Biomedical Engineering*, 28(4):434–455, 2012.

[40] Cristobal Bertoglio, David Barber, Nicholas Gaddum, Israel Valverde, Marcel Rutten, Philipp Beerbaum, Philippe Moireau, Rodney Hose, and Jean-Frédéric Gerbeau. Identification of artery wall stiffness: In vitro validation and in vivo results of a data assimilation procedure applied to a 3D fluid–structure interaction model. *Journal of Biomechanics*, 47(5):1027–1034, 2014.

[41] Vincent Martin, Francois Clément, Astrid Decoene, and Jean-Frédéric Gerbeau. Parameter identification for a one-dimensional blood flow model. In *ESAIM: Proceedings*, volume 14, pages 174–200, Centre International de Rencontres Mathematiques, Marseille, France, 2005. EDP Sciences.

[42] Ryan L Spilker and Charles A Taylor. Tuning multidomain hemodynamic simulations to match physiological measurements. *Annals of Biomedical Engineering*, 38(8):2635–2648, 2010.

[43] Toni Lassila, Andrea Manzoni, Alfio Quarteroni, and Gianluigi Rozza. A reduced computational and geometrical framework for inverse problems in hemodynamics. *International Journal for Numerical Methods in Biomedical Engineering*, 29(7):741–776, 2013.

[44] Lucian Itu, Puneet Sharma, Tiziano Passerini, Ali Kamen, Constantin Suciu, and Dorin Comaniciu. A parameter estimation framework for patient-specific hemodynamic computations. *Journal of Computational Physics*, 281:316–333, 2015.

[45] A Caiazzo, F Caforio, G Montecinos, LO Muller, PJ Blanco, and EF Toro. Assessment of reduced-order unscented Kalman filter for parameter identification in one-dimensional blood flow models using experimental data. *International Journal for Numerical Methods in Biomedical Engineering*, 2016.

[46] Kristen DeVault, Pierre A Gremaud, Vera Novak, Mette S Olufsen, Guillaume Vernieres, and Peng Zhao. Blood flow in the circle of Willis: modeling and calibration. *Multiscale Modeling & Simulation*, 7(2):888–909, 2008.

[47] Andrew C Lorenc. *Atmospheric data assimilation*. Meteorological Office, 1995.

[48] Rudolph Emil Kalman. A new approach to linear filtering and prediction problems. *Journal of Fluids Engineering*, 82(1):35–45, 1960.

[49] Philippe Courtier, E Andersson, W Heckley, D Vasiljevic, M Hamrud, A Hollingsworth, F Rabier, M Fisher, and J Pailleux. The ECMWF implementation of three-dimensional variational assimilation (3D-Var). I: Formulation. *Quarterly Journal of the Royal Meteorological Society*, 124(550):1783–1807, 1998.

[50] Geir Evensen. *Data assimilation: the ensemble Kalman filter*. Springer Science & Business Media, 2009.

[51] Simon J Julier and Jeffrey K Uhlmann. New extension of the Kalman filter to nonlinear systems. In *AeroSense'97*, pages 182–193. International Society for Optics and Photonics, 1997.

[52] Simon J Julier and Jeffrey K Uhlmann. Unscented filtering and nonlinear estimation. *Proceedings of the IEEE*, 92(3):401–422, 2004.

[53] Arthur Gelb. *Applied optimal estimation*. MIT press, 1974.

[54] Eric A Wan and Rudolph Van Der Merwe. The unscented Kalman filter for nonlinear estimation. In *Adaptive Systems for Signal Processing, Communications, and Control Symposium 2000. AS-SPCC. The IEEE 2000*, pages 153–158. IEEE, 2000.

[55] Geir Evensen. Sequential data assimilation with a nonlinear quasi-geostrophic model using Monte Carlo methods to forecast error statistics. *Journal of Geophysical Research: Oceans (1978–2012)*, 99(C5):10143–10162, 1994.

[56] Susan Dunne and Dara Entekhabi. An ensemble-based reanalysis approach to land data assimilation. *Water Resources Research*, 41(2), 2005.

[57] Peter L Houtekamer and Herschel L Mitchell. Data assimilation using an ensemble Kalman filter technique. *Monthly Weather Review*, 126(3):796–811, 1998.

[58] Roger Daley. *Atmospheric data analysis*. Number 2. Cambridge university press, 1993.

[59] F Bouttier and P Courtier. Data assimilation concepts and methods March 1999. *Meteorological Training Course Lecture Series. ECMWF*, 2002.

[60] François-Xavier LE Dimet and Olivier Talagrand. Variational algorithms for analysis and assimilation of meteorological observations: theoretical aspects. *Tellus A*, 38(2):97–110, 1986.

[61] Andrew H Jazwinski. *Stochastic Processes and Filtering Theory*. Academic Press, 1970.

[62] Paul R Houser, Gabriëlle JM De Lannoy, and Jeffrey P Walker. Land surface data assimilation. In *Data Assimilation*, pages 549–597. Springer, The Netherlands, 2010.

[63] Anneke Hommels, Akira Murakami, and Shin-Ichi Nishimura. A comparison of the ensemble Kalman filter with the unscented Kalman filter: application to the construction of a road embankment. *Geotechniek*, 13(1):52, 2009.

[64] William A Lahoz and Philipp Schneider. Data assimilation: making sense of earth observation. *Frontiers in Environmental Science*, 2:16, 2014.

[65] Jeffrey L Anderson. An ensemble adjustment Kalman filter for data assimilation. *Monthly Weather Review*, 129(12):2884–2903, 2001.

[66] Geir Evensen. The ensemble Kalman filter for combined state and parameter estimation. *Control Systems, IEEE*, 29(3):83–104, 2009.

[67] Steven Gillijns and Bart De Moor. Model error estimation in ensemble data assimilation. *Nonlinear Processes in Geophysics*, 14(1):59–71, 2007.

[68] Seung-Jong Baek, Brian R Hunt, Eugenia Kalnay, Edward Ott, and Istvan Szunyogh. Local ensemble Kalman filtering in the presence of model bias. *Tellus A*, 58(3):293–306, 2006.

[69] Hamid Moradkhani, Soroosh Sorooshian, Hoshin V Gupta, and Paul R Houser. Dual state–parameter estimation of hydrological models using ensemble Kalman filter. *Advances in Water Resources*, 28(2):135–147, 2005.

[70] Youmin Tang, Jaison Ambandan, and Dake Chen. Nonlinear measurement function in the ensemble Kalman filter. *Advances in Atmospheric Sciences*, 31(3): 551–558, 2014.

[71] R Srikanthan, GE Amirthanathan, and G Kuczera. Real-time flood forecasting using ensemble Kalman filter. In *MODSIM 2007 International Congress on*

Modelling and Simulation. Modelling and Simulation Society of Australia and New Zealand, pages 1789–1795, Christchurch, New Zealand, 2007.

[72] Nasanao Aoki. *State space modeling of time series*. Cambridge Univ Press, 1990.

[73] Peter J Brockwell and Richard A Davis. *Time series: theory and methods*. Springer Science & Business Media, 2009.

[74] Andrew C Harvey. *Forecasting, structural time series models and the Kalman filter*. Cambridge university press, 1990.

[75] Peter Wallis and Kenneth F Burridge. Prediction theory for autoregressive-moving average processes. *Time Series Analysis and Macroeconometric Modelling: The Collected Papers of Kenneth F. Wallis*, 7(1):236, 1995.

[76] James Douglas Hamilton. *Time series analysis*, volume 2. Princeton university press Princeton, 1994.

[77] Ricardo Todling and Stephen E Cohn. Suboptimal schemes for atmospheric data assimilation based on the Kalman filter. *Monthly Weather Review*, 122(11): 2530–2557, 1994.

[78] M Hoshiya and A Sutoh. Extended Kalman filter-weighted local iteration method for dynamic structural identification. In *Proceedings of the tenth world conference on Earthquake Engineering*, pages 3715–3720, 1992.

[79] RG Brown and Patrick YC Hwang. Introduction to random signals and applied Kalman filtering with MATLAB exercises and solutions, 1996.

[80] Girish Chowdhary and Ravindra Jategaonkar. Aerodynamic parameter estimation from flight data applying extended and unscented Kalman filter. *Aerospace Science and Technology*, 14(2):106–117, 2010.

[81] Rambabu Kandepu, Bjarne Foss, and Lars Imsland. Applying the unscented Kalman filter for nonlinear state estimation. *Journal of Process Control*, 18(7): 753–768, 2008.

[82] Jonathan Ko and Dieter Fox. Gp-bayesfilters: Bayesian filtering using Gaussian process prediction and observation models. *Autonomous Robots*, 27(1):75–90, 2009.

[83] Jonathan Ko, Daniel J Klein, Dieter Fox, and Dirk Haehnel. GP-UKF: Unscented Kalman filters with Gaussian process prediction and observation models. In *Intelligent Robots and Systems, 2007. IROS 2007. IEEE/RSJ International Conference on*, pages 1901–1907. IEEE, 2007.

[84] Philippe Moireau and Dominique Chapelle. Reduced-order unscented Kalman filtering with application to parameter identification in large-dimensional systems. *ESAIM: Control, Optimisation and Calculus of Variations*, 17(02):380–405, 2011.

[85] Stephen J Thomas, JP Hacker, and JL Anderson. A robust formulation of the ensemble Kalman filter. *Quarterly Journal of the Royal Meteorological Society*, 135 (639):507–521, 2009.

[86] Pavel Sakov and Peter R Oke. A deterministic formulation of the ensemble Kalman filter: an alternative to ensemble square root filters. *Tellus A*, 60(2):361–371, 2008.

[87] Geir Evensen. The ensemble Kalman filter: Theoretical formulation and practical implementation. *Ocean Dynamics*, 53(4):343–367, 2003.

[88] PL Houtekamer and Herschel L Mitchell. Ensemble Kalman filtering. *Quarterly Journal of the Royal Meteorological Society*, 131(613):3269–3289, 2005.

[89] Thomas M Hamill and Chris Snyder. A hybrid ensemble Kalman filter-3D variational analysis scheme. *Monthly Weather Review*, 128(8):2905–2919, 2000.

[90] Craig H Bishop, Brian J Etherton, and Sharanya J Majumdar. Adaptive sampling with the ensemble transform kalman filter. part i: Theoretical aspects. *Monthly Weather Review*, 129(3):420–436, 2001.

[91] Jeffrey S Whitaker and Thomas M Hamill. Ensemble data assimilation without perturbed observations. *Monthly Weather Review*, 130(7):1913–1924, 2002.

[92] Edward Ott, Brian R Hunt, Istvan Szunyogh, Aleksey V Zimin, Eric J Kostelich, Matteo Corazza, Eugenia Kalnay, DJ Patil, and James A Yorke. A local ensemble Kalman filter for atmospheric data assimilation. *Tellus A*, 56(5):415–428, 2004.

[93] Steven Gillijns, O Barrero Mendoza, J Chandrasekar, BLR De Moor, DS Bernstein, and A Ridley. What is the ensemble Kalman filter and how

well does it work? In *Proceedings of the 2006 American Control Conference, 2006*, Minneapolis, Minnesota, USA, 2006. IEEE.

[94] Zheqi Shen and Youmin Tang. A modified ensemble Kalman particle filter for non-gaussian systems with nonlinear measurement functions. *Journal of Advances in Modeling Earth Systems*, 2015.

[95] Bijan Mohammadi. Ensemble Kalman filters and geometric characterization of sensitivity spaces for uncertainty quantification in optimization. *Computer Methods in Applied Mechanics and Engineering*, 290:228–249, 2015.

[96] Gerrit Burgers, Peter Jan van Leeuwen, and Geir Evensen. Analysis scheme in the ensemble Kalman filter. *Monthly weather review*, 126(6):1719–1724, 1998.

[97] Peter L Houtekamer and Herschel L Mitchell. A sequential ensemble Kalman filter for atmospheric data assimilation. *Monthly Weather Review*, 129(1):123–137, 2001.

[98] Jaison Thomas Ambadan and Youmin Tang. Sigma-point Kalman filter data assimilation methods for strongly nonlinear systems. *Journal of the Atmospheric Sciences*, 66(2):261–285, 2009.

[99] Humberto C Godinez, Jon M Reisner, Alexandre O Fierro, Stephen R Guimond, and Jim Kao. Determining key model parameters of rapidly intensifying hurricane guillermo (1997) using the ensemble Kalman filter. *ArXiv Preprint ArXiv:1107.4407*, 2011.

[100] Jane Liu and Mike West. Combined parameter and state estimation in simulation-based filtering. In *Sequential Monte Carlo methods in practice*, pages 197–223. Springer, New York, 2001.

[101] Ahmed H Elsheikh, CC Pain, F Fang, JLMA Gomes, and IM Navon. Parameter estimation of subsurface flow models using iterative regularized ensemble Kalman filter. *Stochastic environmental research and risk assessment*, 27(4):877–897, 2013.

[102] NK Nichols. Mathematical concepts of data assimilation. In *Data Assimilation*, pages 13–39. Springer, 2010.

[103] Sally Epstein, Marie Willemet, Phil J Chowienczyk, and Jordi Alastruey. Reducing the number of parameters in 1D arterial blood flow modeling: less

is more for patient-specific simulations. *American Journal of Physiology-Heart and Circulatory Physiology*, 309(1):H222–H234, 2015.

[104] Lucas O Müller and Eleuterio F Toro. A global multiscale mathematical model for the human circulation with emphasis on the venous system. *International Journal for Numerical Methods in Biomedical Engineering*, 30(7):681–725, 2014.

[105] Harvey Ho, Kumar Mithraratne, and Peter Hunter. Numerical simulation of blood flow in an anatomically-accurate cerebral venous tree. *IEEE Transactions on Medical Imaging*, 32(1):85–91, 2013.

[106] Thomas JR Hughes and J Lubliner. On the one-dimensional theory of blood flow in the larger vessels. *Mathematical Biosciences*, 18(1):161–170, 1973.

[107] AP Avolio. Multi-branched model of the human arterial system. *Medical and Biological Engineering and Computing*, 18(6):709–718, 1980.

[108] JC Stettler, P Niederer, and M Anliker. Theoretical analysis of arterial hemodynamics including the influence of bifurcations. *Annals of Biomedical Engineering*, 9(2):145–164, 1981.

[109] N Stergiopulos, DF Young, and TR Rogge. Computer simulation of arterial flow with applications to arterial and aortic stenoses. *Journal of Biomechanics*, 25(12): 1477–1488, 1992.

[110] Mette S Olufsen, Charles S Peskin, Won Yong Kim, Erik M Pedersen, Ali Nadim, and Jesper Larsen. Numerical simulation and experimental validation of blood flow in arteries with structured-tree outflow conditions. *Annals of Biomedical Engineering*, 28(11):1281–1299, 2000.

[111] Luca Formaggia, Daniele Lamponi, and Alfio Quarteroni. One-dimensional models for blood flow in arteries. *Journal of Engineering Mathematics*, 47(3-4): 251–276, 2003.

[112] SJ Sherwin, V Franke, J Peiró, and K Parker. One-dimensional modelling of a vascular network in space-time variables. *Journal of Engineering Mathematics*, 47 (3-4):217–250, 2003.

[113] David Bessems, Marcel Rutten, and Frans Van De Vosse. A wave propagation model of blood flow in large vessels using an approximate velocity profile function. *Journal of Fluid Mechanics*, 580:145–168, 2007.

[114] JP Mynard and P Nithiarasu. A 1D arterial blood flow model incorporating ventricular pressure, aortic valve and regional coronary flow using the locally conservative galerkin (LCG) method. *Communications in Numerical Methods in Engineering*, 24(5):367–417, 2008.

[115] Leif Rune Hellevik, Jan Vierendeels, T Kiserud, N Stergiopulos, F Irgens, Erik Dick, K Riemslagh, and Pascal Verdonck. An assessment of ductus venosus tapering and wave transmission from the fetal heart. *Biomechanics and Modeling in Mechanobiology*, 8(6):509–517, 2009.

[116] Philippe Reymond, Yvette Bohraus, Fabienne Perren, Francois Lazeyras, and Nikos Stergiopulos. Validation of a patient-specific one-dimensional model of the systemic arterial tree. *American Journal of Physiology-Heart and Circulatory Physiology*, 301(3):H1173–H1182, 2011.

[117] K Low, R van Loon, I Sazonov, RLT Bevan, and P Nithiarasu. An improved baseline model for a human arterial network to study the impact of aneurysms on pressure-flow waveforms. *International Journal for Numerical Methods in Biomedical Engineering*, 28(12):1224–1246, 2012.

[118] VG Eck, J Feinberg, HP Langtangen, and LR Hellevik. Stochastic sensitivity analysis for timing and amplitude of pressure waves in the arterial system. *International Journal for Numerical Methods in Biomedical Engineering*, 31(4), 2015.

[119] LO Müller and EF Toro. An enhanced closed-loop model for the study of cerebral venous blood flow. *Journal of Biomechanics*, 47:3361–3372, 2014.

[120] Pablo J Blanco, Sansuke M Watanabe, Enzo A Dari, Marco Aurélio RF Passos, and Raúl A Feijóo. Blood flow distribution in an anatomically detailed arterial network model: criteria and algorithms. *Biomechanics and Modeling in Mechanobiology*, 13(6):1303–1330, 2014.

[121] Pablo J Blanco, Sansuke M Watanabe, Marco Aurélio RF Passos, Pedro A Lemos, and Raúl A Feijóo. An anatomically detailed arterial network model for one-dimensional computational hemodynamics. *IEEE Transactions on Biomedical Engineering*, 62(2):736–753, 2015.

[122] Wouter Huberts, Koen Van Canneyt, Patrick Segers, Sunny Eloot, JHM Tordoir, Pascal Verdonck, FN van de Vosse, and EMH Bosboom. Experimental validation

of a pulse wave propagation model for predicting hemodynamics after vascular access surgery. *Journal of Biomechanics*, 45(9):1684–1691, 2012.

[123] Jordi Alastruey, Ashraf W Khir, Koen S Matthys, Patrick Segers, Spencer J Sherwin, Pascal R Verdonck, Kim H Parker, and Joaquim Peiró. Pulse wave propagation in a model human arterial network: assessment of 1-D visco-elastic simulations against in vitro measurements. *Journal of Biomechanics*, 44(12):2250–2258, 2011.

[124] Brooke N Steele, Jing Wan, Joy P Ku, Thomas JR Hughes, and Charles A Taylor. In vivo validation of a one-dimensional finite-element method for predicting blood flow in cardiovascular bypass grafts. *IEEE Transactions on Biomedical Engineering*, 50(6):649–656, 2003.

[125] Marie Willemet, Valérie Lacroix, and Emilie Marchandise. Validation of a 1d patient-specific model of the arterial hemodynamics in bypassed lower-limbs: simulations against in vivo measurements. *Medical Engineering & Physics*, 35 (11):1573–1583, 2013.

[126] Emilie Marchandise, Marie Willemet, and Valérie Lacroix. A numerical hemodynamic tool for predictive vascular surgery. *Medical Engineering & Physics*, 31(1):131–144, 2009.

[127] Alfio Quarteroni and Luca Formaggia. Mathematical modelling and numerical simulation of the cardiovascular system. In *Computational Models for the Human Body*, volume 12 of *Handbook of Numerical Analysis*, pages 3 – 127. Elsevier Amsterdam, 2004. doi: http://dx.doi.org/10.1016/S1570-8659(03)12001-7.

[128] Sansuke M Watanabe, Pablo J Blanco, and Raúl A Feijóo. Mathematical model of blood flow in an anatomically detailed arterial network of the arm. *ESAIM: Mathematical Modelling and Numerical Analysis*, 47(4):961–985, 2013.

[129] Joaquim Peiró and Alessandro Veneziani. Reduced models of the cardiovascular system. In *Cardiovascular Mathematics*, pages 347–394. Springer Milan, 2009.

[130] Bernard W Schaaf and Peter H Abbrecht. Digital computer simulation of human systemic arterial pulse wave transmission: a nonlinear model. *Journal of Biomechanics*, 5(4):345–364, 1972.

[131] JJ Wang and KH Parker. Wave propagation in a model of the arterial circulation. *Journal of Biomechanics*, 37(4):457–470, 2004.

[132] Eleuterio F Toro and Annunziato Siviglia. Flow in collapsible tubes with discontinuous mechanical properties: mathematical model and exact solutions. *Communications in Computational Physics*, 13(02):361–385, 2013.

[133] Lucas O Müller and Eleuterio F Toro. Well-balanced high-order solver for blood flow in networks of vessels with variable properties. *International Journal for Numerical Methods in Biomedical Engineering*, 29(12):1388–1411, 2013.

[134] Karim Azer and Charles S Peskin. A one-dimensional model of blood flow in arteries with friction and convection based on the womersley velocity profile. *Cardiovascular Engineering*, 7(2):51–73, 2007.

[135] FY Liang, S Takagi, R Himeno, and H Liu. Biomechanical characterization of ventricular–arterial coupling during aging: a multi-scale model study. *Journal of Biomechanics*, 42(6):692–704, 2009.

[136] Irene E Vignon and Charles A Taylor. Outflow boundary conditions for one-dimensional finite element modeling of blood flow and pressure waves in arteries. *Wave Motion*, 39(4):361–374, 2004.

[137] Xiaofei Wang, Jose-Maria Fullana, and Pierre-Yves Lagrée. Verification and comparison of four numerical schemes for a 1D viscoelastic blood flow model. *Computer Methods in Biomechanics and Biomedical Engineering*, 18(15):1704–1725, 2015.

[138] Luca Formaggia, Alfio Quarteroni, and Alessandro Veneziani. *Cardiovascular Mathematics: Modeling and simulation of the circulatory system*, volume 1. Springer Milan, 2010.

[139] Tao Du, Dan Hu, and David Cai. Outflow boundary conditions for blood flow in arterial trees. *PloS One*, 10(5):e0128597, 2015.

[140] Jing Wan, Brooke Steele, Sean A Spicer, Sven Strohband, Gonzalo R Feijo, Thomas JR Hughes, and Charles A Taylor. A one-dimensional finite element method for simulation-based medical planning for cardiovascular disease. *Computer Methods in Biomechanics & Biomedical Engineering*, 5(3):195–206, 2002.

[141] J Alastruey, KH Parker, J Peiró, and SJ Sherwin. Lumped parameter outflow models for 1-D blood flow simulations: effect on pulse waves and parameter estimation. *Communications in Computational Physics*, 4(2):317–336, 2008.

[142] Wilco Kroon, Wouter Huberts, Marielle Bosboom, and Frans van de Vosse. A numerical method of reduced complexity for simulating vascular hemodynamics using coupled 0D lumped and 1D wave propagation models. *Computational and Mathematical Methods in Medicine*, 2012, 2012.

[143] N Stergiopulos, Patrick Segers, and N Westerhof. Use of pulse pressure method for estimating total arterial compliance in vivo. *American Journal of Physiology-Heart and Circulatory Physiology*, 276(2):H424–H428, 1999.

[144] J Alastruey, SM Moore, KH Parker, T David, J Peiró, and SJ Sherwin. Reduced modelling of blood flow in the cerebral circulation: coupling 1-D, 0-D and cerebral auto-regulation models. *International Journal for Numerical Methods in Fluids*, 56(8):1061, 2008.

[145] Mette S Olufsen, Ali Nadim, and Lewis A Lipsitz. Dynamics of cerebral blood flow regulation explained using a lumped parameter model. *American Journal of Physiology-Regulatory, Integrative and Comparative Physiology*, 282(2):R611–R622, 2002.

[146] Nan Xiao, Jordi Alastruey, and C Alberto Figueroa. A systematic comparison between 1-D and 3-D hemodynamics in compliant arterial models. *International Journal for Numerical Methods in Biomedical Engineering*, 30(2):204–231, 2014.

[147] Irene E Vignon-Clementel, CA Figueroa, KE Jansen, and CA Taylor. Outflow boundary conditions for 3D simulations of non-periodic blood flow and pressure fields in deformable arteries. *Computer methods in Biomechanics and Biomedical Engineering*, 13(5):625–640, 2010.

[148] E Messas, M Pernot, and M Couade. Arterial wall elasticity: state of the art and future prospects. *Diagnostic and Interventional Imaging*, 94(5):561–569, 2013.

[149] William Lahoz, Boris Khattatov, and Richard Menard. *Data assimilation: making sense of observations*. Springer-Verlag Berlin Heidelberg, 2010.

[150] JD Annan, JC Hargreaves, NR Edwards, and R Marsh. Parameter estimation in an intermediate complexity earth system model using an ensemble Kalman filter. *Ocean modelling*, 8(1):135–154, 2005.

[151] Xiaosong Yang and Timothy Delsole. Using the ensemble Kalman filter to estimate multiplicative model parameters. *Tellus A*, 61(5):601–609, 2009.

[152] Dusanka Zupanski and Milija Zupanski. Model error estimation employing an ensemble data assimilation approach. *Monthly Weather Review*, 134(5):1337–1354, 2006.

[153] François Massonnet, Hugues Goosse, Thierry Fichefet, and F Counillon. Calibration of sea ice dynamic parameters in an ocean-sea ice model using an ensemble Kalman filter. *Journal of Geophysical Research: Oceans*, 119(7):4168–4184, 2014.

[154] D Mohan, V Munteanu, T Coman, and AV Ciurea. Genetic factors involves in intracranial aneurysms–actualities. *Journal of Medicine and Life*, 8(3):336, 2015.

[155] Chi Zhang, Shuyu Li, Fang Pu, Yubo Fan, and Deyu Li. The effect of anatomic variations of circle of Willis on cerebral blood distribution during posture change from supination to standing: A model study. *Bio-medical Materials and Engineering*, 24(6):2371–2380, 2014.

[156] Laura M Ellwein, Hien T Tran, Cheryl Zapata, Vera Novak, and Mette S Olufsen. Sensitivity analysis and model assessment: mathematical models for arterial blood flow and blood pressure. *Cardiovascular Engineering*, 8(2):94–108, 2008.

[157] Leopold Grinberg, Tomer Anor, Elizabeth Cheever, Joseph R Madsen, and George Em Karniadakis. Simulation of the human intracranial arterial tree. *Philosophical Transactions of the Royal Society of London A: Mathematical, Physical and Engineering Sciences*, 367(1896):2371–2386, 2009.

[158] Yuan Ren, Qiang Chen, and Zhi-Yong Li. A 3D numerical study of the collateral capacity of the circle of Willis with anatomical variation in the posterior circulation. *Biomedical Engineering Online*, 14(1):1, 2015.

[159] Xiao-qing Cheng, Jian-ming Tian, Chang-jing Zuo, Jia Liu, Qi Zhang, and Guang-ming Lu. Quantitative perfusion computed tomography measurements

of cerebral hemodynamics: correlation with digital subtraction angiography identified primary and secondary cerebral collaterals in internal carotid artery occlusive disease. *European Journal of Radiology*, 81(6):1224–1230, 2012.

[160] Benard J Alpers, Richard G Berry, and Richard M Paddison. Anatomical studies of the circle of Willis in normal brain. *AMA Archives of Neurology & Psychiatry*, 81(4):409–418, 1959.

[161] Kanchan Kapoor, Balbir Singh, and Late Inder Jit Dewan. Variations in the configuration of the circle of Willis. *Anatomical Science International*, 83(2):96–106, 2008.

[162] G Mulder, ACB Bogaerds, P Rongen, and FN van de Vosse. The influence of contrast agent injection on physiological flow in the circle of Willis. *Medical Engineering & Physics*, 33(2):195–203, 2011.

[163] M Ursino and M Giulioni. Quantitative assessment of cerebral autoregulation from transcranial doppler pulsatility: a computer simulation study. *Medical Engineering & Physics*, 25(8):655–666, 2003.

[164] KT Moorhead, CV Doran, JG Chase, and T David. Lumped parameter and feedback control models of the auto-regulatory response in the circle of Willis. *Computer Methods in Biomechanics and Biomedical Engineering*, 7(3):121–130, 2004.

[165] A Ferrandez, T David, and MD Brown. Numerical models of auto-regulation and blood flow in the cerebral circulation. *Computer Methods in Biomechanics & Biomedical Engineering*, 5(1):7–19, 2002.

[166] George D Byrne and Alan C Hindmarsh. Stiff ODE solvers: A review of current and coming attractions. *Journal of Computational physics*, 70(1):1–62, 1987.

[167] SP Corwin, S Thompson, and SM White. Solving ODEs and DDEs with impulses. *JNAIAM J. Numer. Anal. Indust. Appl. Math*, 3:139–149, 2008.

[168] Mette S Olufsen. Structured tree outflow condition for blood flow in larger systemic arteries. *American Journal of Physiology-Heart and Circulatory Physiology*, 276(1):H257–H268, 1999.

[169] Mette S Olufsen, Ali Nadim, et al. On deriving lumped models for blood flow and pressure in the systemic arteries. *Math Biosci Eng*, 1(1):61–80, 2004.

[170] Matthew D Ford, Noam Alperin, Sung Hoon Lee, David W Holdsworth, and David A Steinman. Characterization of volumetric flow rate waveforms in the normal internal carotid and vertebral arteries. *Physiological Measurement*, 26(4): 477, 2005.

[171] A. Caiazzo, Federica Caforio, Gino Montecinos, Lucas O. Muller, Pablo J. Blanco, and Eluterio F. Toro. Assessment of reduced-order unscented Kalman filter for parameter identification in 1-dimensional blood flow models using experimental data. *International Journal for Numerical Methods in Biomedical Engineering*, pages n/a–n/a, 2017. ISSN 2040-7947. doi: 10.1002/cnm.2843. URL http://dx.doi.org/10.1002/cnm.2843. cnm.2843.

[172] Aram V Chobanian, George L Bakris, Henry R Black, William C Cushman, Lee A Green, Joseph L Izzo, Daniel W Jones, Barry J Materson, Suzanne Oparil, Jackson T Wright, et al. Seventh report of the joint national committee on prevention, detection, evaluation, and treatment of high blood pressure. *Hypertension*, 42(6):1206–1252, 2003.

[173] HD Kiers, JM Hofstra, and JFM Wetzels. Oscillometric blood pressure measurements: differences between measured and calculated mean arterial pressure. *Neth J Med*, 66(11):474–479, 2008.

[174] Anselmo A Abdo, Roberto Castellanos, Maykel Rocha, Emi Hernández, Geydy Leal, Juliette Suárez, Juan A Gutiérrez, Francisco Gómez, and Alain Cueto. Continuous venovenous hemodiafiltration in patients with multiple organ dysfunction syndrome in an intensive care unit. *MEDICC Review*, 14(3):26–30, 2012.

[175] Howard D Sesso, Meir J Stampfer, Bernard Rosner, Charles H Hennekens, J Michael Gaziano, JoAnn E Manson, and Robert J Glynn. Systolic and diastolic blood pressure, pulse pressure, and mean arterial pressure as predictors of cardiovascular disease risk in men. *Hypertension*, 36(5):801–807, 2000.

[176] Fred M Kusumoto. *Cardiovascular pathophysiology*. Hayes Barton Press, 2004.

[177] Joseph E Parrillo and R Phillip Dellinger. *Critical Care Medicine: Principles of Diagnosis and Management in the Adult (Expert Consult-Online and Print)*. Elsevier Health Sciences, 2013.